Plasmonic Nanodisk Metamaterial Photocatalyst Sheets for Photocatalytic Applications

Von der Fakultät für Elektrotechnik und Informationstechnik der
Rheinisch-Westfälischen Technischen Hochschule Aachen
zur Erlangung des akademischen Grades eines

Doktors der Naturwissenschaften

genehmigte Dissertation vorgelegt von

Benny Ku, M. Sc. RWTH
aus Friedrichroda

Berichtende: Univ.-Professor Dr.-Ing. Max Lemme
Univ.-Professor Jochen Schneider, Ph. D.

Tag der mündlichen Prüfung: 22.09.2025

Diese Dissertation ist auf den Internetseiten der
Universitätsbibliothek online verfügbar.

Abstract

Photocatalysis is a promising approach for harnessing solar energy to drive chemical reactions, converting light into chemical energy. Solar fuel generation or water purification are impactful photocatalytic applications as they can contribute to providing energy and clean water resources. Notably, photocatalytic water splitting converts water into its single component H_2 and O_2. Moreover, photocatalytic CO_2 reduction allows generating a broad range of hydrocarbons, such as CH_4. Lastly, photocatalysis decomposes harmful chemical and bacterial contaminants in water by generating reactive oxygen species (ROS), enabling a chemical-free cleaning method that only relies on sunlight.

Photocatalytic materials are most commonly nanostructure composites based on semiconductors and metals. When exposed to light, photo-excited carriers undergo charge carrier separation, resulting in free-moving electrons and holes. These charge carriers can contribute to photocatalytic reactions once specific redox potentials are met. One promising strategy to enhance photocatalytic materials is the integration of plasmonic nanostructures. These function as nano-antennas that confine incoming light, leading to amplified electric fields through plasmon resonance. This plasmonic effect creates high-energetic states for the charge carriers to trigger redox reactions but can also extend the photocatalytic functionality toward the visible light spectrum.

Photocatalysts in the form of planar sheets are favorable because of their potential scalability, efficiency, durability, and modular mountability. This thesis explores the development and optimization of a plasmonic nanodisk metamaterial photocatalyst sheet design for water splitting, CO_2 reduction, and bacterial inactivation. The base design consists of a periodically arranged plasmonic nanodisk array on a TiO_2 thin film, which is further modified by 2D materials.

In the first part of the thesis, nanodisk materials based on Ag, Au, Pt, and Pd are compared and tested regarding their water splitting and CO_2 reduction properties. The photocatalytic experiments were conducted in a custom-built reactor under visible light illumination. **The highest H_2 and CH_4 generation were achieved under Pt/TiO_2 and Pd/TiO_2 with rates up to 37.63 mmol/gh H_2 and**

5.68 mmol/gh CH_4, respectively. Part of this work was shown at the 48th International Micro and Nano Engineering Conference (MNE 2022) [V] and the European Material Research Society (E-MRS) 2025 Spring Meeting [VI]. Moreover, one patent application was filed to secure the intellectual property (IP) of the metamaterial photocatalyst sheet design [VII], alongside two further patent applications for technological concepts to expand this work [VIII, IX]. A publication in a scientific journal for this work is under preparation [I].

The second part of the thesis demonstrates an adjusted metasurface design. This study explores graphene (Gr) modifications on the Pd/TiO_2-metasurface. For one modification, Gr was wet-transferred to the metasurface, resulting in a suspended Gr layer. In the other modification, carbon black layers were directly grown on the metasurface to show bulk-like properties. **Once modified with the suspended Gr layer, the reactivity is significantly enhanced by 305 % in H_2 and 49 % in CH_4 gas yield rate. The results prove the advantages of Gr layers in photocatalysis due to their high carrier mobility and reactivity. Moreover, the Gr layers suspended between Pd nanodisks create a specific electronic configuration, turning the Gr-Pd contact region into a favorable reaction center.** A publication in a scientific journal for this work is in preparation [II].

The final study investigates the MoS_2-modification of the Pd/TiO_2 metamaterial for Escherichia coli (*E. coli*) bacteria inactivation. **The study reveals that all MoS_2 modifications improve inactivation outcomes, with thinner MoS_2 showing the best results, with up to 99.92 % inactivation due to an optimized type-II heterojunction.** A publication in a scientific journal for this work is under preparation [III].

This work shows the proof-of-principle of efficient and potentially scalable application-oriented photocatalyst sheet designs for water splitting, CO_2 reduction, and bacterial inactivation. It demonstrates the synergy of combining plasmonic metals, 2D materials, and semiconductor oxides as metamaterial structures in photocatalyst sheets. A publication in a scientific journal as a perspective paper about metamaterial photocatalyst sheets for solar fuel generation is under preparation [IV].

Zusammenfassung

Photokatalyse ist ein vielversprechender Ansatz zur Nutzung von Solarenergie zur Ausführung chemischer Reaktionen, bei dem Licht in chemische Energie umgewandelt wird. Die Erzeugung von solaren Brennstoffen oder die Degradation von Verunreinigungen im Wasser sind wichtige photokatalytische Anwendungen, da sie zur Bereitstellung von Energie und sauberen Wasserressourcen beitragen können. Beispielsweise wandelt die photokatalytische Wasserspaltung Wasser in seine Einzelkomponenten H_2 und O_2 um. Darüber hinaus ermöglicht die photokatalytische CO_2-Reduktion die Erzeugung einer Vielzahl von Kohlenwasserstoffen wie z.B. CH_4. Schließlich kann die Photokatalyse genutzt werden um schädliche chemische und bakterielle Verunreinigungen in Wasser durch die Erzeugung reaktiver Sauerstoffspezies (engl. Reactive Oxygen Species, ROS), was eine chemikalienfreie Reinigungsmethode ermöglicht, die ausschließlich auf der Nutzung von Sonnenlicht beruht.

Photokatalytische Materialien sind meist nanostrukturierte Kompositmaterialien auf Basis von Halbleitern und Metallen. Innerhalb des Festkörpers führt Lichteinwirkung zu photoangeregten Ladungsträgern und deren Trennung, wodurch frei bewegliche Elektronen und Löcher entstehen. Beide Ladungsträger können zu photokatalytischen Reaktionen beitragen, sofern bestimmte Redoxpotentiale erreicht werden. Ein vielversprechender Ansatz zur Verbesserung photokatalytischer Materialien ist die Integration plasmonischer Nanostrukturen. Diese fungieren als Nanoantennen, die einfallendes Licht einschließen und durch Plasmonenresonanz verstärkte elektrische Felder erzeugen. Dieser plasmonische Effekt schafft hoch-energetische Zustände für die Ladungsträger, um Redoxreaktionen auszulösen, und kann zudem die photokatalytische Funktionalität in den sichtbaren Wellenlängenbereich erweitern.

Photokatalysatoren in Form planarer Platten sind aufgrund ihrer potenziellen Skalierbarkeit, Effizienz, Stabilität und modularen Montierbarkeit vorteilhaft. Diese Dissertation untersucht die Entwicklung und Optimierung eines Designs von einer plasmonischen Nanodisk-Metamaterial-basierten photokatalytischen Platten für Wasserspaltung, CO_2-Reduktion und Bakterieninaktivierung. Das Grunddesign besteht aus einer periodisch-angeordneten plasmonischen Nanodisks auf

einer TiO_2-Dünnschicht. Dieser wird im Lauf der Arbeit durch 2D-Materialien weiter modifiziert.

Im ersten Teil der Arbeit werden Nanodisk-Materialien auf Basis von Ag, Au, Pt und Pd hinsichtlich ihrer Eigenschaften zur Wasserspaltung und CO_2-Reduktion verglichen und getestet. Die photokatalytischen Experimente wurden in einem speziell konstruierten Reaktor unter Beleuchtung mit sichtbarem Licht durchgeführt. **Die höchsten H_2- und CH_4-Erzeugungsraten wurden mit Pt/TiO_2 bzw. Pd/TiO_2 mit bis zu 37.63 mmol/gh H_2 und 5.68 mmol/gh CH_4 erreicht.** Teile dieser Arbeit wurden auf der 48^{th} International Micro and Nano Engineering Conference (MNE 2022) [V] und dem European Material Research Society (E-MRS) 2025 Spring Meeting präsentiert [VI]. Zudem wurde eine Patentanmeldung zum Schutz des geistigen Eigentums (engl. Intellectual Property, IP) des Metamaterial-Photokatalysator-Designs eingereicht [VII], sowie zwei weitere Patentanmeldungen für technologische Konzepte zur Erweiterung dieser Arbeit [VIII, IX]. Eine Publikation in einer wissenschaftlichen Zeitschrift zu dieser Arbeit ist in Vorbereitung [I].

Der zweite Teil der Arbeit demonstriert ein angepasstes Design der Meta-Oberfläche. Diese Studie untersucht Modifikationen mit Graphen (Gr) auf der Pd/TiO_2-Meta-Oberfläche. Bei der ersten Modifikation wurden Gr-Lagen mittels nass-transfer auf die Meta-Oberfläche übertragen, was zu einer hängenden Gr-Lage führte. Bei der zweiten Modifikation wurden Carbon Black Schichten direkt auf der Meta-Oberfläche gewachsen um bulk-ähnliche Eigenschaften zu zeigen. **Durch die hängende Gr-Lage erhöhte sich die Reaktivität signifikant um 305 % in der H_2- und um 49 % in der CH_4-Gasausbeute. Die Ergebnisse belegen die Vorteile von Gr in der Photokatalyse aufgrund ihrer hohen Ladungsträgermobilität und Reaktivität. Zudem bilden die zwischen Pd-Nanodisks hängenden Gr-Lagen eine spezifische elektronische Konfiguration aus, die den Gr-Pd-Kontaktbereich zu einem Reaktionszentrum macht.** Eine Publikation in einer wissenschaftlichen Zeitschrift zu dieser Arbeit ist in Vorbereitung [II].

Der letzte Teil der Arbeit untersucht die MoS_2-Modifikation der Pd/TiO_2-Metamaterialien zur Inaktivierung von Escherichia coli (*E. coli*)-Bakterien. **Die Ergebnisse zeigen, dass alle MoS_2-Modifikationen die Inaktivierungsergebnisse verbessern, wobei dünnere MoS_2-Schichten die besten Resultate mit bis zu 99.92 % Inaktivierung aufgrund einer optimierten Typ-II-Heteroübergangskonfiguration erzielen.** Eine Publikation in einer wissenschaftlichen Zeitschrift zu dieser Arbeit ist in Vorbereitung [III].

Diese Dissertation zeigt das Prinzip effizienter und potenziell skalierbarer,

anwendungsorientierter Photokatalysator-Designs für Wasserspaltung, CO_2-Reduktion und Bakterieninaktivierung. Sie demonstriert die Synergie von plasmonischen Metallen, 2D-Materialien und Halbleiteroxiden als Metamaterialstrukturen in Photokatalytischen-Platten. Eine Publikation in einer wissenschaftlichen Zeitschrift als Perspective Paper zu Metamaterial- basierten Photokatalysator-Platten für die Erzeugung von solaren Brennstoffe ist in Vorbereitung [IV].

List of Publications

Scientific Journals

[I] **B. Ku**, L. Feierabend, C.-W. Su, C.-C. Huang, G. Aguila Flores, U. Plachetka, M. C. Lemme, "TiO_2 Thin-Film with Metal Nanodisks as Plasmonic Metamaterials Photocatalyst Sheet for IPA-Assisted CO_2 Reduction“, *submitted*

[II] **B. Ku**, L. Feierabend, C.-W. Su, C.-C. Huang, K.-T. Wang, A. Esteki, G. Aguila Flores, U. Plachetka, M. C. Lemme, „Graphene-coupled Pd/TiO_2 Metamaterial Photocatalyst Sheet for IPA-Assisted CO_2 Reduction in Visible Light”, *in preparation*

[III] **B. Ku**, C.-W. Su, H.-E. Chang, V. Jangra, J. Lee, C.-C. Huang, G. Aguila Flores, C.-C. Huang, U. Plachetka, J. Schneider, Y.-J. Hsu, M. C. Lemme, “$MoS_2/Pd/TiO_2$–based Metamaterial Photocatalyst Sheet for Enhanced E. Coli Bacteria Inactivation”, *in preparation*

[IV] **B. Ku**, H.-H. Kuo, U. Plachetka, M. C. Lemme, Y.-J. Hsu, „Periodic Nanostructures for Photocatalytic Water Splitting and CO_2 Reduction: Challenges and Opportunities”, *submitted*

Conferences

[V] **B. Ku**, L. Feierabend, C.-W. Su, U. Plachetka, M. C. Lemme, „Solar Fuel Generation from CO_2 Reduction using Photocatalytic Devices based on Plasmonic Nanodisc Arrays“, poster, 48^{th} International Micro and Nano Engineering Conference (MNE 2022), September 2022, Leuven, Belgium

[VI] **B. Ku**, L. Feierabend, C.-W. Su, C.-C. Huang, G. Aguila Flores, U. Plachetka, M. C. Lemme, „Plasmonic Nanodisk Metamaterial Photocatalyst Sheet for Photocatalytic CO_2 Reduction“, oral, European Materials Research Society (E-MRS), 2025 Spring Meeting, May 2025, Strasbourg, France

Patents

[VII] U. Plachetka, D. Daskalova, **B. Ku**, J. Ruhkopf, G. Aguila Flores, M. C. Lemme, “Strukturiertes Halbleiterbauteil und Verfahren zur Herstellung eines strukturierten Halbleiterbauteils”, Application No. 24 15 9303.7

[VIII] U. Plachetka, D. Daskalova, **B. Ku**, J. Ruhkopf, G. Aguila Flores, M. C. Lemme, „Verfahren zur Herstellung eines strukturierten Bauteils, sowie strukturiertes Bauteil“, Application No. 24 17 3407.8

[IX] **B. Ku**, M. C. Lemme, U. Plachetka, O. Cheong, „Photokatalytischer Reaktor und Verfahren zur Herstellung eines photokatalytischen Panels“, Application No. 10 2024 114 942.6

Acknowledgements

My PhD journey began in October 2019. Although very unusual, I was inspired to pursue a PhD through industry internships at TSMC and ASML during my master studies. There, I discovered that I was passionate to turn semiconductor-related technologies into an application through scientific ways. Before my PhD studies, I was a theorist mainly working on simulations for semiconductor-related problems: I started from optical simulations, went into EUV simulations, and dealt with contamination issues from a theory perspective.

At ASML, which was also my master thesis project, this was also the first time I came into contact with my supervising professor Prof. Dr.-Ing. Max Lemme. I found my path to AMO through one open PhD position at that time that was offered by Dr.-Ing. Ulrich Plachetka, my group leader and daily supervisor. This position was about photocatalytic CO_2 reduction using a periodic-arranged plasmonic nanodisk structure for solar fuel generation. My interest immediately sparked, as I have not expected this sustainable functionality to be possible for nanostructured semiconductor surfaces. At AMO, there was not too much know-how about this approach yet and I was involved to work on this first of a kind project. Moreover, I had the chance to work more experimentally, being fully responsible to fabricate the photocatalytic functional structures.

I want to express my sincere thanks for Max, for his overall leadership, patience and trust. Equally, I thank Ulrich, for his daily guidance and support. Especially in times when I had the entrepreneurial idea for our photocatalyst research to have an open ear for me. Although we did not follow up this plan in the end, it led to filing three patents.

Of course, more people were involved in my five years of research work. The photocatalytic measurements for water splitting and CO_2 reduction were conducted by our project partner Lukas Feierabend, who is a group leader and engineer at Zentrum für Brennstoffzellentechnik (ZBT) GmbH in Duisburg. Although not included in the thesis, I want to thank my colleague Gonzalo Aguila Flores for the methylene blue experiments and all his attempts to build our own custom-built photocatalytic reactor for solar fuel generation.

I am grateful to my master students, Chun-Wei Su (蘇浚瑋) and Chih-Chi

(Dale) Huang (黃至祺), for their significant contributions to our research. For this, I want to express my thanks to you, not only for our time together, but also for trusting me being your supervisor!

From August to October 2023, I was on a short visiting scholar trip to the National Yang-Ming Chiao-Tung University (NYCU) in Hsinchu, Taiwan. There, I joined the group of Prof. Dr. Yung-Jung Hsu (徐雍鎣教授) to learn more about powder-based photocatalyst but also to discover more about their characterization methods. I thank you for hosting and I am looking forward to your future collaborations with Ulrich and Max. From his group, I thank Shan-Jen Yang (楊善任), Hsuan-Hung Kuo (郭軒宏), and Huai-En Chang (張懷恩) for their support in experiments but also being open for any discussions and questions.

At AMO and ELD, I want to express my thanks to the other Sensor group colleagues for all their fruitful discussion: Jasper Ruhkopf, Dessislava (Dessy) Daskalova, and Mustafa Özyurt. Many further special thanks go to Bárbara Canto, Martin Otto, Michael Möller, Thomas Mollenhauer, Horst Windgassen, Florian Schlachter, and Christoph Nowak, who had contribution to my work. Thank you for Marc Dirrichs, especially with the parcels to Taiwan and from Taiwan that was stuck at the local customs! Thank you for all other facility- and administration-related colleagues!

Thank you for all the mensa lunches (at least most of you) but also for afterwork activities to Dr.-Ing. Agata Piacentini, Dr. rer. nat. Dennis Braun, Shayan Parhizkar, Dr.-Ing. Ardedshir Esteki, Kun-Ta Wang, Enes Şeker, Dr.-Ing. Jimin Lee, Vikas Jangra, Maksim Lipkin, Liudmila Starodubtceva, Dr. rer. nat. Giovanna Capraro, Dr.-Ing. Eros Reato, Dr. rer. nat. Lukas Völkel, Niko Rademacher, and Dr.-Ing. Sebastian Lukas. I am happy to have you not only as colleagues but also as friends. And I hope we can maintain our network as long as possible!

Special thanks go to Ulrich, Dennis, Giovanna, Ardedshir, Enes and Jasper for proof-reading my thesis!

My heartfelt gratitude goes to my family: my sisters, Amalie Ku and Cindy Ku, and my parents, for their unwavering support. I am proud to be the first doctor in our family. Finally, I thank my lovely wife, Hsin-Yu (Jade) Ku (顧心瑜), for her constant support and for shaping me into the person I am today. Our wedding during this PhD journey has been a beautiful milestone, and I look forward to our future together.

The research work was financially funded by the projects Hypersol (EFRE-0801494), ACOMAT (UW-01-041B), and COMSOL (BMWK, 49VF210041).

Curriculum Vitae

20.09.2025	Doctoral Examination for Dr. rer. nat.
08/2023–10/2023	Visiting Researcher Nanomaterials and Optoelectronic Devices (NOD) Lab National Yang-Ming Chiao-Tung University Hsinchu, Taiwan
10/2019-09/2025	Research Associate AMO GmbH Aachen, Germany
10/2019-09/2025	Doctoral Student Chair of Electronic Devices RWTH Aachen University, Germany
10/2017–09/2019	Physics (M. Sc.) RWTH Aachen University, Germany
09/2015-07/2016	Exchange Student National Tsinghua University Hsinchu, Taiwan
10/2013–08/2017	Physics (B. Sc.) RWTH Aachen University, Germany
2005–2013	General Higher Education Entrance Qualification (Abitur) Brackweder Gymnasium Bielefeld, Germany
1994	born in Friedrichroda, Germany

Contents

Abstract i

Zusammenfassung iii

List of Publications vii

Acknowledgements ix

Curriculum Vitae xi

Introduction 1

State-of-the-art . . . 2

Scope of this work . . . 6

1 Fundamentals 9

1.1 Band Diagram . . . 9

1.1.1 Metal-Semiconductor Junctions . . . 11

1.1.2 Heterojunctions . . . 13

1.1.3 2D Materials . . . 15

1.2 Plasmonics . . . 16

1.2.1 Plasmon Resonance . . . 17

1.2.2 Hot Electrons . . . 19

1.2.3 Periodic Structures/Metamaterials . . . 19

1.3 Photocatalysis . . . 20

1.3.1 Reaction Potentials . . . 20

Water Splitting . . . 21

CO_2 Reduction . . . 22

Reactive Oxygen Species . . . 24

1.3.2 Adsorption Energy . . . 25

1.3.3 Reaction Evaluation . . . 27

1.4 Photocatalytic Mechanism of Metamaterials . . . 28

2 Methods **33**
2.1 Fabrication Methods . . . 33
2.1.1 Magnetron Sputtering . . . 33
2.1.2 Annealing . . . 34
2.1.3 Laser Interference Lithography . . . 35
2.1.4 Nanoimprint Lithography . . . 36
2.1.5 Reactive Ion Etching . . . 37
2.1.6 Electron Beam Evaporation . . . 38
2.2 Characterization Methods . . . 39
2.2.1 Scanning Electron Microscopy . . . 39
2.2.2 Atomic Force Microscopy . . . 41
2.2.3 Raman Spectroscopy . . . 42
2.2.4 UV-Vis-NIR Spectroscopy . . . 43
2.2.5 Tauc Analysis . . . 44
2.3 Simulations . . . 45
2.3.1 FDTD Simulations . . . 45
2.3.2 FEM Simulations . . . 46
2.3.3 Simulation Output . . . 46

3 Metal Nanodisk Metamaterial Photocatalyst Sheet **47**
3.1 Photocatalyst Design . . . 47
3.2 Fabrication . . . 49
3.3 Characterization . . . 50
3.4 Photocatalytic Water Splitting and CO_2 Reduction . . . 55
3.4.1 Reactor Setup . . . 55
3.4.2 Mass Spectrometry . . . 56
3.4.3 Metamaterial Photocatalyst Mass Calculation . . . 58
3.4.4 Light Source . . . 59
3.4.5 Experimental Results . . . 60
3.4.6 Limitations of the Photocatalytic Reactor . . . 67
3.5 Plasmonic Field Enhancement Simulation . . . 69
3.6 Proposed Charge Carrier Dynamics . . . 70
3.7 Conclusion . . . 72

4 Graphene-modified Pd/TiO_2 Metamaterial Photocatalyst Sheet **73**
4.1 Photocatalyst Design . . . 73
4.2 Fabrication . . . 74
4.2.1 Graphene Wet Transfer . . . 75

4.2.2 Plasma-Enhanced Chemical Vapor Deposition 76
4.3 Characterization 77
4.4 Photocatalytic Water Splitting and CO_2 Reduction 81
4.4.1 Metamaterial Photocatalyst Mass Calculation 81
4.4.2 Experimental Results 82
4.5 Simulations 88
4.6 Proposed Charge Carrier Dynamics 90
4.7 Conclusion 92

5 MoS_2-modified Pd/TiO_2 Metamaterial Photocatalyst Sheet 93
5.1 Photocatalyst Design 94
5.2 Fabrication 95
5.2.1 Sulfurization by Chemical Vapor Deposition 97
5.3 Characterization 98
5.4 Photocatalytic Bacterial Inactivation 104
5.4.1 Method 104
5.4.2 Experimental Results 105
5.5 Simulations 107
5.6 Proposed Charge Carrier Dynamics 108
5.7 Conclusion 110

6 Summary and Outlook 113
6.1 Summary 113
6.2 Outlook 115

A Material Data 119

B Raw Data 125

Bibliography 133

List of Abbreviations

2D	two dimensional
AFM	**a**tomic **f**orce **m**icroscopy
AM1.5	**a**ir **m**ass 1.5 (sunlight spectrum standard)
CB	**c**onduction **b**and
CFU	**c**olony-**f**orming **u**nits
CVD	**c**hemical **v**apor **d**eposition
DC	**d**irect-**c**urrent
DFT	**d**ensity **f**unctional theory
DMSO	**d**i**m**ethyl **s**ulf**o**xide
e-beam	**e**lectron-**beam**
E. coli	**E**scherichia coli
EBL	**e**lectron **b**eam **l**ithography
EDX	**e**nergy-**d**ispersive **X**-ray spectroscopy
EUV	**e**xtreme **u**ltraviolet **l**ithography
FDTD	**F**inite **D**ifferences **T**ime **D**omain
FEM	**F**inite **E**lement **M**ethod
GC	**g**as **c**hromatography / **c**hromatograph
ICP	**i**nductively **c**oupled **p**lasma
IPA	**i**so**p**ropyl **a**lcohol
LB	**l**ysogeny **b**roth
LIL	**l**aser **i**nterference **l**ithography
MFC	**m**ass **f**low **c**ontroller
MPT	**M**oS_2-**P**d-**T**iO_2
MS	**m**ass **s**pectrometry / **s**pectrometer
NIL	**n**ano**i**mprint **l**ithography
NIR	**n**ear **i**nfra**r**ed
ND	**n**ano**d**isk
OD	**o**ptical **d**ensity
PBS	**p**hosphate-**b**uffered **s**aline
PC	**p**hoto**c**atalysis / **p**hoto**c**atalyst
PDE	**p**artial **d**ifferential **e**quation

PDMS	**p**oly**d**i**m**ethyl**s**iloxane
PECVD	**p**lasma-**e**nhanced **c**hemical **v**apor **d**eposition
PMMA	**p**oly (**m**ethyl **m**eth**a**crylate)
PTO	**P**d-**T**i$\mathbf{O_2}$
PVD	**p**hysical **v**apor **d**eposition
RIE	**r**eactive **i**on **e**tching
RF	**r**adio **f**requency
ROS	**r**eactive **o**xygen **s**pecies
SC	**s**emi**c**onductor
sccm	**s**tandard **c**ubic **c**entimeter per **m**inute
SEM	**s**canning **e**lectron **m**icroscopy
SERS	**s**urface-**e**nhanced **R**aman **s**cattering
SPP	**s**urface **p**lasmon **p**olariton
SPR	**s**urface **p**lasmon **r**esonance
STH	**s**olar-**t**o-**h**ydrogen
TOF	**t**urn**o**ver **f**requency
UV	**u**ltra**v**iolet
VB	**v**alence **b**and
Vis	**vis**ible
Ag	silver
$\mathbf{Ag_2O}$	silver oxide
Al	aluminum
Ar	argon
Au	gold
$\mathbf{CH_3OH}$/MeOH	methanol
$\mathbf{CH_4}$	methane
Cd	cadmium
CO	carbon monoxide
$\mathbf{CO_2}$	carbon dioxide
g-$\mathbf{C_3N_4}$/GCN	graphitic carbon nitride
$\mathbf{CF_4}$	tetrafluoromethane
$\mathbf{CHF_3}$	trifluoromethane
$\mathbf{e^-}$	electrons
Gr	graphene
$\mathbf{H^+}$	protons
$\mathbf{H_2}$	hydrogen
$\mathbf{H_2O}$	water

H_2O_2	hydrogen peroxide
He	helium
Mo	molybdenum
MoS_2	molybdenum disulfide
N_2	nitrogen
O_2	oxygen
$O_2^{\bullet -}$	superoxide anion radicals
$^1O_2$	singlet oxygen
$OH^{\bullet}$	hydroxyl radical
Pd	palladium
Pt	platinum
S	sulfur
Si	silicon
SiO_2	silicon dioxide (glass)
$SrTiO_3$/STO	strontium titanate
Ti	titanium
TiO_2	titanium dioxide
Zn	zinc

Physical Constants

Speed of Light (in vacuum)	$c = 2.997\,924\,58 \times 10^{8}\,\mathrm{m/s}$ (exact)
Planck's constant	$h = 6.626 \times 10^{-34}\,\mathrm{Js}$
Ag mass density	$\varrho_{\mathrm{Ag}} = 10.49\,\mathrm{g/cm^3}$
Au mass density	$\varrho_{\mathrm{Au}} = 19.3\,\mathrm{g/cm^3}$
Gr mass density	$\varrho_{\mathrm{Gr}} = 2.26\,\mathrm{g/cm^3}$
Pt mass density	$\varrho_{\mathrm{Pt}} = 21.45\,\mathrm{g/cm^3}$
Pd mass density	$\varrho_{\mathrm{Pd}} = 12.02\,\mathrm{g/cm^3}$
TiO_2 mass density	$\varrho_{\mathrm{TiO_2}} = 4.23\,\mathrm{g/cm^3}$
Avogadro's constant	$N_A = 6.022 \times 10^{23}\,1/\mathrm{mol}$
H_2 Gibbs free energy	$\Delta G_{\mathrm{H_2}} = 237\,\mathrm{kJ/mol}$
CO_2 Gibbs free energy	$\Delta G_{\mathrm{CO_2}} = -394.4\,\mathrm{kJ/mol}$

List of Symbols

A	absorption	-
A_{hex}	unit cell area of a hexagonal periodicity	m^2
A_{PC}	photocatalyst area	m^2
A	absorption	-
D_{ND}	nanodisk diameter	m
E	extinction	-
$\vec{E}$	electric field	V/m
E_{CB}	conduction band level	eV
E_{F}	Fermi level	eV
E_{G}	bandgap energy	eV
E_{vac}	vacuum level	eV
E_{VB}	conduction band level	eV
ΔG	Gibbs free energy	J/mol
H	height / thickness	m
H_{ND}	nanodisk height / thickness	m
H_{SC}	semiconductor height / thickness	m
L_{PC}	photocatalyst sheet length	m
M	molar mass	kg/mol
m	mass	kg
m_{PC}	photocatalyst mass	kg
m/z	mass-to-charge ratio	
N_{ND}	total number of nanodisks	-
n	amount of substances	mol
P	periodicity	m
P_{X}	periodicity in X-direction	m
P_{Y}	periodicity in Y-direction	m
Q_{m}	mass stream	kg/h
Q_{n}	molar stream	mol/h
Q_{V}	volume stream	m^3/h
r	radius	m
r	gas yield rate	mol/h

r_A	area-normalized gas yield rate	mol/m^2h
r_m	mass-normalized gas yield rate	mol/kgh
R	reflection	-
S	scattering	-
t	time	s
T	transmission	-
V_{ND}	nanodisk volume	m^3
V_{SC}	semiconductor layer volume	m^3
α	polarizability	-
χ	electron affinity	eV
χ_S	semiconductor electron affinity	eV
ϵ_m	dielectric function	-
η_{AQY}	apparent quantum yield	-
η_{STF}	solar-to-fuel efficiency	-
η_{STH}	solar-to-fuel efficiency	-
λ	wavelength	m
ϱ	mass density	kg/m^3
ω	angular frequency	1/s
ϕ	work function	eV
ϕ_B	barrier height	eV
ϕ_M	metal work function	eV
ϕ_S	semiconductor work function	eV

Introduction

Light is a major energy source on earth and has over the last century also become one of our most important tool in and for technological development. To date, light-based technologies, such as photovoltaics, lasers, and optics, have become integral to human society, revolutionizing industries, communications, healthcare, energy generation, and more. Among these technologies, photocatalysis, often referred to as artificial photosynthesis, stands out for its potential to harness light for direct conversion into chemical energy [1, 2]. Despite being under extensive research for decades already, its application is considered to be highly promising as it can contribute to sustainable energy solutions [3, 4].

In 1972, Fujishima and Honda [5] first discovered the possibility of photocatalytic water splitting, which is the conversion of water (H_2O) into its single component hydrogen (H_2) and oxygen (O_2). This opened up new avenues for clean energy production, with H_2 emerging as a promising emission-free energy carrier [6]. Over the past half-century, researchers have aimed to unlock its full potential toward a scalable technology [3, 4].

The spectrum of photocatalytic applications is versatile and includes methods such as water purification [7], nitrogen (N_2) fixation [8], or ammonia (NH_3) splitting [9]. Furthermore, photocatalysis offers a pathway to reduce carbon dioxide (CO_2) with protons (H^+) into valuable solar fuels [10] such as methane (CH_4), carbon monoxide (CO), and methanol (CH_3OH; MeOH). These solar fuels present significant advantages over traditional solar-generated electricity, as they can be produced through direct conversion, easily be stored and transported in large-scale in available infrastructures. Conclusively, they can overcome some of the limitations associated with renewable electricity [11, 12].

Despite its promises, photocatalysis remains predominantly confined to academic research, with only a few attempts toward large-scale adaptation [13, 14, 15]. Typical bottlenecks are low efficiency, limited yield, and stability issues, have slowed its transition from laboratory to industry [3, 4]. Optimization approaches to improve photocatalysts typically includes adjusting the material choice, crystallinity, geometry, and reactor designs.

State-of-the-art

Photocatalysis requires in general a well-designed photocatalyst material, a light source, a reactor chamber, and a targeted chemical reaction. Fundamentally, a photocatalytic reaction is a complex multiphysical process that needs to consider different fields of physics and chemistry [16]. A photocatalyst material is an assembly or mixture based on semiconductors in combination with other materials like metals which may be combined to form tailored nanostructures [17]. Semiconductor materials are used due to their unique property of charge carrier separation. When excited by a sufficient energy to overcome their bandgap, they create free charge carriers (electrons and holes) that can drive chemical reactions. However, to combat the inherent challenge of charge recombination in semiconductors, co-catalyst materials are often integrated to obtain efficient photocatalysts [18].

There are several material classes used to improve photocatalysis, including plasmonic metals [19], metal-organic frameworks (MOF) [20], perovskites [21], and two-dimensional (2D) materials [22]. Plasmonic metals, like gold (Au) [23] or silver (Ag) [24], can contribute to the photocatalytic reactivity by enhancing charge separation, increase the availability of free charge carriers, and extend the activity of the photocatalyst material into the visible light spectrum. Specifically, 2D materials, such as graphene (Gr) [25, 26] or molybdenum disulfide (MoS_2) [27, 28], have atomically thin-layers, allows not only chemical stability [29] but also ideal charge carrier transport properties [30]. Optimizing the electronic structure of a photocatalyst material is the key approach to improve its overall performance.

Photocatalysts are typically synthesized as solid powders made of nanostructures, including particle-decorated heterostructures [31, 32], core-shell particles [33, 34], or yolk-shell nanocrystals [35, 36]. These photocatalysts are powder-based and immersed in a liquid phase within stirring reactors during the reaction process [37]. This setup maximizes the exposure of the photocatalyst to the reactant, hence enhancing reactivity by ensuring that active sites on it are accessible in all directions within a three-dimensional space [38, 39].

In contrast, there are photocatalyst sheets which are based on photocatalytic active materials deposited onto planar substrates in fixed positions [40]. They are limited by their exposing surface area, as only the top surface participates in the photocatalytic reactions. To address this drawback, designs for photocatalyst sheets aim to facilitate the efficient collection and utilization of charge carrier transfer for surface reactions.

Photocatalyst sheets have a significant advantage in large-area fabrication in comparison to powder-based photocatalysts. The photocatalyst material can be randomly deposited or grown on the sheet surface, for example by spray-coating [41], printing [42], magnetron sputtering [43], or chemical vapor deposition (CVD) [44]. Alternatively, nanostructures can also be arranged systematically by lithography [45, 46]. Given the crucial role of light interaction for the photocatalytic functionality, the use of periodic structures is reasonable because they can provide plasmon resonance [47], diffraction [48] or light-trapping effects [49], that contribute to the overall absorption. As periodic structures do not occur in nature, they are also known as metamaterials, metasurfaces, or metastructures [50]. Figure 1 illustrates the conceptional setting for the solar fuel generation by a functional metamaterial photocatalyst sheet.

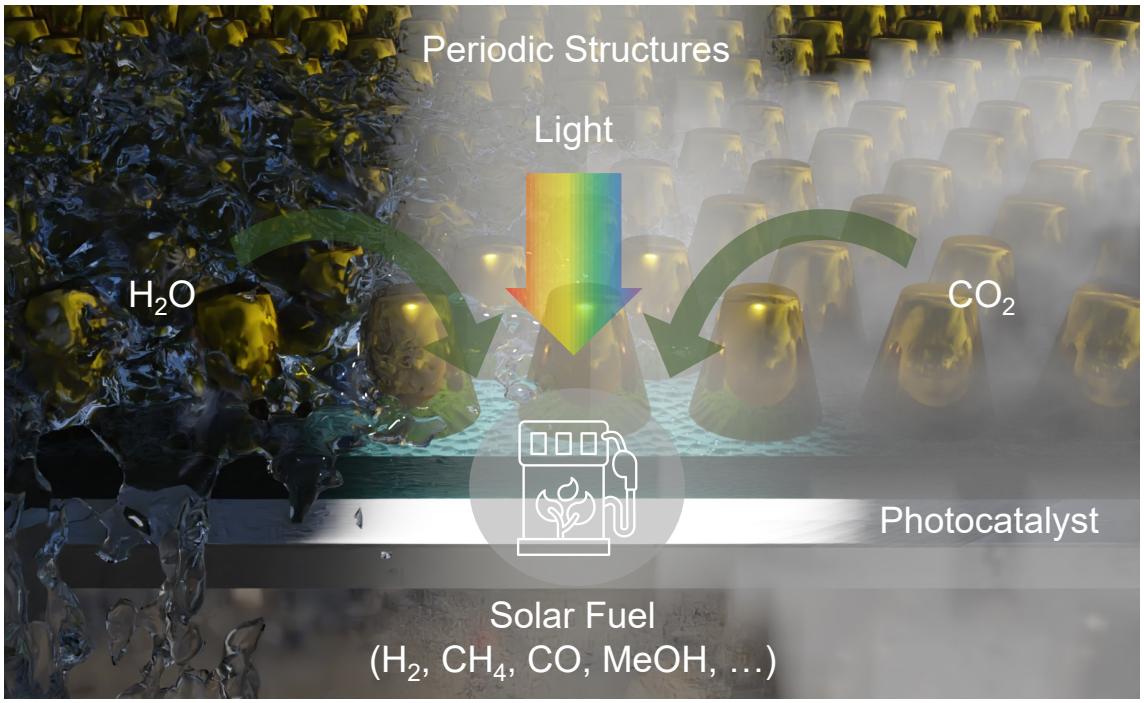


FIGURE 1: Visualization of photocatalytic solar fuel generation on a metamaterial photocatalyst sheet. This image depicts a photocatalyst thin film material on a substrate, featuring a hexagonal-arranged periodic pillar structure. Upon exposure to a light source, the photocatalyst sheet facilitates two key reactions: water splitting (left) and CO_2 reduction (right), both occurring on its surface and yielding solar fuel as the outcome.

A major challenge facing photocatalysis is its low efficiency compared to other sustainable solar fuel generation technologies, such as photovoltaic-coupled electrolysis or photoelectrochemical cells [51]. For instance, efficiency is often reported using metrics such as gas evolution rates which states the yielded amount

of gas, normalized by time, photocatalyst mass or surface area [6, 52]. Specifically for water splitting, the solar-to-hydrogen (STH) efficiency is also often used to quantify the ratio of converted solar into chemical energy [6]. While gas evolution rates quantify the absolute yielded volume of gases produced over time, the STH efficiency provides a broader picture by accounting for the overall energy conversion across the solar spectrum. To date, most reported STH efficiencies for photocatalytic water splitting remain low, typically in the range 1–2 % [3, 40, 53]. Recent advancements, such as those by Zhou et al. [54], have achieved a jump to record-high STH efficiencies of up to 9.2 % in laboratory conditions with deionized water, and 6.2 % under sunlight with tap water. To be economically viable, efficiencies must reach 5-10 %, highlighting the need for continued research and development [3].

The reactor design plays a crucial role in enhancing photocatalytic performance as well. However, most studies focus on lab-scale reactors aimed on understanding reaction kinetics rather than optimizing reactor architectures [37, 55]. There are key parameters that are fixed by the individual reactor setup, such as its geometry, material, and phase configuration. Moreover, there are tunable process parameters like feedstock flow rate [56], feedstock ratio [57], and process temperature [39], that can lead to an increased output once optimized. The choice of light source in laboratory setups [58] and its light path management [59] is another critical factor. However, cross-comparisons between studies challenging as commercial reactor setups are not widely used.

To date, there are only a few promising developments in pilot-scale reactor designs. Goto et al. [41] first achieved a (1×1) m^2 sized photocatalyst panel based on aluminum (Al)-doped strontium titanate ($SrTiO_3$) as photocatalyst material. Under sunlight illumination, they achieved an STH efficiency of 0.4 % (Figure 2a). In a first follow-up work of the same research group, Nishiyama et al. [14] built a large-scale 100 m^2 photocatalytic panel reactor based on the same photocatalyst panel for photocatalytic water splitting. The setup was tested outdoors for one year in Japan under different weather conditions, achieving a peak H_2 generation rate of 3.6–3.7 L/min. In another follow-up work, Yamada et al. [15] extended the setup with thermocatalytic methanation of CO_2 using the photocatalytically generated H_2 (Figure 2b), and demonstrated 43.9 L CH_4 production from 639 L H_2 in three days in Italy. Another pilot reactor, designed by Cao et al. [13], employed parabolic mirrors (Figure 2c) and achieved seasonal variations in H_2 production rates, ranging from 2.9 L/h in spring to 4.0 L/h in summer using

a cadmium (Cd), zinc (Zn) and sulfur (S) composite $Cd_{0.5}Zn_{0.5}S$ as the photocatalyst. While pilot reactors demonstrate the feasibility in scaling-up a photocatalytic setup, they remain not easily accessible to their costs and complexity to implement [3, 4]. Nonetheless, these pilot projects are crucial for demonstrating the state of the art, as they push the boundaries of photocatalysis toward industrial adaptation.

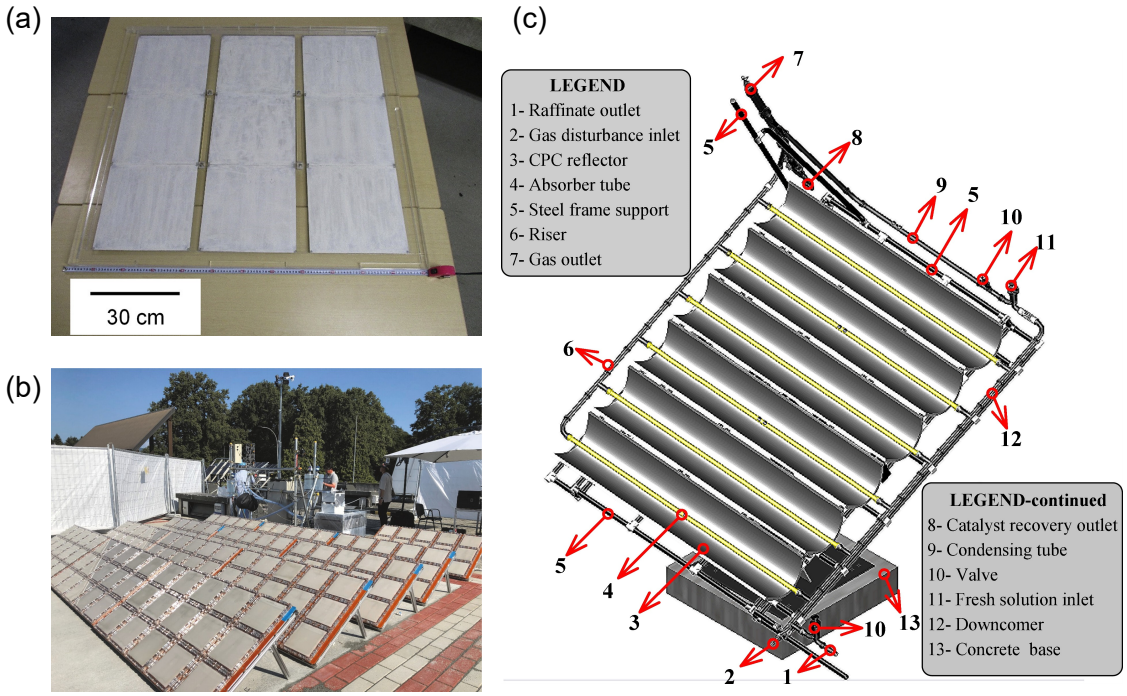


FIGURE 2: (a) Al-doped $SrTiO_3$ first of its kind $(1 \times 1)m^2$ sized photocatalyst panel with 0.4 % STH efficiency under sunlight illumination [Reproduced from [41], Copyright 2017, Elsevier Inc.]. (b) Al-doped $SrTiO_3$ based photocatalyst panel farm for H_2 production [Reproduced from [15], Copyright 2023, The Authors. Published by American Chemical Society]. (c) Photocatalytic reactor setup enhanced by parabolic through mirrors showing a large-scale approach by efficient light management [Reproduced from [13], Copyright 2018, Elsevier Ltd.].

Photocatalysis offers another sustainable application in water purification, addressing the pressing global challenge which is the scarcity of clean water resources in developing countries or crisis regions [60]. This process is based on the generation of reactive oxygen species (ROS) [61] under visible light exposure, eliminating chemical [7], pharmaceutical [62], bacterial [63, 64, 65], and viral [66] contaminants in water. This application provides a sustainable pathway to purify water without the needs for toxic chemicals. Especially, after the COVID-19 pandemic between the years 2019–2022, the awareness of bacterial elimination has

significantly increased and has become more important [67]. Compared to approaches based on photocatalyst powders [68], the use of photocatalyst sheets in water purification is advantageous as it is not required to filter it from the liquid. Despite several setups with scalability approach, photocatalytic water treatment also largely still remains in the academic scope [69].

Scope of this work

This thesis covers five years of research on metamaterial photocatalyst sheets for water splitting, CO_2 reduction, and bacterial inactivation. The metamaterial structure is a periodically-arranged plasmonic metal nanodisk array on a titanium dioxide (TiO_2) thin film. The photocatalyst sheet was fabricated by semiconductor fabrication methods, allowing reproducibility, systematic patterning, flexibility in choice of material and geometry, and potential scalability.

Chapter 1 lays the theoretical foundation covering the basic concepts of photocatalysis. Since this process covers various physical phenomena, this chapter delves into essential topics such as the energy band model, Schottky and Ohmic junctions, plasmonics, periodic structures, chemical potentials, and adsorption properties. Understanding these concepts is required for interpreting the interactions and mechanisms that govern photocatalytic systems, offering a robust knowledge for this thesis.

Chapter 2 outlines the experimental and computational methodologies. It details the fabrication and characterization techniques used to develop the metamaterial photocatalyst sheets, the photocatalytic measurement setups, alongside with the simulation tools to understand charge carrier mechanisms. These simulation tools played a pivotal role in predicting light absorption properties and in designing optimized photocatalysts, as well as in validating experimental results.

Chapter 3 focuses on the base metamaterial photocatalyst sheet design for this thesis, which is a circular-shaped plasmonic metal nanodisk array arranged in a rectangular periodic pattern on a sputtered TiO_2 thin film on a glass substrate. Silver (Ag), gold (Au), platinum (Pt), and palladium (Pd) were chosen as plasmonic metals and tested on photocatalytic CO_2 reduction. As proton source, water splitting was conducted in the same reaction chamber. All four photocatalysts have shown functionality and generated H_2 and CH_4 with different selectivities. Among these metals, the photocatalyst with Pd nanodisk has shown the best CH_4 yield rates.

In Chapter 4, an alternative pattern design was tested to verify the concept of the nanodisk-based metamaterial photocatalyst sheet: Elliptical-shaped nanodisk

arranged in a hexagonal pattern. This chapter focuses again on photocatalytic CO_2 reduction, but only on Pd nanodisks on TiO_2 thin film (Pd/TiO_2), as it has shown the best CH_4 yield rates in the chapter before. The photocatalyst sheet was modified by graphene (Gr), which was wet-transferred or grown by plasma-enhanced chemical vapor deposition (PECVD). These Gr-modified photocatalyst were tested on photocatalytic CO_2 reduction. The first modification shows an outstanding enhancement of the reactivity, while the second one still shows a functioning photocatalyst but with slight differences in the selectivity compared without PECVD-grown Gr.

Chapter 5 proposes the enhancement of Pd/TiO_2-based metamaterial photocatalyst by CVD-synthesized molybdenum disulfide (MoS_2). Instead of photocatalytic CO_2 reduction, this nanodisk-based metamaterial photocatalyst design was tested on photocatalytic inactivation of Escherichia coli (*E. coli*) bacteria. The results show that the integration of MoS_2 leads to an improvement in bacteria inactivation rate through the formation of charge-separating heterojunctions. It shows the proof-of-principle of this nanodisk-based metamaterial photocatalyst sheet design to functions for applications besides solar fuel generation.

Chapter 6 summarizes the findings of this thesis. The outlook of the work is comprehensively discussed, which includes optimization suggestions such as different material choices, design, reactor parameter, and fabrication approaches.

1 Fundamentals

Photocatalysis is a multiphysical process that harnesses the interaction between light and matter. To drive chemical reactions on the photocatalyst surface, suitable electronic properties are required. Hence, a comprehensive theoretical understanding of various scientific principles is needed, covering electrodynamics, solid-state physics, physical chemistry, and thermodynamics [16]. This chapter provides a foundation for the theory underlying photocatalysis, with a particular focus on photocatalyst sheets based on metamaterials.

Photocatalytic processes rely on the unique characteristics of semiconductors, to absorb light and generate free charge carriers (electrons and holes). When reactant molecules adsorb on the photocatalyst surface, the free charge carriers can subsequently contribute reduction and oxidation (redox) reactions. Practically, the process of photocatalysis converts light energy into chemical energy. The integration of metamaterials on photocatalyst sheets provides systematic control over light-matter interactions, opening up new opportunities for enhancing photocatalytic reactivity and selectivity.

1.1 Band Diagram

An understanding of the band diagram is essential for the basic charge carrier mechanisms. This band diagram model simplifies the more complex quantum mechanical theory of solids, providing an useful framework describing the electronic properties of semiconductors and metals [70]. Figure 1.1 illustrates typical band diagrams of a semiconductor and a metal, showing their key properties:

- Fermi Level (E_F): The Fermi level represents the highest energy level that electrons can achieve at absolute zero temperature. It provides a reference point for the distribution of electrons within a semiconductor at any given temperature and influences the position of the valence and conduction band. For semiconductors, E_F lies within the bandgap. At finite temperatures, the probability to find an electron with E_F is fixed at 50 % according to the Fermi-Dirac distribution. [70]

- Valence Band Energy (E_{VB}): The valence band is defined as the highest energy level that is fully occupied by electrons at absolute zero temperature. It represents the energy levels that electrons can occupy without any external energy input. Electrons in this band are tightly bound to atoms and cannot contribute to electrical conduction without excitation. For a semiconductor, E_{VB} lies below E_F.

- Conduction Band Energy (E_{CB}): The conduction band consists of higher energy states that electrons can move into if they are excited by sufficient energy. Electrons in the conduction band are free to move through the material, thus contributing to electrical conductivity. For a semiconductor, E_{CB} lies above E_F.

- Band Gap Energy (E_G): The band gap is the energy difference between the valence and conduction band. To raise electrons from the valence to the conduction band, they must absorb energy equivalent to or greater than the band gap. This energy can be provided through photons (light), thermal excitation, or an electric field. The size of the band gap determines whether a material behaves as a conductor/metal ($E_G = 0\,\text{eV}$), semiconductor ($0\,\text{eV} < E_G \leq 4\,\text{eV}$), or insulator ($E_G > 4\,\text{eV}$).

- Vacuum Level (E_{Vac}): The vacuum level is defined as the energy level that is required for an electron to be removed from the material surface into a surrounding vacuum. Band diagrams are often defined in respect to the vacuum by setting it to $E_{Vac} = 0\,\text{eV}$.

- Electron Affinity (χ): The electron affinity is the energy required to move an electron from the conduction band to the vacuum level in a semiconductor. This parameter helps determining the band alignment at semiconductor interfaces, which is crucial in metal-semiconductor and heterojunctions. χ is defined by the difference between E_{Vac} and E_{CB}.

- Work Function (ϕ): The work function is the minimum energy required to remove an electron from the solid to the vacuum level. It is a critical factor in determining whether the charge carriers transfer to reactants in a photocatalytic process. ϕ is defined by the difference between E_{Vac} and E_{CB}.

All listed key parameters are relevant for semiconductor materials (Figure 1.1a). In the ground state, electrons occupy energy levels below E_F. To get free charge carriers for conduction in a semiconductor, an energy excitation of at least E_G is required. In contrast for a metal, E_F is inherently higher than E_{CB}, resulting

in no bandgap and constant conductivity (Figure 1.1b). Therefore, only E_F and ϕ remain relevant among these parameters for metals.

These band diagram parameters can be fine-tuned through various methods, such as doping [71] and defects [72]. A thorough understanding of the band diagram is essential for designing, optimizing, but also analyzing photocatalysts with enhanced efficiency and selectivity. This knowledge enables the modification of properties like charge carrier generation, separation, and transfer, leading to improved photocatalytic performance.

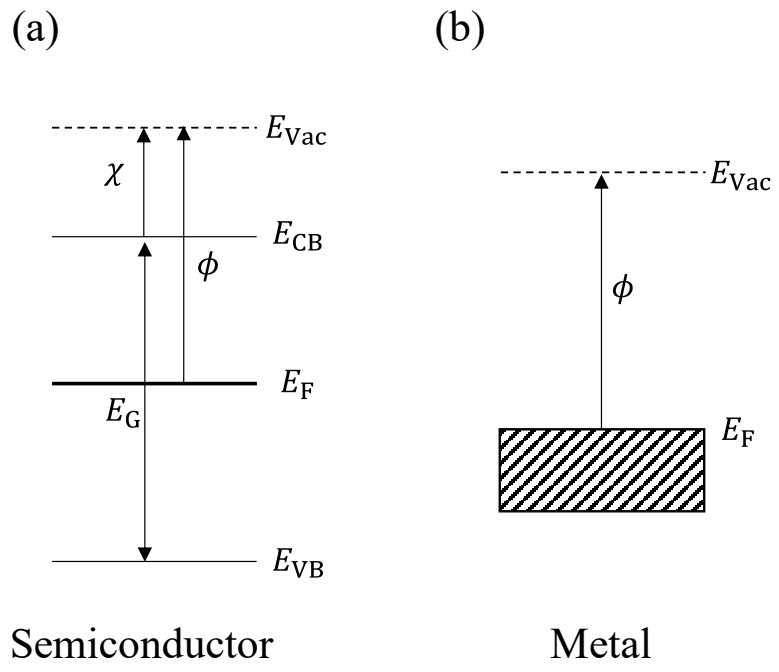


FIGURE 1.1: Schematic band diagram for (a) semiconductors and (b) metals, showing the relation between the key parameter Fermi level (E_F), valence band level (E_{VB}), conduction band level (E_{CB}), band gap energy (E_G), vacuum level (E_{Vac}), work function (ϕ), and electron affinity (χ).

1.1.1 Metal-Semiconductor Junctions

When a metal and a semiconductor are brought into contact, they can form two distinct types of junctions — Schottky or Ohmic — depending on their electronic properties and the relative alignment of their energy levels [73]. These junctions play a critical role in determining the behavior of charge carriers at the interface, which directly influences the electrical characteristics of the resulting material stack and improves the charge separation. In a metal-semiconductor junction, E_F of semiconductor and metal must align in equilibrium, leading to band bending at the interface. For an n-type semiconductor, this results in the upward bending

of the valence and conduction band near the junction, while for a p-type semiconductor, the bands bend downward.

A Schottky junction (Figure 1.2a) creates an energy barrier between the metal and the semiconductor. For an n-type semiconductor, this type of junction arises when

$$\phi_M > \phi_S, \tag{1.1}$$

where ϕ_M and ϕ_S are the work functions of the metal and semiconductor, respectively.

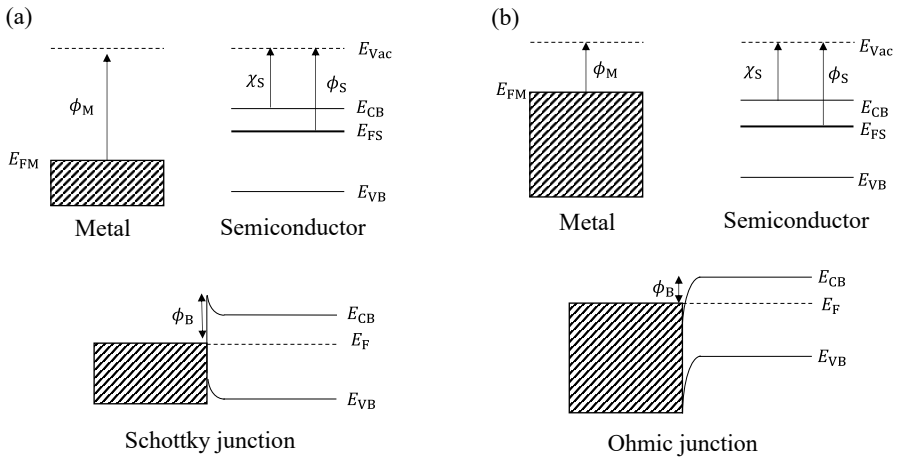


FIGURE 1.2: Schematic energy band diagram for metal-semiconductor junctions. (a) For $\phi_M > \phi_S$, a Schottky junction is formed. (b) For $\phi_M < \phi_S$, an Ohmic junction is formed.

The difference between ϕ_M and the semiconductor's electron affinity (χ_S) results in a rectifying behavior. This allows current to flow more easily in one direction than the other one. The Schottky barrier height (ϕ_B) is the key parameter that controls the movement of charge carriers across the junction. It represents the energy difference that electrons in an n-type semiconductor (or holes in a p-type semiconductor) must overcome to move from the semiconductor into the metal. For an ideal metal-semiconductor contact, the barrier height can be expressed as

$$\phi_B = \phi_M - \chi_S. \tag{1.2}$$

An Ohmic junction (Figure 1.2b) is formed when no energy barrier exists between the metal and the semiconductor, resulting in linear current-voltage (I-V) characteristics. In this case, the metal and semiconductor create a low-resistance contact, allowing current to flow freely in both directions. Ohmic junctions are essential for device contacts where efficient injection and extraction of charge carriers are required.

For n-type semiconductors, an Ohmic junction occurs when

$$\phi_M < \phi_S, \tag{1.3}$$

as this condition ensures that electrons can easily move from the metal into the semiconductor's conduction band.

ϕ_B for an Ohmic junction is typically very small and is defined as

$$\phi_B = \phi_M - \phi_S. \tag{1.4}$$

In theory, the case $\phi_M = \phi_S$ can also exists and would result in no band bending, as E_F of materials would also match each other. This would also create an Ohmic junction as there would not be any barrier ($\phi_B = 0$).

Optimizing metal-semiconductor junctions is one key approach to improve electrical properties of a photocatalyst material stack. This can involve selecting appropriate metals to control the junction type and the barrier height, adjusting semiconductor doping levels, modifying the interface through surface treatments, or thin interlayers to fine-tune the junction properties [74].

1.1.2 Heterojunctions

A heterojunction is formed when two different semiconducting materials are brought into contact, creating an interface with distinct electrical and optical properties [75]. Both semiconductors typically have different band parameters, including E_{VB}, E_{CB}, E_G, ϕ, and χ. The interplay of these parameters is crucial, making heterojunctions an important mechanism in many advanced electronic and photonic devices.

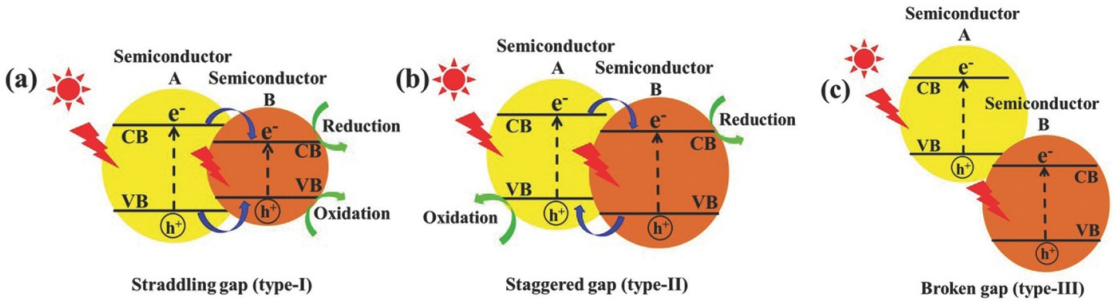


FIGURE 1.3: Schematic band diagram for the three types of heterojunctions under light-excitation: (a) type I (straddling gap), (b) type II (staggered gap), (c) type III (broken gap). All diagrams indicate possible oxidation and reduction reaction, which highly depends on which type of heterojunction. [Modified and reproduced from [76], Copyright 2017, WILEY-VCH Verlag GmbH & Co. KGaA]

The band diagrams of heterojunctions (Figure 1.3) can be explained by the Anderson rule [77], which first assumes that two distinct and separated semiconductor materials have the same E_{vac}. Once in contact, both semiconductor materials encounter an offset in their band parameters. This results in a band alignment, in which the band parameters of both semiconductor materials are adjusted to match E_F. Depending on the relative energy levels of the valence and conduction band of the two materials, three types of heterojunctions can be formed [76]:

- Type I (straddling gap): In this type of heterojunction, the valence and conduction band of one semiconductor lie within the bandgap of the other semiconductor (Figure 1.3a). Both, electrons and holes, are confined to the same material in this configuration. In type I heterojunctions, one material effectively "straddles" the band gap of the other, leading to charge carrier into the semiconductor layer with smaller band gap. Despite several reports of functioning type I heterojunction based photocatalyst, it is less favorable, due to possible charge recombination [78].

- Type II (staggered gap): Here, the conduction band of one semiconductor is lower than that of the other, and the valence band is also shifted similarly (Figure 1.3b). As a result, electrons tend to localize in one material while holes are confined to the other. This spatial separation of charge carriers can lead to longer recombination lifetimes, making type II heterojunctions useful for photocatalysts due to efficient charge carrier separation [79].

- Type III (broken gap): In this configuration, the conduction band of one semiconductor material lies below the valence band of the other. This creates a scenario where there is no energy overlap between valence and conduction band, resulting in a "broken" band alignment (Figure 1.3c). As type III heterojunction does not allow efficient charge carrier transfer between both semiconductor materials, it does not allow efficient electron-hole separation. Hence, it is not suitable as a photocatalyst [79].

For photocatalysts, only type II heterojunctions are advantageous for controlled charge carrier dynamics [76, 79]. The band alignments in these junctions have an influence on the charge carrier generation, separation, and transfer processes, which all contribute to the photocatalytic reactivity. Moreover, the integration of heterojunctions with other approaches, such as co-catalyst loading, surface modification, and nanostructuring, can lead to synergistic effects that further enhance photocatalytic performance [80].

1.1.3 2D Materials

Two-dimensional (2D) materials are well-known for their outstanding electrical, optical and chemical properties that can be beneficial for photocatalysts [81]. For instance, graphene (Gr) [25, 26] and molybdenum disulfide (MoS_2) [27, 28] are two 2D materials with suitable band structures that have often been reported for photocatalytic applications.

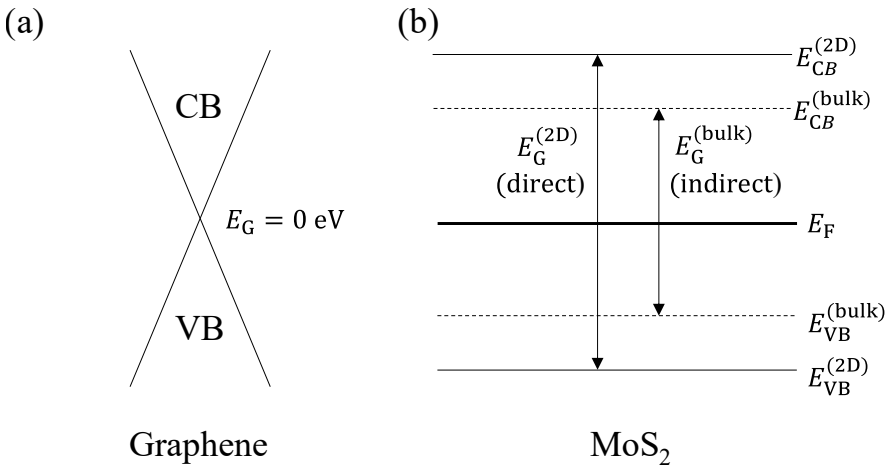


FIGURE 1.4: Band diagram sketch for 2D materials: (a) Gr with Dirac cone and its zero bandgap. (b) MoS_2 with layer-dependent band property tuning, showing the monolayer (2D) and bulk case.

Gr, a single layer of carbon atoms arranged in a hexagonal lattice, exhibits a unique band structure characterized by Dirac cones (Figure 1.4a) [82]. It has semimetallic properties, allowing Gr to have high electron mobility and conductivity [83]. However, the lack of a bandgap limits its direct use in photocatalysis. To overcome this limitation, Gr is turned into an electron sink, such as by creating defects, doping, or forming heterostructures with other materials [84].

In contrast, MoS_2 possesses a bandgap that varies with the number of layers [85]. Monolayer MoS_2 has a direct bandgap of approximately 1.8 eV, while bulk MoS_2 has an indirect bandgap of about 1.2 eV [86]. This layer-dependent band structure allows for tunable optoelectronic properties (Figure 1.4b), making MoS_2 particularly useful for photocatalysis. The bandgap of MoS_2 falls within the optimal range for efficient visible light absorption, enabling it to generate electron-hole pairs under visible light illumination.

The formation of heterostructures with 2D materials can further enhance the electronic properties of the material structure. For instance, combining Gr [25, 26] or MoS_2 [27, 28] with other semiconductors or co-catalysts can lead to improved charge separation and transfer. In these van der Waals heterostructures [87],

photo-generated electrons in the semiconductor can transfer to the 2D material. With appropriate band alignment, the 2D material layers function effectively as electron sinks and transport channels. This approach is essential in photocatalyst design, as it provides systematic control over the location of free charge carriers. Directed towards the surface, 2D materials serve as active reaction centers, thereby enhancing the overall photocatalytic performance.

1.2 Plasmonics

Plasmonics is a field of science and technology that focus on the interaction between electromagnetic radiation and free electrons in metals, semiconductors and their interfaces at the nanoscale [88]. This interaction leads to the generation of surface plasmons, which are quantized collective oscillations of electrons at the interface between a metal and a dielectric material. Plasmonic nanostructures have unique properties that allow for the manipulation and confinement of light at dimensions far below the diffraction limit, resulting in enhanced light-matter interactions.

Plasmonic structures for photocatalysts are beneficial due to their ability to significantly enhance light absorption and charge carrier dynamics. Figure 1.5 shows an overview of the most important mechanisms of plasmonic interactions. Plasmonic nanostructures, often made from gold (Au) [89] or silver (Ag) [90], can act as nanoscale antennas that confine electromagnetic fields into sub-wavelength volumes. This concentration effect leads to the generation of highly energetic "hot electrons" that can contribute to chemical reactions [91]. Furthermore, the localized surface plasmon resonance (LSPR) of these nanostructures can be tuned to selectively enhance the light absorption, allowing for more efficient utilization of solar energy in photocatalytic processes [92, 93]. These unique characteristics make the integration of plasmonics in photocatalysis a promising approach.

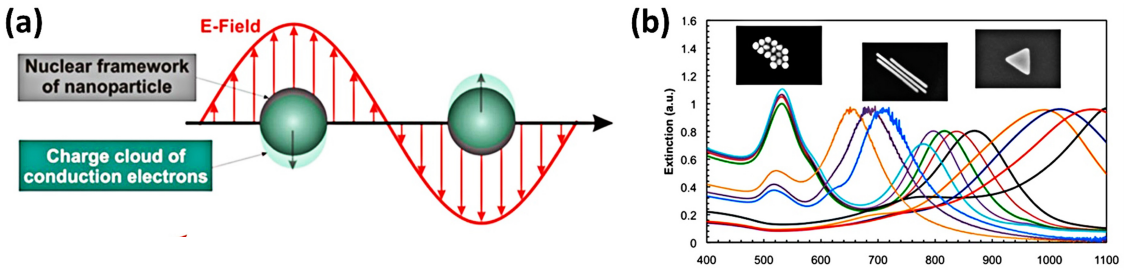


FIGURE 1.5: Overview illustration of plasmonic mechanisms: (a) surface plasmon resonance, (b) geometrical influence in shape and size for plasmon resonance [Reproduced and modified from [94], Copyright 2023, Elsevier Ltd.]

1.2.1 Plasmon Resonance

Plasmon polaritons are quasiparticles that result from the strong coupling between electromagnetic waves and collective oscillations of free electrons in a metal or semiconductor [95]. These hybrid excitations combine the properties of both photons and plasmons, leading to unique optical and electronic characteristics.

Surface plasmon polaritons (SPPs) are a specific type of plasmon polariton that propagate along the surface, or the interface between a metal and a dielectric material [96]. SPPs are characterized by their ability to localize the electromagnetic field at the interface, resulting in light confinement to subwavelength dimensions that is fundamentally enabled by the SPP's higher momentum compared to free-space photons. This confinement leads to enhanced electromagnetic fields at the interface, making SPPs particularly useful for various applications. The dispersion relation of SPPs differs from that of free-space photons, allowing the manipulation of light at the nanoscale. SPPs can be excited by photons, eventually reaching the LSPR-state when excited at a specific frequency (Figure 1.5a). This is known as plasmon resonance frequency and its position is highly dependent on the material, size and shape of the nanostructure (Figure 1.5b) [97, 98].

The analytical expression for plasmonic resonance can be derived by using a simple model (Figure 1.6) [47]: a sphere of radius a exposed to incident light with an electric field component given by $\vec{E} = E_0 \exp(-\omega t)\vec{z}$, where E_0 is the amplitude, ω the light frequency, t the time interval, and $\vec{z}$ the unit vector in z direction. The sphere is surrounded by an isotropic and non-absorbing medium with the dielectric constant ϵ_m. The dielectric response of the sphere is characterized by the dielectric function $\epsilon(\omega)$.

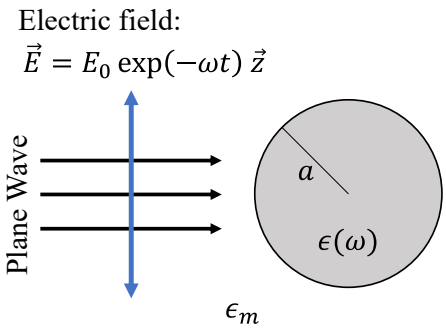


FIGURE 1.6: Model of the optical response of a spherical particle with radius a and dielectric function $\epsilon(\omega)$ irradiated by an E-field $\vec{E}$ in a medium with dielectric constant ϵ_m. [Reproduced from [47], Copyright 2013, IOP Publishing]

The dipole moment $\vec{p}$ is linearly proportional to $\vec{E}$, and can be written as:

$$\vec{p} = \epsilon_m \alpha \vec{E}. \tag{1.5}$$

The polarizability of the sphere is α, which is given by [88]:

$$\alpha = 4\pi\epsilon_0 a^3 \frac{\epsilon(\omega) - \epsilon_m}{\epsilon(\omega) + 2\epsilon_m}. \tag{1.6}$$

By examining the denominator of α, $\vec{p}$ can reach resonance, when

$$\mathrm{Re}\left[\epsilon(\omega)\right] = -2\epsilon_m \tag{1.7}$$

is fulfilled as a condition.

In the Drude model [88], $\epsilon(\omega)$ is defined as

$$\epsilon(\omega) = 1 - \frac{\omega_P^2}{\omega^2 + i\gamma\omega} = \epsilon_1(\omega) + i\epsilon_2(\omega), \tag{1.8}$$

where ω_P is the plasmon frequency for bulk materials and γ is the intraband damping frequency. The complex dielectric function ϵ is defined by its real part

$$\epsilon_1(\omega) = 1 - \frac{\omega_P^2}{1 + \omega^2\tau^2}, \tag{1.9}$$

and imaginary part

$$\epsilon_2(\omega) = \frac{\omega_P^2 \tau}{\omega(1 + \omega^2\tau^2)}, \tag{1.10}$$

where $\tau = 1/\gamma$ is the relaxation time of a free electron.

Combining Equations (1.7) and (1.9), the LSPR frequency ω_{LSPR} is derived from the resonance condition

$$\omega_{LSPR} = \omega_P \sqrt{\frac{1}{1 + 2\epsilon_m} - \frac{1}{\omega_P^2\tau^2}} \approx \frac{\omega_p}{\sqrt{1 + 2\epsilon_m}}, \tag{1.11}$$

due to $\omega_P^2\tau^2 \gg (1 + 2\epsilon_m)$.

Table 1.1 shows an overview of the plasmonic metals that are relevant in this thesis. It shows that the term $\omega_P^2\tau^2$ are negligibly small for the plasmonic metals in this work. Hence, Equation (1.11) is approximated by neglecting the expression $1/\omega_P^2\tau^2$. It can be concluded that $\omega_{LSPR} < \omega_P$ due to ϵ_m of the surrounding dielectric, as the denominator is $\sqrt{1 + \epsilon_m} > 1$. This results in a red-shift as decreasing frequencies lead to increasing wavelengths.

Material	ω_p ($10^{15}\,s^{-1}$)	γ ($10^{12}\,s^{-1}$)	τ ($10^{-15}\,s$)	$\omega_P^2\tau^2$	Ref.
Ag	2.18	4.353	230	5.2×10^5	[99]
Au	2.183	6.46	155	1.1×10^5	[99]
Pt	1.244	16.73	59.8	5.5×10^3	[99]
Pd	1.86	66.67	15	7.8×10^2	[100, 101]

TABLE 1.1: List of relevant plasmonic metals in this work and their plasmon resonance related properties.

1.2.2 Hot Electrons

The LSPR driven at ω_{LSPR} generates intense electromagnetic fields near the surface. These oscillations decay through several mechanisms, one of which involves the generation of high-energetic states, particularly hot electrons [102]. The energy from the LSPR can be transferred to individual electrons within the metal, exciting them to higher-energy states above the Fermi level. Concurrently, the vacancies left behind are then referred to as hot holes [103].

Hot electrons are crucial in photocatalysis because they can be injected into the conduction band of the semiconductor if their energy exceeds the Schottky barrier at the metal-semiconductor interface [91]. The probability of this injection process depends on the energy of the hot electrons and the height of the Schottky barrier (Equation 1.2). In addition, hot electrons may even tunnel from the metal into the semiconductor layer [104]. The generation and injection of hot electrons are determined by the material layer properties, requiring a large Schottky barrier height. Hot electrons can also directly interact with adsorbed reactant molecules, triggering chemical reactions. Their high energy create thermal energy which is beneficial for chemical reactions, as well [91, 105].

1.2.3 Periodic Structures/Metamaterials

Nanostructures arranged in a periodic pattern can act as optical gratings that create diffraction of the incoming light path [106]. When periodic nanostructures are within the sub-wavelength range of the illuminating light, they can cause diffraction peaks that are known as Wood-Rayleigh anomalies [107, 48]. This periodic arrangement enables the structure to exhibit absorption activity in wavelength regions where they would normally be reflective or transparent. In the case of visible light (λ = 400–700 nm), sub-wavelength sized nanostructure dimensions below 400 nm in periodic arrangements can greatly enhance the absorption. The repetitive pattern of these structures modifies the optical path through diffraction

at each unit structure, providing further optimization potential through geometrical modifications and material selection.

The integration of plasmonic nanostructures as periodic structures can lead to repetitive plasmon resonance spots. As they do not occur naturally with these features, these nanostructures are often referred to as metastructures, metamaterials, or metasurfaces. They offer systematic control over light-matter interactions at the nanoscale, enabling the design of highly efficient photocatalysts [108, **?**, 109].

In this thesis, the focus is on metamaterials based on nanodisk arrays. Nanodisks serve as versatile building blocks due to their simple geometry and tunable optical response. In addition, their lithography-based fabrication allows reproducibility and potential scalability [110]. By adjusting the dimensions, material composition, and arrangement of these disks, metasurfaces can be created with tailored optical properties suitable for specific applications.

1.3 Photocatalysis

Photocatalysis is a process that harnesses light energy to drive chemical reactions in the presence of a catalyst. This phenomenon typically involves a semiconductor material, such as titanium dioxide (TiO_2) [111, 112, 113], which absorbs free photons and generates electron-hole pairs. These charge carriers can then participate in reduction and oxidation (redox) reactions, enabling the transformation of reactant molecules into various substances. The unique ability of photocatalysts to initiate and accelerate reactions under moderate conditions has positioned photocatalysis as a promising approach for addressing numerous environmental and energy challenges.

This section provides a comprehensive understanding of several key aspects of photocatalysis. It begins by examining the fundamental principles of reaction potentials, which determine the thermodynamic feasibility of photocatalytic reactions. Afterward, various reaction mechanisms involved in photocatalysis are explained, as well as the roles of surface-adsorbed species and bulk defects.

1.3.1 Reaction Potentials

Photocatalytic reactions are fundamentally categorized into redox reactions, distinguished by their interaction with charge carriers. Oxidation reactions leverage free holes from the valence band, while reduction reactions utilize free electrons from the conduction band.

Water Splitting

Photocatalytic water splitting is taken as an example model for explaining the reaction potentials. The initiation of these reactions depends on specific energetic conditions, which are precisely mapped through the energy band model [114]. The intrinsic suitability for a material functioning as a photocatalyst is defined by its band properties (E_{VB}, E_{CB}, E_G). Hence, the positioning of these energy levels determines whether it can induce the reaction of interest or not. A comprehensive overview of potential photocatalyst materials for water splitting is shown in Figure 1.7.

A common practice in photocatalysis is the normalizeation of the energy levels of the redox reactions by the normal hydrogen electrode (NHE) [115]. The NHE is a reference defined by the hydrogen redox half-cell reaction completed with a Pt electrode in acidic solution (pH $= 0$) at 25 °C and a pressure of 1 bar bubbled with H_2 gas. The theoretical oxidation and reduction potentials for water splitting are given by [116, 117]

$$2H_2O + 4h^+ \longrightarrow O_2 + 4H^+, \qquad E_{ox} = -5.73\,\text{eV} = +1.23\,\text{V vs. NHE} \tag{1.12}$$

$$2H^+ + 2e^- \longrightarrow 2H_2, \qquad E_{red} = -4.5\,\text{eV} = 0\,\text{V vs. NHE} \tag{1.13}$$

$$H_2O \longrightarrow 2H_2 + O_2. \tag{1.14}$$

Hence, the conversion from E(eV) in vacuum level to E(V vs. NHE) is

$$E(\text{V vs. NHE}) = -4.5\,\text{eV} - E(\text{eV}). \tag{1.15}$$

It is important to note that this potential is pH-dependent and shifts by -59 mV for each pH unit increase, following the Nernst equation [115, 118]. However, the overall potential for water splitting remains constant at 1.23 eV. Practically, this is the activation energy for photocatalytic water splitting and must be provided by a semiconductor material with a greater E_G [6]. To function as a photocatalyst for water splitting, the energy level of the valence band E_{VB} and the conduction band E_{CB} must fulfill the following conditions [114]

$$E_{VB} < E_{Ox} = -5.73\,\text{eV} = 1.23\,\text{eV vs. NHE}, \tag{1.16}$$

$$E_{CB} < E_{Red} = -4.5\,\text{eV} = 0\,\text{eV vs. NHE}. \tag{1.17}$$

TiO_2 [111, 112, 113] is one material fulfilling this condition among the range of materials shown in Figure 1.7. This thesis only focuses on TiO_2 despite the

large range of suitable photocatalyst materials. This is due to its availability, non-toxicity, low cost and stability, which gives clear advantages over the other mentioned materials [111, 112, 113]. It is the most researched photocatalyst in the literature [119], which allows for extensive benchmarking and gives more insight into the underlying mechanisms.

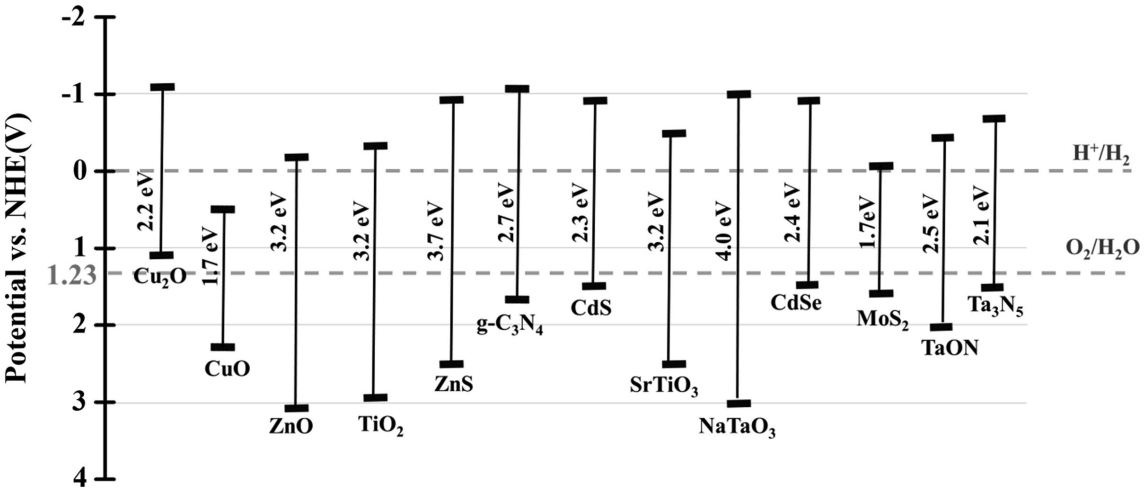


FIGURE 1.7: Band potentials of various photocatalyst materials in NHE scale, illustrating their band positions and bandgaps, indicate their suitability for photocatalytic water splitting [Reproduced from [114], Copyright 2020, Elsevier Ltd.]

Besides TiO_2, there are also research efforts to apply other materials such as copper oxide (CuO) [120], zinc oxide (ZnO) [121], graphitic carbon nitride (g-C_3N_4) [122], and strontium titanate ($SrTiO_3$) [123] for photocatalysis. Especially g-C_3N_4 is a very promising material due to its intrinsic suitability (E_{VB}, E_{CB}, E_G) for photocatalytic water splitting in visible light. On the other hand, a wide band gap semiconductor like TiO_2 is only active under UV-light exposure, thus requiring further modifications to extend its photocatalytic functionality into the visible wavelength range. This can be achieved by integrating plasmonic metals that acts as co-catalyst to conduct charge separation and provide active reaction sites through hot electrons.

CO_2 Reduction

Analogously to water splitting, photocatalytic CO_2 reduction is a promising approach for light-driven conversion of CO_2 and protons (H^+) into valuable fuels and chemicals, such as CO, CH_4, or CH_3OH [124]. The reaction mechanism is more complex as it can have different reaction paths depending on the available potential (Table 1.2). In addition, it requires a source for a sufficient amount of

H^+, which can be provided by water splitting. The energy requirements are significantly higher than for the 1.23 eV in water splitting, which is why reported yields are usually lower.

Reactions	E vs. NHE (V)
$CO_2 + 2\,H^+ + 2\,e^- \longrightarrow HCOOH$	-0.61 V
$CO_2 + 2\,H^+ + 2\,e^- \longrightarrow CO + H_2O$	-0.53 V
$CO_2 + 4\,H^+ + 4\,e^- \longrightarrow HCHO + H_2O$	-0.48 V
$CO_2 + 6\,H^+ + 6\,e^- \longrightarrow CH_3OH + H_2O$	-0.38 V
$CO_2 + 8\,H^+ + 8\,e^- \longrightarrow CH_4 + H_2O$	-0.24 V

TABLE 1.2: Reaction equation and redoxpotentials (E vs. NHE, pH = 7) for CO_2 reduction into its different hydrocarbon-based solar fuel [111].

The Gibbs free energy ΔG is a fundamental thermodynamic parameter that determines the energy requirements of chemical reactions. Specifically for CO_2 reduction and water splitting reactions, it amounts -394.4 kJ/mol for CO_2 [119], 237 kJ/mol for water [125]. The higher Gibbs free energy values for CO_2 reduction compared to water splitting underscore the greater energy input required for these reactions. This limitation is compounded by kinetic barriers, including the stability of the CO_2 molecule and the multi-electron process of the reduction process.

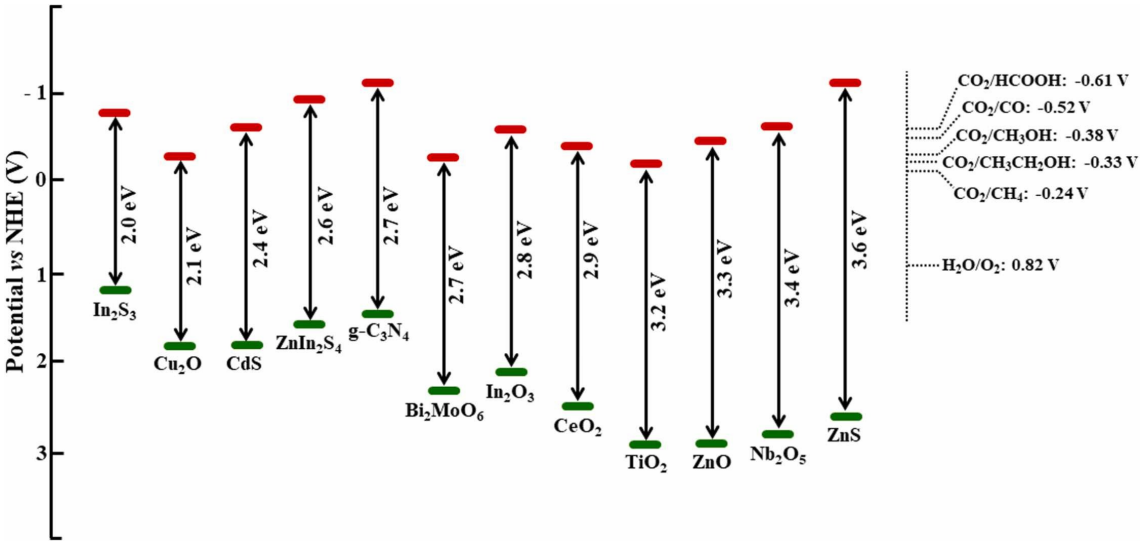


FIGURE 1.8: Band potentials of various photocatalyst materials, illustrating their band positions and bandgaps, indicate their suitability for photocatalytic CO_2 reduction. [Reproduced from [126], Copyright 2024, Elsevier Ltd.]

Photocatalysts for CO_2 reduction must not only have appropriate band positions to drive the desired reactions with a high selectivity, they also require to be

designed to manage multi-electron transfers efficiently. This often involves the use of co-catalysts, defect engineering, and nanostructuring to enhance charge separation and provide active sites for CO_2 activation and conversion.

Reactive Oxygen Species

Reactive oxygen species (ROS) play a crucial role in photocatalytic water purification processes, serving as key intermediates in the degradation of chemical [7], pharmaceutical [62], bacterial [63, 64, 65], and viral [66] contaminants in water. The variety of ROS includes superoxide anion radicals ($O_2^{\bullet -}$), hydrogen peroxide (H_2O_2), singlet oxygen ($^1O_2$), and hydroxyl radical ($OH^\bullet$). They are all relevant for photocatalytic water purification processes, as they can break the bindings of the contaminant molecules or organisms.

Figure 1.9 shows the working principle with the example of photocatalytic bacteria disinfection. Under light illumination with sufficient amount of energy, electron-hole pairs in the photocatalyst separate and turn into free charge carriers. On the photocatalyst surface, they undergo redox reactions in water to generate ROS. Table 1.3 shows the simplified reaction equations and redox potentials, as they are actually multi-steps mechanisms [61].

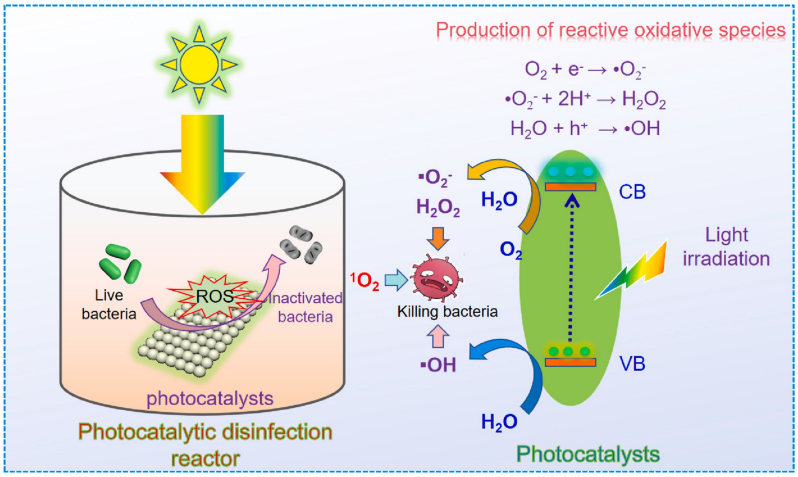


FIGURE 1.9: Schematic band diagram for ROS generation with the example of photocatalytic bacteria disinfection. [Reproduced from [65], Copyright 2024, Elsevier Ltd.]

The specific ROS generation processes include the formation of $O_2^{\bullet -}$ when conduction band electrons (e^-) react with adsorbed oxygen molecules. H_2O_2 is produced through the reaction of $O_2^{\bullet -}$, protons (H^+), and electrons [61]. $OH^\bullet$ is generated when valence band holes (h^+) oxidize water molecules or hydroxide ions (OH^-). The latter are available in water due to its self-ionization. Singlet

oxygen ($^1O_2$) is created through energy transfer from the excited photocatalyst to ground state oxygen. The amount of generated ROS depends on various factors, including the photocatalyst properties, the illuminating light power density, wavelength, and the presence of electron donors and acceptors in the aqueous environment.

Reactions	E vs. NHE (V)
$O_2 + e^- \longrightarrow O_2^{\bullet -}$	$-0.33\,V$
$O_2^{\bullet -} + 2\,H^+ + e^- \longrightarrow H_2O_2$	$1.72\,V$
$OH^- + h^+ \longrightarrow OH^\bullet$	$1.5\,V$
$O_2^{\bullet -} + h^+ \longrightarrow {}^1O_2$	-

TABLE 1.3: Reaction equation and redoxpotentials (E vs. NHE, $pH = 0$) for ROS generation [61].

Photocatalytic water treatment by ROS generation is a sustainable process as it does not require additional chemicals and can be powered by sunlight. Despite its potential, it still faces several challenges that limit its efficiency. The redox potentials demand a higher amount of energy thus requiring large bandgap materials. As this limits the visible light activity, there are many modification approaches explored, often involving another co-catalyst material [109] or increasing the active surface area [127].

1.3.2 Adsorption Energy

The adsorption capabilities between the photocatalyst surface and the reactant molecules are crucial in photocatalytic reactions, as they represent the strength of interaction in between [128]. In fact, adsorption is often the first step in the reaction process, making it a critical factor in determining the overall reaction kinetics and mechanism besides charge carrier mechanisms.

The adsorption energy can vary, depending on the nature of the interaction between the adsorbate and the photocatalyst [129, 130]. On the one hand, there is physisorption, which is characterized by weak van der Waals forces. On the other hand, there is chemisorption, which involves the formation of chemical bonds between the adsorbate and the catalyst surface. The magnitude of the adsorption energy can significantly impact the reaction process, affecting the residence time of reactants on the catalyst surface and the likelihood of subsequent reactions. Strong adsorption allows the photocatalyst to effectively trap reactant molecules, facilitating photocatalytic reactions.

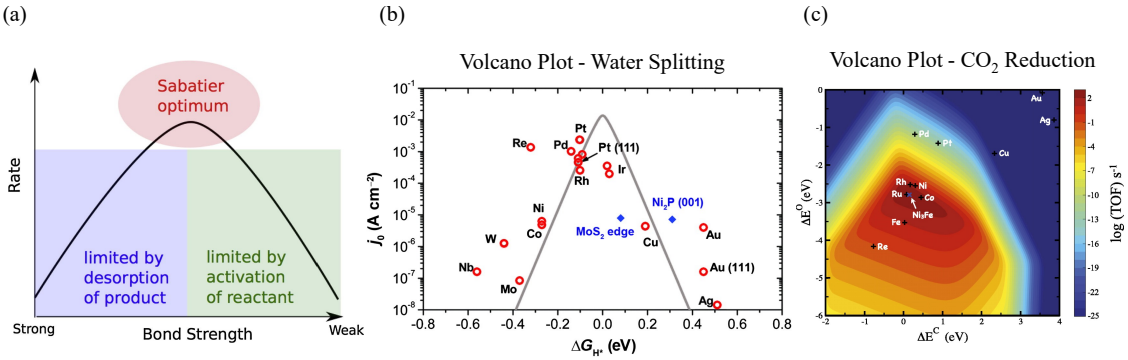


FIGURE 1.10: (a) Sabatier principle showing that the bond strength and reaction rate has a parabolic relation. There is an ideal bonding strength, known as Sabatier optinum, at which the reaction rate maximizes. [Reproduced from [131], Copyright 2015, Elsevier Ltd.]. (b) Volcano plot for water splitting for a variety of materials scaled by the current density as reaction indicator [Reproduced from [132], Copyright 2017, Taylor & Francis Group]. (c) 3D volcano plot for CO_2 reduction for a variety of metals scaled by the logarithmic TOF as reaction indicator [Reproduced from [133], Copyright 2011, National Academy of Sciences].

Therefore, an optimal bonding strength has to be found which is known as the Sabatier principle (Figure 1.10a) [131]. The optimal photocatalyst surface material can be identified by plotting their interaction forces against the reaction rate of the reactant molecule of interest. This reveals an inverse parabolic relation, often simply called volcano plot. The optimal materials are in the region of the peak. Related work to identify new optimal materials for specific reactions are often conducted with computational tools, specifically density functional theory (DFT) [134]. As this would highly exceed the scope of this thesis, only literature results are discussed here.

One volcano plot with metal surfaces for water splitting is depicted in Figure 1.10b [132]. A variety of metals were studied and plotted by their current density j_0, which indicates the reactivity in electro- and photoelectro chemical experiments. The volcano plot shows that Pd and Pt are at the top of the volcano and have the optimal bonding strength. Notably, Pt is well-known as the best reactive material in electrolysis for H_2 generation [135]. On the other hand, plasmonic metals like Au and Ag have lower reaction rates due to weak adsorption forces, further confirming the Sabatier principle. Nevertheless, this data does not take plasmonic properties into consideration, which makes Ag [24] and Au [136] still worthwhile materials to be studied.

Figure 1.10c shows the volcano plot for CO_2 reduction for a variety of metals [133]. This three-dimensional mapping takes into the adsorption data for C- and O-atoms into consideration, along with the turnover frequency (TOF), which is a

measure to quantify the activity of catalytic reactions. Instead of Pd and Pt, metals like rhodium (Rh) [137, 138], ruthenium (Ru) [139, 140], cobalt (Co) [141] and nickel (Ni) [142] are expected to have superior reaction rates for CO_2 reduction. For Pt and Pd, the adsorption properties toward CO_2 molecule are in a moderate range, Ag and Au are even less favorable. Despite the unfavorable adsorption properties, Ag, Au, Pt and Pd are the metals on which this thesis focuses to reveal their synergy between plasmonic and adsorption properties.

1.3.3 Reaction Evaluation

The performance of photocatalytic reactions are often reported using metrics such as gas evolution rates and apparent quantum yield (AQY) [143, 144]. In particular for photocatalytic water splitting, the solar-to-hydrogen (STH) efficiency is also often used [14, 31].

The gas evolution rate r [145] quantifies the yield of the gas amount n produced over its reaction time t and is defined by

$$r = \frac{n}{t}. \tag{1.18}$$

As a larger photocatalyst amount leads to increased reaction rates, r is often normalized by the photocatalyst mass m or area A

$$r_{\mathrm{m}} = \frac{n}{m \times t}, \tag{1.19}$$

$$r_{\mathrm{A}} = \frac{n}{A \times t}, \tag{1.20}$$

where r_{m} and r_{A} are the mass- and area-normalized gas rate, respectively. While r_{m} is used for both photocatalyst powders and sheets, r_{A} is only used for sheets.

AQY states how effectively the photon energy at a specific wavelength is converted into chemical energy. It is defined as the ratio of the number of electrons involved in a specific reaction to the total number of incident photons in the system under specific wavelength conditions [144]

$$\eta_{\mathrm{AQY}} = \frac{\text{Number of reacted electrons}}{\text{Number of incident photons}} = \frac{h \times c \times N_{\mathrm{A}} \times n}{P_{\mathrm{light}} \times S_{\mathrm{light}} \times t \times \lambda}, \tag{1.21}$$

where h is the Planck's constant, c is the speed of light, N_{A} is the Avogadro's constant, n is the amount of evolved gas product, P_{light} is the light power density, S_{light} is the exposed light area, t is the reaction time, and λ is the incident wavelength.

Instead of the classical quantum yield, AQY is used more often in photocatalysis research [146]. This is due to the difficulty to determine the actual number of photons absorbed by the catalyst which are lost by light scattering and reflection. Therefore, AQY is based on the assumption that a specific number of incident photons are required to trigger the photocatalytic reaction of interest, while the classical quantum yield is based on the measured absorbed photon count. This makes this sort of quantum yield an "apparent" measurement. However, measuring AQY accurately requires a monochromatic light source and a blackbody reactor chamber to ensure all photons are directed into the reaction system.

The STH efficiency η_{STH} is a key metric used to evaluate the performance of photocatalytic water splitting systems. It is defined as the ratio of the energy output in the form of hydrogen to the energy input from solar radiation. The formula for calculating STH efficiency is [14, 31]

$$\eta_{\mathrm{STH}} = \frac{\text{Output energy as } \mathrm{H_2}}{\text{Energy of incident light}} = \frac{r_{\mathrm{H_2}} \times \Delta G_{\mathrm{H_2}}}{P_{\mathrm{light}} \times S_{\mathrm{light}}}, \tag{1.22}$$

where $r_{\mathrm{H_2}}$ is the $\mathrm{H_2}$ rate, $\Delta G_{\mathrm{H_2}}$ is the Gibbs free energy for water splitting, P_{light} is the light power density, and S_{light} is the incident light area.

This definition allows for a standardized comparison of different photocatalytic systems, taking into account both the rate of hydrogen production and the solar energy input. It is important to note that STH efficiency is typically reported as a percentage, with higher values indicating more efficient conversion of solar energy to $\mathrm{H_2}$.

There is also the definition for solar-to-fuel (STF) efficiency η_{STF} [147]. Analogously to Equation (1.22), it is defined by

$$\eta_{\mathrm{STF}} = \frac{\text{Output energy as fuel}}{\text{Energy of incident light}} = \frac{r_{\mathrm{fuel}} \times \Delta G_{\mathrm{fuel}}}{P_{\mathrm{light}} \times S_{\mathrm{light}}}, \tag{1.23}$$

where r_{fuel} and ΔG_{fuel} are the rate and Gibbs free energy of the specific fuel, respectively. η_{STF} is not used in photocatalytic $\mathrm{CO_2}$ reduction literature, as product rates are too low to be reported in reasonable STF efficiency values.

1.4 Photocatalytic Mechanism of Metamaterials

Figure 1.11 illustrates all important processes and charge transfer mechanisms occurring in a metamaterial photocatalyst sheet. The metamaterial in this example is based on a periodic plasmonic metal nanostructure on a wide bandgap (only

UV-active) photocatalyst thin film under sunlight exposure. It is assumed that there is a Schottky barrier formed between the metal structures and semiconductor layer.

In this example, the photocatalyst sheet harnesses both UV and visible light photons of the solar spectrum to drive efficient photocatalytic reactions, showcasing the synergy between semiconductor photocatalysis and plasmonic enhancement:

(1) Charge generation by light excitation: In the semiconductor layer, the UV portion of the sunlight excites electron-hole pairs, raising electrons from the valence to the conduction band, leaving behind holes in the valence band.

(2) Electron-hole recombination: There are statistical processes due to the random diffusion of charge carriers. One of them is the electron-hole recombination that can occur, which would lowering the excited electrons from the conduction band back to the valence band. During this process, the electrons lose energy, dissipating it as heat or light.

(3) Charge carrier drifting: Another statistical process is the charge carrier drifting within the space charge region. This region is an area near the surface or interface of a semiconductor where mobile charge carriers are depleted [47]. Due to the separation of charges, a built-in electric field drives the movement of photogenerated charge carriers, enhancing their overall separation.

(4) Localized surface plasmon resonance (LSPR): The visible light portion of sunlight excites electrons within the plasmonic metal nanostructures. These nanostructures act as resonance cavities, where light scattering induces collective oscillations of electrons. This phenomenon results in an amplified electric field and LSPR. This process creates hot electrons that can migrate to the plasmonic metal surface and overcome the Schottky barrier due to their high energy states.

(5) Photocatalytic reaction at the metal structure surface: Hot electrons that remain at the metal nanostructure surface primarily drive reduction reactions, while their corresponding holes may contribute to oxidation ones, further enhancing the overall photocatalytic efficiency.

(6) Photocatalytic reaction at photocatalyst surface: In the semiconductor layer, the remaining surface charge carriers drive photocatalytic reactions if they have not recombined or drifted apart before. The conduction band electrons

facilitate reduction reactions and valence band holes contribute to oxidation reactions.

(7) Light (γ) interaction at the metal structures: In periodic nanostructures, the plasmonic effects are amplified through increased scattering and absorption mechanisms. The individual metal nanostructures serve as diffraction surfaces, effectively reusing reflected and transmitted light. As light interacts with these metal structures, it undergoes multiple scattering or absorption processes, leading to a substantial amplification of the overall plasmonic effects. The magnitude of these effects is highly dependent on the size, shape, and material composition of the nanostructures. In structures with subwavelength dimensions, interference effects can further intensify the LSPR and localized electric fields, which creates reaction centers of enhanced photocatalytic activity.

(8) LSPR-coupling between two neighboring metal nanostructures: An additional mechanism occurs when the gap between periodic nanostructures is sufficiently small. In this case, the induced LSPR can couple with neighboring structures through near-field dipolar interactions [88]. This coupling generates additional collective LSPR-induced electric field amplifications, creating localized regions of high charge density. These regions act as potent active reaction sites, increasing the photocatalytic performance. Due to the periodic nature of the nanostructure array, these effects are replicated across all plasmonic nanostructures in the photocatalyst sheet, leading to enhanced photocatalytic efficiency.

.

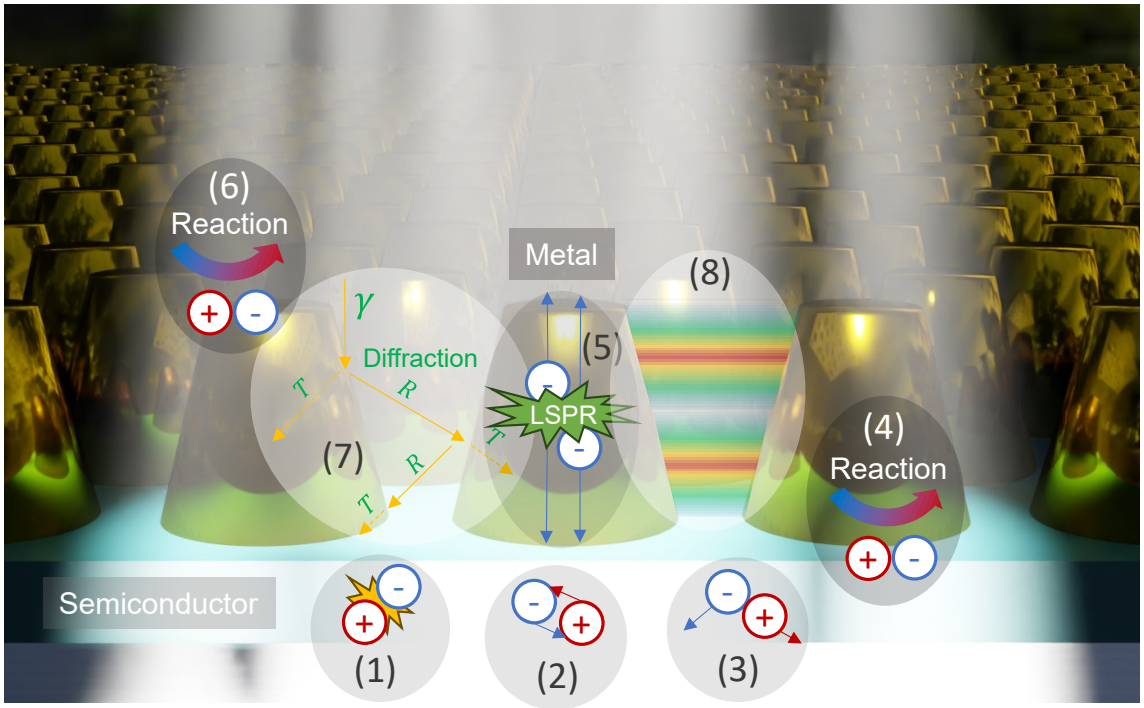


FIGURE 1.11: Major mechanism in plasmonic photocatalysis with metamaterial nanostructures: (1) Charge generation by light excitation, (2) electron-hole recombination, (3) charge carrier drifting, (4) LSPR, (5) photocatalytic reaction with free charge carrier at metal structure surface, (6) photocatalytic reaction with free charge carriers at photocatalyst surface, (7) light (γ) diffraction, reflection (R) and transmission (T) at the metal structures, and (8) LSPR-coupling between two neighboring metal nanostructures. These mechanisms repeat at every individual metal structure within the periodic pattern.

2 Methods

This chapter outlines the methods used in this thesis for the preparation and characterization of the photocatalyst sheets. It provides an overview of the experimental and theoretical methods conducted throughout this thesis. The following sections describe the specific techniques and processes involved in the fabrication of the photocatalysts, along with the methods used for their characterization, simulation studies, and the evaluation of these datasets.

2.1 Fabrication Methods

The metamaterial photocatalyst sheets are created through a series of fabrication process steps. The photocatalyst is structured on up to $(5 \times 5)\text{cm}^2$ sized substrates of either silicon (Si) or glass, depending on the specific requirements of each characterization method. Despite being fragile and reflective, Si substrates are advantageous for cross-sectional analysis and Raman spectroscopy. On the other hand, glass substrates are transparent, which is needed for the evaluation of the extinction spectra. The following sections provide a detailed breakdown of each fabrication process step.

2.1.1 Magnetron Sputtering

As a widely used physical vapor deposition (PVD) technique, magnetron sputtering is utilized to deposit thin films by accelerating atoms from a target material and condensing them onto a substrate within a vacuum chamber (Figure 2.1a). In this process, a high voltage is applied between the cathode (the target material) and the anode, ionizing an inert gas to create a plasma. The typical carrier gas is argon (Ar), while oxygen (O_2) or nitrogen (N_2) can additionally be applied for reactive sputtering. A magnetic field confines electrons near the target surface, increasing the deposition rate while minimizing potential damage to the substrate from ion bombardment. The positive gas ions in the plasma collide with the negatively charged target material, ejecting atoms from the target, which then condense on the substrate to form a thin film on a substrate.

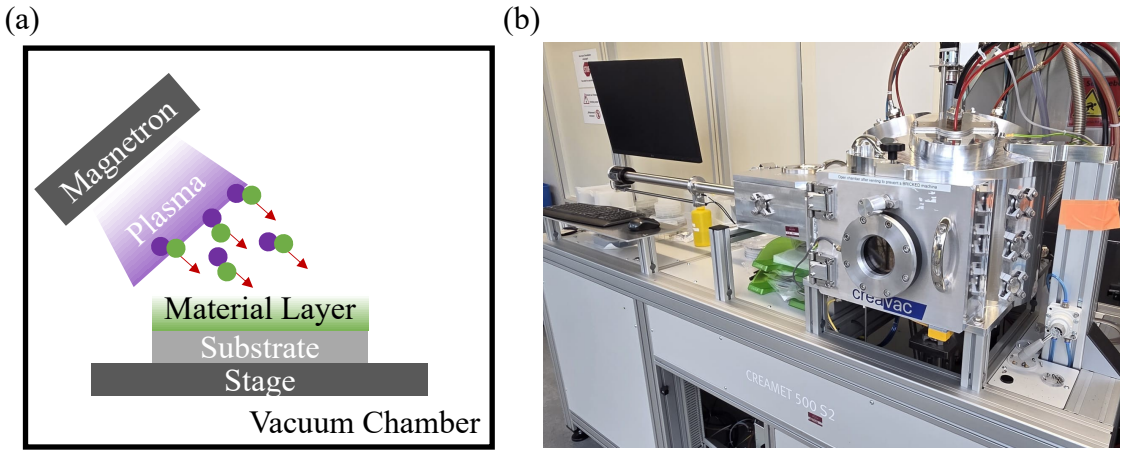


FIGURE 2.1: (a) Principle of magnetron sputtering showing a sketched vacuum chamber, a stage sample, and magnetron during ion-bombarding. This setup was a confocal sputter tool. (b) Photograph of the commercial sputtering model 'CREAMET S2' from the company 'CREAVAC PVD AG'.

In this thesis, the TiO_2 thin film was deposited onto Si or glass substrates with a commercial sputter tool (CREAMET S2, CREAVAC PVD AG, Figure 2.1b). A titanium (Ti) target with a 100 mm/4 inch diameter and a 99.99 % purity was used for a reactive process. The vacuum chamber was initially pumped down to a base pressure below 1×10^{-4} mbar prior to deposition. The sputtering process was conducted in an atmosphere of 80 sccm Ar and 6 sccm O_2, with a working pressure of 4.2×10^{-3} mbar. A direct-current (DC) sputtering power of 400 W was applied for a duration of one hour, with the substrate rotating at 1 rpm, yielding a TiO_2 deposition rate of 80–90 nm/h.

In Chapter 5, magnetron was also used to deposit few layers of molybdenum (Mo). From an Mo target with 99.95 % purity, it was sputtered with a 100 W DC process for a few seconds. The Mo was then post-processed by chemical vapor deposition (CVD) to form it into molybdenum disulfide (MoS_2) by a high-temperature sulfurization process (Section 5.2.1).

2.1.2 Annealing

An annealing process was conducted to modify the crystallinity of the sputtered TiO_2 layer (Figure 2.2a). Annealing typically consists of three phases: recovery, recrystallization, and grain growth. During the recovery stage, the thermal energy induces the movement and annihilation of dislocations, thereby reducing internal stresses within the material. In the recrystallization phase, as the material reaches its recrystallization temperature, new crystals nucleate, forming a more organized crystal structure with smaller grains. Finally, in the grain growth

phase, these newly formed crystals expand as the temperature rises, leading to larger grain sizes and further material stabilization.

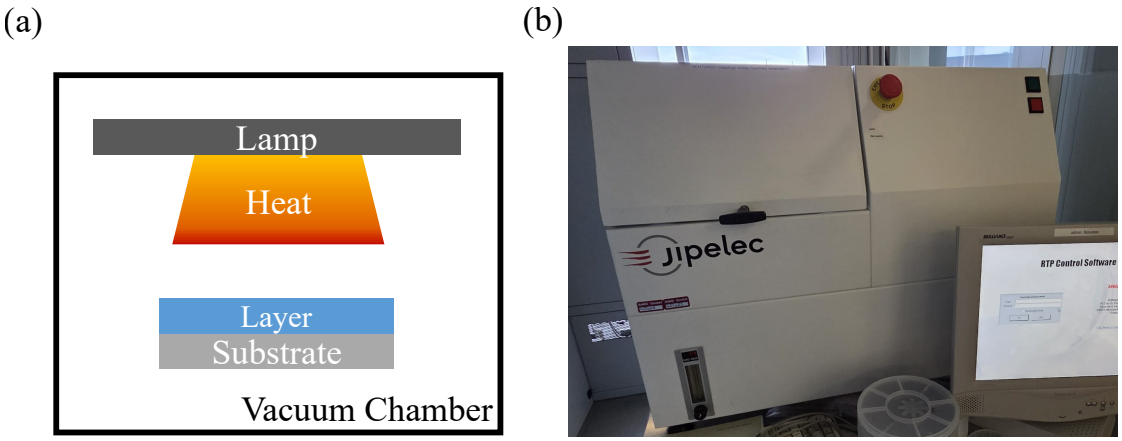


FIGURE 2.2: (a) Principle of annealing, showing a vacuum chamber, a lamp emitting heat, and a substrate with a material layer that requires the heat treatment. (b) Photograph of the commercial sputtering model 'Jipelec JetFirst 150' from the company 'ANNEALSYS SAS'.

In this thesis, the sputtering-deposited TiO_2 thin film was initially in an amorphous phase. In photocatalytic research, TiO_2 is mostly used in its anatase crystal phase, as it possesses favorable properties for an improved reaction processes [148, 149, 150]. The annealing process was conducted at 650 °C for 1 h in a commercial rapid thermal processing (RTP) furnace (Jipelec JetFirst 150, ANNEALSYS SAS, Figure 2.2b) under a continuous flow of 200 sccm Ar as the chamber gas.

2.1.3 Laser Interference Lithography

Laser interference lithography (LIL) is an efficient method to pattern periodic patterns over large areas without the need for photomasks [151]. This technique is particularly useful for producing structures such as line gratings, hole arrays, and pillar arrays [152]. The fundamental principle of LIL is based on the interference pattern generated by the phase difference between two or more laser light paths.

A typical LIL setup incorporates various optical elements, including lenses, mirrors, objectives and pinholes. This optical system direct two laser beams toward the substrate, resulting in an interference pattern of constructive and destructive interactions between the phase-shifted laser beams. The final periodic structure is based on this interference pattern.

In this thesis, LIL was used to define master structures for the subsequent nanoimprint lithography (NIL) step. This part of work was conducted at a custom-made setup for 150 mm/6 inch exposure area by Michael Möller, who is a process engineer at AMO GmbH, Germany.

2.1.4 Nanoimprint Lithography

Nanoimprint lithography (NIL) is a highly regarded technique for fabricating nanostructures due to its ability to produce large-area nano-sized patterns [46]. Compared to other nanolithography technique, such as extreme ultraviolet (EUV) lithography or electron beam lithography (EBL), NIL can be operated at a relatively low cost and high reproducibility for large areas [153]. Unlike photolithography, NIL mechanically forms a resist material, which is then cured using heat or UV light to transfer the pattern (Figure 2.3a). This direct imprinting process allows NIL to overcome the resolution limits typically constrained by light diffraction or beam scattering.

In this thesis, NIL was employed to fabricate periodic nanostructure arrays on samples using UV-curable resist AMONIL[1] MMS10. The process began with the creation of a transparent stamp replica containing the master structure patterned by LIL. The stamp replica is made by a polydimethylsiloxane (PDMS) solution. This PDMS was cured by heating at 50 °C for three days, resulting in a solidified, elastic, and structured stamp after being separated from the master structure.

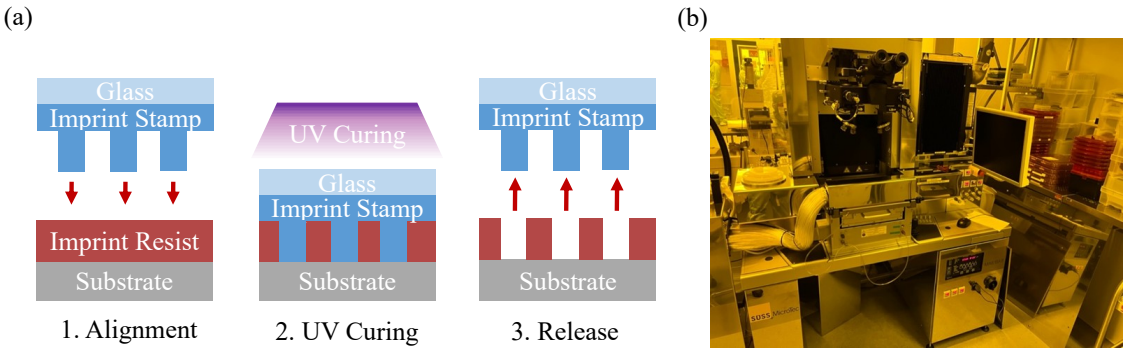


FIGURE 2.3: (a) Principle of NIL sketched by the three main steps: alignment of the imprint stamp on the sample, UV-curing for resist solidification, and release of the imprint stamp. (b) Photograph of the commercial NIL model 'MA8' from the company 'SUSS Microtec AG'.

The pattern transfer process involved spin-coating a double-layer resist stack onto the samples [110]. First, a layer of polymethylmethacrylate (PMMA) 950k

[1] commercial imprint resist from AMO GmbH, Germany

A4 is spin-coated at 4500 rpm for 60 s, followed by baking at 180 °C for 10 min. PMMA serves as a sacrificial layer for a later lift-off step. Before applying the second resist, a thin layer of AMOPRIME[2] is spin-coated at 3000 rpm for 30 s. AMOPRIME is used as an adhesion promoter to prevent an off-lifting of the AMONIL layer. Afterward, AMONIL MMS10 was spin-coated as the second resist layer using the same parameters as the AMOPRIME one and baked at 115 °C for 1 min to increase its viscosity.

The transparent PDMS stamp was then pressed onto the substrate, deforming the AMONIL layer to create the periodic hole structures. The stamp and substrate were exposed to UV light for 3 min in a commercial mask aligner (MA8, SUSS MicroTec AG, Figure 2.3b) to cure and solidify the AMONIL layer. Afterward, the stamp was separated from the sample, successfully transferring the nanostructured pattern onto the sample surface.

2.1.5 Reactive Ion Etching

Reactive ion etching (RIE) is a dry etching technique to remove material from substrates with high precision (Figure 2.4a). In this process, plasma is generated from reactive gases such as oxygen (O_2), argon (Ar), helium (He), carbon tetrafluoromethane (CF_4), or trifluoromethane (CHF_3), which are used to etch the specific target material. Plasma formation occurs when a strong radio-frequency (RF) power is applied to create an electric field, ionizing the gas molecules. The resulting ions and radicals react with the substrate surface, removing material to shape it into the desired pattern. If masked properly, these processes are used to shape a target material top-down.

One of the primary advantages of RIE over wet etching is its ability to etch materials more isotropic and with greater precision while minimizing damage to the substrate. The high kinetic energy of the ions enables efficient material removal, and the predominantly vertical delivery of reactive ions results in highly anisotropic etch profiles, allowing for well-defined patterns with steep sidewalls. Furthermore, the plasma conditions can be easily controlled by adjusting factors like gas composition, pressure, and RF power, making RIE a highly tunable etching technique.

[2] commercial adhesion promoter from AMO GmbH, Germany

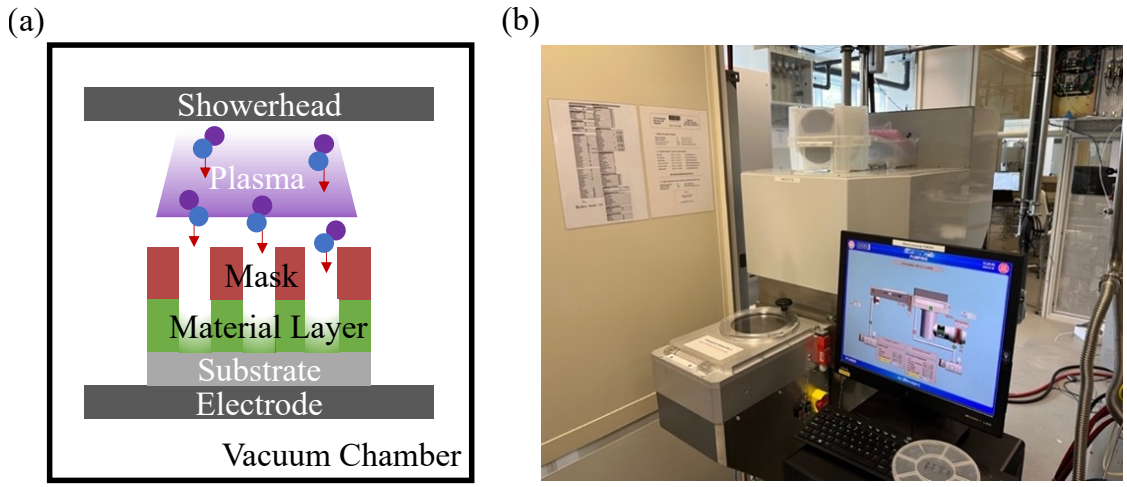


FIGURE 2.4: (a) Principle of RIE showing a vacuum chamber, an electrode that functions as a stage, and a layered sample with material layer and etching mask. The showerhead creates a plasma that bombards ion towards the electrode, etching the material layer the region that is not covered by the mask. (b) Photograph of the commercial RIE model 'Plasmalab System 100' from the company 'Oxford Instruments plc'.

In this thesis, a commercial RIE tool (Plasmalab System 100, Oxford Instruments plc, Figure 2.4b) was used to etch the AMONIL and PMMA double-layer resist stack on the samples, creating the desired array patterns for subsequent metal deposition. The etching process was conducted in two stages. First, the AMONIL layer was etched using a mixture of CHF_3 and Ar to remove the residual layer, which are leftover nanolayers of AMONIL from the NIL process. In the second stage, the exposed regions of the PMMA layer were etched with a combination of CF_4, O_2, and He, ensuring complete removal of any residual material in the patterned holes.

2.1.6 Electron Beam Evaporation

An electron-beam (e-beam) evaporator is another PVD technique used for depositing material thin films onto a mounted substrate. The process involves heating a target material to its evaporation temperature using an e-beam, causing the material to vaporize and condense as a thin film on the substrate. The e-beam evaporator operates in a high-vacuum environment, where the electron beam is directed at the target material, typically held in a crucible. The intense localized heating evaporates the material, which then travels through the vacuum chamber and deposits on the substrate. The key benefits of this method include precise control of the deposition rate and film thickness by adjusting the electron

beam current and deposition time, along with minimal heat transfer to the substrate since the energy of the e-beam is concentrated only on the target material. Moreover, the deposition direction is only vertical, making it suitable for lift-off processes.

During the years of the research work for this thesis, three different commercial e-beam evaporator tools were used (Classic 580, Pfeiffer Vacuum GmbH; PLS 500, Pfeiffer Vacuum GmbH; FHR Anlagenbau GmbH) to deposit metal thin films. The vacuum chamber was pumped down to a pressure of approximately 10^{-6} mbar, ensuring a high-vacuum environment necessary for the evaporation process, which increases the mean-free path of the deposited particles. The e-beam evaporator were used to deposit the plasmonic metals: Ag, Au, Pt, and Pd.

2.2 Characterization Methods

Quantifying and analyzing the material properties of photocatalysts is crucial for understanding their mechanisms. This section introduces several key characterization methods that provide insights into the topographical, optical, crystalline, electronic, and chemical properties of photocatalysts. From nanoscale surface features to bulk crystal structures, from light absorption profiles to charge carrier dynamics, these characterization methods unveil the intricate properties that influence a photocatalytic functionality to harness light and drive chemical reactions. Understanding these properties not only provides an overview of the fundamental mechanisms underlying photocatalytic processes but also guides to optimized photocatalyst designs with enhanced performances.

2.2.1 Scanning Electron Microscopy

Scanning electron microscopy (SEM) is an imaging technique that is used to resolve surface features and composition of materials with nanoscale precision (Figure 2.5a). Unlike optical microscopes, SEM utilizes a focused beam of electrons to interact with the sample, hence exceeding the wavelength limit of visible light, allowing for much higher resolution and detailed topographical analysis.

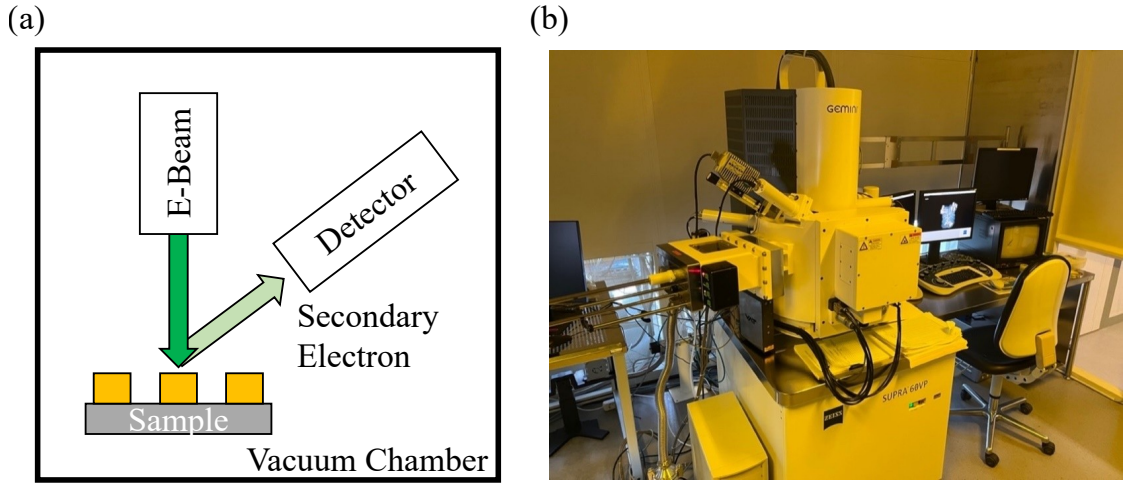


FIGURE 2.5: (a) Principle of SEM showing a vacuum chamber, an e-beam gun, and a sample that is to be scanned. The interaction between electron beam and sample surface creates secondary electrons which are collected by a detector to generate the surface topography image. (b) Photograph of the commercial SEM model 'SUPRA 60VP' from the company 'Carl Zeiss AG'.

The SEM operates by directing a focused e-beam onto the sample. To reduce electron scattering and prevent contamination, the sample chamber is maintained under a high vacuum. Inside of it, detectors collect the electrons produced by the interaction of the electron beam with the atomic structure of the investigated sample. These interactions generate various signals, including secondary electrons, backscattered electrons, and X-rays. The secondary electrons signals are used to produce highly detailed images of the surface topography of the sample, while backscattered electrons and X-rays can provide atomistic properties of the investigated sample.

In this thesis, a commercial SEM (SUPRA 60VP, Carl Zeiss AG, Figure 2.5b) is used to characterize the surface topography of the materials. It allows scanning the XY-plane of the sample surface, but also the cross-sectional scan by tilting the sample holder. However, the cross-sectional scan requires the break the sample. For this reason, cross-section SEM scanned samples are fabricated on Si substrates, as they can precisely be cleaved by a diamond knife and hands.

In addition, the energy-dispersive X-ray spectroscopy (EDX) can be conducted at the same SEM instrument. This method allows the elemental analysis by their characteristic X-ray excitation. It will be used in Chapter 5.

2.2.2 Atomic Force Microscopy

Atomic force microscopy (AFM) is a high-resolution scanning probe microscopy technique used to image and analyze surfaces at the nanoscale (Figure 2.6a). It achieves resolutions down to the single nanometer range, and enables detailed examination of the surface morphology. The AFM operates using a cantilever with an ultra-sharp tip, typically made from Si or other nanoscale materials, which interacts with the sample surface due to intermolecular forces during scanning.

In tapping mode, the AFM provides non-destructive surface imaging by oscillating the cantilever near the sample surface. The interaction between the tip and the surface is monitored by a focused laser on the cantilever. It measures changes in the cantilever's oscillation amplitude, which are influenced by the local forces on the surface. These amplitude variations are recorded to generate a detailed surface topographic map, offering insights into the sample's morphology without damaging it.

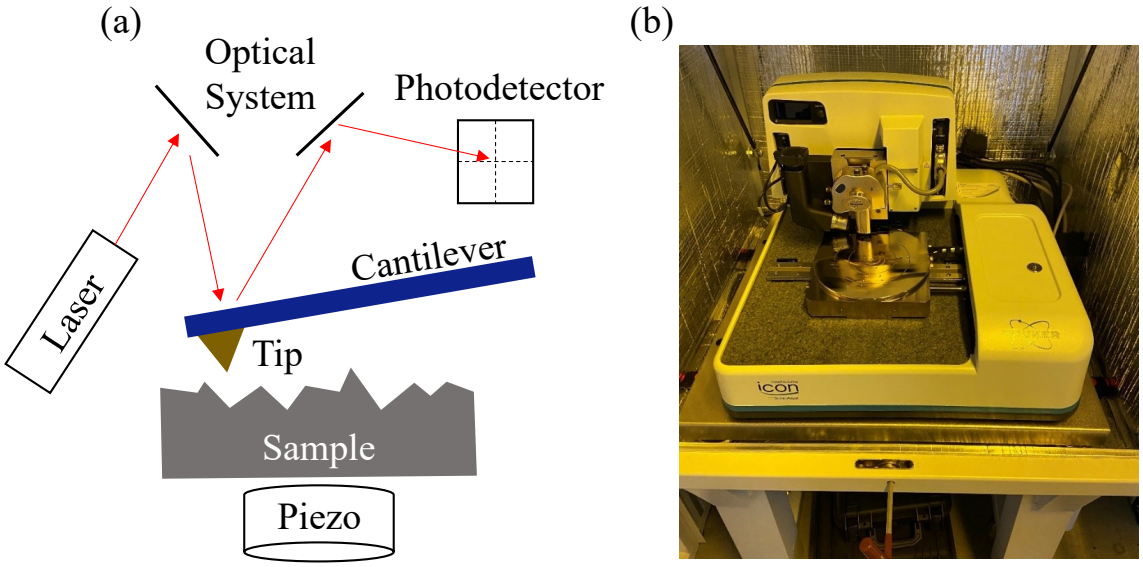


FIGURE 2.6: (a) Principle of AFM showing a laser, an optical system, and a piezo stage on which a sample is placed. The laser beam is directed on the AFM cantilever which reflects the beam through the optical system to a photodetector. The surface features on the sample cause interactions with the tip of cantilever, leading to mechanical oscillations of the cantilever which are tracked by the laser beam. (b) Photograph of the commercial AFM model 'Dimension Icon' from the company 'Bruker Corporation'.

In this thesis, a commercial AFM (Dimension Icon, Bruker Corporation, Figure 2.6b) was conducted in tapping mode to measure the topography of the photocatalyst surface. The obtained geometrical data provided information about the

fabricated metamaterial structure in thickness, length, periodicity, and surface roughness.

2.2.3 Raman Spectroscopy

Raman spectroscopy is an analytical technique that provides detailed insights into the chemical structure, crystallinity, and phase of a material (Figure 2.7a). It functions by analyzing the interaction between laser light and the chemical bonds within the sample material under study. When the laser energy excites the molecular vibrations in the sample, it results in both elastic and inelastic scattering of the incident photons. The elastic scattering, known as Rayleigh scattering, occurs at the same frequency as the laser source and does not yield useful information. Inelastic scattering, known as Raman scattering, leads to a shift in the wavelength of the scattered light. This wavelength shift is directly related to the vibrational energy of the molecular bonds of the investigated material. The Raman spectra are characterized by peaks that represent the intensity and wavelength of the Raman-scattered light. Each peak corresponds to a specific molecular bond, offering information about the chemical structure and phase of the material.

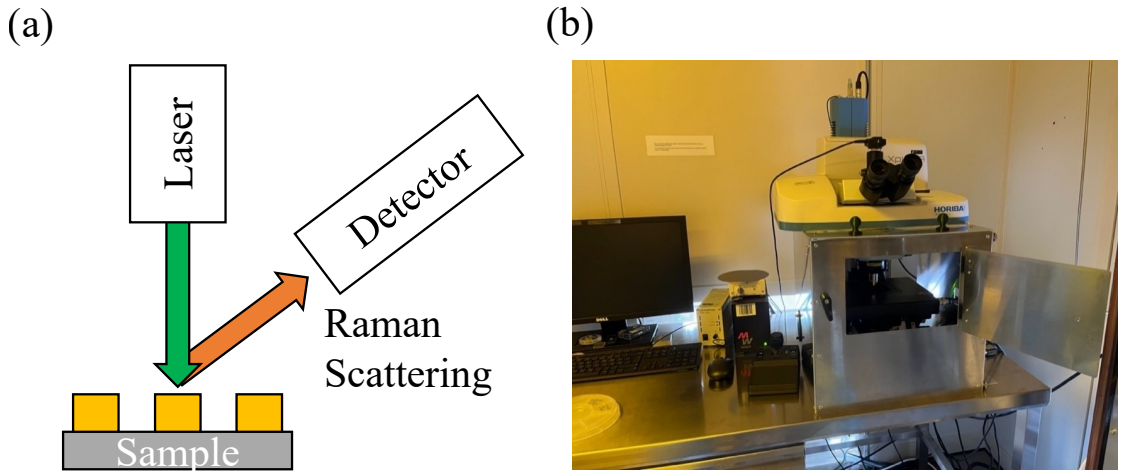


FIGURE 2.7: (a) Principle of Raman spectroscopy showing a laser, a nanostructured sample, and the scattering-caused Raman-shifted light reaching a detector. (b) Photograph of the commercial AFM model 'XploRA' from the company 'K. K. Horiba Seisakusho'.

In summary, Raman spectroscopy is a versatile and non-destructive analytical method that delivers spectroscopic data about the composition and structure of materials on a microscopic scale. Its sensitivity and precision make it ideal for examining a broad range of samples across various fields. In this thesis, Raman

measurements were conducted using a commercial Raman microscope (XploRA, K. K. Horiba Seisakusho, Figure 2.7b). A 532 nm laser was employed for excitations, and the spectra were dispersed using a high-resolution 1800 lines/mm grating. It was used to obtain the characteristic Raman signals of the photocatalyst materials but also to understand the modifications among similar photocatalyst designs.

2.2.4 UV-Vis-NIR Spectroscopy

An ultraviolet-visible-near infrared (UV-Vis-NIR) spectrophotometer is an instrument used to measure the reflection R and transmission T of light with certain wavelength range through transparent samples (Figure 2.8a). During the measurement, light from a source is directed through the sample, and the amount of light transmitted and reflected is measured by photodetectors. The absorption A, which indicates how much light is absorbed by the sample, is crucial for evaluating photocatalysts.

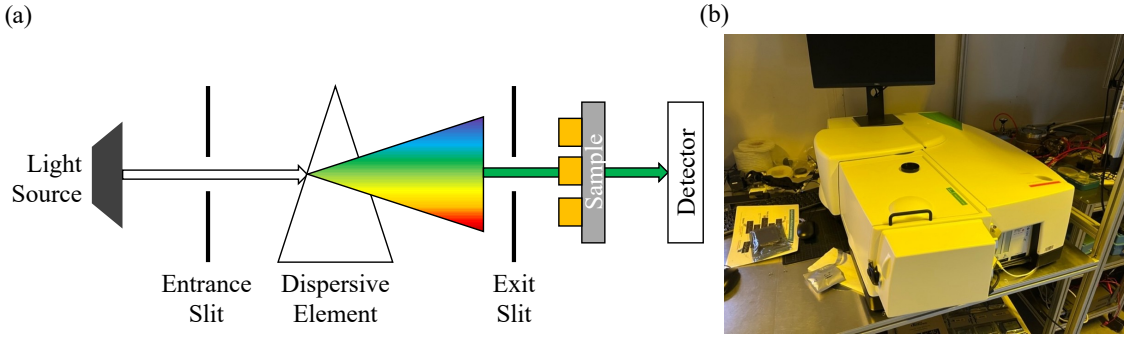


FIGURE 2.8: (a) Principle of UV-Vis-NIR spectroscopy showing a boardband light source, an entrance slit, and a dispersive element splitting the wavelength of the light source. The exit slit controls the passing wavelength that is then used to measure R and T of the sample. (b) Photograph of the commercial UV-Vis-NIR spectroscope model 'Lambda 1050+' from the company ' PerkinElmer Inc.'.

Derived from energy conversion law and classical optics, the absorption A is defined by

$$A = 1 - R - T. \tag{2.1}$$

In fact, A defines also the loss of energy here that is accounted in the sample. In the quantum physical view, incoming photons excite to reach higher energetic states through absorption, but also statistically exhibit scattering [88]. By taking

scattering S into consideration along with A in the following relation:

$$E = A + S, \tag{2.2}$$

the extinction E can be defined to quantify the total loss of light.

In this thesis, the R and T measurements were conducted on a commercial UV-Vis-NIR spectrophotometer (Lambda 1050+, PerkinElmer Inc., Figure 2.8b). The measurements were conducted across a wavelength range from 200 nm up to 1500 nm. Photocatalyst sheets based on glass substrates were used for UV-Vis-NIR spectrocopy to enable the complete optical characterization.

2.2.5 Tauc Analysis

The dataset of UV-Vis-NIR spectroscopy measurement can be further analyzed by Tauc analysis [154]. This analytical technique, developed by Jan Tauc in 1966 [155], has become a method for determining the bandgaps of both crystalline and amorphous materials. In particular, material modifications, such as integration of plasmonic nanostructures, also have an influence on the bandgap, often expressed by a shift of it.

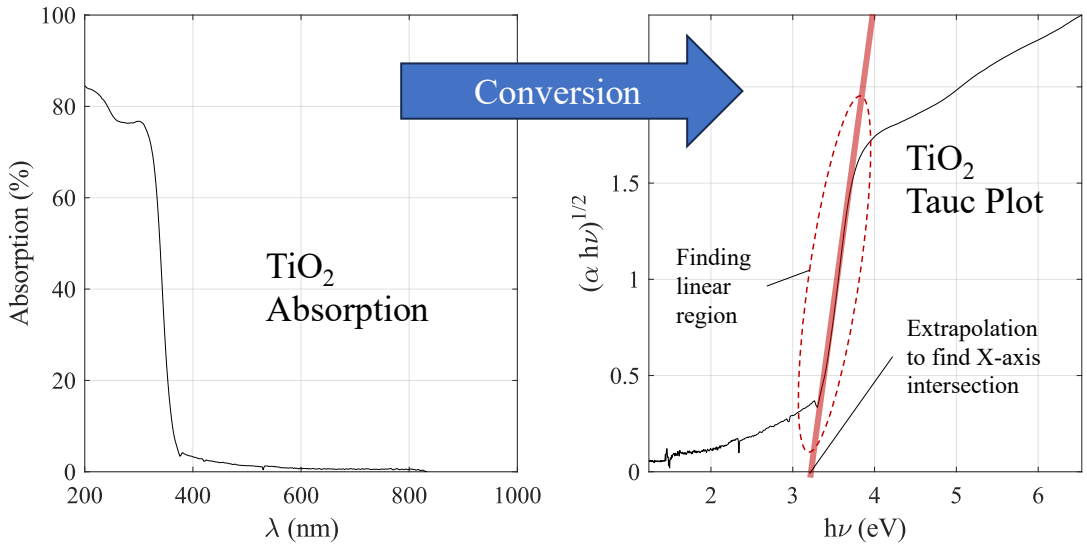


FIGURE 2.9: Methodology of Tauc plot shown with experimental TiO_2 absorption data. First, the dataset is converted by Equation (2.3) and plotted against $h\nu$. Then, the linear region of the absorption edge is identified and extrapolated to find the intersection point with the X-axis. This is where E_G is then extracted.

The Tauc plot analysis transforms the absorption spectrum data into a format that allows the evaluation of the bandgap energy E_G by an extrapolation at the

absorption edge by

$$(\alpha \cdot h\nu)^{1/\gamma} = B(h\nu - E_G), \tag{2.3}$$

where α is the absorption coefficient, h is the Planck's constant, ν is the light frequency, E_G is the bandgap energy and B is a constant. γ depends on the type of electron transition within the material and is defined by

$$\gamma = \begin{cases} 1/2 & \text{, if direct transition bandgap,} \\ 2 & \text{, if indirect transition bandgap.} \end{cases} \tag{2.4}$$

Equation (2.3) shows that $h\nu = E_G$ must be fulfilled for $(\alpha \cdot h\nu)^{1/\gamma} = 0$. Hence, E_G can be directly extracted from the x-axis intersection of the linear fit. Figure 2.9 depicts the methodology of the Tauc plot analysis.

2.3 Simulations

The interaction between light and the photocatalyst structure is a complex mechanism, hence it requires simulation tools for its computation. In principle, they numerically solve the Maxwell equations, which are a set of partial differential equations (PDE). Simulation can serve for prediction and optimization calculation, but also to understand the mechanism of a structure of interest that are else difficult to measure. In this thesis, two methods are used, which are Finite Domain Time Difference (FDTD) and Finite Element Method (FEM) [16].

2.3.1 FDTD Simulations

The FDTD algorithm is a numerical method for solving Maxwell equations in the time domain [156]. It discretizes both space and time, using a staggered grid known as the Yee lattice, where electric and magnetic field components are offset from each other. The algorithm employs central-difference approximations to evaluate spatial and temporal derivatives of the electromagnetic fields. It then iteratively updates these field values in a leapfrog manner: first calculating the electric field components at one time step, then the magnetic field components at the next time step, and repeating this process. This approach allows for the direct simulation of electromagnetic wave propagation through various materials and structures. In this thesis, Lumerical FDTD by Ansys was used as simulation tool. It was applied for the simulation studies in Chapter 3 and Chapter 5.

2.3.2 FEM Simulations

The FEM is a numerical technique used to approximate solutions to complex physical problems described by PDEs, hence also the Maxwell equations [157, 158]. The method involves the discretization of a continuous domain into smaller, simpler subdomains called finite elements, often geometrically represented as triangles. Each element is associated with a set of equations that describe its behavior, typically derived from the weak formulation of the governing PDE. By applying boundary conditions and assembling the equations from all elements, FEM transforms the problem into a system of linear algebraic equations that can be solved using numerical methods. This approach allows for the analysis of various phenomena in engineering and physics, such as structural mechanics, heat transfer, and electrodynamics, while accommodating complex geometries and material properties. In this thesis, the Electromagnetic package from COMSOL is used as simulation tool. It was applied for the simulation studies in Chapter 4 to consider the hexagonal periodicity.

2.3.3 Simulation Output

Simulation studies are used to find and optimize an ideal photocatalyst sheet design, but are as well used to understand experimental behavior. In particular, the simulation results can provide important optical properties such as R, T, S, A, E, and electric field amplification maps for a specific wavelength range. Moreover, it is used to understand localized surface plasmon resonance (LSPR) across different geometries, allowing for a detailed examination of how these interactions influence the photocatalytic activity.

While the optical simulations provide an indication where strong light-coupling occurs, it is not the key parameter to theoretically predict the performance of a photocatalyst. Beside optical properties, an ideal photocatalyst has to be understood by its charge carrier dynamics or adsorption properties with its reactants by density functional theory (DFT) [133, 134]. However, such theoretical work would be beyond the scope of this thesis. Therefore, it is only mentioned in context with literature reference.

3 Metal Nanodisk Metamaterial Photocatalyst Sheet

Metamaterials represent a field in physics and materials science, offering systematic control over the optical and electrical properties of engineered structures [159, 160, 161]. Often in periodic arrangements, these structures are not found in nature, enabling the manipulation of electromagnetic waves and charge carriers in ways that were previously unattainable. Through careful design and fabrication of metamaterials, remarkable modifications to the material properties can be achieved, opening up a wide range of applications across various fields [162].

In photocatalysis, metamaterials can create supporting effects such as diffraction patterns, light and charge trapping mechanisms, and localized reaction center regions [108, **?**, 109]. Diffraction effects can increase the plasmonic mechanisms, while light trapping mechanisms can significantly enhance the efficiency of photocatalysts by increasing the optical path length within the active material. Similarly, charge trapping can be utilized in photocatalysts to improve reactivity and charge carrier lifetime, enhancing the overall photocatalytic performance.

In this chapter, the focus is set on the fundamental metamaterial structure for this thesis: a periodically-arranged plasmonic metal nanodisk array on a TiO_2 thin film layer. This basic yet versatile structure serves as a model system for understanding the principles underlying metamaterial behavior. Analyzing and discussing the metal nanodisk in detail can provide insights into how its size, shape, material composition, and arrangement influence its optical and electrical characteristics.

3.1 Photocatalyst Design

An ideal photocatalyst sheet design requires considerations on the optimization of optical and electrical properties but also on the technical limitations, such as given fabrication requirements. The LIL setup in this work (Section 2.1.3) has a recommended technical limitation at $P = 300\,\text{nm}$ for reliable operation, resulting in a spot size diameter of the interference pattern at $D_{\text{ND}} = P/2$, thus $D_{\text{ND}} =$

150 nm. To ensure a reliable lift-off process, it is recommended not to exceed 1/3 of the resist layer thickness. Thus, the nanodisk height was set at $H_{\mathrm{ND}} = 30\,\mathrm{nm}$.

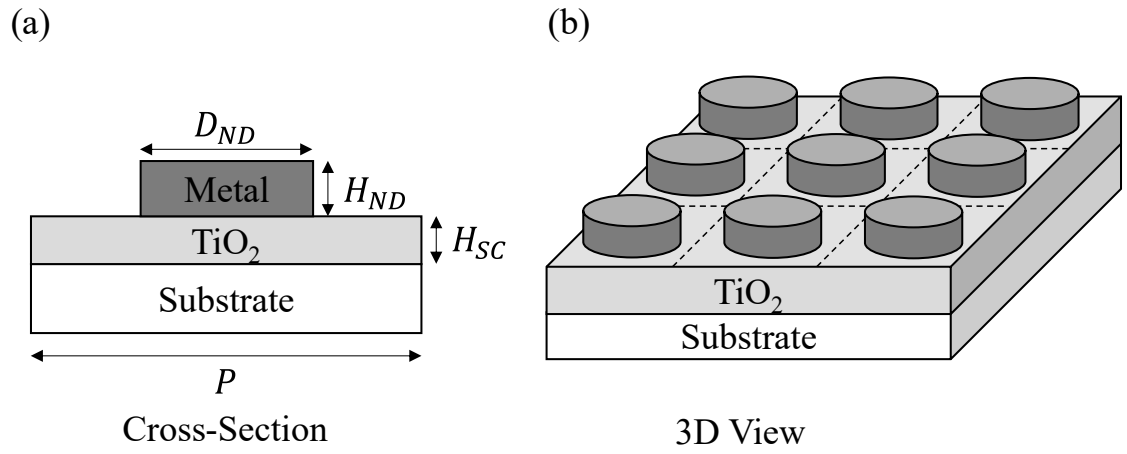


FIGURE 3.1: Plasmonic nanodisk metamaterial photocatalyst sheet design: (a) cross-sectional view and (b) 3D view. The nanodisk are arranged in a rectangular array. The geometrical parameters are the nanodisk diameter D_{ND}, nanodisk height H_{ND}, semiconductor/photocatalyst material thin film thickness/height H_{SC}, and the periodicity P.

TiO_2 was used as a photocatalyst layer due to its well-known photocatalytic activity and stability [111, 112, 113]. On-top of it, a plasmonic nanodisk array was patterned, completing the metamaterial structure. Four different metals are studied which are Ag, Au, Pt and Pd, hence labeled by Ag/TiO_2, Au/TiO_2, Pt/TiO_2, and Pd/TiO_2, respectively. The photocatalyst design is shown in Figure 3.1.

Furthermore, a FDTD simulation study was conducted with the focus on the plasmonic nanodisk metamaterial structure to understand the photocatalyst design in optical properties. The results for a Au/TiO_2 structure on a glass substrate are presented here as a representative example (Figure 3.2), while the results for the other metals are shown in Appendix A. In the computation, the value for P was varied in 5 nm steps between 100–700 nm, while maintaining fixed parameters of $H_{SC} = 250\,\mathrm{nm}$, $H_{ND} = 30\,\mathrm{nm}$ and $D_{ND} = P/2$. The results are visualized as three-dimensional (3D) map plots, showing the impact of P on scattering (Figure 3.2a), absorption (Figure 3.2b) and extinction (Figure 3.2c).

Overall, the variations are mainly accounted by the geometry of the plasmonic nanodisk pattern. The results show that Au nanodisk structures with $P = 300\,\mathrm{nm}$ are in the ideal region to achieve the optimal scattering in the visible and near infrared (NIR) range ($\lambda = 400$–$1000\,\mathrm{nm}$), reaching values above 80 %. Scattering leads to enhanced plasmon resonance, and therefore more expected hot electrons. The absorption data suggest the wavelengths at which photo-excited electrons

can be created. Its highest activity is at a 60–70 % plateau for $\lambda < 400\,\text{nm}$, which correspond to the 3.2 eV bandgap energy of the TiO_2 layer resulting in an absorption edge at $\lambda = 387\,\text{nm}$ [148, 149]. As it does not significantly change in dependency of P, it is an intrinsic outcome of the TiO_2 layer. The extinction is the sum of scattering and absorption, indicating the overall light response independent of plasmonic or light excitation effects.

These outcomes remain the similar for Ag/TiO_2 (Figure A.2). However, the results differ for Pt/TiO_2 (Figure A.3) and Pd/TiO_2 (Figure A.4) suggest smaller structures with $P < 300\,\text{nm}$ for improved optical properties. The differences are due to the dielectric constants of the individual material. While these chosen parameters are primarily motivated by technical consideration for achieving the smallest and most reproducible structure size ($P = 300\,\text{nm}$), the simulation study confirms that this design choice also yields to good optical properties.

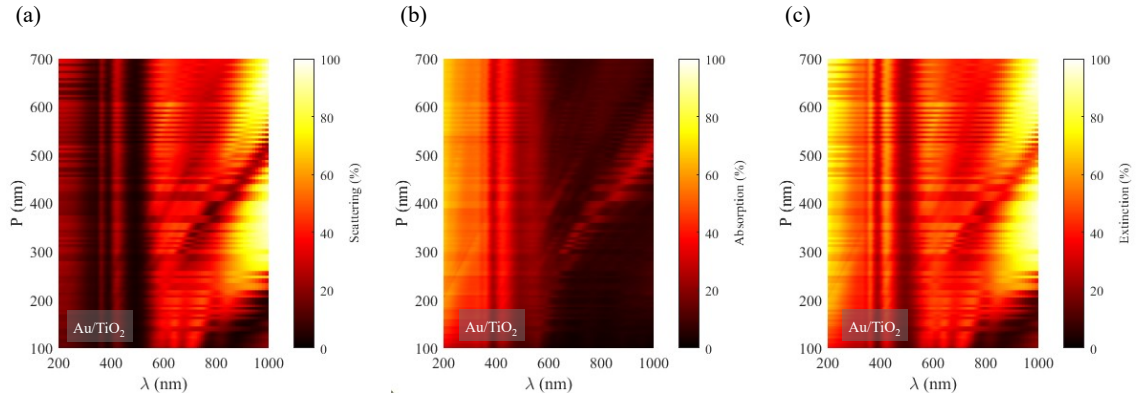


FIGURE 3.2: Periodicity-dependent ($P = 100$–$700\,\text{nm}$) FDTD simulation study for an Au nanodisk array on a TiO_2 thin film: (a) scattering, (b) absorption, and (c) extinction map. The other geometrical parameters are fixed with $D_{ND} = P/2$, $H_{ND} = 30\,\text{nm}$, and $H_{SC} = 250\,\text{nm}$.

3.2 Fabrication

The photocatalyst sheet is fabricated on planar $(5 \times 5)\text{cm}^2$ glass substrates with the following workflow (Figure 3.3):

1. Deposition of 250 nm TiO_2 (blue layer) on the substrate by DC magnetron sputtering. Afterward, an annealing process at 650 °C for 1 h is conducted to turn the amorphous TiO_2 layer into the anatase crystal phase.

2. Spin-coating of 100 nm PMMA (green layer) and 100 nm (red layer) AMONIL.

3. Patterning of a periodic rectangular-arranged hole pattern ($P = 300\,\text{nm}$, $L = 150\,\text{nm}$) by NIL.

4. Plasma etching by RIE of the AMONIL and PMMA layer to achieve an undercut profile in the PMMA layer.

5. Deposition of plasmonic metal (Ag, Au, Pt, or Pd) with 30 nm thickness by e-beam evaporation.

6. Lift-off step to remove the double-layer resist structure by acetone, IPA and deionized (DI) water.

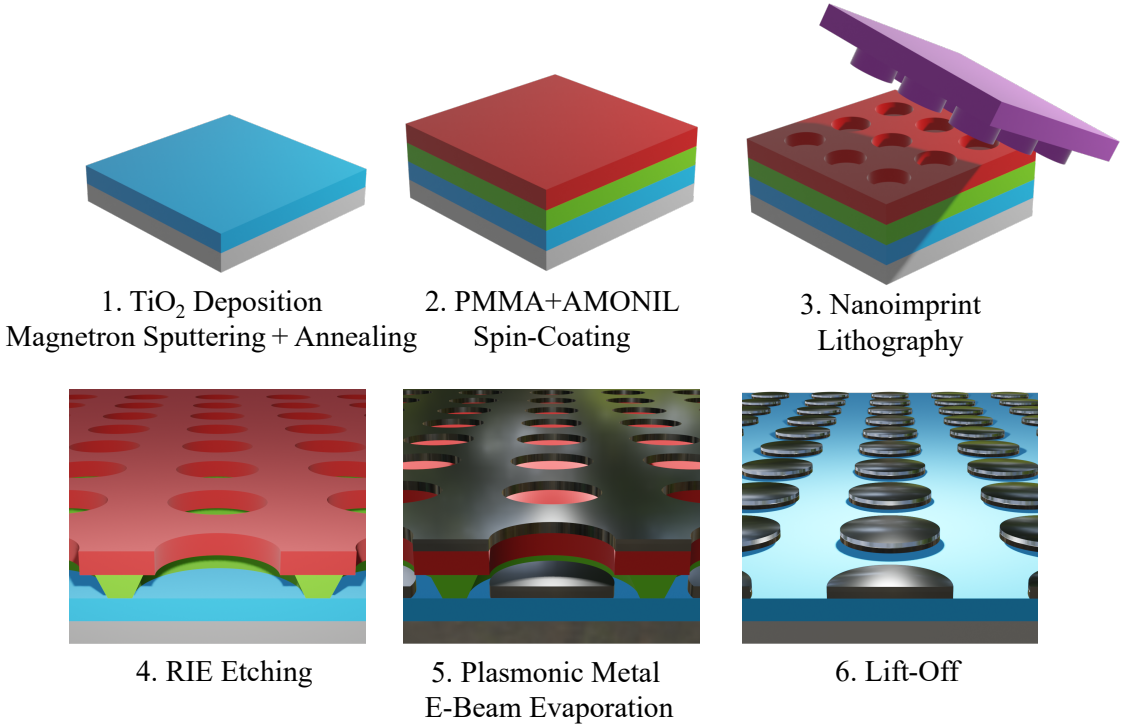


FIGURE 3.3: Fabrication process flow for periodic metal nanodisk pattern, involving multiple process steps such as magnetron sputtering, spin-coating, NIL, RIE, e-beam evaporation, and lift-off.

3.3 Characterization

The surface topography of the photocatalyst sheet was characterized using SEM and AFM, with the Au/TiO_2 photocatalyst sheet serving as a representative example. This comprehensive analysis provides a multi-faceted view of the material structure, offering insights into its geometrical properties and surface characteristics.

SEM imaging was conducted from both a top-down (Figure 3.4a) and a cross-sectional (Figure 3.4b) perspective, allowing for a more detailed examination of the photocatalyst surface features. Complementing this, AFM analysis provided

topography images (Figure 3.4c) and a generated 3D view (Figure 3.4d), showcasing the nanoscale precision in surface mapping.

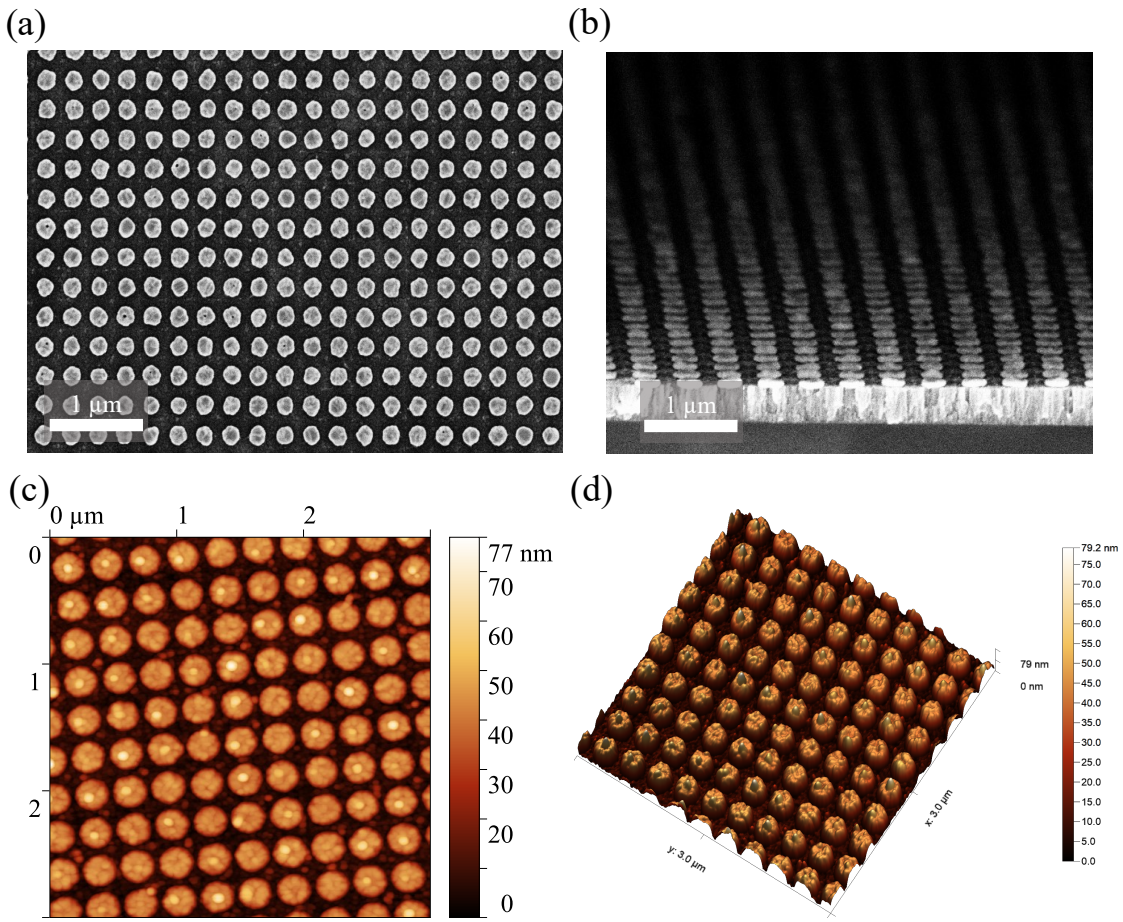


FIGURE 3.4: Topography analysis of the Au/TiO_2 photocatalyst sheet. (a) Top-down and (b) cross-sectional SEM images. (c) Top-down and (d) 3D-generated AFM images.

The cross-sectional SEM image (Figure 3.4b) shows particularly valuable insights into the internal structure of the photocatalyst sheet. It reveals the crystal grain structure of the 250 nm thick TiO_2 layer in its anatase phase. This crystalline configuration is advantageous for photocatalytic applications, offering several benefits over amorphous TiO_2 layers [148, 149]. The grain structure increases the effective surface area, providing more active sites for photocatalytic reactions. In addition, the presence of grain boundaries enhances charge carrier separation which is a critical factor in improving photocatalytic efficiency [163].

The AFM image (c Figure 3.4c) presents height data for a $(3 \times 3)\mu m^2$ area of

the metasurface. It reveals a well-arranged nanodisk pattern along with particle-like features on both the nanodisk and the TiO_2 surfaces. In Appendix A, additional AFM scans compare TiO_2 thin films subjected to different annealing heating temperatures (Figure A.1a-c). These scans demonstrate that the crystal formation induced by the annealing process influences the TiO_2 surface morphology, resulting in the observed particle-like structures.

Figure 3.4d illustrates a generated 3D visualization of the data shown in Figure 3.4b, offering an additional representation of the metasurface topography. This 3D illustration provides an enhanced view on the surface features, including the height variations of the nanodisks and the particle-like structures on both the nanodisks and the TiO_2 substrate.

Raman spectroscopy analysis provides insights into the characteristic crystalline structure of the TiO_2 thin film, confirming that it is predominantly in the anatase phase. The characteristic anatase peaks are observed at 141 cm^{-1}, 193 cm^{-1}, 513 cm^{-1}, and 635 cm^{-1} (Figure 3.5a) [150]. Notably, a minor peak at 392 cm^{-1} indicates the presence of a partial brookite phase, likely a result of the 650 °C annealing treatment [150]. This temperature regime is known to be optimal for the formation of anatase crystals while also initiating minor brookite phase development [148, 149]. In the end, the presence of a partial brookite is not critical for the photocatalytic functionality [150].

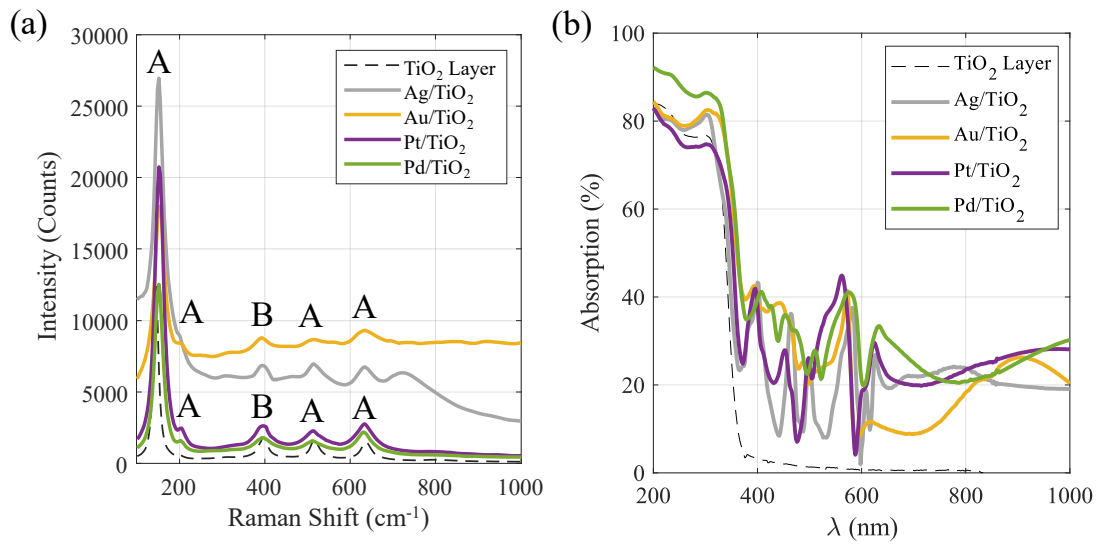


FIGURE 3.5: (a) Raman spectra showing characteristic anatase peaks of TiO_2 and SERS effect by the various metal nanodisks. (b) Absorption spectra evaluated by UV-Vis-NIR measurements showing the absorption activity in the visible and NIR wavelength range.

The Raman spectra show the enhanced background signal for Ag/TiO_2 and

Au/TiO_2 photocatalyst sheets due to surface-enhanced Raman scattering (SERS) [164]. This phenomenon is an indicator of strong plasmonic activity in the nanodisk pattern. The SERS effect results from the interaction between the incident light and the localized surface plasmons of the metal nanostructures. As the enhanced Raman signal is caused by increased scattering, it is an indication for potential improvements in light scattering, hence stronger plasmonic activity, eventually contributing to the overall photocatalytic performance of these materials [165].

The Pt/TiO_2 and Pd/TiO_2 photocatalyst sheets exhibit lower Raman intensities. Their inclusion in the study is due to their stronger adsorption properties and catalytic activity, particularly in water splitting and CO_2 reduction reactions [132, 133]. In the end, the lower Raman intensity does not necessarily indicate weaker photocatalytic performance. Instead, it reflects the different scattering properties of these metals compared to between these metals. While less effective in plasmonic enhancement, Pt and Pd offer more favorable catalytic sites for specific reactions, potentially compensating for their lower light interaction through enhanced chemical kinetics at the catalyst surface [132, 133].

The UV-Vis-NIR spectroscopy analysis reveals differences between the reference TiO_2 thin film and the metal nanodisk metamaterial photocatalyst sheets (Figure 3.5b). The nanodisk array leads to the rise of multiple extinction peaks and dips in the visible range, which is attributable to their periodic arrangement and sub-wavelength geometry. This is similar to the behavior of a diffraction grating, highlighting the light-matter interactions at play in the metasurfaces. For wavelengths below 650 nm, absorption peaks can be observed and known as Wood-Rayleigh anomalies [107, 48], which typically occur in periodic structures. For wavelengths above 650 nm, localized surface plasmon resonance (LSPR) peaks are observed beyond this wavelength.

The LSPR peaks for Ag/TiO_2 and Au/TiO_2 are located at 786 nm and 892 nm, respectively. In contrast, the LSPR peaks for Pt/TiO_2 and Pd/TiO_2 are shifted into the NIR range [166]. This spectral positioning of the plasmonic resonances is crucial for visible light-driven photocatalytic reactions, as it allows for the harvesting of a broader range of the solar spectrum. Tuning these plasmonic effects through careful selection of metal and nanostructure geometry is crucial for optimizing photocatalytic performance.

The Tauc plot analysis (Figure 3.6) can reveal the effective bandgap E_G of the metamaterial structure. The anatase TiO_2 thin film exhibits a band gap of 3.25 eV, which aligns well with established literature values [149]. Upon the integration of the plasmonic nanodisks, a red-shift in the absorption edges is observed, leading

to a narrowing of the effective band gaps. This phenomenon is important in photocatalysis, as it extends the light absorption range of the materials into the blue visible light spectrum, enhancing their solar energy utilization efficiency. The effective band gaps were determined to be 3.09 eV, 2.62 eV, 2.93 eV, and 2.81 eV for Ag/TiO_2, Au/TiO_2, Pt/TiO_2, and Pd/TiO_2, respectively. These values show a lowering in E_G compared to the reference TiO_2 layer, with Au/TiO_2 showing the highest band gap narrowing.

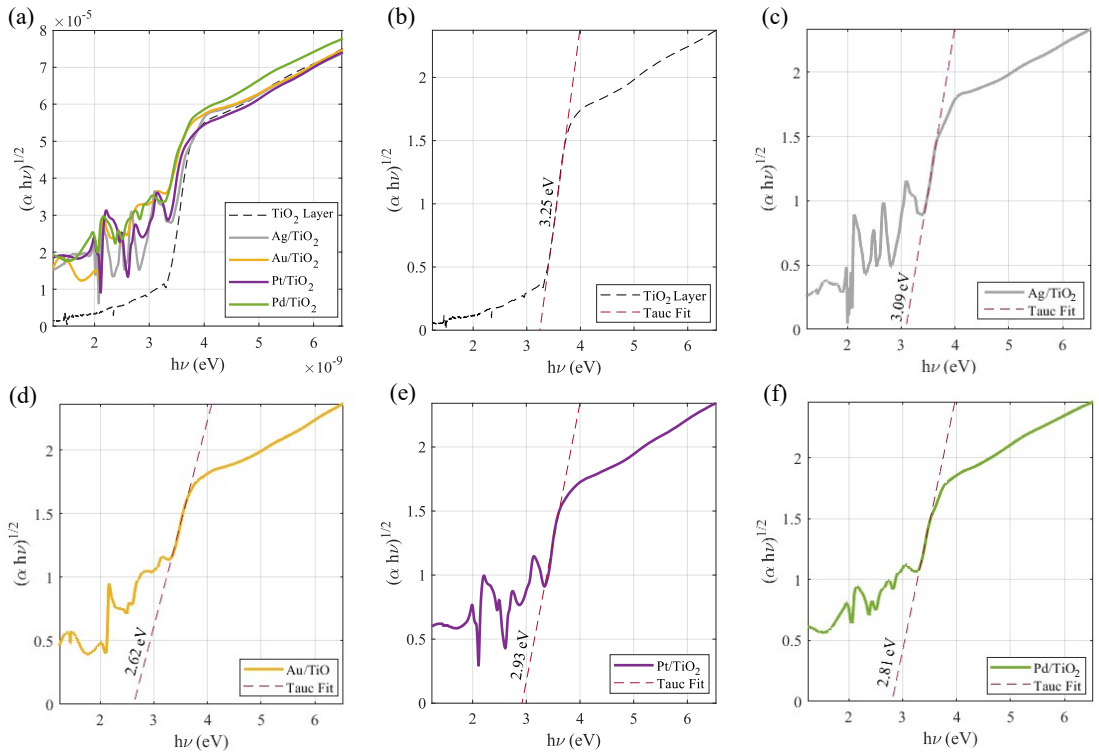


FIGURE 3.6: (a) Tauc analysis overview of all metal nanodisk metamaterial photocatalyst sheets extracted from the absorption spectra. Detailed bandgap evaluated view on (b) 250 nm TiO_2 layer, (c) Ag/TiO_2, (d) Au/TiO_2, (e) Pt/TiO_2, and (f) Pd/TiO_2. The band gap can be extracted by the x-axis intersection by an linear extrapolation of the absorption edge. All evaluated bandgap values are included in each plot.

The varying degrees of band gap narrowing observed for different metals (Ag, Au, Pt, Pd) can be attributed to their distinct plasmonic properties and work functions. Au/TiO_2, with its strong plasmonic response in the visible range, shows the most significant band gap reduction, potentially offering the best visible light harvesting capabilities among the studied materials. The less pronounced but still significant E_G narrowing in Pt/TiO_2 and Pd/TiO_2 systems suggests a balance between their moderate plasmonic effects and strong catalytic properties. As the only metal in this work facing native oxidation [167], Ag/TiO_2 shows the highest effective E_G. This effect can be accounted to natively-grown silver oxide

(Ag_2O), which is also known as functioning photocatalyst material [168]. Hence, it is not regarded as a disadvantage for the photocatalytic functionality.

3.4 Photocatalytic Water Splitting and CO_2 Reduction

Photocatalytic activity measurement are conducted to evaluate the performance and efficiency of photocatalysts in various applications. The quantification of photocatalytic activity provides insight into the effectiveness of different materials, optimization of reaction conditions, and comparison of results across studies.

The photocatalytic water splitting and CO_2 reduction were conducted simultaneously in one custom-built reactor setup and operated by the research partner Lukas Feierabend, a group leader and engineer at ZBT GmbH in Duisburg, Germany.

3.4.1 Reactor Setup

The solar fuel generation of the photocatalysts was tested using a custom-built, lab-scale flow reactor specifically designed for gas-phase reactions (Figure 3.7). During the experiments, a CO_2 gas flow rate of 1 sccm was maintained, while the liquid feed-composed of deionized water and 1 mol/L isopropanol (IPA) as a hole scavenger [169] was introduced at a rate of 0.6 mL/h. The IPA was included to enhance signal detection during the reaction. To ensure the process occurred entirely in the gas phase, the reactor chamber was continuously heated to 120 °C.

The liquid feed was combined with the CO_2 inlet stream upstream of the reaction chamber, where a microporous carbon felt ensured controlled evaporation of the liquid. Mass flow controllers (MFC) regulated the flow of reactant gases, while the product gases were monitored in real-time using mass spectrometry. Prior to analysis, any condensed liquid in the product stream was separated to avoid interference with gas-phase measurements.

The photocatalyst sheet was irradiated by a 150 W metal-halide lamp positioned 20 cm above the catalyst. The light was directed through a 3 mm thick fused silica glass window, providing an overall flux density of approximately 500 mW/cm^2 on the photocatalyst sheet surface.

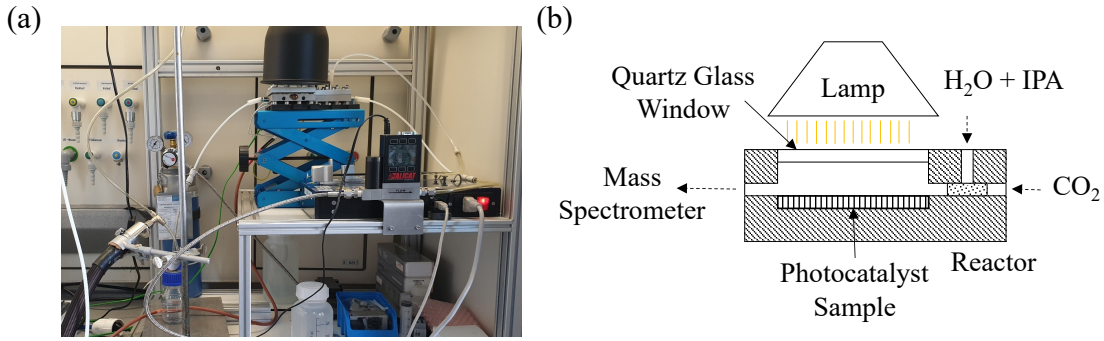


FIGURE 3.7: (a) Photograph and (b) schematic illustration of the custom-built and lab-scale photocatalytic reactor for gaseous-phased reactions by Lukas Feierabend from ZBT GmbH in Duisburg, Germany.

3.4.2 Mass Spectrometry

The principle of mass spectrometry involves the generation of ions from a gas sample, followed by the separation of these ions based on their mass-to-charge ratio (m/z). Initially, the gas sample is ionized, which creates positively charged ions. These ions are then accelerated and subjected to electromagnetic fields, causing them to be deflected. Lighter ions are deflected stronger than heavier ones due to centrifugal forces. This separation allows for the detection of the ions, typically by using a detector that measures the abundance of each ion. The resulting data is presented as a mass spectrum, illustrating the relative abundance of ions at different m/z ratios, thereby providing insights into the material composition of the gas sample. In this thesis, the gases inside the reaction chamber (Figure 3.7b)) was analyzed by a commercial mass spectrometer (OmniStar, Pfeiffer Vacuum AG).

The m/z ratios are measured in signals and require a calibration to calculate the amount of substance n of the specific gas. This calibration measurement was carried out with a known amount of H_2 and CH_4 (Figure 3.8). Although carbon monoxide (CO) is also expected to be generated in the experiments, it was not possible to clearly characterize it due to the overlapping peak with N_2 from air at $m/z = 28$. Further methods, such as isotope labeling, would have been required, but were not available [170, 171]. For this reason, it is excluded in the evaluation. The calibration curve for this individual mass spectrometer is estimated through linear regression:

$$H_2 : y(x) = 2.510 \times 10^9 \cdot x - 6.310 \times 10^{-2}, \tag{3.1}$$

$$CH_4 : y(x) = 5.753 \times 10^9 \cdot x + 9.523 \times 10^{-3}, \tag{3.2}$$

where x is the measurement signal in V, and y the volume percentage.

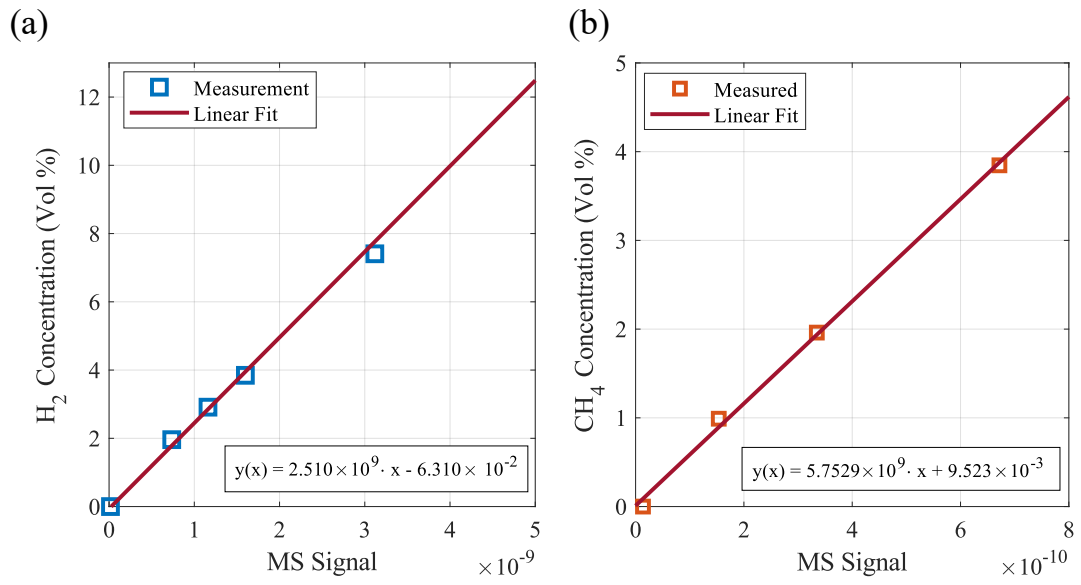


FIGURE 3.8: Signal-to-volume ratio calibration curve for (a) H_2 and (b) CH_4.

In the setup, the volume stream Q_V of the CO_2 can be set by the MFC that is connected to the setup. Technically, these data are set in units of standard cubic centimeter per minute (sccm), which would covert into $1\,\text{sccm} = 1\,\text{cm}^3/\text{min}$ in SI units. With the known Q_V, this input data can be converted into a mass stream Q_M with the help of the formula of the mass density $\varrho = m/V$ by

$$Q_m = \frac{m}{t} = \varrho\frac{V}{t} = \varrho Q_V. \tag{3.3}$$

Furthermore, a molar stream Q_n can be expressed by the definition $n = m/M$ with

$$Q_n = n/t = \frac{1}{M}\frac{m}{t} = \frac{\varrho}{M}Q_V, \tag{3.4}$$

where m is the mass, and M the molar mass.

Because $n \propto V$, the calibration function y can be used as well be used to calculate n with

$$n = y \cdot Q_n = y \cdot \frac{\varrho}{M}Q_V. \tag{3.5}$$

Equation (3.5) is the main equation to analyze results from mass spectrometry and obtain the absolute yield of the product gas. In photocatalysis research, it is a common practice to normalize n by the photocatalyst mass m_{PC} or area A_{PC} to make results better understandable and comparable (Equation 1.18- 1.20). In this thesis, all results are provided with these three values.

3.4.3 Metamaterial Photocatalyst Mass Calculation

The calculation of the photocatalyst mass m_{PC} requires additional derivation, while the photocatalyst sheet area A_{PC} is defined by the photocatalyst sheet length. The derivation for the metamaterial can be conducted geometrically by the photocatalyst design and its mass density ϱ, as it require a high-precision balance to determine m_{PC} by measurement.

Starting from the definition $\varrho = m/V$, the photocatalyst mass m_{PC} can generally be expressed by

$$m_{PC} = \varrho_{SC} V_{SC} + N_{ND} \varrho_{ND} V_{ND}, \tag{3.6}$$

where ϱ_{SC} is the mass density of the semiconductor thin film material, V_{SC} the volume of the semiconductor thin film, N_{ND} the number of individual nanodisks, ϱ_{ND} the mass density of the nanodisk material, and V_{ND} the volume of a single nanodisk.

V_{SC} can be assumed as a cuboid by

$$V_{SC} = L_{PC}^2 H_{SC}, \tag{3.7}$$

where L_{PC} refers the photocatalyst sheet length and H_{SC} the thin film thickness.

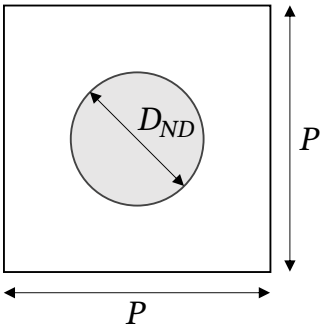


FIGURE 3.9: Geometrical sketch of the unit cell in top-down view of a circular-shaped nanodisk pattern arranged in a square lattice.

The photocatalyst geometry is a circular-shaped nanodisk arranged in a square lattice, as sketched in Figure 3.9. One unit cell of an individual nanodisk is defined by the periodicity P. Therefore, the total number of nanodisks on the photocatalyst is

$$N_{ND} = \frac{L_{PC}^2}{P^2}. \tag{3.8}$$

Then, V_{ND} can be expressed by the volume of a cylinder by

$$V_{ND} = \pi r_{ND}^2 H_{ND} = \frac{\pi}{4} D_{ND}^2 H_{ND}, \tag{3.9}$$

where r_{ND} refers to the nanodisk radius, D_{ND} is the nanodisk diameter, and H_{ND} is the nanodisk height.

Finally, m_{PC} can be calculated by inserting Equation (3.7), (3.8) and (3.9) into Equation (3.6):

$$m_{PC} = \varrho_{SC} L^2 H_{SC} + \varrho_{ND} \frac{\pi}{4} \frac{L_{PC}^2}{P^2} D_{ND}^2 H_{ND}. \tag{3.10}$$

3.4.4 Light Source

The light source in the setup is a commercial 150 W metal halide lamp based on commercial hydrargyrum medium-arc iodide (HMI; Lucky Reptile). It generates a broad light spectrum, covering the UV, visible, and NIR range. Figure 3.10 shows the difference between its measured light spectrum and the air mass (AM) 1.5 spectrum, which is considered the standard for solar light. While both spectra have a similar broad band properties, the intensity differs for all wavelengths, with a more intense UV portion for the HMI lamp. Although the weaker intensity differences in the HMI lamp starting from 500 nm wavelength compared to the AM1.5 spectrum, it emits sufficient spectral intensity to excite photocatalytic reactions in the visible spectrum. The HMI lamp spectrum can also be further adjusted by decreasing the illumination distance.

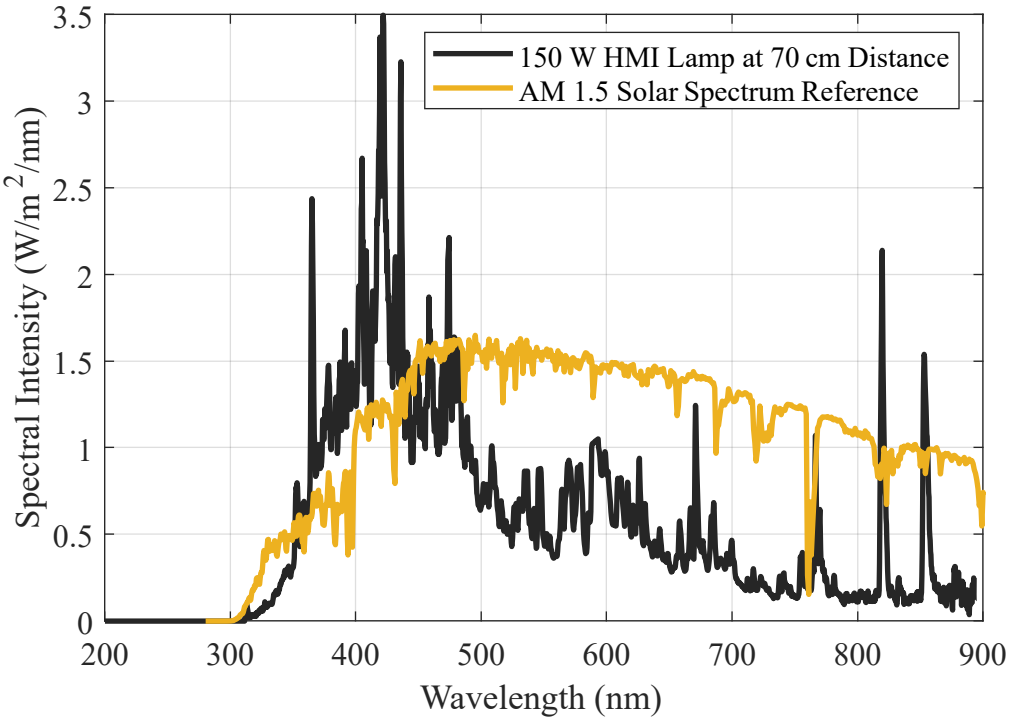


FIGURE 3.10: Comparison between the HMI lamp spectrum and AM1.5 filtered light.

3.4.5 Experimental Results

The photocatalytic CO_2 measurements were conducted as described in Section 3.4. Figure 3.11 and Figure 3.12 show the calibrated data of the measured H_2 (Equation 3.1) and CH_4 signal (Equation 3.2) for each metal nanodisk metamaterial photocatalyst sheet, respectively. All raw data from the mass spectrometer are provided in Appendix B.

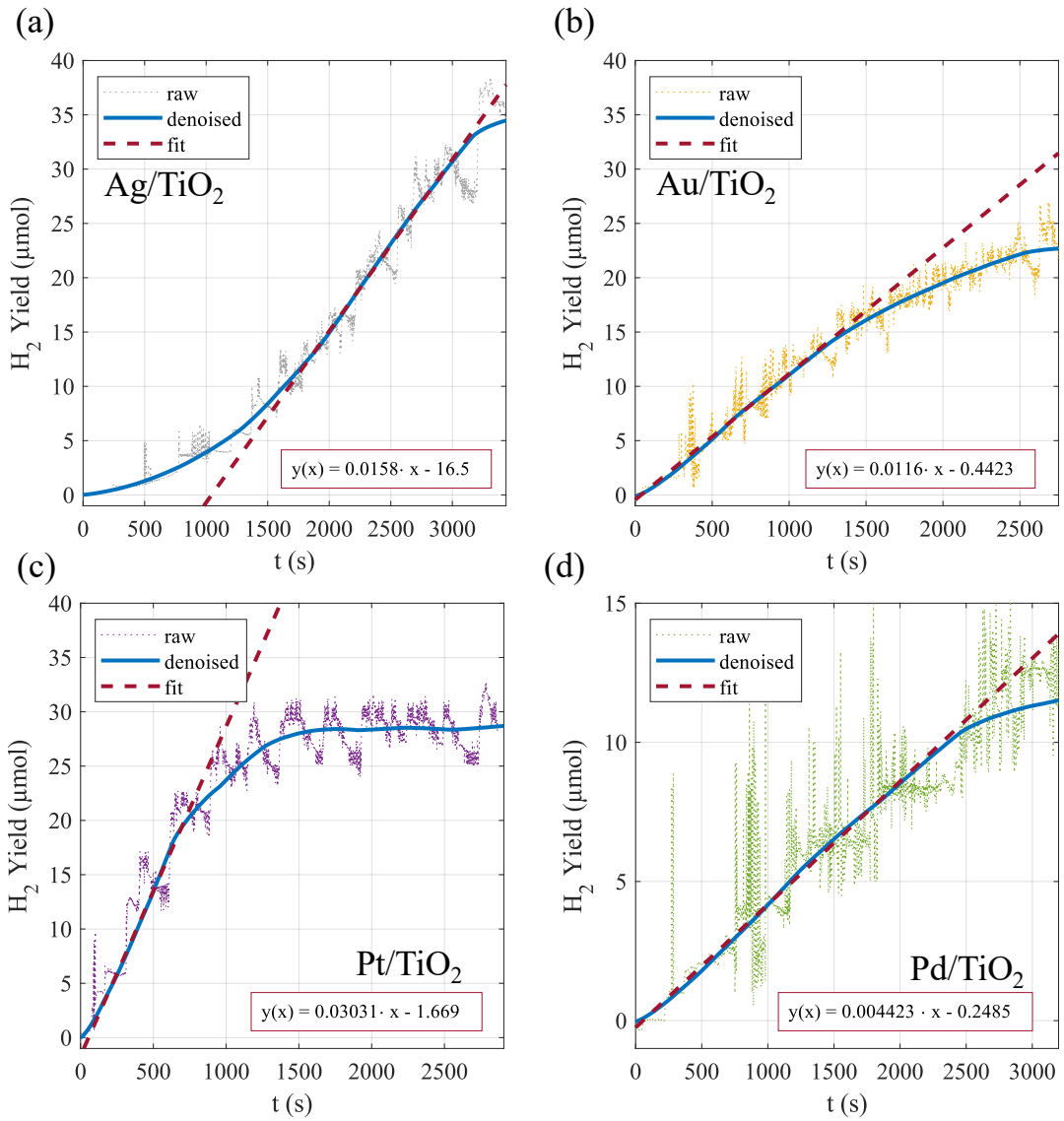


FIGURE 3.11: Evaluation procedure for the H_2 generation of (a) Ag/TiO_2, (b) Au/TiO_2, (c) Pt/TiO_2, and (d) Pd/TiO_2.

The continuously measured signals show a noise pattern (dotted curve) due to a water bubbler, which is placed between the reactor chamber and the mass spectrometer. The water bubbler serves as a collector of the gas samples from the reaction chamber. Hence, the gas samples reached the mass spectrometer only

in portions of gas bubbles that have crossed the water bubbler. For each dataset, the signals are processed with a Bayesian denoising algorithm by the MATLAB Wavelet Signal Denoiser (solid curve) [172]. A linear regression is then performed in the linear region of the reaction curve (dashed curve). The evaluated slope is then taken as the reaction rate and converted into units of μmol/h.

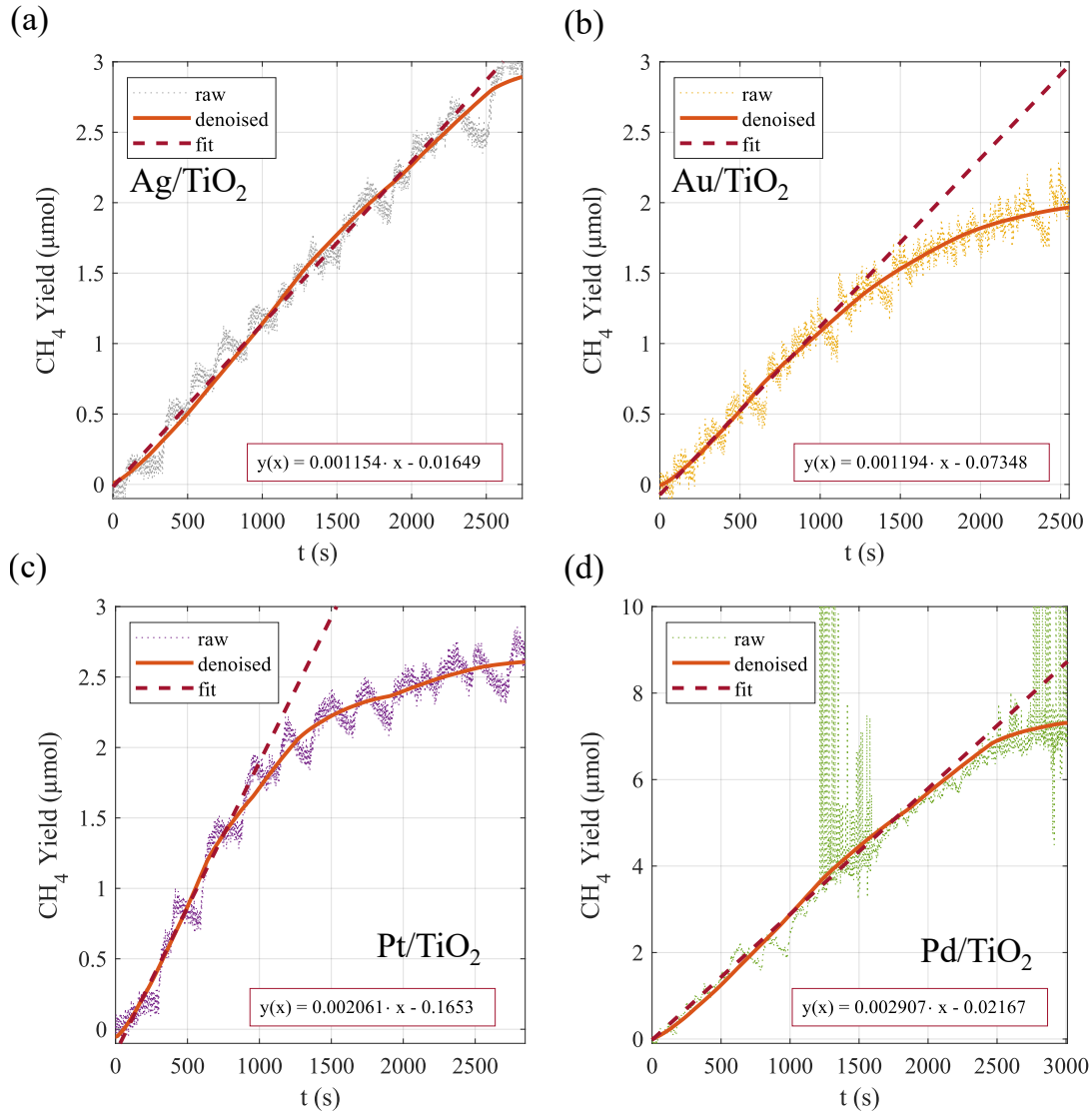


FIGURE 3.12: Evaluation procedure for the CH_4 generation of (a) Ag/TiO_2, (b) Au/TiO_2, (c) Pt/TiO_2, and (d) Pd/TiO_2.

Figures 3.13a and 3.13b display the respective denoised gas yield of H_2 and CH_4 for each photocatalyst sheet: Ag/TiO_2 (grey line), Au/TiO_2 (yellow line), Pt/TiO_2 (green line), and Pd/TiO_2 (violet line). The curves represent the different photocatalyst sheets that exhibit varying reaction times, speeds, and selectivities due to the different metals used. The measurements were stopped once a lowering slope of linear region was observed, which can be seen by the saturation of the

gas evolution. This is why the datasets show different lengths of measurement time.

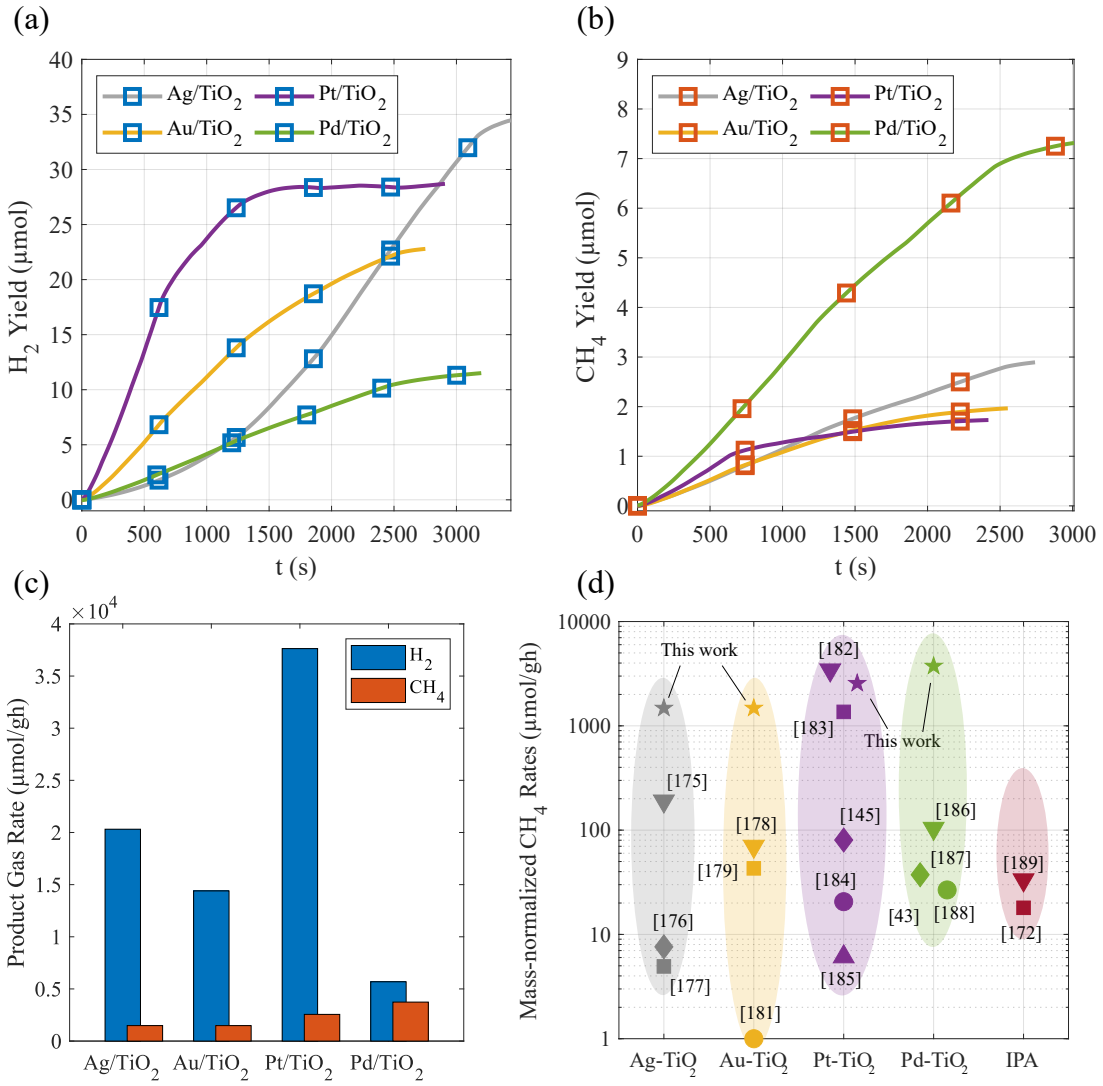


FIGURE 3.13: (a) H_2 (blue square) and (b) CH_4 (orange square) generation on-line measured by mass spectrometer for the Ag/TiO_2 (grey line), Au/TiO_2 (yellow line), Pt/TiO_2 (green line), and Pd/TiO_2 (purple line) nanodisk photocatalyst. (c) Summarized results for the generated gas rate normalized by the photocatalyst mass. (d) Literature benchmark comparison of mass-normalized CH_4 yield rates with plasmonic TiO_2-based photocatalyst and photocatalytic IPA conversion (red).

All the measurements exhibit an increasing linear H_2 and CH_4 yield region before reaching the saturation region. A slight time shift in the onset of CH_4 formation can be observed. It occurs with a time delay after the H_2 generation started (see raw data in Appendix B). This suggests that the CH_4 formation by the CO_2 reduction utilizes the H^+ generated from the water splitting. In addition, one measurement was done without a photocatalyst (Figure B.8) and only one set

with the TiO_2 thin film (Figure B.5) was conducted to verify that these reactions are of photocatalytic characteristics.

Table 3.1 summarizes the results in absolute product rate (Equation 1.18), mass-normalized product rate (Equation 1.19), and area-normalized product rate (Equation 1.20) evaluated at the linear region of the slope. The mass calculation accounts for the mass of the TiO_2 layer and the plasmonic nanodisk array on their geometry and mass density (Equation (3.10)). The photocatalyst mass for this design is highly dominated by the TiO_2 layer with 2.6 mg. Thus, the choice of metal has a very minor impact, resulting in photocatalyst masses of 2.8 mg, 2.9 mg, 3.0 mg, and 2.8 mg for Ag/TiO_2, Au/TiO_2, Pt/TiO_2, and Pd/TiO_2, respectively. The area of the photocatalyst sheets amount to $(5 \times 5)\text{cm}^2 = 25\,\text{cm}^2$. Both normalizations are used to quantify the results and compare them with other works. The mass normalization lead to a better comparability with powder-based photocatalysts, while the area normalization is more reasonable to compare photocatalyst sheets.

TABLE 3.1: Overview of the absolute, mass- and area-normalized H_2 and CH_4 for each photocatalyst sheet.

Photocatalyst	Absolute Product Rate (μmol/h)		Mass Normalized Product Rate (mmol/gh)		Area Normalized Product Rate (μmol/cm^{2}h)	
	H_2	CH_4	H_2	CH_4	H_2	CH_4
Ag/TiO_2	56.88	4.15	20.31	1.48	2.28	0.17
Au/TiO_2	41.76	4.30	14.40	1.48	1.67	0.17
Pt/TiO_2	109.13	7.42	37.63	2.56	4.37	0.30
Pd/TiO_2	15.92	10.47	5.68	3.74	0.64	0.42

Pt/TiO_2 exhibits the fastest reaction in H_2 formation, reaching saturation after approximately 1500 s of reaction time. The best CH_4 formation is achieved by Pd/TiO_2 but also with the weakest H_2 formation. The longest reaction time is achieved by Ag/TiO_2, while Au/TiO_2 has moderate results for both H_2 and CH_4 formation. The different metals show different product selectivity, which is expected due to their different catalytic properties [124, 173]. Additional measurements were conducted on copper (Cu; Figure B.6) and aluminum (Al; Figure B.7) nanodisks, demonstrating either negligible small or very weak photocatalytic reactivity.

The simultaneous water splitting and CO_2 reduction processes require H_2O and CO_2 molecules to be adsorbed at the photocatalyst surface. As discussed in

Section 1.3.1, H_2 generation requires in total four protons (H^+) and two electrons (e^-), while CH_4 generation needs $8H^+$ and $8e^-$. This means that the reaction requirements to generate CH_4 is more difficult than H_2. These charge carriers are either provided by the photocatalyst surface or created by oxidation reactions of H_2O. The results of Pd/TiO_2 suggest that H^+ and e^- were favorably utilized to generate CH_4 and were not then available to produce H_2. Instead, Pt/TiO_2 shows a high reaction selectivity for H_2 compared to CH_4, which indicates significant favorable adsorption toward H_2O molecules. The results further show that the reaction rate for both H_2 and CH_4 for Ag/TiO_2 and Au/TiO_2 are lower, which can be accounted to a lower H_2O and CO_2 adsorption. This behavior aligns with the before discussed volcano plots (Figure 1.10b-c), which explains the increased amounts of H^+ for the solar fuel generation.

In Figure 3.13d, the results are benchmarked for the CH_4 production rate with comparable results from the literature. Metal-TiO_2 photocatalyst sheets were compared in the categories Ag-TiO_2 (gray) [174, 175, 176], Au-TiO_2 (yellow) [177, 178, 179, 180], Pt-TiO_2 (green) [181, 182, 144, 183, 184], and Pd-TiO_2 (purple) [185, 186, 187] to the best knowledge of the author. Here, '-' is used to express the general material system, while '/' is used for the specific plasmonic nanodisk metamaterial photocatalyst sheet. In addition, literature results with photocatalytic IPA conversion (red) were evaluated to show the effect of the scavenger [171, 188]. Even though photocatalytic water splitting was simultaneously conducted in many publications for photocatalytic CO_2 reduction, the H_2 production rate is often not mentioned. Therefore, only the CH_4 production rates are compared in Figure 3.13d. More detailed information about this benchmark study is summarized in Table 3.2.

Except for Pt/TiO_2, the outcome for the Ag/TiO_2, Au/TiO_2, and Pd/TiO_2 photocatalyst sheets show significant improvements compared to state-of-the-art results. Despite a higher CH_4 production rate with a Pt-TiO_2-based photocatalyst has been achieved before [182], the Ag/TiO_2, Au/TiO_2, and Pd/TiO_2 photocatalysts have shown a 7.8- [174], 21.1- [177], and 35.9-fold [185] enhancement, respectively. This is mainly due to the thin film structure used as a component in the photocatalyst sheet, making less material significantly more efficient.

One major drawback of the metamaterial photocatalyst sheets is their limited stability. All measurements have shown saturation points and decreased performances within 1 h (3600 s). It is possible that H- and C-atoms from the water splitting and CO_2 reduction are adsorbed by the photocatalyst surface, which then causes a deactivation of the photocatalytic functionality.

TABLE 3.2: Benchmark studies of comparable photocatalyst composites (Ag-TiO_2, Au-TiO_2, Pt-TiO_2, Pd-TiO_2) for CO_2 reduction and CH_4 production. In addition, reports on IPA conversion into solar fuels are compared.

Photocatalyst	Setup	Reactant	Yield/Rate	Remark	Ref.
Ag nanodisks on TiO_2 thin film (Ag/TiO_2)	•150 W metal-halide lamp •500 mW/cm^2 •aluminum reactor •MS analysis	CO_2 + H_2O (vapor)	H_2: 20.314 μmol/gh CH_4: 1.484 μmol/gh	•1 h stability •IPA scavenger	This work
Ag decorated TiO_2 nanoparticles	•Xe lamp •UV filter ($<$ 400 nm) •35 mW/cm^{2}power density •Stainless steel reactor •GC and GC-MS analysis	CO_2 + H_2O (liquid phase)	H_2: $\sim$20 μmol/gh CH_4: $\sim$190 μmol/gh CO: 200 μmol/gh	•stable performance for 20 cycles •3 h per cycle •isotope labeling	[174]
Ag-TiO_2 core-shell nanoparticles	•300 W XEF-300 solar simulator •AM1.5 filter •pyrex glass reactor with 11.58 mL volume •GC analysis with 200 μL sample	CO_2 + H_2O (vapor)	CH_4: 14.8 μmol/g	•3 h stability •3 repeated measurements •isotope labeling	[175]
Double-shelled Ag-TiO_2 hollow sphere	•300 W Xe lamp •420 nm cutoff filter •circular glass reactor with 230 mL volume •GC analysis	CO_2 + H_2O (liquid)	CH_4: 7.6 μmol/gh	•8 h stability •0.1 g photocatalyst	[176]
Au nanodisks on TiO_2 thin film (Au/TiO_2)	•150 W metal-halide lamp •500 mW/cm^2 •aluminum reactor •MS analysis	CO_2 + H_2O (vapor)	H_2: 14.400 μmol/gh CH_4: 1.482 μmol/gh	•1 h stability •IPA scavenger	This work
Au nanoparticles decorated TiO_2 nanosheets	•300 W Xe lamp •pyrex glass reactor (200 mL) •GC analysis of 0.8 mL gas sample	CO_2 + H_2O (vapor) from $NaHCO_3$ + HCl reaction	CH_4: 70 μmol/gh C_2H_5OH: 19.75 μmol/gh CO: $\sim$2.7 μmol/gh	•functionality also shown with monochromatic light •50 mg photocatalyst dispersed in water	[177]
Au nanoparticles decorated TiO_2 nanowires	•35 W Xe lamp •batch reactor •GC analysis	CO_2 + H_2O (vapor)	CH_4: 43 μmol/gh CO: 1237 μmol/gh CH_3OH: 12.65 μmol/gh	•2 h measurement time •10 mg photocatalyst distributed in the reactor	[178]

Photocatalyst	Setup	Reactant	Yield/Rate	Remark	Ref.
Au nanoisland on TiO_2 thin film	•532 nm laser •51.6 mL stainless steel reactor •GC analysis	CO_2 + H_2O (vapor)	CH_4: 22.4 μmol/m^2h	•15 h measurement •10 cm^2 surface area	[179]
Au-TiO_2 core-shell nanoparticles	•200 W Hg/Xe lamp •infrared filter •GC analysis from 1 ppm gas sample	CO_2 + H_2O (vapor)	H_2: ∼50 μmol/g CH_4: ∼6 μmol/g CO: ∼4 μmol/g	•shown 6 h stability •no saturation	[180]
Pt-coated and graphene wrapped TiO_2 nanotubes	•400 W metal halide lamp •Stainless steel batch reactor •GC analysis	CO_2 + H_2O (vapor) from $NaHCO_3$ + HCl reaction	CH_4: 3432 μmol/gh	•12 h measurement	[181]
Pt nanodisks on TiO_2 thin film (Pt/TiO_2)	•150 W metal-halide lamp •500 mW/cm^2 •aluminum reactor •MS analysis	CO_2 + H_2O (vapor)	H_2: 37.631 μmol/gh CH_4: 2.558 μmol/gh	•1 h stability •IPA scavenger	This work
Pt-TiO_2 single crystals	•400 W Xe lamp •flow reactor •GC analysis	CO_2 + H_2O (vapor)	CH_4: 1361 μmol/gh	•Shown at least 5 h stability	[182]
Pt nanoparticles + "blue" TiO_2	•100 W Xe, AM1.5 filter •GC analysis	CO_2 gas 1 mol/min	CH_4: 80.35 μmol/gh	•Shown 3 h stability •5 cycles	[144]
Pt with Bi-doped TiO_2	•400 W Hg lamp •glass reactor	CO_2 + H_2O (vapor)	CH_4: 20.6 μmol/h	•10 h measurement time •3 cycles •2 g photocatalyst	[183]
Pt nanoparticles TiO_2	•100 W Xe lamp •stainless-steel reactor	CO_2 + H_2O (vapor)	H_2: 36 μmol/gh CH_4: 6.1 μmol/gh CO: 0.54 μmol/gh	•10 h measurement time •3 cycles	[184]
Pd nanodisks on TiO_2 thin film (Pd/TiO_2)	•150 W metal-halide lamp •500 mW/cm^2 •aluminum reactor •MS analysis	CO_2 + H_2O (vapor)	H_2: 5.687 μmol/gh CH_4: 3.740 μmol/gh	•1 h stability •IPA scavenger	This work
Pd–TiO_2 nanoparticles	•300 W Xe lamp •420 nm cut-off filter •10 cm light-source distance •glass reactor •GC analysis	CO_2 + 2 mLH_2O (vapor)	CH_4: 104 μmol/gh	•shown 4 h stability •no saturation •30 mg photocatalyst powder	[185]
Pd-TiO_2 nanoparticles	•500 W Hg lamp •GC analysis	CO_2 + H_2O (liquid)	CH_4: ∼28 μmol	•5 h measurement •150 mg PC nanoparticles dispersed in water	[186]

Photocatalyst	Setup	Reactant	Yield/Rate	Remark	Ref.
Pd-TiO_2 nanowires	•400 W Hg lamp •Pyrex glass reactor •GC analysis	CO_2 + H_2O (vapor)	CH_4: 26.7 μmol/gh CO: 50.43 μmol/gh	•8 h stability	[187]
$CsPbBr_3$/ Bi_2WO_6 2D/ 2D hetero-junction	•150 W Xe lamp, AM 1.5 filter •40 ml Pyrex bottle	CO_2 + + ethyl acetate + IPA	H_2: $\sim$ 40 μmol/g CH_4: $\sim$ 200 μmol/g CO: $\sim$ 4100 μmol/g	•6 h measure-ment times •5 cycles	[188]
TiO_2 / CdS	•450 W Xe lamp •320 nm and 420 nm cut-off filter •reaction tempera-ture 20 $-$25 °C •GC analysis, GC-MS analysis	CO_2 + H_2O + IPA	H_2: $\sim$ 8 μmol CH_4: $\sim$ 18 μmol CO: 0.8 μmol	•10 h measure-ment times •0.1 g photocat-alyst dissolved in liquid feed-stock	[171]

3.4.6 Limitations of the Photocatalytic Reactor

The interpretation of the H_2 and CH_4 rates are constrained by the use of IPA as a hole scavenger. Since IPA is itself a carbon-containing molecule, it can serve as an alternative carbon source, and the detected CH_4 can therefore not be attributed exclusively to CO_2 reduction. To separate the CO_2 as contributions, control experiments were conducted without CO_2 with Ag/TiO_2 and Pt/TiO_2 (Figure 3.14). The MS raw data of the control experiments are shown in Figure B.9 and B.10. It results show the impact of IPA by a partial but significant H_2 and CH_4 portion. The selectivity again is dependent on the nanodisk metal. The H_2 and CH_4 rates reported in Table 3.1 represent the combined contribution of CO_2 reduction and IPA conversion rather than CO_2 reduction alone. Hence, the CO_2 reduction and water splitting experiments in this work must be considered as IPA-assisted.

The illumination heats the photocatalyst sheet during operation, so a thermally driven contribution to the measured activity has to be considered. The raw measurement data (Appendix B) show no product formation that can be attributed to a purely thermocatalytic pathway. The reactions always start after unblocking the light source, indicating that the reaction is light-driven rather than thermally activated. However, the setup does not allow the sample temperature to be controlled or monitored independently of the illumination, so a photothermal contribution, in which the light-induced heating enhances the photocatalytic reaction kinetics, cannot be ruled out. The exact share of heat in the reported rates therefore remains unclear.

A further limitation concerns the absolute quantification of the reaction rates. The water bubbler placed between the reaction chamber and the mass spectrometer delivers the product gas in discrete bubble portions rather than as a continuous stream, which is the origin of the noise pattern in the measured signals. The

rates are extracted by Bayesian denoising followed by a linear regression over the initial linear region of the reaction curve, so the absolute values carry a corresponding uncertainty and depend on the choice of the evaluation window.

Finally, the benchmark in Figure 3.13d is affected by the differing reactor geometries, light sources, and scavenger conditions across the compared studies. The mass-normalization reduce but do not fully remove these differences, so the reported enhancement factors should be understood as indicative rather than exact.

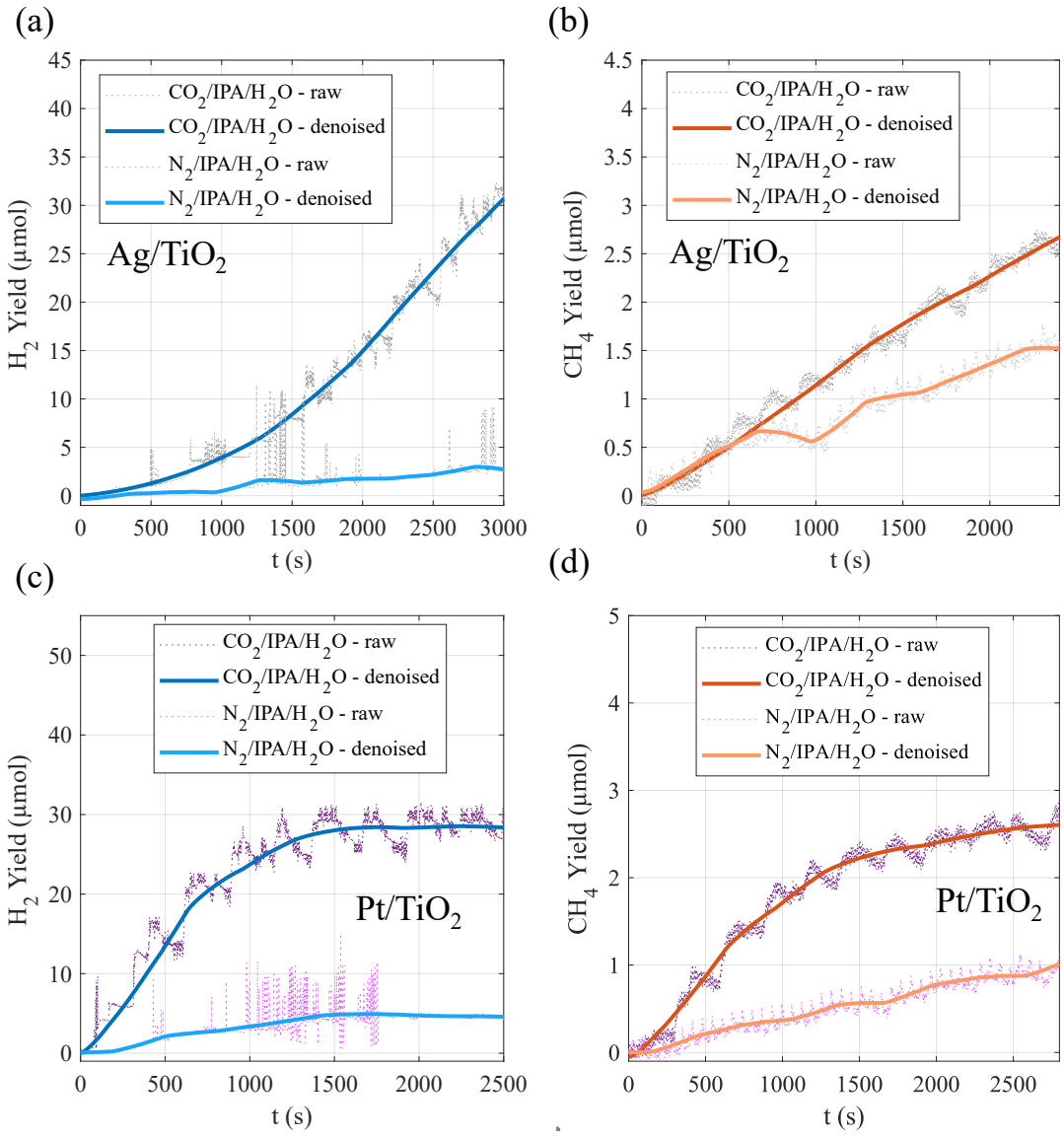


FIGURE 3.14: Control experiment with N_2 as carrier gas instead of CO_2 to exclude CO_2 as carbon source. Comparison between the measurements results: (a) H_2 and (b) CH_4 yield data for Ag/TiO_2, (c) H_2 and (d) CH_4 yield data for Pt/TiO_2.

3.5 Plasmonic Field Enhancement Simulation

FDTD simulation studies were conducted to compute the cross-section E-field enhancement distribution for each photocatalyst. The computation was conducted for $H_{ND} = 30\,nm$, $D_{ND} = 150\,nm$, and $P = 300\,nm$. The plasmonic nanodisks were defined on a TiO_2 layer with $H_{SC} = 250\,nm$ on top of a SiO_2 substrate. The results are plotted as a function of incident wavelength λ from 300–1000 nm to cover the UV-Vis-NIR range (Figure 3.15).

The dielectric constant of a metal can indicate the plasmonic properties, which has a primary impact on the LSPR response. From the complex permittivity ϵ of a material, the real part ϵ_1 determines the polarization response and the imaginary part ϵ_2 its optical loss [189]. The ratio of the complex permittivity $|\epsilon_1/\epsilon_2|$ is used as an indicator for the LSPR response. These ratios for Ag, Au, Pt, and Pd between $\lambda = 620$–$640\,nm$ are 37.96, 7.33, 0.71, and 0.91, respectively [190]. It can be expected that Ag exhibit the highest LSPR response, followed by Au. However, the functionality of Ag suffers significantly from growth of a native oxide layer [167]. The ratios for Pt and Pd indicate a vast LSPR peak, and there is a less intense LSPR response. This trend has also been shown already in the Raman spectra (Figure 3.5a), aligning with the measured SERS effect.

The simulated E-field enhancements (Figure 3.15) indicate that the nanodisk structure confines the incident light. In addition, the nanodisks interact as plasmonic resonators due to their sub-wavelength geometrical size. All four metals show resonating E-fields at the outer boundary region of the nanodisk. These intensified E-field at those regions indicates higher charge carrier densities, in which high energetic electrons are located. Especially at the boundary regions of the nanodisks, the charge carriers may inject into the TiO_2 layer and trigger photocatalytic reactions at the structure surface.

For Ag/TiO_2 and Au/TiO_2, E-field enhancements by factor 100 are achieved in the Vis-NIR range (600–1000 nm), which makes them the stronger plasmonic resonators within this study compared to Pt/TiO_2 and Pd/TiO_2. In addition, Ag/TiO_2 also shows a strong plasmonic activity at 400 nm. The LSPR effect is less prominent for the Pt/TiO_2 and Pd/TiO_2 in the UV-Vis range, indicating that these photocatalyst sheets act as a plasmonic absorber and not a resonator. At the NIR range, Pd/TiO_2 shows the most intense LSPR response by an E-field enhancement by factor 100. Pt/TiO_2 has the lowest E-field enhancements compared to Ag/TiO_2, Au/TiO_2, and Pd/TiO_2.

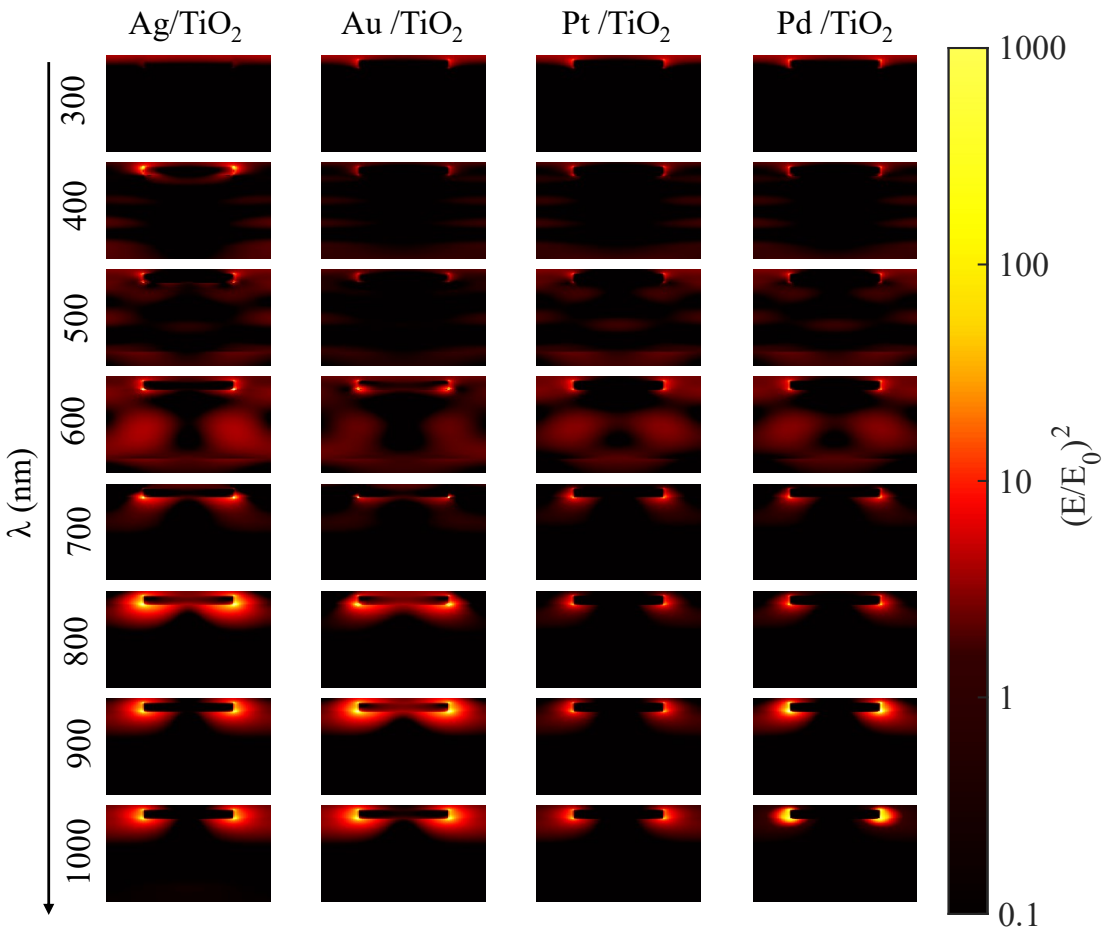


FIGURE 3.15: Cross-section FDTD simulation results of the E-field enhancement of the Ag/TiO_2, Au/TiO_2, Pt/TiO_2, and Pd/TiO_2. The plasmonic nanodisks have a 30 nm disk height, 150 nm disk diameter, and 300 nm periodicity. The nanodisks are placed on a 250 nm TiO_2 layer. The E-field enhancement is plotted on a fixed logarithmic scale from 0.1 to 1000 for better comparison. The results are plotted as a function of the incident wavelength from 300 to 1000 nm to cover the UV-Vis-NIR range.

3.6 Proposed Charge Carrier Dynamics

The band diagram provides a simplified model for the charge carrier mechanism of the metamaterial. All relevant electronic property data for TiO_2, Ag, Au, Pt and Pd are listed in Table A.1. In contact with TiO_2 Au, Pt, and Pd form Schottky junctions, which is due to the corresponding work function being larger than the electron affinity of TiO_2. On the other hand, Ag in contact with TiO_2 forms an Ohmic junction due to its lower work function [191].

A generalized bandgap diagram for this metamaterial is presented in Figure 3.16. Depending on the metal, a Schottky (solid line) and Ohmic (dashed line) junction can be formed. While illuminated by a broad band (UV-Vis-NIR) light

source, the UV portion photo-excites valence band electrons in the TiO_2 and raises them into the conduction band, leaving behind a hole in the valence band. The free valence band holes and conduction band electrons can then contribute to oxidation and reduction reactions, respectively. This triggers the multi-step reaction processes for water splitting and CO_2 reduction, generating H^+, H_2 and CH_4.

The visible portion of the wavelengths excites electron in the plasmonic metal nanodisk into the LSPR state. This leads to hot electrons, which have sufficient kinetic energy migrate into the conduction band of the TiO_2 layer. In case of the Schottky junction, hot electrons can overcome the Schottky barrier. On the other hand, electrons in the metal layer, especially close to the surface, can be excited to hot electrons by the collective oscillations caused by external light excitation in the LSPR-state. This effect let them potentially migrate into the TiO_2 layer [192]. From there, it can also migrate back into the metal nanodisk layer and excite again into the LSPR state. The hot electron can also contribute to reduction reaction from the LSPR state. As the LSPR excitation creates a high-energetic vacancy in the metal, this effect creates a hot hole that can contribute to oxidation reactions.

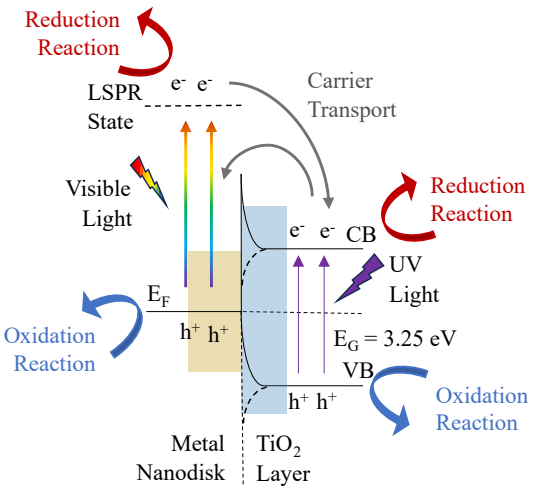


FIGURE 3.16: Proposed bandgap diagram schematic of this plasmonic metal nanodisk-TiO_2 metasurface structure. The solid line at the material transition indicates a Schottky junction (Au, Pt, Pd), while the dashed line represents an Ohmic junction (Ag). Illuminated by solar light, the visible portion excite electrons in the metal layer into the LSPR-state. The UV-portion of the light can photo-excite TiO_2 valence band (VB) electrons into the conduction band (CB).

The metal-TiO_2 transition supports the charge separation of both material layers as it reduces the recombination probability. This increases the overall reactivity of the metamaterial structure. The experimental results show that the specific type of junctions is not relevant for photocatalytic functionality, but still required

for charge separation. However, both simulation and experimental data show contradicting results if those are only evaluated by plasmonic properties. On the basis of the literature results, Pt and Pd surfaces establish significantly better adsorption conditions with H-, C-, and O-atoms than to Ag and Au surfaces (Figure 1.10b-c) [132, 133]. While electrodynamical simulations can still provide valuable data to evaluate the light response of a material structure, it is also required to consider the adsorption properties by density functional theory (DFT). Further modeling for the optimization of a photocatalytic system may involve multiphysical simulations to consider thermodynamical properties [193]. In the end, only experimental validations can confirm the performance of photocatalyst. This work shows that both plasmonic interactions and adsorption properties are important and that the latter dominate.

3.7 Conclusion

A functional metamaterial photocatalyst sheet design based on a periodically-arranged plasmonic nanodisks for photocatalytic CO_2 reduction has been presented in this chapter. The photocatalyst sheet is created by semiconductor fabrication processes with NIL as key processing step. Results have been shown for Ag, Au, Pt, and Pd on a TiO_2 thin film layer.

This work shows efficient photocatalytic activity for water splitting and CO_2 reduction with up to 37.63 mmol/gh for H_2 and 3.74 mmol/gh for CH_4. While higher H_2 rates have been achieved in pure photocatalytic water splitting experiments [194], the best CH_4 rates in this work by Pd/TiO_2 have achieved an enhancement factor of 35.9 compared with Pd-TiO_2-based photocatalysts [186]. For the further work in this thesis, the Pd/TiO_2 design will be used and modified. Notably, the results are among the top-performing plasmonic photocatalysts based on state-of-the-art knowledge. This is mainly ascribed to the metasurface that is based on a periodic arrangement of the nanodisk. This design provides an interchanging material layer between the plasmonic co-catalyst (Ag, Au, Pt, Pd) and photocatalytic thin film material (anatase-phased TiO_2) by providing reaction centers and improved charge separation, increasing the overall reactivity.

4 Graphene-modified Pd/TiO_2 Metamaterial Photocatalyst Sheet

Graphene (Gr), a single layer of carbon atoms arranged in a hexagonal lattice, has revolutionized materials science since its isolation in 2004 by Andre Geim and Konstantin Novoselov at the University of Manchester [195]. This groundbreaking discovery, which earned them the Nobel Prize in Physics in 2010, marked a turning point in the field of 2D materials [196].

The exceptional properties of Gr make it a suitable material for enhancing photocatalytic CO_2 reduction [25]. Its high electron mobility, large specific surface area, and excellent conductivity contribute to improved charge separation and transfer in photocatalytic systems. When combined with semiconductors like TiO_2, Gr forms composites that exhibit enhanced visible-light absorption and increased photocatalytic activity. These Gr-based composites have shown promising results in the conversion of CO_2 to solar fuels [197].

4.1 Photocatalyst Design

In this chapter, only Pd was used as plasmonic metal as it has revealed the best CH_4 rates for photocatalytic CO_2 reduction in Chapter 3. Therefore, Pd-TiO_2 was chosen as material combination but with an alternative geometrical design. The metasurface design was changed from a rectangular pattern of circular-shaped nanodisks to a hexagonal pattern of elliptical-shaped nanodisks (Figure 4.1a). As elliptical cylinders have two different parameters, P and D has to be distinguished in X and Y direction. The geometrical parameters for the pattern are $P_X = 700\,\text{nm}$, $P_Y = 400\,\text{nm}$, $D_{NDx} = 420\,\text{nm}$, $D_{NDy} = 250\,\text{nm}$, and $H_{ND} = 30\,\text{nm}$. The thickness of the TiO_2 layer was reduced here to $H_{SC} = 160\,\text{nm}$, as further measurements have shown that a thinner TiO_2 layer has still sufficient anatase crystal properties. This photocatalyst design is labeled 'PTO-Base' and serves as a reference photocatalyst sheet in this chapter (Figure 4.1b).

PTO-Base was further modified with Gr in post-processes. In the first modification, a Gr layer was wet-transferred onto PTO-Base (PTO-G) as a second photocatalyst sheet (Figure 4.1c). The Gr layer had a size of $(1.5 \times 1.5)\text{cm}^2$ and was suspended on top of the Pd nanodisk structures. In the second modification, a carbon black layer was grown by plasma-enhanced chemical vapor deposition (PECVD) onto PTO-Base (PTO-C) as a third photocatalyst sheet (Figure 4.1d). PTO-C serves as a bulk-like reference sample for PTO-G. In this section, the three types of photocatalyst sheets are characterized, analyzed and discussed.

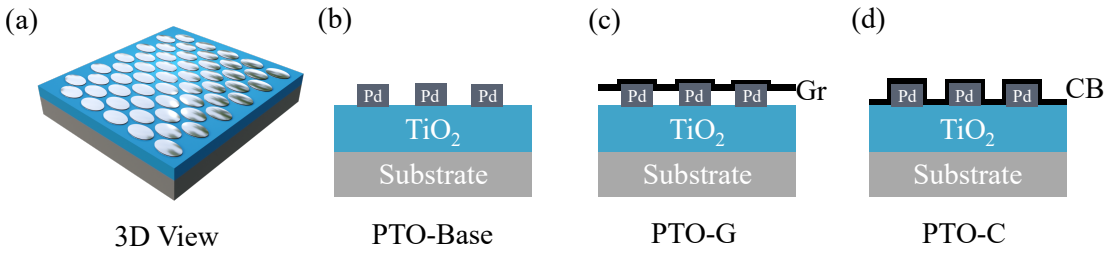


FIGURE 4.1: (a) 3D view on PTO-Base to visualize the elliptical-shaped nanodisk arranged in a hexagonal pattern. Cross-sectional view on the three Gr-modified Pd/TiO_2 metamaterial photocatalyst sheet design: (b) PTO-Base, (c) PTO-G, and (d) PTO-C.

4.2 Fabrication

The Gr-based photocatalyst is fabricated on planar $(5 \times 5)\text{cm}^2$ glass substrate. The fabrication is similiar as the one from Figure 3.3, but with two further process steps for the Gr and carbon black layers. The fabrication flow (Figure 4.2) is outlined as following:

1. Deposition of 160 nm TiO_2 (blue layer) on the glass substrate by DC magnetron sputtering. Afterward, an annealing process at 650 °C for 1 h is conducted to obtain the anatase crystal phase for the TiO_2 layer.
2. Spin-coating of 100 nm PMMA (green layer) and 100 nm (red layer) AMONIL.
3. Patterning of the hexagonal-arranged elliptic-shaped hole pattern by NIL.
4. Plasma-etching by RIE of the AMONIL and PMMA layer to achieve an undercut profile in the PMMA layer.
5. 30 nm Pd (dark-grey) deposition by e-beam evaporation.
6. Lift-off step to remove the double-layer resist structure by acetone, IPA and DI water (PTO-Base).

7. Post-processing with Gr (black):

   (a) Wet transfer of the suspended $(1.5 \times 1.5)\text{cm}^2$ Gr layer (PTO-G)

   (b) Carbon black deposition by PE-CVD. (PTO-C)

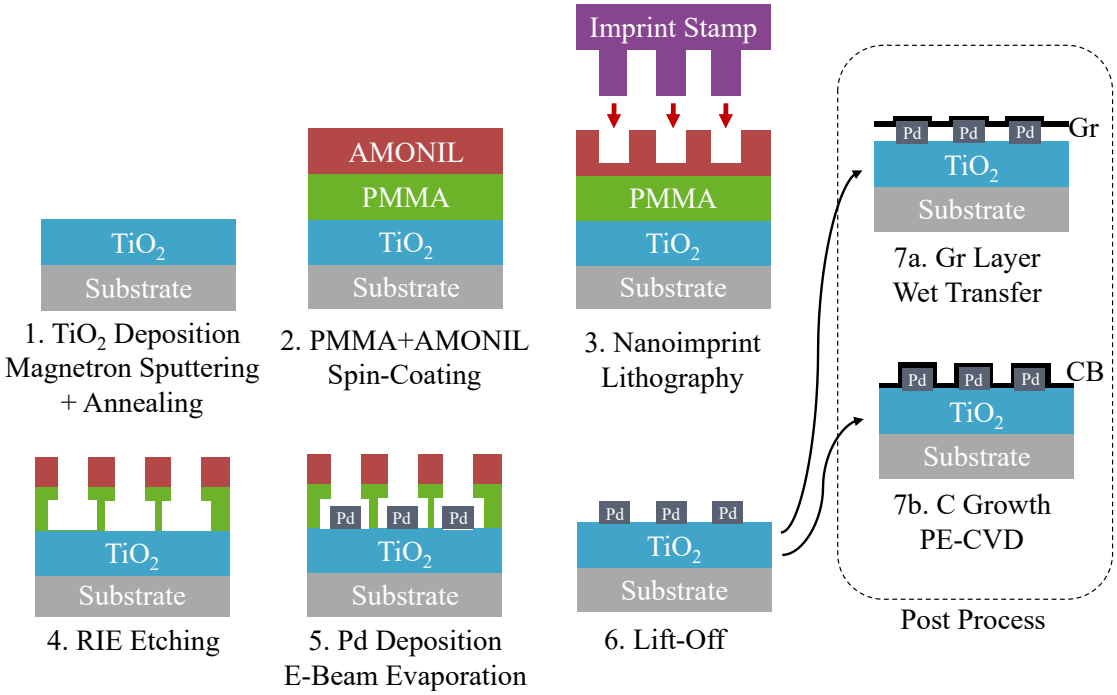


FIGURE 4.2: Fabrication workflow for the PTO-Base (Step 1–6) involving multiple process steps such as magnetron sputtering, spin-coating, NIL, RIE, e-beam evaporation, and lift-off. The Gr modifications are conducted as post-processes. Gr is wet-transferred for PTO-G (Step 1–7a), and is grown by PECVD for PTO-C (Step 1–7b) photocatalyst sheet.

4.2.1 Graphene Wet Transfer

Gr wet transfer involves transferring Gr grown on a metal surface, often a Cu foil, onto a target substrate [198]. For this thesis, commercially available single-layer CVD-grown Gr on copper foil (Grolltex. Inc, USA) was used, protected with PMMA and transferred onto the metasurface of the photocatalyst sheet.

Afterward, the Cu foil was etched using a water/HCl/H_2O_2 (10:1:1 ratio) solution, which left the PMMA/Gr structure floating on the etchant. After rinsing with DI water, the PMMA/Gr was carefully scooped onto the desired target substrate and dried under ambient conditions for 24 h. Once dried, the photocatalyst sheet was heated to 100 °C on a hotplate to remove residual water layers. Then, the PMMA was removed with acetone, leaving the Gr adhered to the new substrate.

This method allows for the creation of high-quality Gr sheets that can be integrated into complex photocatalytic systems, enhancing their performance through improved electron transport and increased active surface area [199].

4.2.2 Plasma-Enhanced Chemical Vapor Deposition

The carbon black layer on the Pd and TiO_2 surface was synthesized by using a PECVD process (Figure 4.3a). This method was originally developed for growing pristine Gr layers on copper (Cu) surfaces [200]. Even though this PECVD process yielded carbon black layers instead of Gr on PTO-Base, the incorporation of C-based materials into photocatalytic material composites is known to enhance electron transport properties. In combination with metamaterial structures, they have not been studied yet for water splitting and CO_2 reduction.

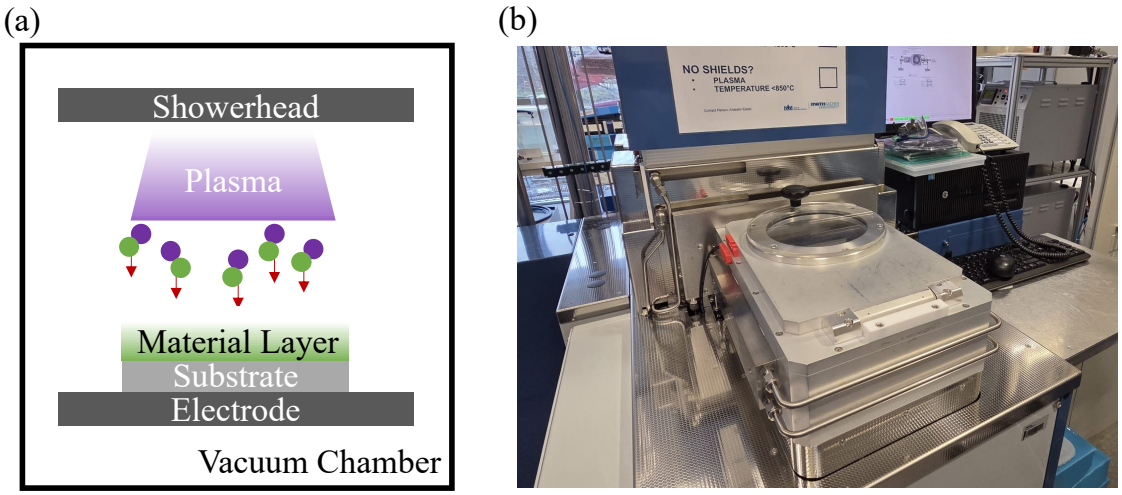


FIGURE 4.3: (a) Principle of PECVD showing a vacuum chamber, an electrode that functions as a stage, and a substrate that is to be deposited. The showerhead creates a plasma that bombards ion towards the electrode. (b) Photograph of the ICP-CVD tool from the company 'Oxford Instruments plc'.

PECVD allows Gr growth on Cu surfaces at lower process temperatures, shorter durations compared to conventional CVD, and it offers the potential for catalyst-free deposition [201]. In PECVD, a plasma environment is used to activate precursor molecules (H_2-CH_4-mixture), which then react to form Gr on the Cu surface. The energy provided by the plasma leads to the efficient decomposition of the precursors and enhanced surface reactions, facilitating Gr growth at temperatures as low as 650 °C. However, when this process is applied on non-Cu surfaces, the C-atoms fail to arrange into the crystalline Gr lattice, instead forming a carbon black layer.

For the PTO-C photocatalyst sheet, the carbon black layer was synthesized by PECVD at 800 °C in an in-house inductively coupled plasma chemical vapor deposition (ICP-CVD) tool (Oxford Instruments plc, Figure 4.3b).

4.3 Characterization

The topographical characteristics of each photocatalyst sheet are presented in Figure 4.4 by SEM and AFM images. All images consistently reveal a hexagonal periodicity and the presence of elliptical-shaped nanodisks. For PTO-G (Figure 4.4b), a boundary area showcasing regions with and without Gr in the SEM image is selected to highlight the contrast between these zones. In comparison to PTO-Base (Figure 4.4a), the SEM image of PTO-C (Figure 4.4c) distinctly displays a surface coated with carbon black, which appears to have a rough surface.

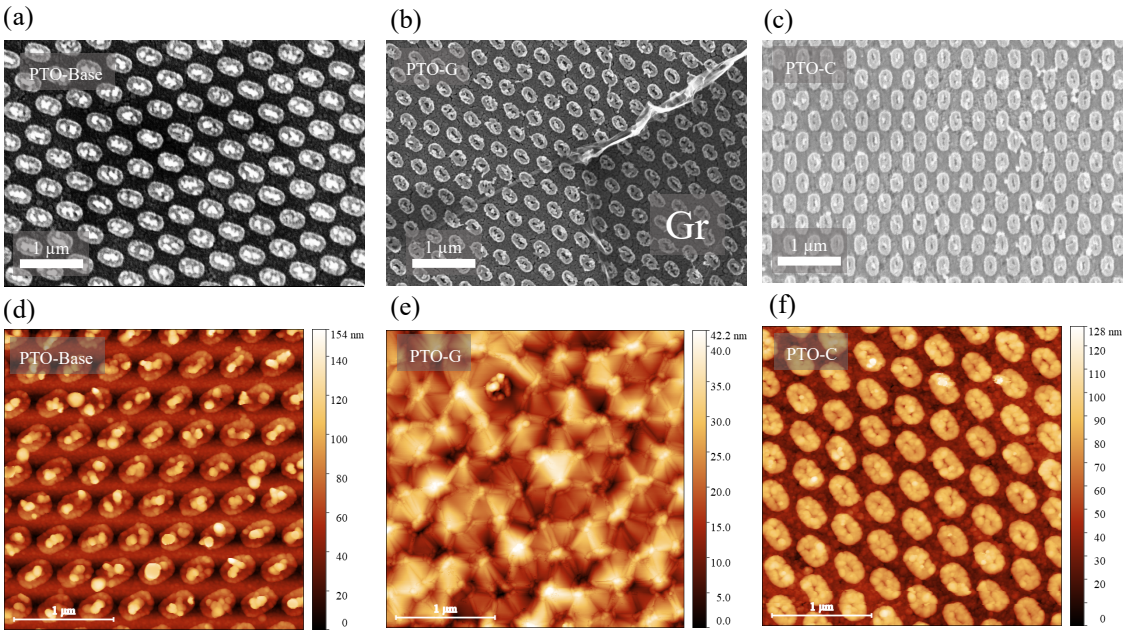


FIGURE 4.4: Surface topography characterization of all photocatalysts. SEM surface topography scans of (a) PTO-Base, (b) PTO-G , and (c) PTO-C. AFM surface topography images of (d) PTO-Base, (e) PTO-G, and (f) PTO-C.

AFM images offer height information of the surface topography. PTO-Base (Figure 4.4d) shows a particle-like defectivity. These surface features may also be attributed to the underlying the TiO_2 surface roughness, which is a consequence of its anatase crystallinity (Figure A.1). The geometry obtained from this image are $P_X = 706\,\text{nm}$, $P_Y = 408\,\text{nm}$, $D_{NDx} = 408\,\text{nm}$, $D_{NDy} = 245\,\text{nm}$, and $H_{ND} = 32\,\text{nm}$.

The AFM image of PTO-G (Figure 4.4e) implies that the transferred Gr layer was suspended above the Pd nanodisk array without making direct contact with the TiO_2 surface. Figures 4.5a-b show a more detailed scan of the border region of the Gr layer, revealving its suspending characteristics. This suspension creates a distinctive hexagonal network of wrinkles on the Gr layer, indicating the presence of slight strain. The interchanging suspending region and Gr-Pd contact region have an influence on the electrical properties of Gr due to doping effect of Gr on metal contacts [202, 203]. This phenomena has an effect on the charge carrier mechanism and will be discussed later (Section 4.6).

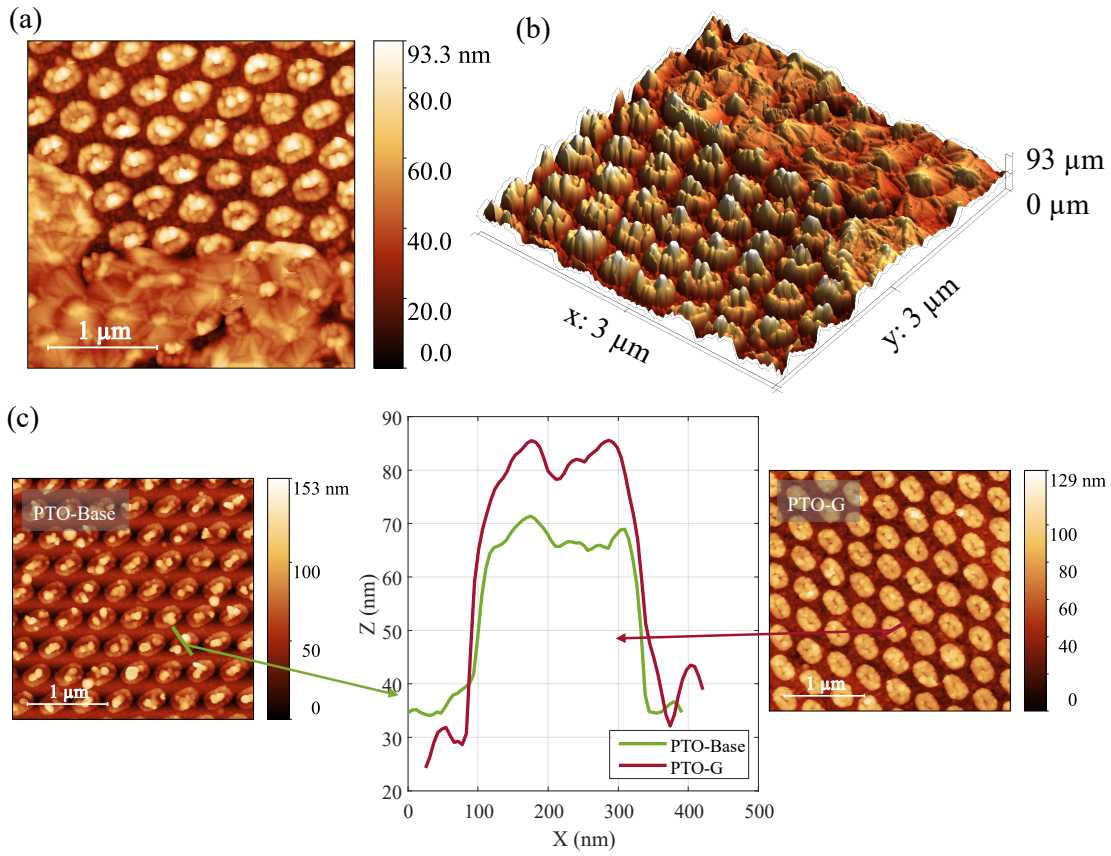


FIGURE 4.5: (a) 2D and (c) 3D AFM image of a boundary region of the suspended Gr layer at PTO-G, proving its suspension characteristics in geometrical terms. (c) Cross-section AFM image comparison of PTO-Base and PTO-C to determine the 10 nm C-layer thickness.

In the case of PTO-C (Figure 4.4f), the disk diameter and height enlarged due to the carbon black layer. A comparison of the nanodisk sizes between PTO-Base and PTO-C reveals a 10 nm increase in diameter and disk height, as shown in Figure 4.5c.

The absorption spectra of each photocatalyst are shown in Figure 4.6a. The absorption spectrum for a 160 nm TiO_2 thin film on a glass substrate is additionally plotted here as a reference. PTO-Base reveals a continuous absorpton activity above 30 % within the Vis-NIR range ($\lambda > 400$ nm), which is accounted for by the Pd nanodisk metasurface. Moreover, there are several peaks resulting from the diffraction effects and Wood-Rayleigh anomalies by the nanodisk structure [107, 204]. The additional suspended Gr layer on PTO-G significantly changes the absorption spectrum between 480–1000 nm wavelength. The absorption spectrum for PTO-C shows an overall high absorption above 70 % for all measured wavelengths between 200–1000 nm due to the Gr multilayer stack. The characteristic peaks at 418 nm and 514 nm from the Pd nanodisk pattern are still observable and broadened. This is attributed to the carbon black coating that acts as a lossy dielectric medium. The carbon black coating reduces the scattering properties of the Pd nanodisk pattern.

The analyzed Tauc fit (Figure 4.6b) concluded that the effective bandgap for the TiO_2 thin film, PTO-Base, and PTO-G are 3.25 eV, 2.48 eV, and 2.53 eV, respectively (Figure 4.7). While the bandgap is shifted by 0.77 eV by the band alignment of the Pd nanodisk, it minimally increases by 0.05 eV for PTO-G. The PTO-C photocatalyst does not show any absorption edge within the measurement range of 200–1000 nm, which indicates that the carbon black layer absorbs all of the incoming light (Figure 4.6a).

The Raman spectra of the respective samples are shown in Figure 4.6c. Here, the Raman spectrum for a 160 nm TiO_2 thin film on a glass substrate is also provided as a reference dataset. Similar Section 3.3, the characteristic TiO_2 anatase signals are located at 141 cm^{-1}, 513 cm^{-1}, and 635 cm^{-1} with an additional minor brookite peak at 392 cm^{-1} [150]. All data are plotted by their absolute counts to better reveal the changes by each modification. PTO-Base shows a small background signal and slightly shifts the peak position, which accounts for its plasmonic response by SERS [165]. For PTO-G and PTO-C, the added Gr further amplifies the signal but also broadens it. This indicates the coupled scattering between the Pd nanodisk and the Gr layers.

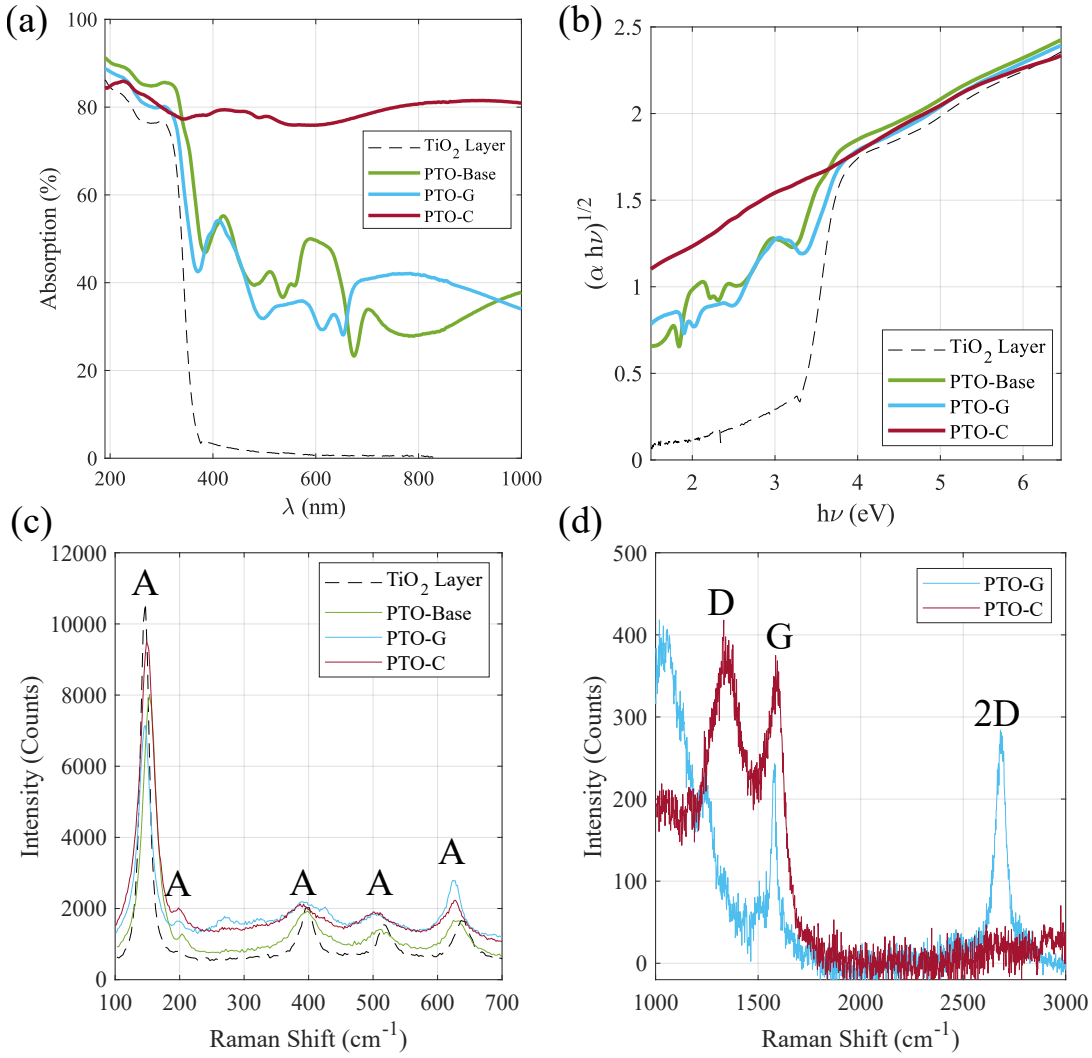


FIGURE 4.6: (a) UV-Vis-NIR measured absorption spectra showing the absorption activity by the Pd nanodisk array and both Gr modification in comparison to the reference TiO_2 sample. (b) Tauc plot evaluated from the absorption spectra for the bandgap evaluation. (c) Measured Raman spectra for TiO_2 crystal phase signals (100–1000 cm^{-1}) of all photocatalysts, additionally showing the SERS effect by the Pd nanodisk array and influence by both Gr-modification. (d) Zoomed region (1000–3000 cm^{-1}) for evaluation of the D-, G-, and 2D-peaks of PTO-G and PTO-C.

The Raman spectra from 1000–3000 cm^{-1} of both PTO-G and PTO-C are depicted in Figure 4.6d. The characteristic Gr peaks, known as D-, G-, and 2D-bands, are measurable at around 1340 cm^{-1}, 1580 cm^{-1}, and 2690 cm^{-1}, respectively [205]. For PTO-G, the intensity ratio between 2D- and G-peak (I_{2D}/I_G) amounts to approximately $270/240 = 1.13$, which corresponds to double layers of Gr [206]. Moreover, the D-peak is very low, indicating a low defectivity [207].

For PTO-C, the Raman spectrum confirms the presence of carbon black [208, 209]. The 2D band is very low while the D-peak is at the same level as the G-peak.

Here, I_{2D}/I_G was 0.07, confirming that the carbon black layer has a disordered crystal structure.

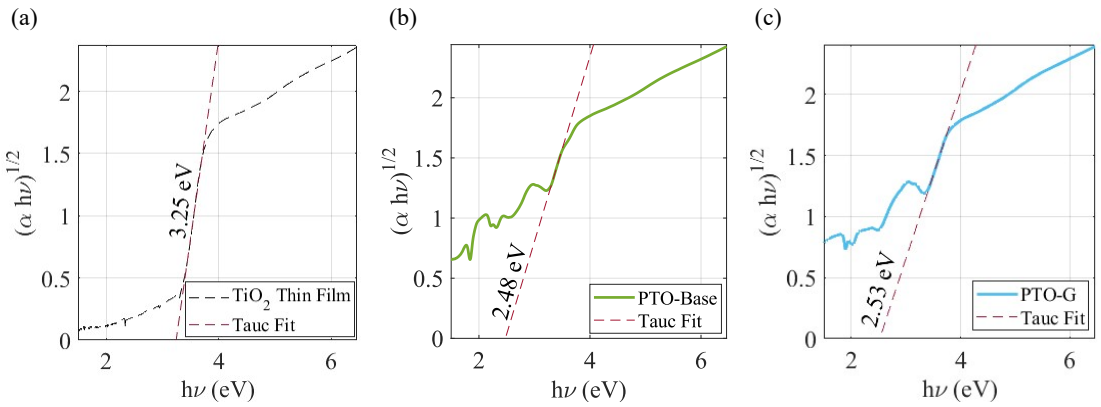


FIGURE 4.7: Tauc Plot analysis for (a) TiO_2 Thin Film (reference sample), (b) PTO-Base, and (c) PTO-G. The extrapolation of the linear fit suggests bandgap values of 3.25 eV, 2.48 eV, and 2.53 eV, respectively. PTO-C was not evaluated as its absorption spectrum did not show an absorption edge.

4.4 Photocatalytic Water Splitting and CO_2 Reduction

The same reactor setup from Section 3.4 was used to measure the photocatalytic water splitting and CO_2 reduction of PTO-Base, PTO-G, and PTO-C. As the geometrical metastructure design differs from 3, the derivation of the mass calculation is explained here. Afterwards, the experimental results are shown and discussed.

4.4.1 Metamaterial Photocatalyst Mass Calculation

In a hexagonal lattice, the unit area of an individual nanodisk is defined by the two periodicities, P_X and P_Y. In comparison to Equation (3.10), the mass calculation is different due to the hexagonal-arranged elliptical-shaped nanodisk pattern. Figure 4.8 illustrates all parameter that has to be considered to determine the m_{PC}.

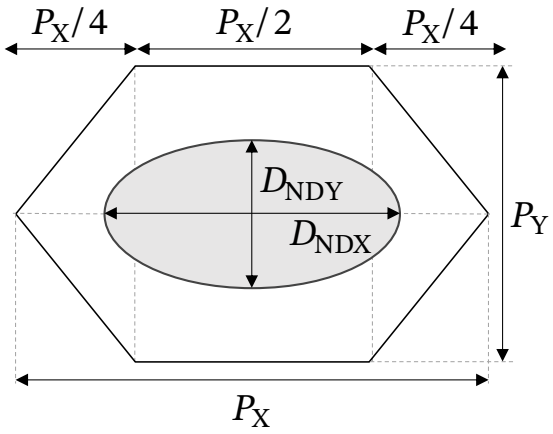


FIGURE 4.8: Geometrical sketch of the unit cell in top-down view of an elliptical-shaped nanodisk pattern arranged in a hexagonal lattice.

Therefore, N_{ND} on the photocatalyst is differently calculated with

$$N_{ND} = \frac{L_{PC}^2}{A_{hex}}, \tag{4.1}$$

where A_{hex} is the area of one hexagonal unit cell.

In the hexagonal pattern, A_{hex} can be geometrically derived by assuming one rectangle and four right-angled triangles with

$$A_{hex} = \frac{P_X}{2} \times P_Y + 4 \times \frac{P_X/4 \times P_Y/2}{2} = \frac{3}{2} P_X P_Y. \tag{4.2}$$

Then, V_{ND} can be expressed by the volume of an elliptical-shaped cylinder by

$$V_{ND} = \pi r_{NDx} r_{NDy} H_{ND} = \frac{\pi}{4} D_{NDx} D_{NDy} H_{ND}, \tag{4.3}$$

where r_{NDx} refers to the nanodisk radius in x-direction, r_{NDy} is the nanodisk radius in y-direction, D_{NDx} is the nanodisk diameter in x-direction, and D_{NDy} is the nanodisk diameter in y-direction.

Finally, m_{PC} can be calculated by inserting Equation (3.7), (4.1), (4.2) and (4.3) into Equation (3.6):

$$m_{PC} = \varrho_{SC} L^2 H_{SC} + \varrho_{ND} \frac{\pi}{6} \frac{L_{PC}^2}{P_X P_Y} D_{NDx} D_{NDy} H_{ND}. \tag{4.4}$$

4.4.2 Experimental Results

The measurements were conducted as described in Section 3.4. Figure 4.9 shows the calibrated data of the measured H_2 and CH_4 signal for each metal nanodisk

metamaterial photocatalyst sheet, respectively. The mass spectrometer raw datasets can be found in Appendix B.

The continuously measured mass spectrometer signals show a noise pattern (dotted curve) due to a water bubbler, which is placed between the reactor chamber and mass spectrometer. For each dataset, the signals are processed with a Bayesian algorithm (solid curve) [172]. A linear regression is then performed in the linear region of the reaction curve (dashed curve). The evaluated slope is then taken as the reaction rate and converted into units of μmol/h.

Figures 4.10a and 4.10b show the mass-normalized H_2 and CH_4 yields for the three photocatalysts, respectively. The evaluated production rates are summarized in Figure 4.10c. The H_2 and CH_4 yield rates for PTO-Base were 4.40 mmol/gh and 7.55 mmol/gh, respectively. For PTO-G, the suspended Gr layer enhances this performance to 17.88 mmol/gh (H_2) and 11.25 mmol/gh (CH_4). PTO-C has a similar H_2 yield rate of 7.22 mmol/gh but has a significantly decreased CH_4 yield rate of 5.54 mmol/gh compared to PTO-Base.

PTO-G exhibits enhancement factors of 4.05 in the H_2 rate and 1.49 in the CH_4 rate compared to PTO-Base. This immense increase can only be attributed to the suspended Gr layer. As Gr is exposed to the outer surface, it functions here as an active reaction center for the water splitting and CO_2 reduction reactions. In addition, Gr has superior material properties [25], such as high mobility and efficient charge separation, which supports the generated charge carrier from the Pd nanodisk reaching there. Moreover, the large specific surface area and 2D structure of Gr provide additional catalytic sites, improving interaction with CO_2 molecules. This synergy between the PTO-Base metasurface and Gr layer led to these overall performance enhancements.

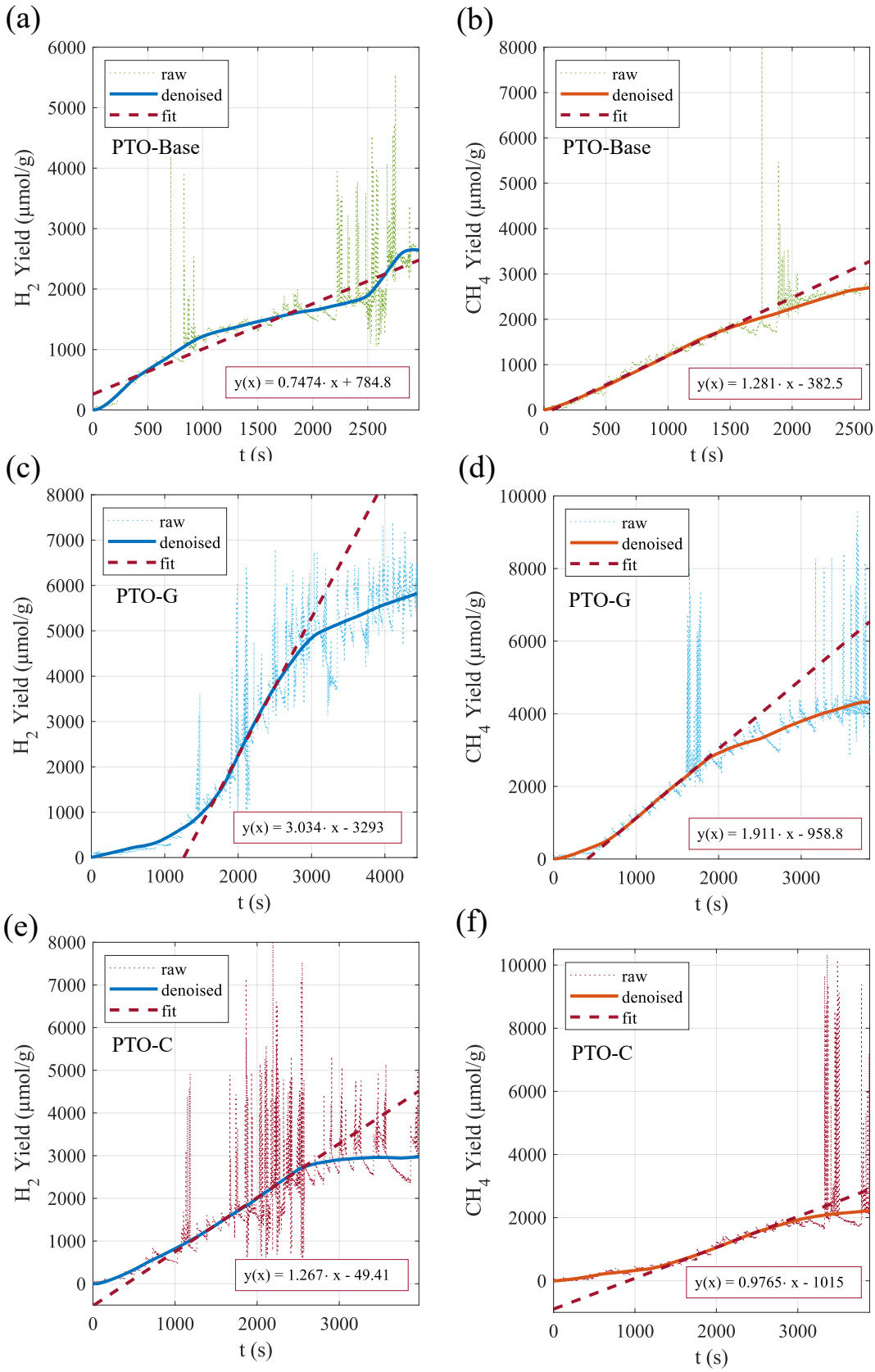


FIGURE 4.9: Detailed analysis of the raw mass spectrometer data for the mass-normalized product yield. (a) H_2 and (b) CH_4 yield for PTO-Base. (c) H_2 and (d) CH_4 yield for PTO-G. (e) H_2 and (f) CH_4 yield for PTO-C.

The mass calculation of the photocatalysts is based on theoretical assumptions on geometries and mass density (Equation 4.4), revealing photocatalyst masses of 1.8 mg, 1.8 mg, and 1.9 mg for PTO-Base, PTO-G, and PTO-C, respectively. Due to the thinness of the Gr layer the Gr-modified photocatalyst sheets, it only has a minor impact on the photocatalyst mass.

Benchmark comparisons (Table 4.2) of photocatalytic CO_2 reduction systems with similar material systems are presented in Figure 4.10d. As explained before in Section 3.4.5, the focus is only on CH_4 yield rates, because H_2 yield rates are often not reported in the photocatalytic CO_2 reduction literature. The highest reported CH_4 rate for Pd/TiO_2-based photocatalyst is 104 μmol/gh [185], which is overperformed by PTO-Base by a factor of 72.60. Similarly, for photocatalysts including pure Gr, the highest reported CH_4 rate is 27.72 μmol/gh [210]. Remarkably, PTO-G surpasses this benchmark by a factor of 405.84, while PTO-C outperforms it by a factor of 199.86.

In these experiments, 10 vol% IPA was used as a sacrificial agent, hence the results were additionally compared to the best photocatalytic IPA conversion data. To date, the highest reported CH_4 yield rate by IPA is around 200 μmol/gh [188]. Although the photocatalysts show exceptional performance, their drawback are that their stability are limited to approximately 1 h (Appendix B). Further optimization is required to enhance durability and long-term performance.

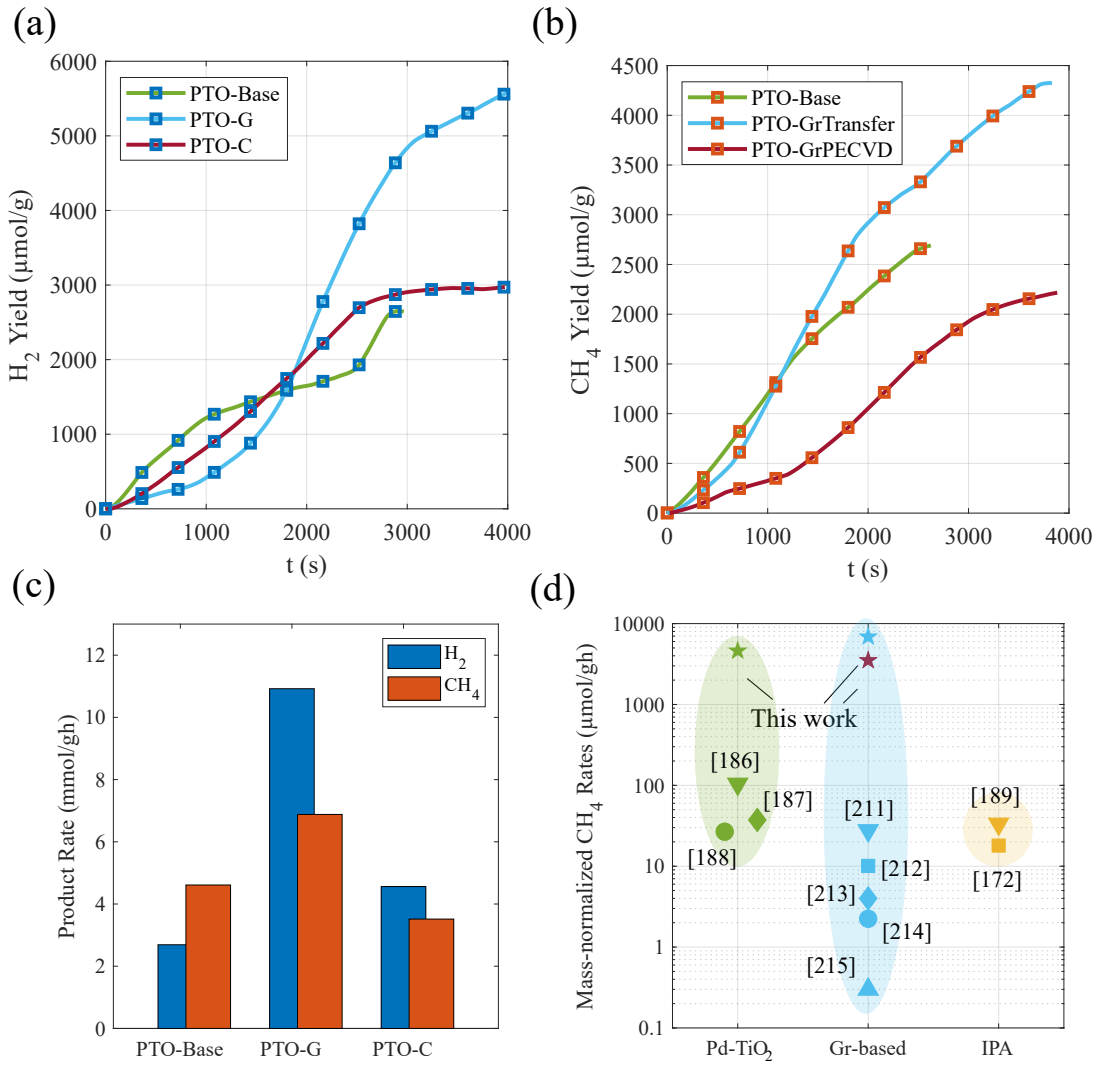


FIGURE 4.10: Denoised (a) H_2 and (b) CH_4 yield data from mass spectrometer measurements. (c) Summarized overview of the H_2 and CH_4 rates for PTO-Base, PTO-G, and PTO-C. (d) Benchmark comparison of similar material systems for photocatalytic CO_2 reduction.

TABLE 4.1: Overview of the absolute, mass- and area-normalized H_2 and CH_4 for each Gr-modified photocatalysts.

Photocatalyst	Absolute Product Rate (μmol/h)		Mass Normalized Product Rate (mmol/gh)		Area Normalized Product Rate (μmol/cm^{2}h)	
	H_2	CH_4	H_2	CH_4	H_2	CH_4
Pd/TiO_2	15,920	10,470	5.68	3.74	0.64	0.42
PTO-Base	4.84	8.30	2.69	4.61	0.19	0.33
PTO-G	19.66	12.38	10.92	6.88	0.79	0.50
PTO-C	8.67	6.68	4.56	3.51	0.35	0.27

TABLE 4.2: Benchmark studies of comparable photocatalyst composites (Pd-TiO_2, Gr-TiO_2) for CO_2 reduction and CH_4 production. In addition, reports on IPA conversion into solar fuels are compared.

Photocatalyst	Setup	Reactant	Yield/Rate	Remark	Ref.
Pd nanodisks on TiO_2 thin film (PTO-Base)	•150 W metal-halide lamp •500 mW/cm^2 •aluminum reactor •MS analysis	CO_2 + H_2O (vapor)	H_2: 2.690 μmol/gh CH_4: 4.610 μmol/gh	•1 h stability •IPA scavenger	This work
Pd–TiO_2 nanoparticles	•300 W Xe lamp •420 nm cut-off filter •10 cm light-source distance •glass reactor •GC analysis	CO_2 + 2 mLH_2O (vapor)	CH_4: 104 μmol/gh	•shown 4 h stability •no saturation •30 mg photocatalyst powder	[185]
Pd-TiO_2 nanoparticles	•500 W Hg lamp •GC analysis	CO_2 + H_2O (liquid)	CH_4: ~28 μmol	•5 h measurement •150 mg PC nanoparticles dispersed in water	[186]
Pd-TiO_2 nanowires	•400 W Hg lamp •Pyrex glass reactor •GC analysis	CO_2 + H_2O (vapor)	CH_4: 26.7 μmol/gh CO: 50.43 μmol/gh	•8 h stability	[187]
Suspended Gr layer on Pd nanodisks on TiO_2 thin film (PTO-G)	•150 W metal-halide lamp •500 mW/cm^2 •aluminum reactor •MS analysis	CO_2 + H_2O (vapor)	H_2: 10.920 μmol/gh CH_4: 6.880 μmol/gh	•1 h stability •IPA scavenger	This work
Carbon black layer on Pd nanodisks on TiO_2 thin film (PTO-C)	•150 W metal-halide lamp •500 mW/cm^2 •aluminum reactor •MS analysis	CO_2 + H_2O (vapor)	H_2: 4.560 μmol/gh CH_4: 3.510 μmol/gh	•1 h stability •IPA scavenger	This work
Polymer-TiO_2-Gr composite	•gas reactor •300 W Xe lamp •420 nm cut-off filter •GC analysis	CO_2 generated by $NaHCO_3$ with H_2SO_4	CO: 21.63 μmol/gh CH_4: 27.62 μmol/gh	•5 h measurements •20 mg photocatalyst powder	[210]
TiO_2-Gr sandwich structure	•4.2 cm^2 and 230 mL glass reactor •300 W Xe lamp •GC analysis	CO_2 + H_2O (vapor)	CH_4: 10.1 μmol/gh C_2H_6: 7.2 μmol/gh	•100 mg photocatalyst powder	[211]

Photocatalyst	Setup	Reactant	Yield/Rate	Remark	Ref.
TiO_2/N-doped Gr hollow sphere	•300 W Xe lamp •10 cm distance •GC and GC-MS analysis	10 mL DI water, CO_2 generated by $NaHCO_3$ with H_2SO_4	CO: $\sim 6\,\mu$mol/gh CH_3OH: $\sim 9\,\mu$mol/gh CH_4: $\sim 4\,\mu$mol/gh	•5 cycles •50 mg photocatalyst powder	[212]
CNNA/rGO	•200 mL Pyrex glass reactor •350 W Xe lamp •AM1.5 filter •GC analysis	10 mL DI water mixed with CO_2	CO: 5.96 μmol/gh CH_4: $\sim 2.24\,\mu$mol/gh CH_3OH: 0.22 μmol/gh C_2H_5OH: 0.82 μmol/gh	•5 cycles •100 mg photocatalyst powder	[213]
CdS hollow sphere + monolayer N-doped Gr	•200 mL Pyrex glass reactor •350 W Xe lamp •420 nm cutoff filter •GC-MS analysis	10 mL DI water, CO_2 + H_2SO_4 + $NaHCO_3$	CO: 2.6 μmol/gh CH_4: 0.3 μmol/gh	•50 mg photocatalyst powder	[214]
$CsPbBr_3$/ Bi_2WO_6 2D/ 2D heterojunction	•150 W Xe lamp, AM 1.5 filter •40 ml Pyrex bottle	CO_2 + + ethyl acetate + IPA	H_2: $\sim 40\,\mu$mol/g CH_4: $\sim 200\,\mu$mol/g CO: $\sim 4100\,\mu$mol/g	•6 h measurement times •5 cycles	[188]
TiO_2 / CdS	•450 W Xe lamp •320 nm and 420 nm cut-off filter •reaction temperature 20 −25 °C •GC analysis, GC-MS analysis	CO_2 + H_2O + IPA	H_2: $\sim 8\,\mu$mol CH_4: $\sim 18\,\mu$mol CO: 0.8 μmol	•10 h measurement times •0.1 g photocatalyst dissolved in liquid feedstock	[171]

4.5 Simulations

The Finite Element Method (FEM) is used in this chapter due to the hexagonal periodicity of the metastructure. This simulation study was conducted to understand the electrodynamical behavior of PTO-Base and the improvement by PTO-G. The measured absorption spectra data for both photocatalysts from Figure 4.6a are used to qualify the simulation results (Figure 4.11a). The simulated absorption is lower in many regions but still shows a similar curved shape and peak positions. The difference is caused by the theoretical refractive index, insufficient geometrical representation, or the neglected surface roughness. For example, the suspended Gr layer in PTO-G is assumed as a planar layer in the simulation. Nevertheless, the absorption peaks near 400 nm, 600 nm, and 700 nm are still present and approximately aligned in peak position and broadness, which allows the valid representation of the simulation results.

Figure 4.11b shows an excerpt of the simulation domain with the hexagonal-shaped unit cells and hexagonal-arranged periodicity. The unit cell has unequal lengths in X- and Y-direction, hence defined by the periodicity ($P_X = 700\,\text{nm}$, $P_Y = 400\,\text{nm}$), and the disk diameter ($L_X = 420\,\text{nm}$ and $L_Y = 250\,\text{nm}$). Moreover, the unit cell requires a disk height ($H_{ND} = 30\,\text{nm}$), photocatalyst thin film thickness ($H_{SC} = 160\,\text{nm}$), and substrate thickness ($D_S = 1000\,\text{nm}$). For PTO-G, the suspended Gr layer is simulated as a plane Gr layer with $D_{Gr} = 0.3\,\text{nm}$ to align with a monolayer Gr thickness [215]. The refractive index for all material layers were taken from the COMSOL standard material database.

To understand the charge carrier dynamics, the absorption peak at 700 nm is further discussed in this section. The resulting E-fields are compared under 735 nm and 715 nm illumination for PTO-Base and PTO-G, respectively (Figures 4.11c-h).

On the XY-plane at $Z = H + D_{Gr}$, a highly intense E-field surrounds the nanodisk (Figure 4.11c, 4.11f), suggesting plasmon resonance and a high charge carrier separation region. However, the region is larger for PTO-Base, which suggests a damping effect caused by the Gr layer for PTO-G [216, 217].

The ZX-plane at $Y = 0\,\text{nm}$ confirms an effect by the Gr layer (Figures 4.11d, 4.11g). Both photocatalysts show plasmon resonance at the Pd nanodisk outer region. In the case of PTO-Base, the plasmon resonance is more focused in the bottom disk region. It shows strong E-fields in the Pd-TiO_2 transition region, indicating charge carrier migration between both material layers. While Figure 4.11c shows a larger region of E-field enhancement, Figure 4.11d suggests that this effect is only in-plane on the Pd nanodisk top surface. For PTO-G, the plasmon resonance is along the side walls and the top layer of the nanodisk.

The YZ-plane at $X = 0\,\text{nm}$ shows comparably weaker E-field amplification, which means that the nanodisk acts preferentially along the X-axis. A direct comparison between Figures 4.11e and 4.11h reveals that the E-field amplification map changes significantly once the Gr layer is transferred to the nanodisks. While the E-field lowers for PTO-Base once reaching the TiO_2 layer, there is an increased E-field in the TiO_2 for PTO-G. This suggest an amplification that is caused by the suspended Gr layer.

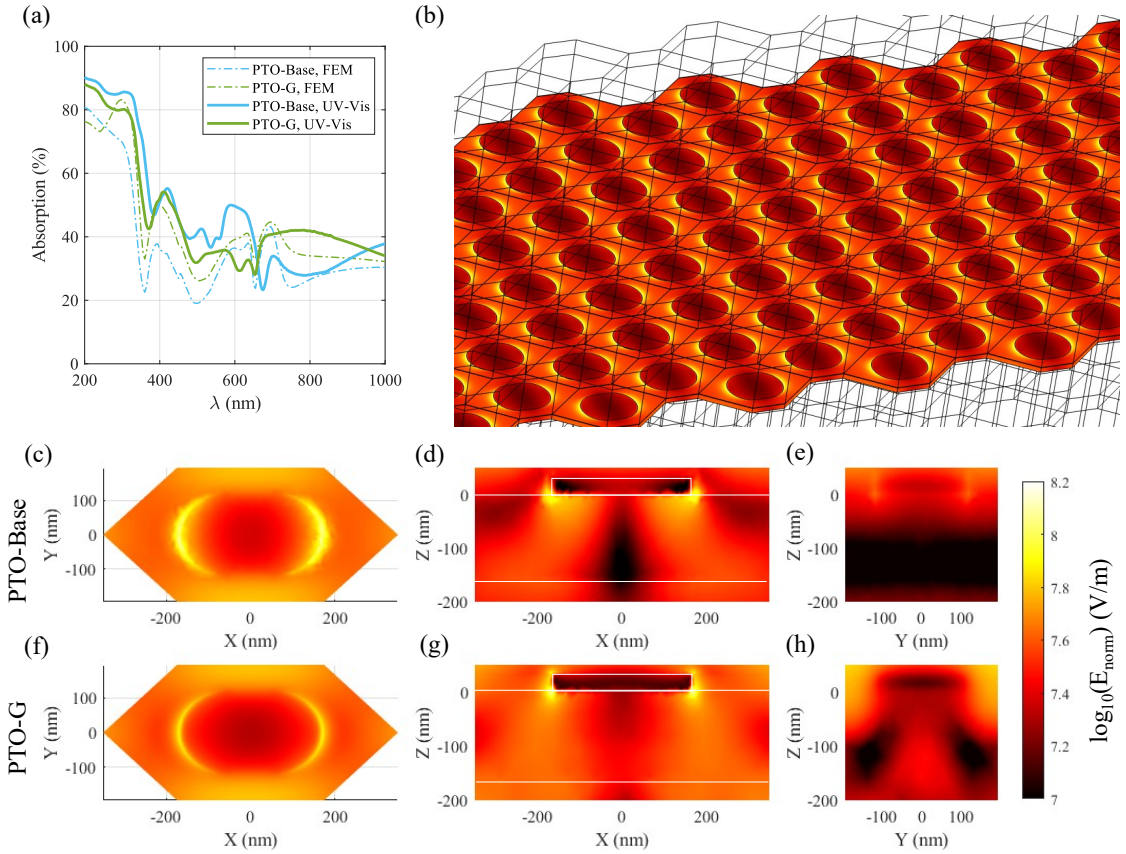


FIGURE 4.11: (a) Absorption spectra comparison between simulated (dashed lines) and UV-Vis measured (solid lines) of PTO-Base (green) and PTO-G (blue). (b) Excerpt of the hexagonal-periodic simulation domain. Logarithmic plotted simulated E-field strength in V/m of (c) XY-, (d) ZX-, and (e) YZ-plane of PTO-Base at 735 nm illumination. Logarithmic plotted simulated E-field strength in V/m of (f) XY-, (g) ZX-, and (h) YZ-plane of PTO-G photocatalyst at 715 nm illumination.

4.6 Proposed Charge Carrier Dynamics

A Schottky junction with a 0.6–1.4eV barrier height is formed between the TiO_2-Pd contact (Table A.1, Equation 1.2). In the photocatalysts, the Schottky junction enables the LSPR effect, increases the charge separation, and allows hot electron generation. For PTO-Base, the hot electron can be injected into the conduction band of the underneath TiO_2 layer and contribute to photocatalytic reactions from there.

As previously shown in the simulation results, the suspended Gr layer in PTO-G damps the plasmon resonance of the Pd nanodisks. Moreover, Gr that is in contact with a metal is doped due to charge transfer [202]. In the case of Gr-Pd contact, this creates a chemisorbed binding, which n-dopes it. In fact, the suspended Gr layer has interchanging contact regions as it is partially attached to

the top Pd nanodisk surface, but is also "free-standing" in air as shown in Figure 4.5a-b. This creates a shift in Fermi level and work function [203].

The band diagram suggests that the Gr-Pd contact region acts as a reaction center for the photocatalytic reaction [199]. It gets filled by hot electrons from the LSPR in the Pd nanodisk, or by electrons from the free-standing Gr region. Moreover, its high mobility allows for significantly minimizing the recombination probability of the free-moving charge carriers [25, 26, 83]. Finally, Gr has favorable adsorption properties toward H_2O [218] and CO_2 molecules [219], which is an additional reason for the enhanced photocatalytic reactions.

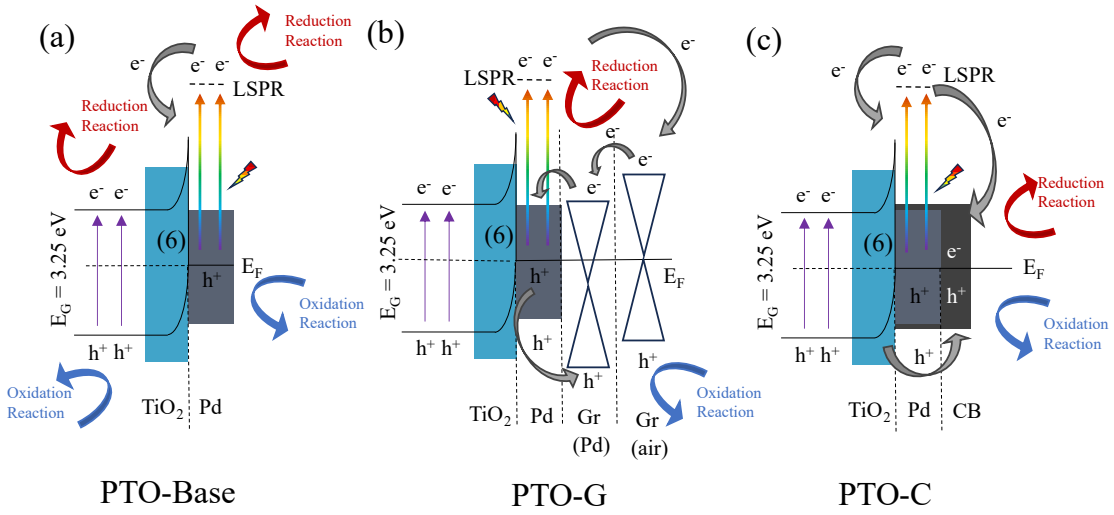


FIGURE 4.12: Proposed band diagram for the (a) PTO-Base, (b) PTO-G, and (c) PTO-C photocatalyst structure. In PTO-Base, the Pd-TiO_2 transition forms a Schottky barrier. The Pd nanodisk acts as a plasmonic resonator in which hot electrons can be generated through LSPR effects through visible light. For PTO-G, the suspended Gr is doped in the region of Pd contact, which shifts the Dirac cone. For PTO-C, the charge carriers must be provided from the carbon black layer surface for the redox reactions.

PTO-C is based on carbon black that still possesses electronic and chemical properties that are advantageous for photocatalysis [220, 221]. Additional measurements with only the carbon black layer on TiO_2 without Pd nanodisks have shown no reactivity (Figure B.14b). This suggests that the PTO-C functions due to its coupling with the Pd nanodisks. Although the carbon black layer completely coated the Pd nanodisk surface and immensely dampened its LSPR properties, it still shows a contributing effect through hot electron and hole injection to the photocatalytic reactions. Another possible mechanism are defect states within the carbon black layer, allowing an enhanced charge separation for photo-excited charge carriers [222]. Nevertheless, the charge carrier must transport through the carbon black layer to contribute in redox reactions.

4.7 Conclusion

In this chapter, a Pd/TiO_2-based metamaterial photocatalyst sheet was varied in its geometry and further modified. In particular, two methods were utilized which were the wet-transfer of a Gr layer and the growth of a carbon black layer by PECVD. While PTO-Base exhibited outstanding photocatalytic performance (H_2: 2.69 mmol/gh, CH_4: 4.61 mmol/gh), the PTO-G system showed further enhancement (H_2: 10.92 mmol/gh, CH_4: 6.88 mmol/gh). Adding a suspended Gr layer led to a significant 4.05-fold and 1.49-fold enhancement in the H_2 and CH_4 rate, respectively. On the other hand, PTO-C showed a significantly lower yield (H_2: 4.56 mmol/gh, CH_4: 3.51 mmol/gh) in comparison with PTO-Base. Despite their different reaction selectivities, it still demonstrates the functionality of the carbon black layer. All yield rates were achieved by only a photocatalyst mass of 1.8 mg.

This work is the first to report a metamaterial-based photocatalyst sheet for photocatalytic CO_2 reduction modified by a 2D material. Together with the metasurface, it unlocks synergistic enhancements in the photocatalytic activity, mainly through its plasmonic properties. The results suggest that the suspended Gr layer improves charge separation and transport due to its characteristic band structure, leading to an enhancement in the reactivity of the photocatalyst sheet.

5 MoS_2-modified Pd/TiO_2 Metamaterial Photocatalyst Sheet

Another widely researched photocatalytic application is water purification [69]. Especially in developing countries or regions in crisis, access to clean water resources is scarce due to chemical [7], pharmaceutical [62], bacterial [63, 64, 65], and viral [66] contamination . In this chapter, the plasmonic nanodisk metamaterial photocatalyst sheet is tested on photocatalytic bacterial inactivation, in particular for Escherichia Coli (*E. coli*) bacteria, which are known to cause food poisoning [223]. This photocatalytic approach offers a sustainable alternative to traditional chemical-based inactivation methods, aligning with global efforts to develop environmentally friendly and energy-efficient water treatment solutions [67].

Molybdenum disulfide (MoS_2) is known as an efficient material for photocatalytic bacterial inactivation [224, 223, 225, 226]. The integration of MoS_2 provides suitable conditions for the generation of reactive oxygen species (ROS) through photocatalytic reactions [61]. In fact, ROS play a crucial role in the inactivation of bacteria and other pathogens present in water. MoS_2 is a widely researched 2D material and a semiconductor, featuring a tunable bandgap (1.4–1.9 eV) that varies with the number of layers [85, 86]. When applied as a co-catalyst, it can exhibit advantageous photocatalytic properties such as chemical stability and increased charge separation, making it a suitable choice for photocatalytic bacterial inactivation.

The Pd/TiO_2 photocatalyst sheet from Chapter 3 is further modified in this part of work by MoS_2 synthesized by chemical vapor deposition (CVD) [227]. Two configurations are studied, in which the MoS_2 layer is either grown between the Pd nanodisk and TiO_2 layer, or on-top of the entire Pd/TiO_2 metasurface. This Chapter covers the fabrication of the MoS_2-modified Pd/TiO_2 metamaterial photocatalyst sheet, material characterization, bacterial inactivation performance, simulation studies, and the discussion of the charge carrier mechanism by its proposed band diagram. This approach reveals a photocatalyst sheet that is functional for photocatalytic bacterial inactivation under visible light.

5.1 Photocatalyst Design

The photocatalyst sheet design is based on the Pd/TiO_2 from Chapter 3, as it demonstrated the highest level of reactivity. However, the geometrical design is changed to a $H_{SC} = 80\,nm$ thick anatase TiO_2 thin film layer and Pd nanodisks with $H_{ND} = 20\,nm$ height, as these specifications the fabrication time and lead to better reproducibility without significant efficiency loss. The periodically-arranged circular-shaped nanodisk pattern remains the same with $D_{ND} = 150\,nm$ and $P = 300\,nm$.

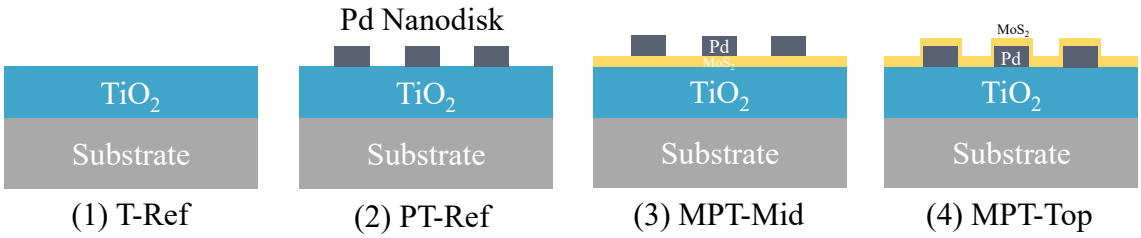


FIGURE 5.1: Overview of the photocatalyst sheet design studied in this chapter. T-Ref is the first reference sample with only a TiO_2 layer. PT-Ref is a second reference sample with the Pd/TiO_2 metasurface. In MPT-Mid, the MoS_2 layer is grown between the TiO_2 layer and Pd nanodisks. In MPT-Top, the MoS_2 layer is grown on-top of the Pd/TiO_2 metasurface.

In total, six photocatalyst configurations will be compared to reveal the impact of each modification on the reactivity (Figure 5.1). There are two reference photocatalysts, one of which is only a 80 nm anatase TiO_2 layer grown on a glass substrate, labeled "T-Ref". The other one is T-Ref patterned with the Pd nanodisk array, labeled "PT-Ref". The other four photocatalysts are further modified with MoS_2, introducing two variations, labeled as “MPT-Mid-NL” and “MPT-Top-NL”. Here, NL refers to the number N of experimentally determined MoS_2 layers. In this chapter, MoS_2 layers with $N = 3$ and $N = 17$ are used to show the photocatalytic performance difference between few-layer and bulk MoS_2. Hence, the discussed samples are labeled "MPT-Mid-3L", "MPT-Mid-17L", "MPT-Top-3L", and "MPT-Top-17L". For better readability, the “NL” notation is removed in general discussions in case the number of layers is not relevant. For MPT-Mid, the MoS_2 layers are grown between the Pd nanodisk and TiO_2 layer, while they are grown on-top of the Pd nanodisk and TiO_2 for MPT-Top.

5.2 Fabrication

The photocatalyst is fabricated on planar $(3.8 \times 3.8)\text{cm}^2$ glass substrate. This substrate size differs from the one in Chapters 3 and 4 as the CVD-sulfurization setup has a size limitation for 4 cm substrate width. Both types of photocatalyst sheet have a similar fabrication with slightly altering in the order of process steps. The fabrication flow for MPT-Mid (Figure 5.2) is outlined as follows:

1. Deposition of 80 nm TiO_2 (blue layer) on the glass substrate by DC magnetron sputtering. Then, an annealing process at 650 °C for 1 h is conducted to obtain the anatase crystal phase for the TiO_2 layer.
2. Deposition of the Mo seed layer (brown layer) by DC magnetron sputtering targeting 1 nm and 4 nm.
3. CVD sulfurization at 800 °C to synthesize the MoS_2 layer (yellow layer).
4. Spin-coating of 100 nm PMMA (green layer) and 100 nm AMONIL (red layer).
5. Patterning of periodic rectangular hole pattern ($P = 300$ nm, $L = 150$ nm) by NIL.
6. Plasma-etching by RIE of the AMONIL and PMMA layer to achieve an undercut profile.
7. 20 nm Pd (grey layer) deposition by e-beam evaporation.
8. Lift-off step to remove the double-layer resist structure by acetone, IPA and DI water.

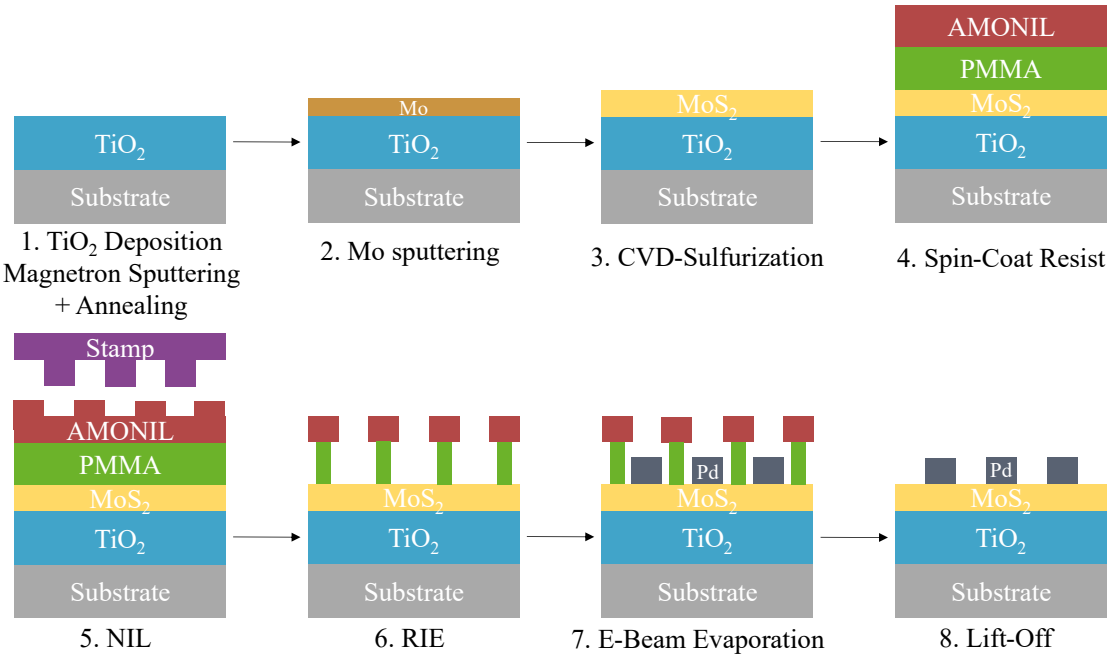


FIGURE 5.2: Fabrication workflow for the MPT-Mid photocatalysts involving multiple process steps such as magnetron sputtering, CVD sulfurization spin-coating, NIL, RIE, e-beam evaporation, and lift-off.

For MPT-Top, the MoS_2 is grown on-top of PT-Ref as a post-process. The complete fabrication flow is (Figure 5.3):

1. Deposition of 80 nm TiO_2 (blue layer) on the glass substrate by DC magnetron sputtering. Then, an annealing process at 650 °C for 1 h is conducted to obtain the anatase crystal phase for the TiO_2 layer
2. Spin-coating of 100 nm PMMA (green layer) and 100 nm AMONIL (red layer).
3. Patterning of periodic rectangular hole pattern ($P = 300$ nm, $L = 150$ nm) by NIL.
4. Plasma-etching by RIE of the AMONIL and PMMA layer to achieve an undercut profile.
5. 20 nm Pd (grey layer) deposition by e-beam evaporation.
6. Lift-off step to remove the double-layer resist structure by acetone, IPA and DI water.
7. Deposition of the Mo seed layer (brown layer) by DC magnetron sputtering targeting 1 nm and 4 nm.
8. CVD sulfurization at 800 °C to synthesize the MoS_2 layer (yellow layer)

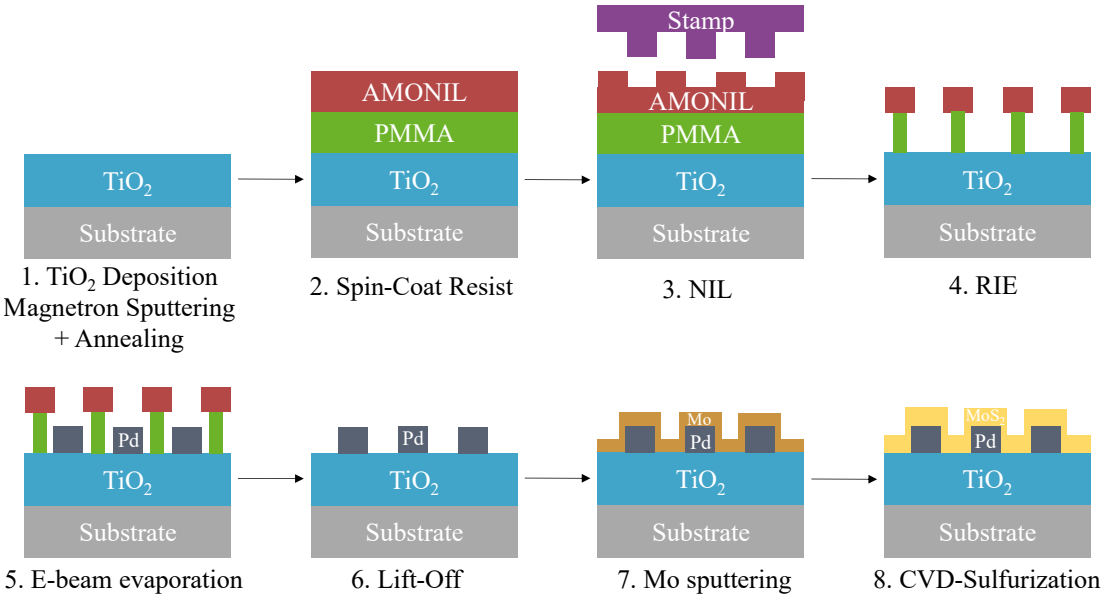


FIGURE 5.3: Fabrication workflow for the MPT-Top photocatalysts involving multiple process steps such as magnetron sputtering, spin-coating, NIL, RIE, e-beam evaporation, and lift-off, and CVD sulfurization

5.2.1 Sulfurization by Chemical Vapor Deposition

Chemical Vapor Deposition (CVD) is a process technique widely used in materials science and engineering for depositing thin films on various substrates (Figure 5.4a). This process involves the chemical reaction of gaseous precursors in a heated chamber, resulting in the formation of a solid film on a target surface. The remarkable flexibility of CVD allows for precise control over the layer thickness, composition, and structure.

A commercial split-type tube furnace (RSH 50, Nabertherm GmbH; Figure 5.4b) was utilized to synthesize MoS_2 from sputtered Mo seed layers. The process involved placing samples with a pre-deposited Mo thin film in the center of a quartz tube. Sulfur powder, serving as the precursor, was positioned in a crucible boat at a calculated distance from the samples. Prior to initiating the CVD process, the working pressure within the chamber was reduced to approximately 2×10^{-2} mbar. Subsequently, a 20 sccm Ar flow was introduced as the carrier gas for the sulfurization, slightly increasing the working pressure to 9.4×10^{-2} mbar. The sulfurization process was conducted at 800 °C process temperature for 30 min.

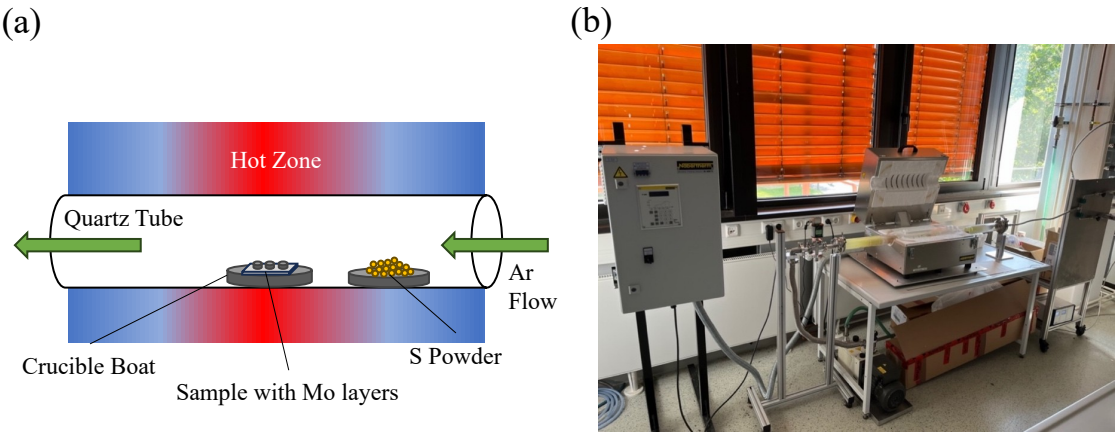


FIGURE 5.4: (a) Principle of CVD showing a quartz tube and a sample placed on a crucible boat. For the MoS_2 sulfurization, Mo layers must be deposited on it before. By creating Ar flow, nearby S powder can be transported to the sample surface and thermally react through providing the required thermal energy. (b) Photograph of the CVD setup, showing the commercial split-type tube furnace of the model 'RSH 50' from the company 'Nabertherm GmbH'.

5.3 Characterization

AFM and SEM were used to measure the surface topography of the photocatalysts. The AFM scans provided qualitative data on surface roughness and height for four different samples: MPT-Mid-3L, MPT-Mid-17L, MPT-Top-3L, and MPT-Top-17L, as shown in Figures 5.5a-d, respectively. The AFM images reveal that MPT-Mid-3L (Figure 5.5a) and MPT-Mid-17L (Figure 5.5b) have an expected disk height, but also shows that there is an enlargement of up to 80 nm for MPT-Top-3L (Figure 5.5c) and MPT-Top-17L (Figure 5.5d). Moreover, it shows that the positions of the nanodisks are distorted. This highlights the distinct characteristics between MPT-Mid and MPT-Top, indicating an interaction of the Pd nanodisk structure with the sulfurization process step.

SEM imaging further provide details of the nanodisk structure, showing a higher quality image of the nanodisk shape. The SEM images of MPT-Mid-3L (Figure 5.5e) and MPT-Mid-17L (Figure 5.5f) demonstrate that the nanodisks deviated from an ideal circular shape, likely due to irregular sidewall etching during the RIE process. Similar observations are made for MPT-Top-3L (Figure 5.5g) and MPT-Top-17L (Figure 5.5h). A comparison of the white color intensity in the disk structure between the MPT-Mid and MPT-Top indicate a significantly greater nanodisk height for both MPT-Top samples. This observation confirms the difference in nanodisk height between the MPT-Mid and MPT-Top variants.

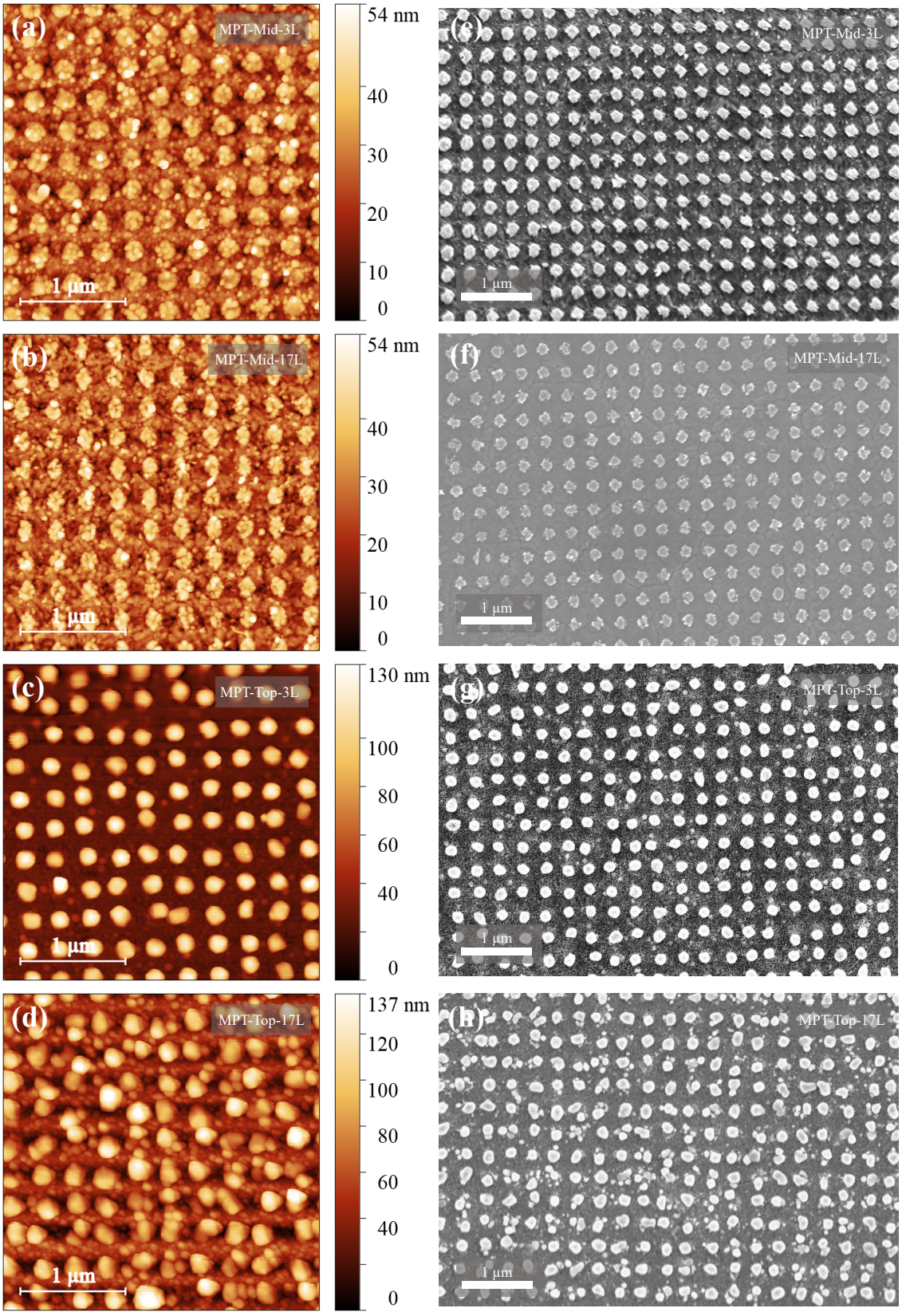


FIGURE 5.5: AFM images of (a) MPT-Mid-3L, (b) MPT-Mid-17L, (c) MPT-Top-3L, (d) MPT-Top-17L, respectively. Top-down SEM images of (e) MPT-Mid-3L, (f) MPT-Mid-17L, (g) MPT-Top-3L, (h) MPT-Top-17L, respectively.

The surface topographies of both MPT-Mid photocatalysts aligned with the expectations, while the MPT-Top photocatalysts exhibited increased nanodisk height of up to 80 nm along with distortions in the nanodisk positions. This difference can be attributed to the varying fabrication process order for the two types of photocatalysts. In the MPT-Top fabrication, the CVD-sulfurization step is performed after the Pd nanodisk patterning, heating the entire photocatalyst including the Pd nanodisks to temperatures of 800 °C for 30 min under a sulfuric atmosphere. This high-temperature treatment sulfurizes the Pd nanodisk structure [228], resulting in the observed height increase and distortion.

The sulfurizations process steps were found to have a significant influence on their structural integrity and surface characteristics of the photocatalysts. Further crystallization and cracking of the underlying TiO_2 layer is observed as a result of high-temperature treatments. To investigate this phenomenon more thoroughly, additional AFM measurements were conducted on a TiO_2 thin film reference samples, evaluating surface roughness changes before and after annealing it by 650 °C for 1 h (Figure A.1b). The impact of the CVD-sulfurization step was also examined by annealing one reference sample at 800 °C for 30 min in the annealing process (Figure A.1c). These heat-treatments, reveal a clear correlation between increasing annealing temperature and heightened surface roughness, along with the formation of cracks. These findings provide an explanation for the observed nanodisk roughness in both PT-Ref and MPT-based photocatalysts.

To gain insights into the MoS_2 layer thickness, AFM measurements were performed on dummy samples featuring MoS_2 structures (Figure A.5). The results demonstrated that a 1 nm Mo seed layer yields a MoS_2 layer with a thickness of 2.2 nm (Figure A.5a). Assuming that a single MoS_2 layer is 0.615 nm thick [229, 230], this corresponds to approximately 3 layers . The 4 nm Mo seed layer results in a MoS_2 layer thickness of 10.5 nm, equivalent to about 17 layers (Figure A.5c).

A Pd thin film with 20 nm step height on an Si substrate was fabricated as a reference sample to understand the Pd interaction on the CVD sulfurization process. AFM images before (Figure 5.6a) and after (Figure 5.6b) the sulfurization process step with the same conditions show the crystallization of Pd [231]. Notably, clusters of several 100 nm height are observed. The element analysis by EDX (Figure 5.6c) shows that sulfur (S) atoms (red) can be found on the Pd (green) clusters. Even though many clusters are red and green, there are some clusters which are orange, suggesting a binding between Pd and S. The EDX spectrum (Figure 5.6d) shows that all expected elements on the reference sample can be measured, including the Si substrate with its native oxide layer. As the

major peak for Pd and S have a similar intensity, it can be concluded that the stoichiometry of the binding is PdS.

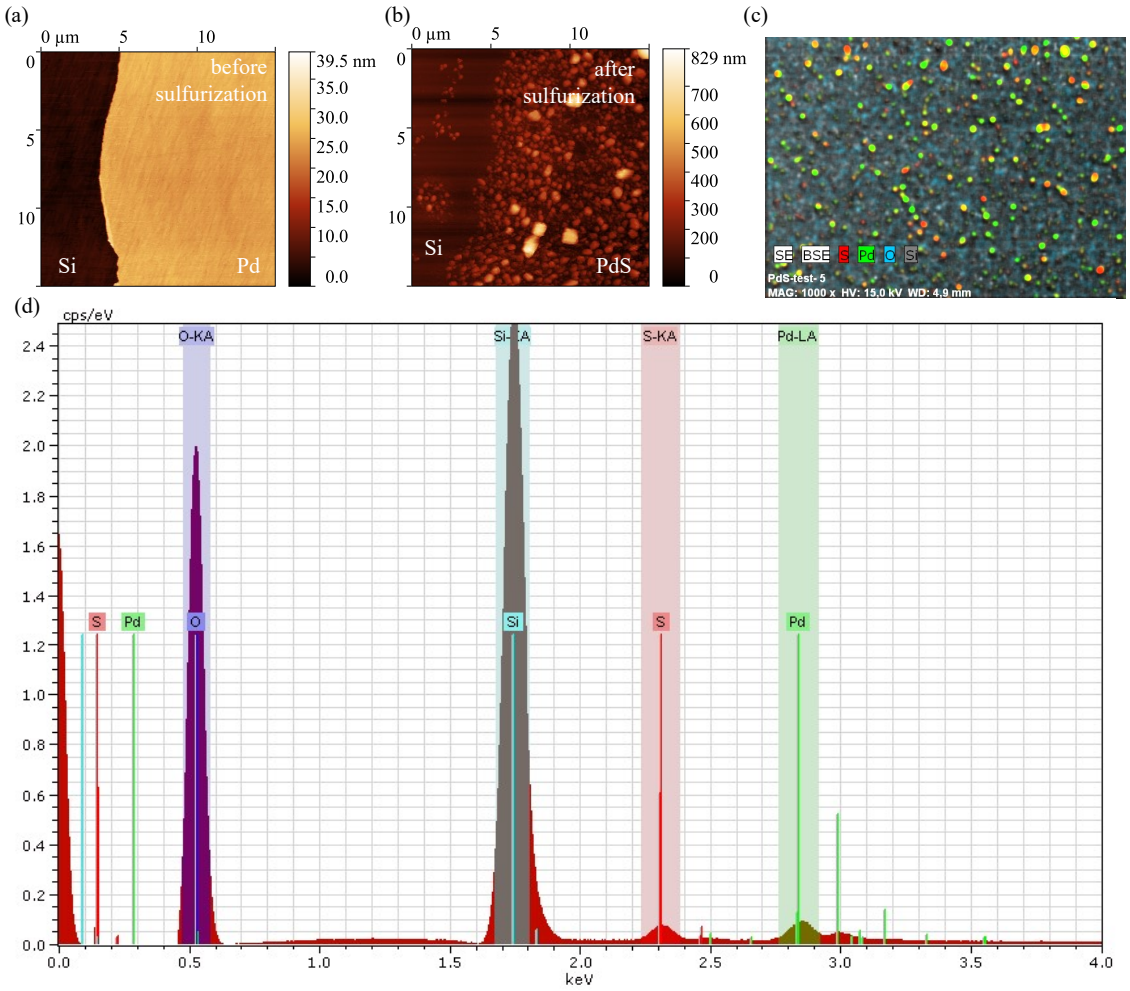


FIGURE 5.6: AFM scan of a 20 nm Pd thin film on a Si substrate (a) before and (b) after 800 °C CVD sulfurization of 30 min. (c) EDX material mapping based on SEM scan, showing the positions of S (red), Pd (green), PdS (orange), O (blue), and Si (grey) atoms. (d) EDX spectrum of the same set of elements in the same SEM image region.

The optical properties of the six photocatalyst sheets were characterized through UV-Vis spectroscopy, revealing distinct features for each sample. The T-Ref sample exhibits an absorption edge at 390 nm wavelength, with a high light absorption (60-80%) in the UV range. Tauc analysis determined the bandgap of the TiO_2 layer to be 3.25 eV (Figure A.1f), consistent with the established value for anatase-phase TiO_2 in literature [149].

The PT-Ref sample, featuring the Pd nanodisk metasurface, demonstrated two

distinct absorption peaks at 450 nm and 512 nm. In particular, its absorption spectra showed overall activity across the entire Vis-NIR range up to 1500 nm, indicating potential photocatalytic activity in this broad spectral region.

Characterization of the few-layer MoS_2 on glass substrates has provided insights into their intrinsic optical properties (Figure A.6). Tauc analysis has revealed bandgap ranges of 1.63–1.82 eV for 3-layer MoS_2 and 1.41–1.52 eV for 17-layer MoS_2, demonstrating a thickness-dependent bandgap variation (Figure A.6).

The MPT-based photocatalyst sheets exhibit varying optical responses depending on the number of MoS_2 layers and the process order. MPT-Mid-3L shows only a minimal red shift compared to PT-Ref, while MPT-Mid-17L displays a more pronounced influence of the MoS_2 layer. This is proven by higher activity in the visible range, and by broader, damped absorption peaks. Both MPT-Top photocatalysts demonstrated significantly higher overall activity in the visible range compared to their MPT-Mid counterparts. This enhanced activity is attributed to the enlargement of the nanodisk structure following CVD sulfurization. Notably, the MPT-Top photocatalyst sheets show no NIR activity due to the conversion of Pd into PdS.

The crystalline properties of the photocatalysts were thoroughly investigated using Raman spectroscopy (Figure 5.7b). The characteristic anatase TiO_2 peaks were identified at 141 cm^{-1}, 195 cm^{-1}, 394 cm^{-1}, 514 cm^{-1}, and 634 cm^{-1}, confirming the crystallinity of the TiO_2 layer. A comparison between T-Ref and PT-Ref samples revealed an enhancement in the Raman signal, attributed to increased scattering from the Pd nanodisk metasurface. The MPT-Top photocatalysts do not exhibit characteristic crystal peaks for PdS [232]. Therefore, it can be concluded that the PdS structure is amorphous.

Upon further synthesis with MoS_2 layers, the MPT photocatalyst sheets exhibited the characteristic E^1_{2g} and A_{1g} peaks (Figure 5.7c), which are well-known Raman active modes of 2H MoS_2 [233]. However, these peaks are less distinguishable for MPT-Mid-3L and MPT-Top-3L due to overlaps between the anatase TiO_2 peak (394 cm^{-1}) and the low signal intensity from the few MoS_2 layers. For reference, Figure A.7 presents the Raman spectra of MoS_2 with varying thicknesses grown on glass substrates without TiO_2 layers, confirming that 3 layers of MoS_2 are measurable. The Raman spectra of MPT-Top photocatalyst sheets indicates vertically aligned MoS_2 formation on the Pd nanodisk metasurface, which is beneficial for photocatalytic reactivity [224].

Figure 5.7d illustrates the peak frequencies and frequency shifts of the E^1_{2g} and A_{1g} modes in the MPT-based photocatalysts. A notable observation is the generally lower peak Raman shift (left y-axis) for MPT-Mid of the A_{1g} mode compared

to MoS_2 layers on glass (Figure A.7). This phenomenon can be attributed to the influence of the substrate material, possibly inducing tensile strain and causing a red-shift. For the MPT-Top photocatalyst sheets, the growth of MoS_2 layers on a structured metasurface (PT-Ref) causes a reduced Raman frequency for the A_{1g} mode, indicating less strain on the out-of-plane vibrations of the S-atoms [234]. The structured surface also induce a slight shift in the E^1_{2g} mode. The frequency shifts for the MPT-based photocatalysts show a trend from few layer MoS_2 sheets (MPT-Top-3L, MPT-Mid-3L) to bulk characteristics (MPT-Top-17L, MPT-Mid-17L), considering the softening effect of the A_{1g} mode.

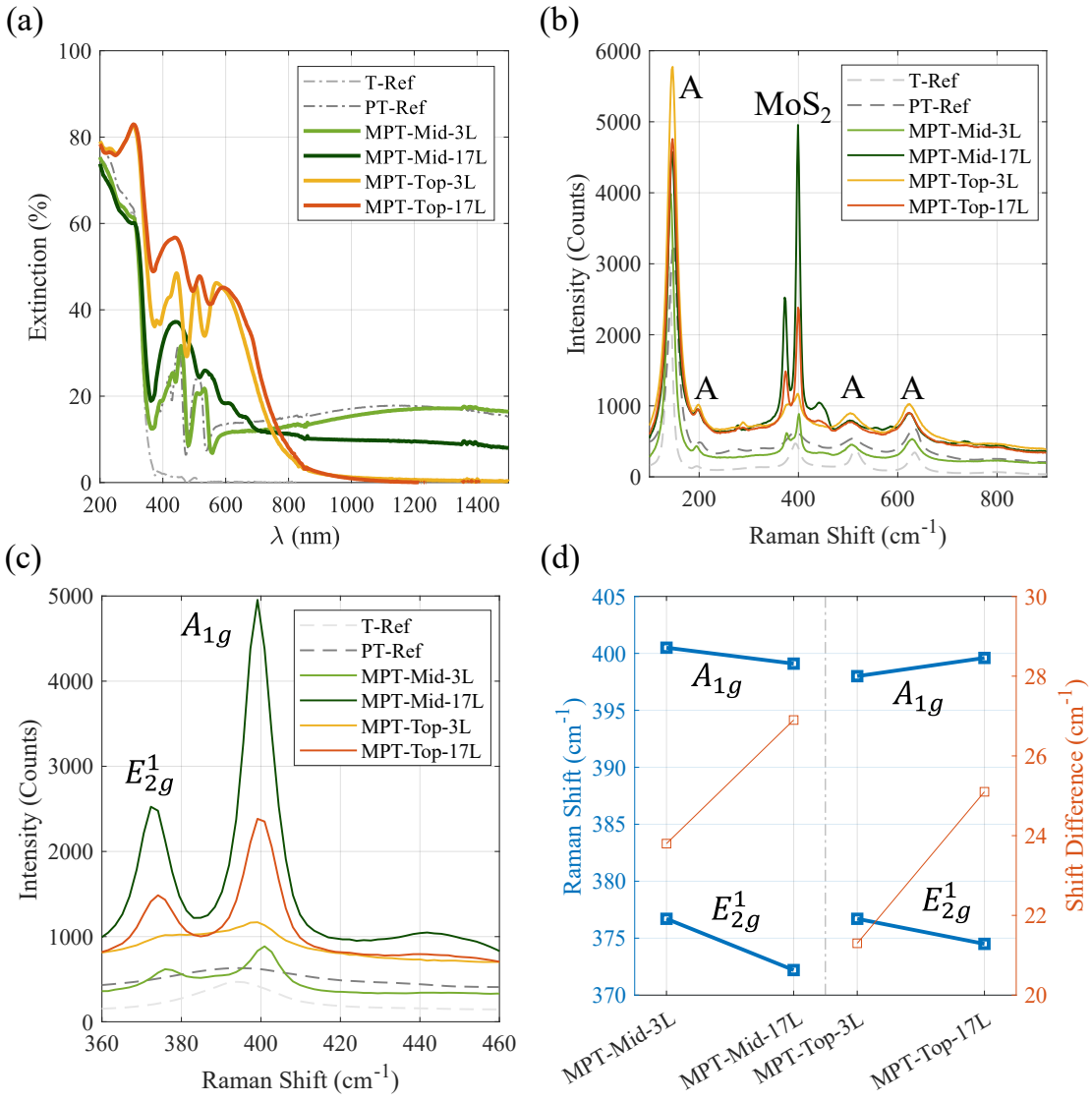


FIGURE 5.7: (a) Absorption spectra evaluated from UV-Vis spectroscopy, (b) Raman spectra in 100–1000 cm^{-1} range for TiO_2 peaks characterization, (c) zoomed Raman spectra between 360–450 cm^{-1} for MoS_2 peaks characterization. (d) Raman shift (left y-axis) and shift difference (right y-axis) of the MPT-based photocatalyst sheets.

The shift differences (right y-axis) for the MPT-based photocatalyst sheets demonstrated a trend from few-layer MoS_2 layers (MPT-Top-3L, MPT-Mid-3L) to bulk characteristics (MPT-Top-17L, MPT-Mid-17L), taking into account the softening effect on the A_{1g} mode. This trend provides valuable insights into the structural evolution of the MoS_2 layers with increasing thickness and their interaction with the underlying substrate.

5.4 Photocatalytic Bacterial Inactivation

The photocatalytic bacteria inactivation is assessed through experiments involving the MoS_2-based metamaterial photocatalyst inactivation of Escherichia coli (*E. coli*) bacteria. The measurements follow a specific procedure to show the biochemical reactions on the bacteria cultures under visible light. Afterwards, the results are analyzed and discussed. In total, six samples are compared to reveal the best inactivation performance. The experiments were executed by Huai-En Chang, PhD student at National Yang-Ming Chiao-Tung University in Hsinchu, Taiwan.

5.4.1 Method

The bacteria were cultivated in lysogeny broth (LB) and subsequently suspended in phosphate-buffered saline (PBS) for the experiments. The initial bacterial concentration was targeted at an optical density (OD) of 0.6, corresponding to approximately 10^7 to 10^9 colony-forming units per milliliter (CFU/ml).

A solar simulator (Xe lamp) equipped with an AM1.5 filter was employed as the light source for these experiments, with the power density set to $10\,mW/cm^2$. This configuration was chosen to minimize the impact of the UV component within the AM1.5 spectrum on E. coli inactivation, thereby providing a more accurate representation of natural sunlight. Unlike other studies, no UV filter was used to better simulate natural sunlight conditions.

To monitor the inactivation process, 0.2 mL samples of the E. coli suspension in PBS were taken at 30 min intervals and analyzed by their OD. This approach allowed for tracking the efficacy of the photocatalytic inactivation over time.

5.4.2 Experimental Results

The experimental methodology is based on Section 5.4. The outcome of the six photocatalyst sheets in inactivating *E. coli* bacteria is visually shown through photographs taken after 240 min of exposure, as shown in Figure 5.8a. All photocatalysts exhibited noticeable improvements compared to the blank test, with obvious visible differences. Figure 5.8b presents a quantitative analysis of the inactivation performance for each sample over the 240 min measurement period, expressed as the survival rate C/C_0. The bacterial samples were tested at 30 min intervals, with each test repeated three times to ensure reliability, and the results were averaged (detailed raw data available in Figure B.15).

The blank test served as a control experiment, revealing the impact of the light source alone on the survival rate. While an initial degradation effect was observed due to the light exposure, the potential intrinsic toxicity of the MoS_2 layer could be ruled out due to its minimal quantity [235]. T-Ref shows similar results to the blank test, indicating that the $10\,mW/cm^2$ power density of the UV portion of the light source is not sufficient to excite electron-hole pairs for a significant photocatalytic activity. Consequently, the outcomes observed for other photocatalysts can be attributed to their specific modifications.

The results for PT-Ref demonstrates improved inactivation compared to T-Ref due to its patterned Pd nanodisk metasurface, which enhances visible light activity. However, the MPT-based photocatalyst sheets show stronger inactivation outcomes. MPT-Mid-3L exhibits the best inactivation performance, closely followed by MPT-Top-3L. Both MPT-Mid-17L and MPT-Top-17L reveal improvements compared to PT-Ref, with MPT-Top-17L performing marginally better.

The superior performance of all MPT-based photocatalysts provides strong evidence for the contribution of few-layer MoS_2 to ROS generation. This creates superoxide anion radicals ($O_2^{\bullet -}$), hydrogen peroxide (H_2O_2), singlet oxygen ($^1O_2$), and hydroxyl radicals (OH^-) that break the cell structure of the *E. coli* bacteria and inactivates them [236]. The results indicate that fewer MoS_2 layers lead to better inactivation outcomes, suggesting the crucial role of the specific photocatalyst design in enhancing photocatalytic efficiency. These findings underscore the importance of precise control over material composition and structure in developing highly effective photocatalysts for bacterial inactivation.

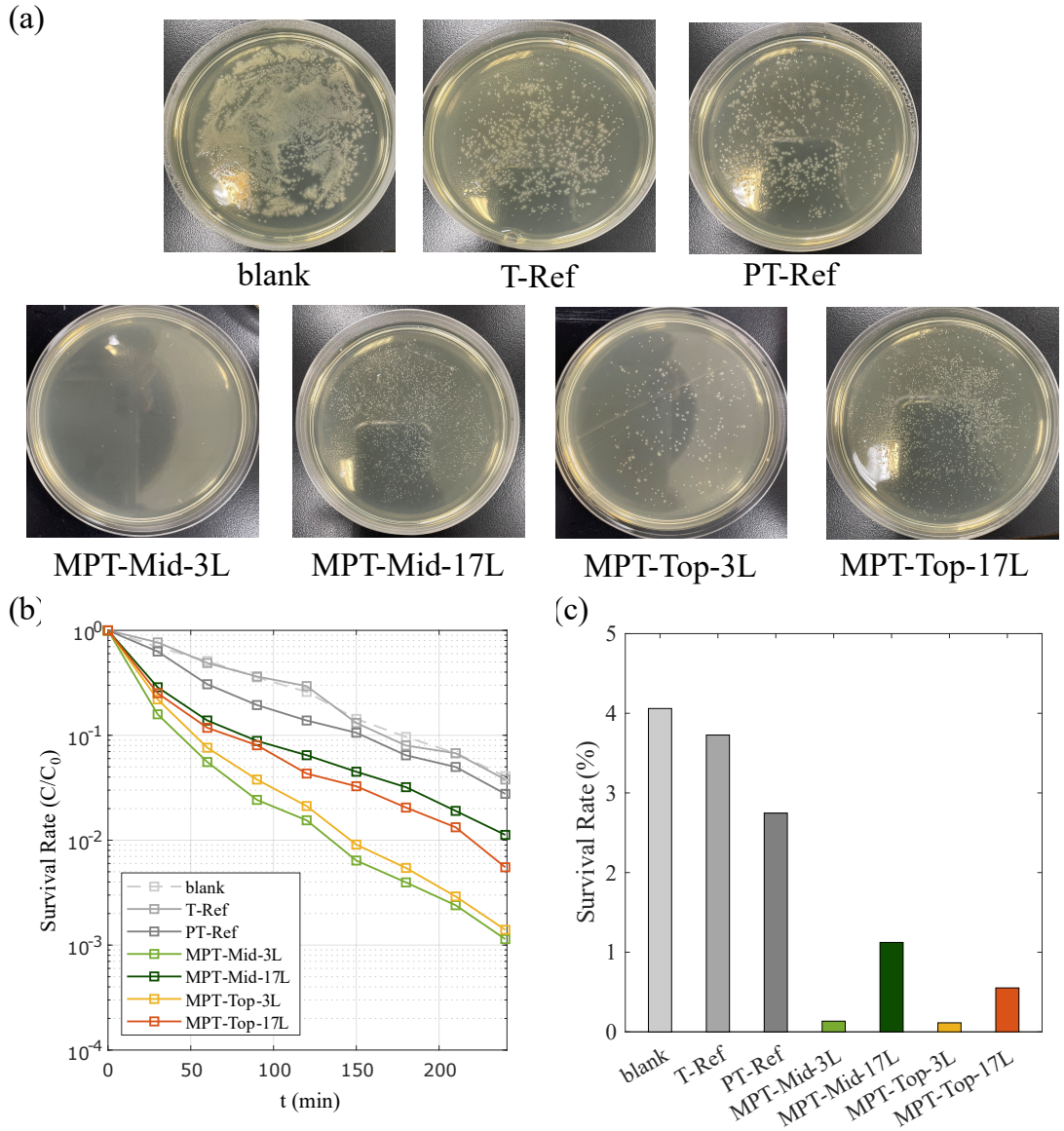


FIGURE 5.8: (a) Photographs of the *E. coli* bacteria after 4 h (240 min) light exposure with the respective samples. (b) Averaged measured survival rates (C/C_0) at every 30 min over the 4 h light exposure. (c) Overview of the performance of each photocatalyst in survival rates (%).

Figure 5.8c provides an overview of the achieved survival rate for each photocatalyst. MPT-Mid-3L shows the best inactivation results (0.08 %), followed by MPT-Top-3L (0.13 %). MPT-Top-17L (0.55 %) and MPT-Mid-17L (1.08 %) also show significant improvements over PT-Ref (2.73 %), with MPT-Top-17L performing slightly better. The overperforming results of all MPT-based photocatalysts proved that the few-layer MoS_2 contributes to ROS generation. Moreover, these results show that fewer MoS_2 layers lead to better photocatalytic activity, emphasizing the importance of specific structural designs in optimizing performance.

5.5 Simulations

The MPT-based photocatalysts were modeled with FDTD simulations, incorporating geometrical data derived from the AFM measurements. For the MPT-Top photocatalysts, the inner disk structure was assumed to consist of PdS due to the sulfurization process. Despite the shifted PdS-MoS_2 nanodisk positions, both MPT-Top were still computed with periodic settings as it would still approximately represent the real situation.

Figures 5.9a and b depict a comparison between simulated extinction spectra (dashed lines) and measured data (solid lines) for the MPT-Mid and MPT-Top photocatalyst sheets, respectively. The measured absorption data, extracted from Figure 5.7a, reveal similar trends. For the MPT-Mid photocatalyst sheets (Figure 5.9a), increasing MoS_2 layer thickness results in broadening and damping of the extinction peaks. Despite variations in extinction intensity, simulated and measured peak positions show minimal shift. Similar effects are observed for MPT-Top photocatalyst sheets (Figure 5.9b), attributed to increased disk structure height.

The E-field enhancement regions, crucial for identifying areas of charge separation, are analyzed for all MPT-based photocatalyst sheets (Figure 5.9c). The upper row displays E-field enhancement in the XY-plane at $Z = 0\,\text{nm}$, while the lower row provides cross-sectional views in the ZX-plane at $Y = 0\,\text{nm}$. Each column represents E-field enhancement at specific wavelengths: 456 nm for MPT-Mid-3L and MPT-Mid-17L, 575 nm for MPT-Top-3L, and 594 nm for MPT-Top-17L.

All photocatalysts exhibit E-field enhancement regions up to a factor of 10, with MPT-Mid photocatalysts showing smaller enhancement regions compared to MPT-Top structures. The plasmonic behavior of Pd nanodisks in MPT-Mid is evident, particularly in the ZX-plane of MPT-Mid-3L. This effect diminishes with thicker MoS_2 layers, as observed in MPT-Mid-17L, aligning with extinction spectra findings.

The MPT-Top photocatalysts significantly outperform their MPT-Mid counterparts in E-field enhancement. The highest enhancement is observed for MPT-Top-3L beneath the nanodisk in the ZX-plane, with a slight damping effect noted for MPT-Top-17L due to increased MoS_2 layer thickness. These results underscore the charge separation capabilities of MPT-Top photocatalysts, especially with thinner MoS_2 layers, indicating their potential for enhanced photocatalytic performance.

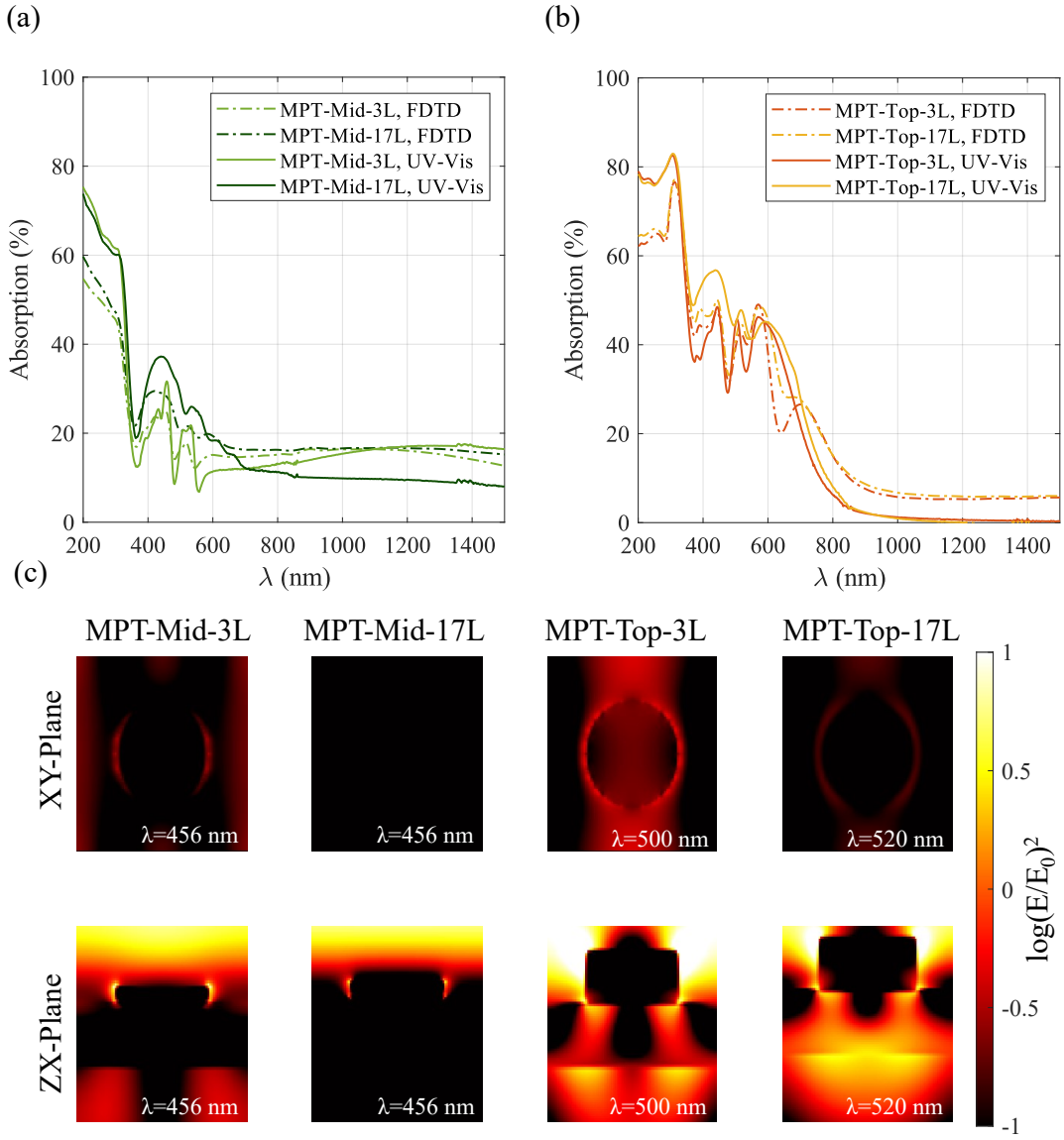


FIGURE 5.9: Simulated and measured (UV-Vis) extinction spectra for (a) MPT-Mid and (b) MPT-Top photocatalysts. (c) Simulated E-field enhancements in $\log_{10}$ scale at specific wavelengths for the XY ($Z = 0\,\text{nm}$) and ZX-plane ($Y = 0\,\text{nm}$) for all photocatalysts.

5.6 Proposed Charge Carrier Dynamics

The proposed band diagram for MPT-Mid and MPT-Top are shown in Figure 5.10a and b, respectively. Due to the unavailability of experimental data, literature values for electronic material properties were used to construct the band diagrams, as detailed in Table A.1 for TiO_2, MoS_2, Pd, and PdS. Both configurations feature a MoS_2 layer forming a type II heterojunction with TiO_2, which

facilitates charge separation and transfer. In the MPT-Mid structure, Pd nanodisks and MoS_2 create a Schottky junction, enabling plasmon resonance and hot electron generation. For the MPT-Top structure, all three interfaces (TiO_2-PdS, TiO_2-MoS_2, PdS-MoS_2) form type II heterojunctions as well.

Upon light exposure, the following processes occur within the photocatalyst structure: Electrons are raised from the valence into the conduction band, resulting in charge separation. These free-charge carriers can migrate between material layers or participate in redox reactions, if they are not recombined before. The MPT-Mid and MPT-Top photocatalysts benefit from the TiO_2-MoS_2 transition under the AM1.5-filtered light. Electrons and holes from the TiO_2 layer migrate toward the MoS_2 layer due to the type I heterojunction. The MoS_2 layer primarily absorbs in the visible spectrum, where non-recombined charge carriers can contribute to the redox reactions.

In the MPT-Mid photocatalysts, the Pd nanodisks exhibit LSPR due to the Schottky barrier, generating hot electrons that can overcome this barrier and migrate into the MoS_2 layer. The absence of the excited electron in the Pd creates a high-energetic vacancy, a hot hole, in the Pd. On Pd nanodisk surface, these hot charge carriers can then directly contribute to redox reactions.

Instead in the MPT-Top photocatalysts, one type I and two type II heterojunctions are formed due to the semiconducting properties of PdS. In this configuration, only the MoS_2 layer is exposed on the surface, making it the primary site for photocatalytic reactions. The band diagram suggest that holes in the MoS_2 valence band are either from photo-excitations in the MoS_2 layer, or migrated from the TiO_2 valence band. On the other hand, electrons in the MoS_2 conduction band are either from photo-excitations as well, or from migrated from the PdS conduction band. In this configuration, TiO_2 and PdS_2 act as electron and hole drain, respectively.

Experimental results of bacteria deactivation (Figure 5.8b) reveal a performance hierarchy: MPT-Mid-3L > MPT-Top-3L > MPT-Top-17L > MPT-Mid-17L. Thinner MoS_2 layers (3L) outperform thicker ones (17L) due to reduced recombination rates. The primary mechanism in MPT-Top is plasmon resonance in the Pd nanodisk, while MPT-Mid relies on the type II heterojunctions.

For 3-layer MoS_2, MPT-Mid-3L outperforms MPT-Top-3L as charge carriers from both Pd nanodisks and MoS_2 layers reach the surface and participate in redox reactions. For the 17-layer MoS_2, plasmonic resonance is significantly dampened in MPT-Mid-17L. In MPT-Top photocatalysts, redox reactions only occur at the MoS_2 surface. The heterojunctions supports the charge separation between all material layers. The thinner MoS_2 layer in MPT-Top-3L allows charge carrier

to reach the surface with higher probability due to its thinner MoS_2 layer.

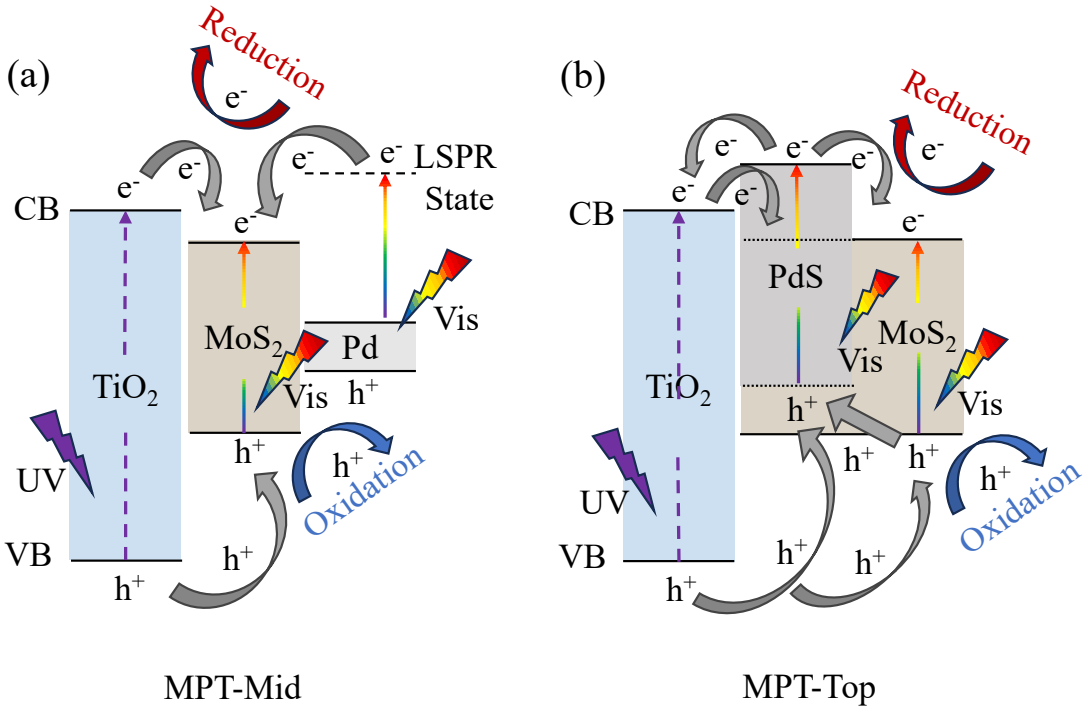


FIGURE 5.10: Proposed bandgap diagram for both MPT photocatalysts. The electrons (e^-) and holes (h^+) tend to migrate toward the material layers indicated by the arrows. (a) In MPT-Mid, the TiO_2-MoS_2 interface forms a type I heterojunction, while the MoS_2-Pd forms a Schottky barrier. Redox reactions only occur on the MoS_2 and Pd surface, to where all charge carriers in MPT-Mid tend to move to. (b) In MPT-Top, the TiO_2-MoS_2 interface is also a type I heterojunction, while the TiO_2-PdS and PdS-MoS_2 interfaces are both type II heterojunctions. Redox reactions only occur at the MoS_2 surface, to where all charge carriers in MPT-Top tend to move to.

5.7 Conclusion

The MPT photocatalysts sheets have demonstrated potential for photocatalytic water inactivation. This study has illuminated the significant impact of various configurations on the performance of the MPT photocatalyst sheets, providing insights into optimizing its inactivation efficiency by few-layer MoS_2. The modification by MoS_2 introduces type II heterojunctions into the photocatalyst. Moreover, the Pd nanodisk structure in MPT-Top sulfurized into PdS, which removes the Schottky barrier for the MPT-Top photocatalyst. By three type II heterojunctions, it still performs as the second best photocatalyst in this study.

These results present a water purification by using a periodic 2D-material-coupled plasmonic-based metamaterial photocatalyst sheet. Utilizing a low-powered AM1.5 filtered solar simulator with 10 mW/cm^2 power density, the most effective photocatalyst sheet (MPT-Mid-3L) achieved an *E. coli* bacteria inactivation rate of 99.92 % within 240 min of illumination. In conclusion, the MPT photocatalyst sheets show high functionality for ROS generation and water purification.

6 Summary and Outlook

Photocatalysis has emerged as a promising approach for harnessing solar energy to drive chemical reactions, offering a direct pathway for converting light into chemical energy. This process has the potential to both break down unwanted molecules and synthesize valuable chemical products. In the context of climate change, photocatalysis presents a sustainable alternative to fossil fuels through solar fuel generation [10]. By employing photocatalytic water splitting [6] or CO_2 reduction [52], it can produce solar fuels such as H_2, CH_4, or methanol.

Access for clean water resources is another global pressing issue [237, 238]. Photocatalysis can offer a sustainable solution to this problem through the generation of reactive oxygen species (ROS) [61], which can effectively eliminate target contaminants. By tailoring the photocatalyst design, researchers can optimize this process for specific pollutants, thereby contributing to improved water quality and public health.

Despite its immense potential for sustainable applications, photocatalysis remain largely confined in the academic realm. Recent developments have focused bringing photocatalysis closer toward large-scale implementation. One promising approach is the fabrication of photocatalytic sheets that can be modularly mounted, offering both effectiveness and durability. Nishiyama et al. [14] have made significant advances in this direction, successfully demonstrating a 100 m^2 large-area photocatalyst sheet setup for H_2 generation from water splitting. This achievement marks a crucial step toward the practical application of photocatalysis at an industrial scale.

6.1 Summary

This thesis has explored a plasmonic nanodisk metamaterial photocatalyst sheet design with scalability potential, demonstrating its effectiveness for photocatalytic applications. The base metamaterial photocatalyst sheet design was defined in Chapter 3 and tested in photocatalytic water splitting and CO_2 reduction, serving as a proof-of-principle. The design consists of periodically-arranged circular-shaped plasmonic nanodisk array in a rectangular pattern patterned on

a photocatalyst material thin film. This thesis focused on TiO_2 as photocatalyst material. Several plasmonic metals (Ag, Au, Pt, Pd) were studied to find out which of them possesses the best photocatalytic reactivity. All metals showed high mass-normalized solar fuel yield rates, among which Pt and Pd nanodisks exhibiting the highest H_2 and CH_4 generation, respectively. The comparison of the different four metals revealed their individual benefits: While Ag and Au are well-known as strong plasmonic materials, Pt and Pd are chemically more suitable in terms of adsorption properties toward H_2O and CO_2 molecules. In conclusion, the adsorption properties dominate in terms of reactivity, but the plasmonic properties still have a significant contribution.

In Chapter 4, the base metamaterial photocatalyst design was adjusted geometrically as a periodically-arranged elliptical-shaped nanodisk array in a hexagonal pattern. The study was focused on Pd nanodisks and on their ability for photocatalytic water splitting and CO_2 reduction, as Pd has shown the best outcomes for CH_4 generation before. Furthermore, the metamaterial was modified with graphene (Gr) in two variations: wet-transferred, resulting in a suspended Gr layer on-top of the Pd nanodisk, and grown by plasma-enhanced chemical vapor deposition (PECVD), resulting as a Gr coating on the entire Pd/TiO_2 metasurface. The results have shown that the suspended Gr layer significantly enhances the reactivity, while the PECVD-grown Gr still provides a functional structure with small changes in the selectivity. This study demonstrates the advantages of 2D materials in combination with a metasurface.

Finally, in Chapter 5 the Pd/TiO_2 metamaterial photocatalyst design was modified with MoS_2 for *E. Coli* bacteria inactivation. Two photocatalyst configurations were tested: In the first variant, MoS_2 was grown between the Pd nanodisk and TiO_2 thin film layer. In the second variant, MoS_2 was grown on-top of the entire Pd/TiO_2 metasurface. MoS_2 is well-known as a semiconducting 2D material with a tunable bandgap and strong photocatalytic properties. 3- and 16-layered MoS_2 were studied for this work to compare 2D- and bulk-like properties of MoS_2. The photocatalytic bacteria inactivation experiment revealed that the modification of the photocatalyst with MoS_2 improves the inactivation efficiency, with all MoS_2 modifications leading to a better reactivity. The best results were achieved with 3-layered MoS_2 grown between the Pd nanodisk and TiO_2 thin film layer.

This work presents a functioning photocatalyst design with high mass-normalized gas rates for solar fuel generation. For this reason, three patents were filed [VII, VIII, IX] (see List of Publication) to secure the intellectual property (IP) for further research and development work.

6.2 Outlook

The photocatalyst sheets in this thesis showed photocatalytic functionality with an overall high efficiency for their respective application. However, they require further optimization in order to be used for large-scale implementation.

In general, the key to high efficiency is a well-designed photocatalyst sheet in terms of material selection and geometry. This will require further exploration and understanding of different material systems, charge carrier dynamics, and their catalytic interaction. In the literature, TiO_2 and Au have been used mostly in plasmonic metamaterial photocatalyst sheets [108, **?**, 109] due to the photocatalytic and plasmonic properties of TiO_2 and Au, respectively [239]. A future work may replace the semiconductor layer to graphitic carbon nitride (g-C_3N_4) [122], or strontium titanate ($SrTiO_3$) [123]. Hence, there are many materials that can be tested in order to find the most promising material system.

In order to achieve industrial adaptation, a large-scale pilot setup must be experimentally tested under outside conditions. Goto et al. [41] demonstrated the first $(1 \times 1)\mathrm{m}^2$ large-area photocatalyst sheet based on $RhCrO_X$-loaded Al-doped $SrTiO_3$ films. After further development, Nishiyama et al. [14] extended these results to a $100\,\mathrm{m}^2$ panel farm based on the same photocatalyst material, demonstrating the large-area implementation and long-term stability in outdoor environments. In another work, Zhou et al. [54] showed solar-to-hydrogen (STH) efficiency of more than 9 , which is considered ground-breaking and economically feasible [3]. This was also achieved by photocatalyst sheet deposited by a complex material system, which are specifically $Rh/Cr_2O/Co_3O_4$-loaded InGaN/GaN nanowires.

These complex material systems can potentially be integrated as metamaterials, which would allow periodically-arranged structures to increase light-trapping and hence its utilization. Torras et al. [**?**] showed the possibility by directly pattern a Au/TiO_2-particle mixture to quickly fabricate highly efficient metamaterial photocatalyst sheets. In addition, this allows high aspect ratio design, increasing the overall surface area. The fabrication of their metasurface only requires a few steps compared to the nanodisk metamaterial photocatalyst design of this thesis. Overall, a direct patterning of particles can reduce processing time and failure risk. Moreover, sophisticated nanostructures, such as core-shell [33, 34] or yolk-shell particles [35, 36], can be considered to be integrated by this method.

For a large-area adaptation, the metamaterial photocatalyst design must be compatible with large-area deposition or patterning processes. Several reports have already demonstrated this by spray-coating [41], printing [42], NIL [**?**, 108],

and LIL [109]. However, there are no reports yet with photocatalyst sheets fabricated by roller-based NIL [240], which would be the choice for sheets with up to kilometer-ranged lengths. This is probably due to the lack of availability and access for this technology among photocatalysis research groups. Lithography-based technologies are crucial as they enable controlled nanostructure patterning over large areas for optimized light utilization and co-catalyst deposition. Finally, they offer immediate large-area scalability due to their technology readiness level and availability, making them highly promising.

The initial efficiency of a photocatalyst is crucial, but the contribution by an optimized photocatalytic reactor is often neglected [58, 241]. In a large-scale adaptation, a photocatalytic reactor is ideally operated under natural sunlight under outdoor environmental conditions. However, there are only a few reports addressing this setting [14, 15, 13, 54]. Moreover, most reports work with fixed process parameters without addressing the possibility of product gas yield increase by e.g. gas flow [56], gas ratio, or reactor temperature [39]. There is also light management [59] that should be considered more often, for instance by solar concentrators [54, 242]. For practical purposes, the gas yield can be increased here through additional thermal energy, leading to a higher reactivity [243].

Alternative photocatalytic processes are also worthwhile to be considered. In fact, photocatalytic water splitting and CO_2 reduction have to overcome the relatively high energy barrier due to their high Gibbs free energy. Alternative processes, such as ammonia [9] or alcohol splitting [244], are worthwhile to be considered as a practical application as well. In the recent years, Lou et al. [245] have demonstrated H_2 generation by H_2S, which is a toxic and unwanted gas byproduct. In principle, any combustion-based chemical process is sustainably reasonable to be developed as a combustion-free photocatalytic process. All these efforts can lead to the reduction of overall CO_2 emission.

In summary, the literature has actually provide many insights how large-scale adaptation of photocatalysis can potentially be achieved. A future experiment for metamaterial photocatalyst sheets can explore alternative materials (e.g. $SrTiO_3$, g-C_3N_4). Finding an efficient fabrication process [**?**] that is compatible with roller-based NIL [240] would be one approach, to significantly reduce further development efforts toward large-scale fabrication. Then, the setup must be qualified under outdoor environments, eventually even in different countries under altering weather conditions [14]. Moreover, reactor process optimization should be taken more into consideration, e.g. by tuning the feed stock properties or implementing a solar concentrator [59]. While the academic realm mostly focuses on photocatalytic water splitting, CO_2 reduction, and water purification, there

are more chemical reactions that can be explored. A first use case can involve a chemical reaction with a significant lower reaction barrier, which could be ammonia [9] or alcohol splitting [244].

In the end, photocatalysis requires one concept that can be developed toward large-scale adaptation with economic feasibility [51, 246, 247]. The obtained findings and know-how can accelerate the development of diverse reactions, thereby broadening the scope of photocatalytic applications. By focusing research and development in these directions, the scientific, engineering and entrepreneurial community can make substantial steps in advancing the practical application of photocatalyst sheets, leading the field toward sustainable and scalable solutions as a new green technology [3, 4].

A Material Data

Material	E_{VB} (eV)	E_{CB} (eV)	E_G (eV)	χ (eV)	ϕ (eV)
TiO_2	-7.25	-4.06	3.25	4.45	5.1
MoS_2 (2D)	-6.13	-4.55	1.58	-	-
MoS_2 (bulk)	-5.9	-4.5	1.4	-	-
PdS	-5.65	-3.85	1.8	-	3.59
Ag	-	-	-	-	4.26–4.74
Au	-	-	-	-	5.1–5.47
Pt	-	-	-	-	5.22–5.60
Pd	-	-	-	-	5.12–5.93

TABLE A.1: Relevant electronic properties for band diagram proposal. For this thesis, the relevant materials are TiO_2 [204, 248, 249], MoS_2 (2D) [250], MoS_2 (bulk) [251], PdS [252], Ag [253], Au [253], Pt [253], and Pd [253].

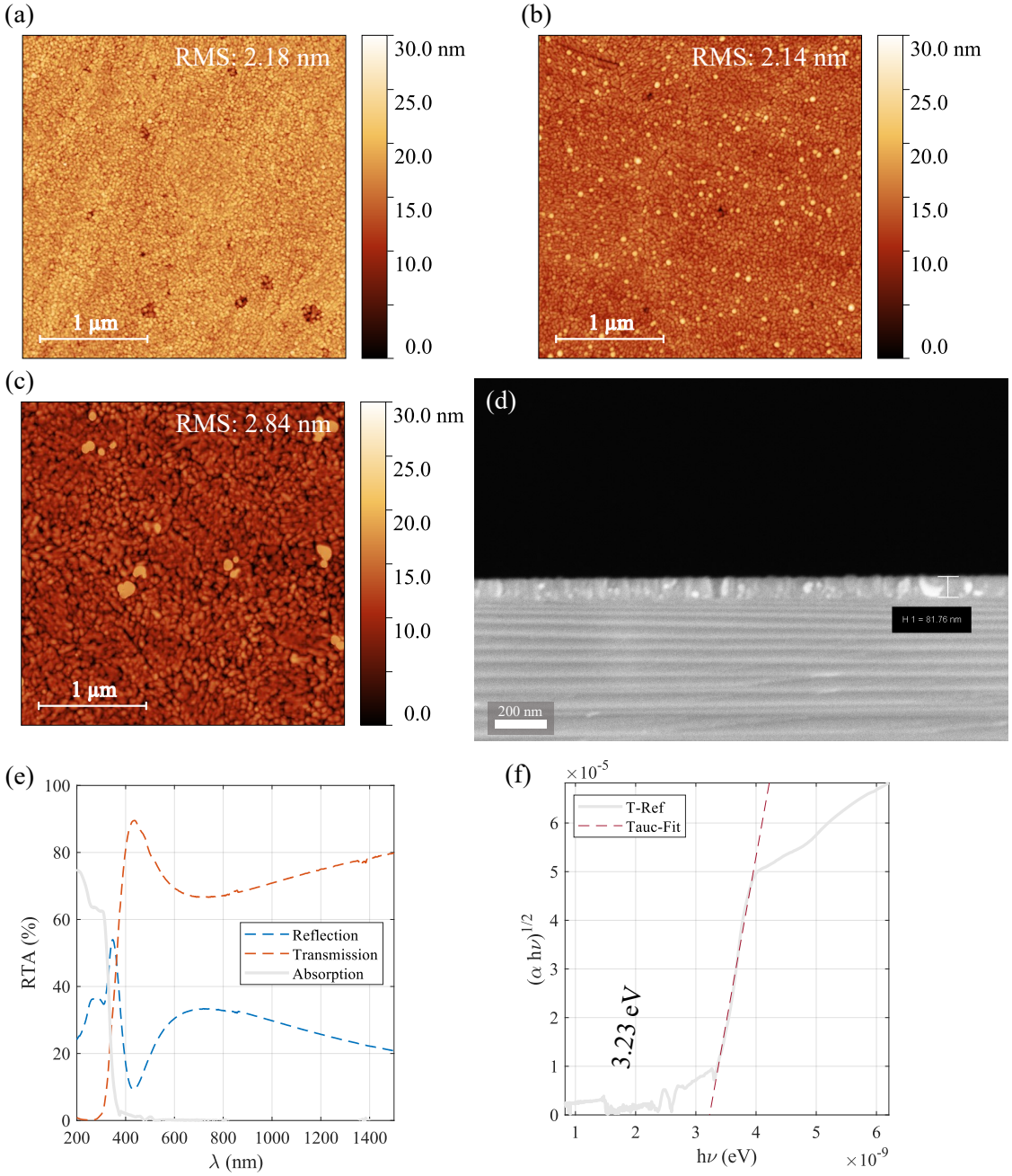


FIGURE A.1: TiO_2 surface topography (a) after magnetron sputtering and before the annealing process, (b) after 650 °C annealing for 60 min, and (c) after 800 °C annealing for 30 min. (d) Cross-sectional SEM image of the magnetron sputtering deposited 80 nm TiO_2 thin film. (e) Reflection and transmission measurement, and extinction evaluation by UV-Vis spectroscopy of anatase-phased TiO_2 layer. (f) Tauc plot analysis with evaluated bandgap at 3.23 eV.

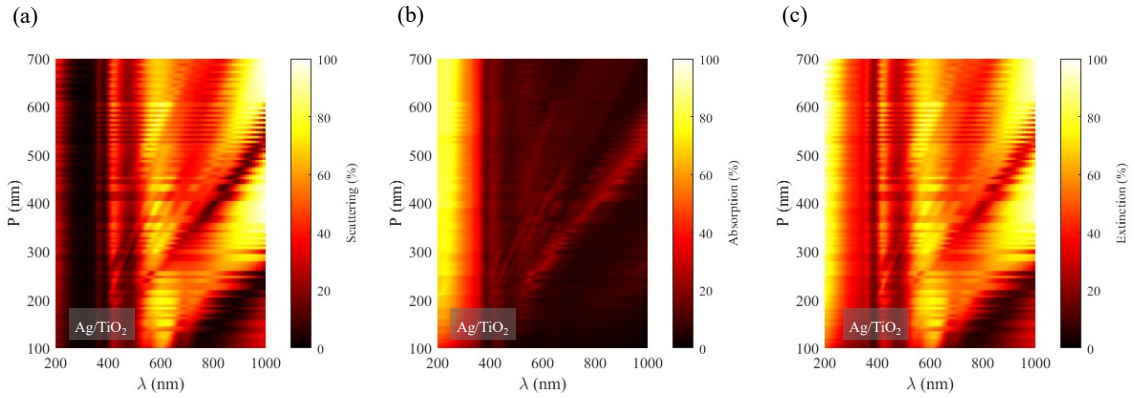


FIGURE A.2: Periodicity-dependent FDTD simulation study for an Ag nanodisk array on a TiO_2 thin film: (a) scattering, (b) absorption, and (c) extinction map. The other geometrical parameters are fixed with $D_{ND} = P/2$, $H_{ND} = 30\,nm$, and $H_{SC} = 250\,nm$.

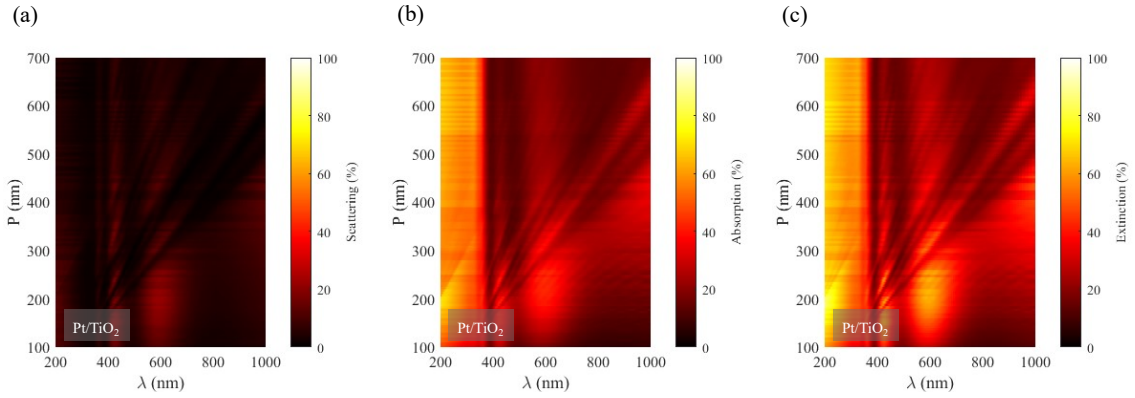


FIGURE A.3: Periodicity-dependent FDTD simulation study for a Pt nanodisk array on a TiO_2 thin film: (a) scattering, (b) absorption, and (c) extinction map. The other geometrical parameters are fixed with $D_{ND} = P/2$, $H_{ND} = 30\,nm$, and $H_{SC} = 250\,nm$.

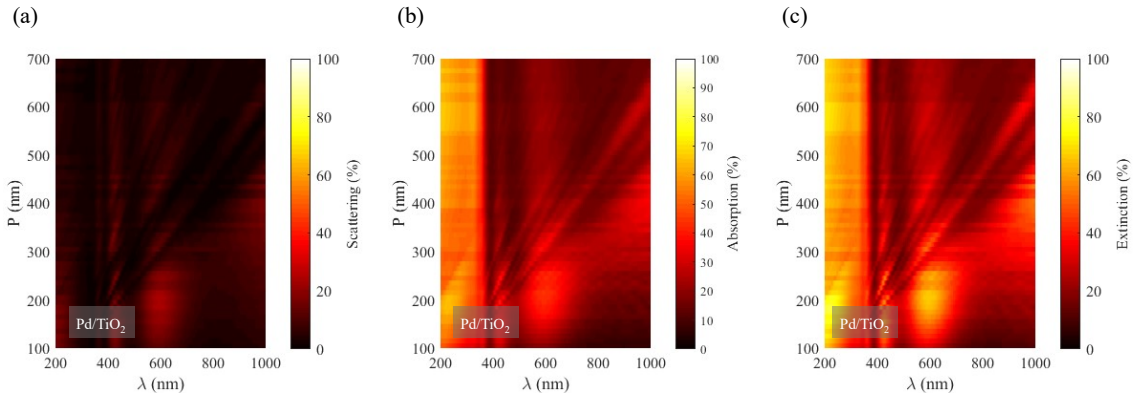


FIGURE A.4: Periodicity-dependent FDTD simulation study for a Pd nanodisk array on a TiO_2 thin film: (a) scattering, (b) absorption, and (c) extinction map. The other geometrical parameters are fixed with $D_{ND} = P/2$, $H_{ND} = 30\,nm$, and $H_{SC} = 250\,nm$.

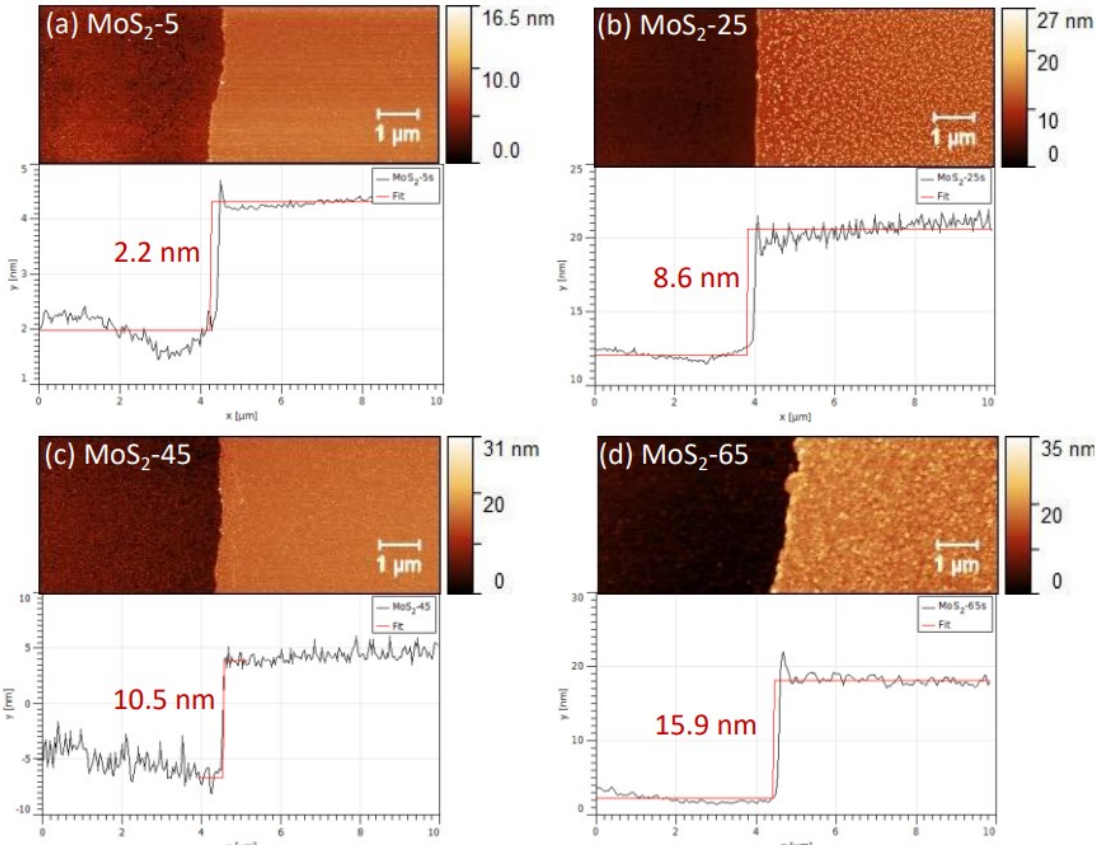


FIGURE A.5: Thickness measurement of few-layer CVD-sulfurization grown MoS_2 layers on a glass substrate: (a) 5 s, (b) 25 s, (c) 45 s, and (d) 65 s magnetron sputtering of Mo.

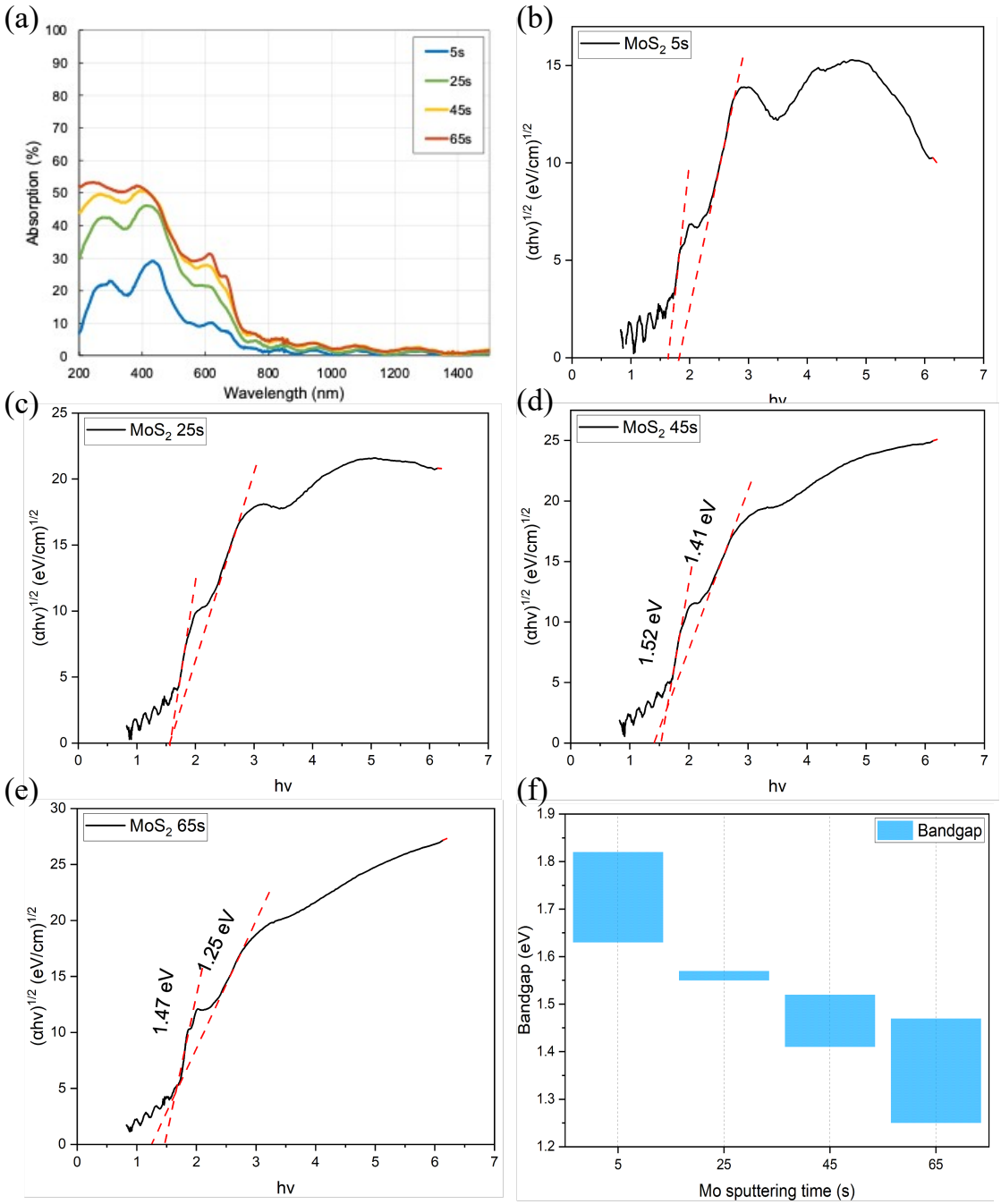


FIGURE A.6: (a) Evaluated absorption spectra of the MoS_2 layers by UV-Vis spectroscopy. Tauc plot analysis of MoS_2 by (b) 5 s, (c) 25 s, (d) 45 s, and (e) 65 s sputtered Mo seed layer. (f) Evaluated Tauc plot for the few-layer MoS_2 layers.

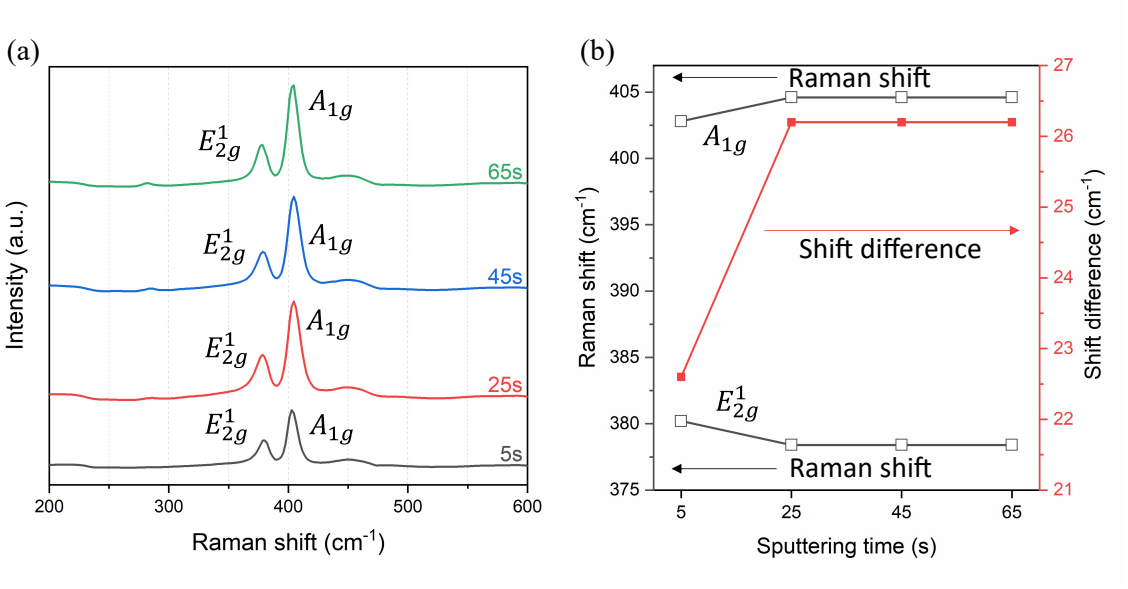


FIGURE A.7: (a) Raman spectroscopy measurement of MoS_2 layers grown on a glass substrate. (b) Analyzed Raman shift (left y-axis) and shift difference (right y-axis).

B Raw Data

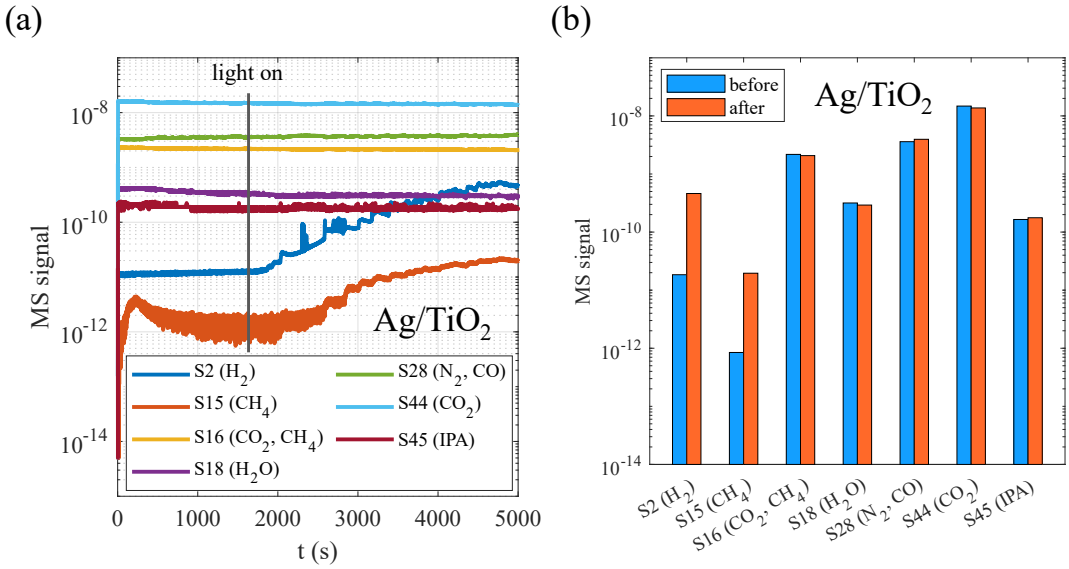


FIGURE B.1: (a) Real-time mass spectrometer signal raw data and (b) bar plot forAg/TiO_2.

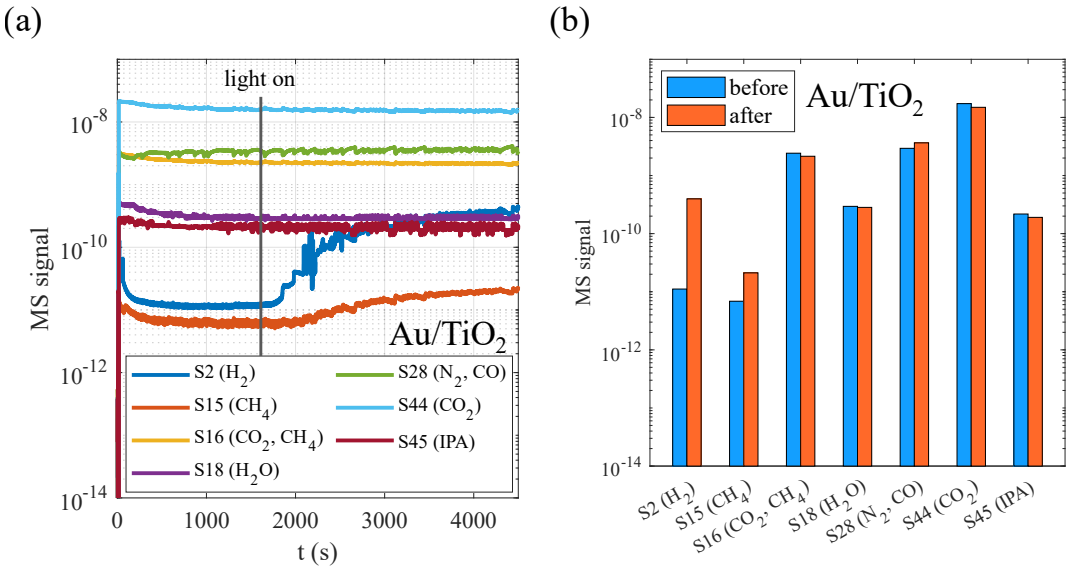


FIGURE B.2: (a) Real-time mass spectrometer signal raw data and (b) bar plot forAu/TiO_2.

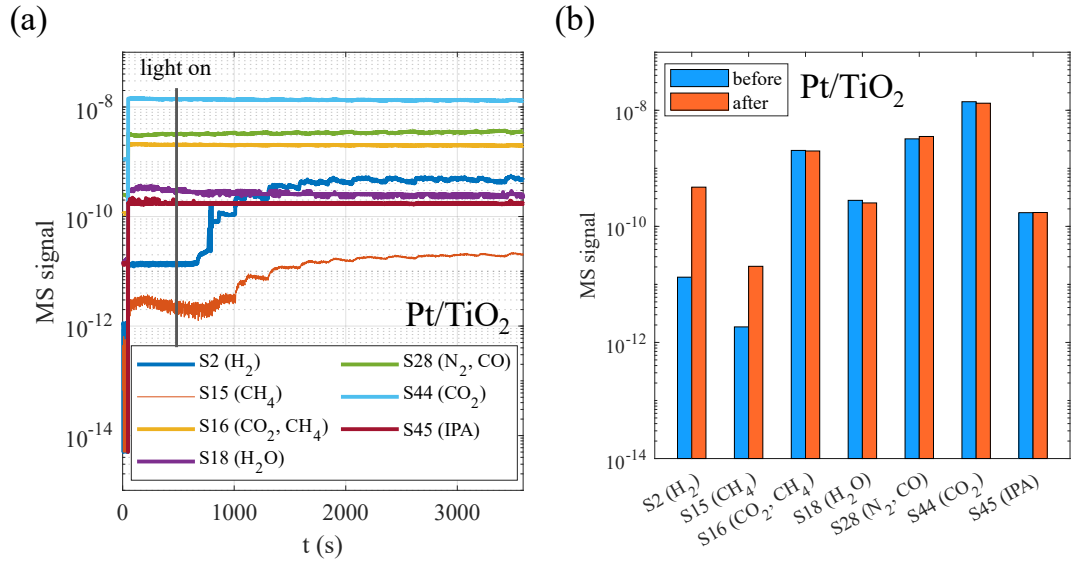


FIGURE B.3: (a) Real-time mass spectrometer signal raw data and (b) bar plot forPt/TiO_2.

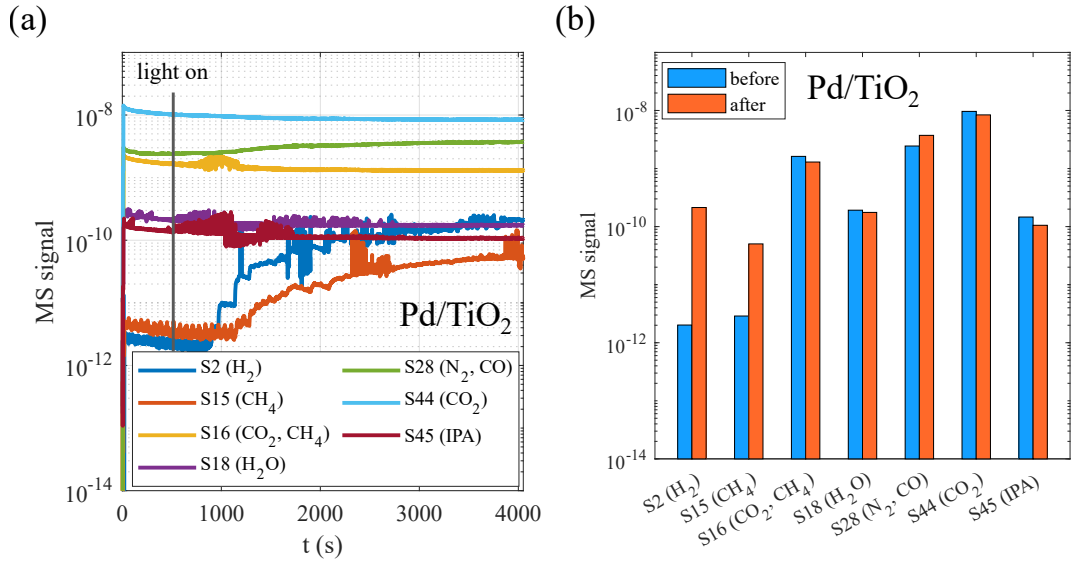


FIGURE B.4: (a) Real-time mass spectrometer signal raw data and (b) bar plot forPd/TiO_2.

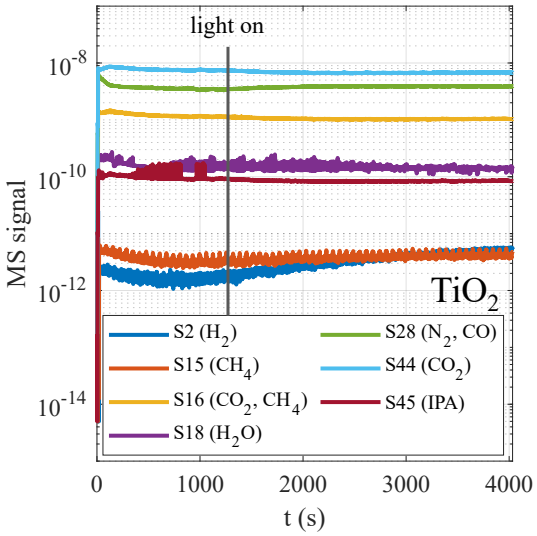


FIGURE B.5: Real-time mass spectrometer signal raw data with sputtered TiO_2 thin film layer only.

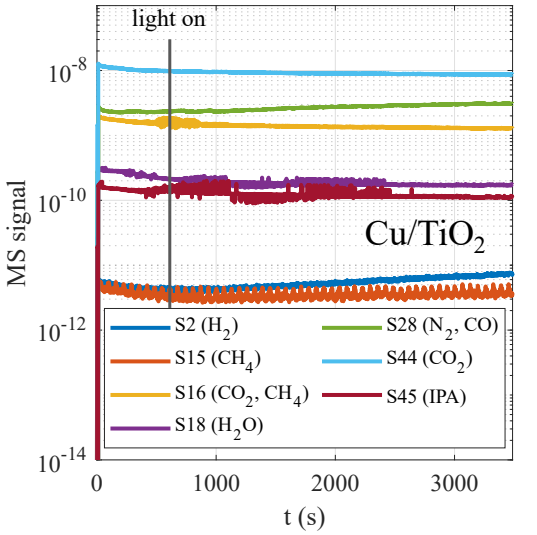


FIGURE B.6: Real-time mass spectrometer signal raw data with Cu nanodisk on TiO_2 thin film layer only.

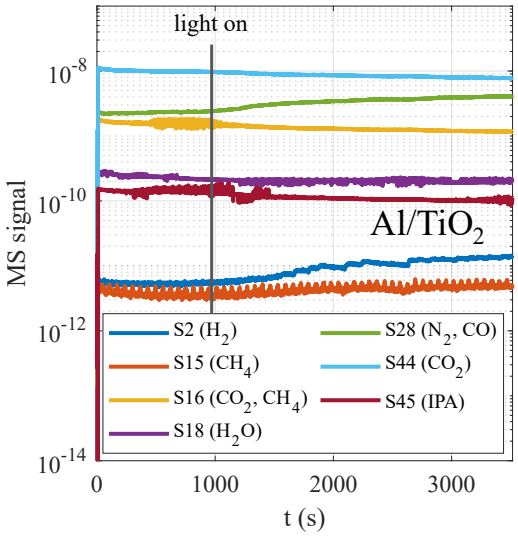


FIGURE B.7: Real-time mass spectrometer signal raw data with Al nanodisk on TiO_2 thin film layer only.

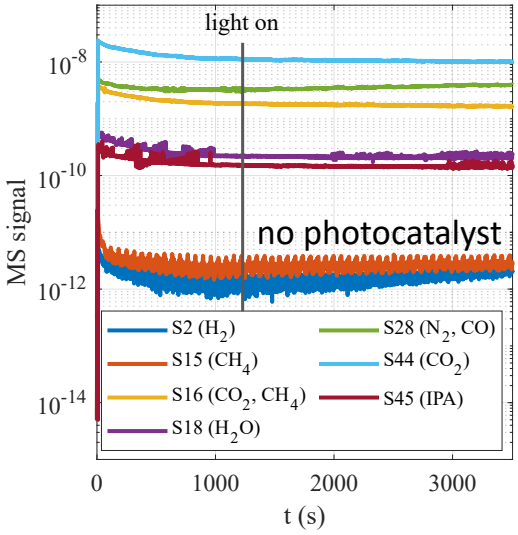


FIGURE B.8: Real-time mass spectrometer signal raw data without photocatalyst

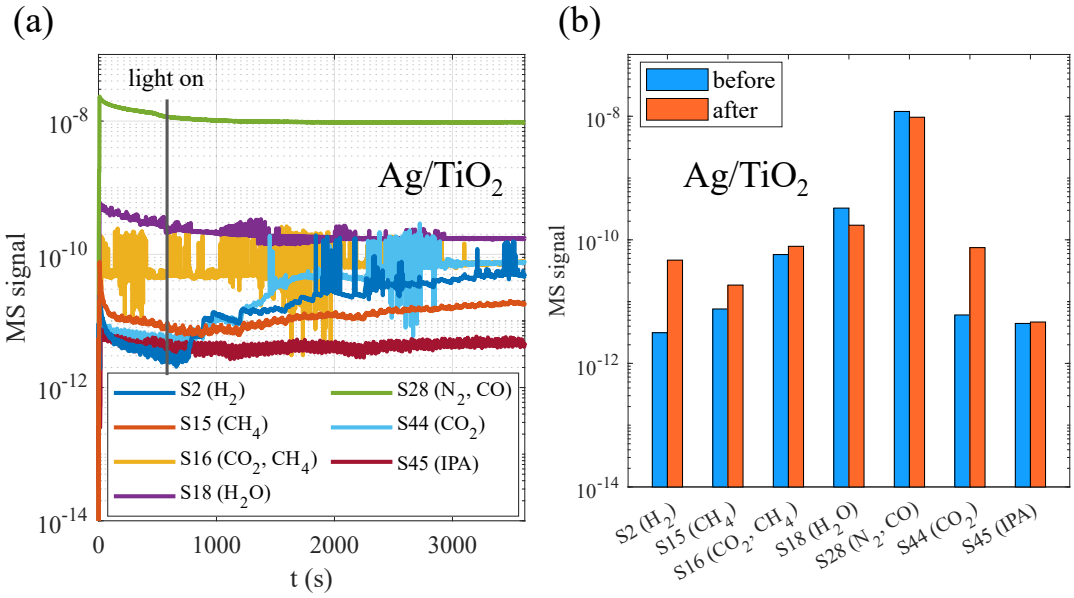


FIGURE B.9: Real-time mass spectrometer signal raw data for Ag/TiO_2 during the control experiment to test N_2 as carrier gas instead of CO_2.

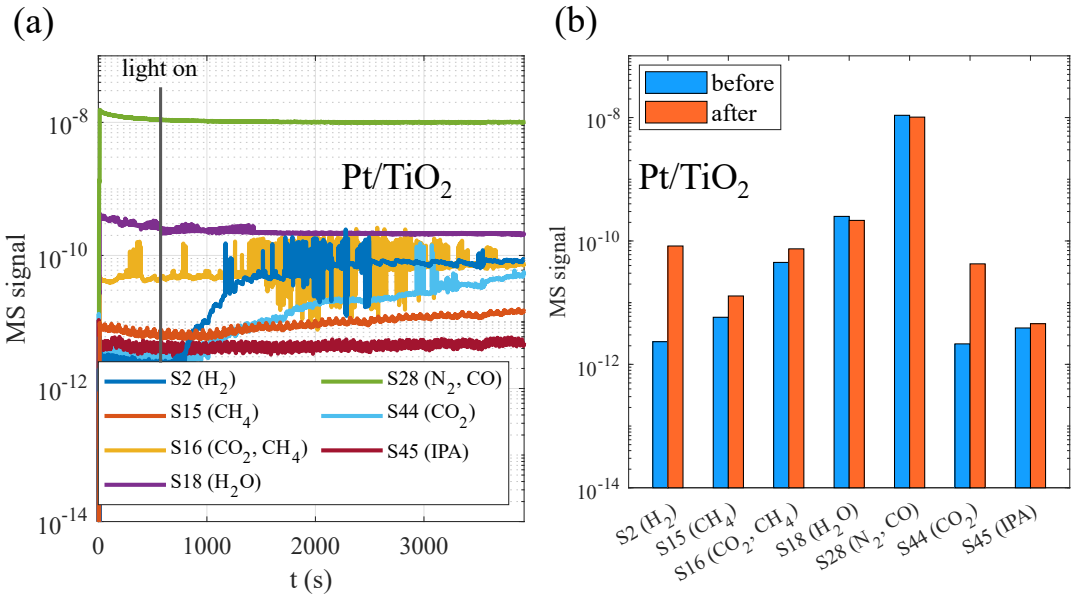


FIGURE B.10: Real-time mass spectrometer signal raw data for Pt/TiO_2 during the control experiment to test N_2 as carrier gas instead of CO_2.

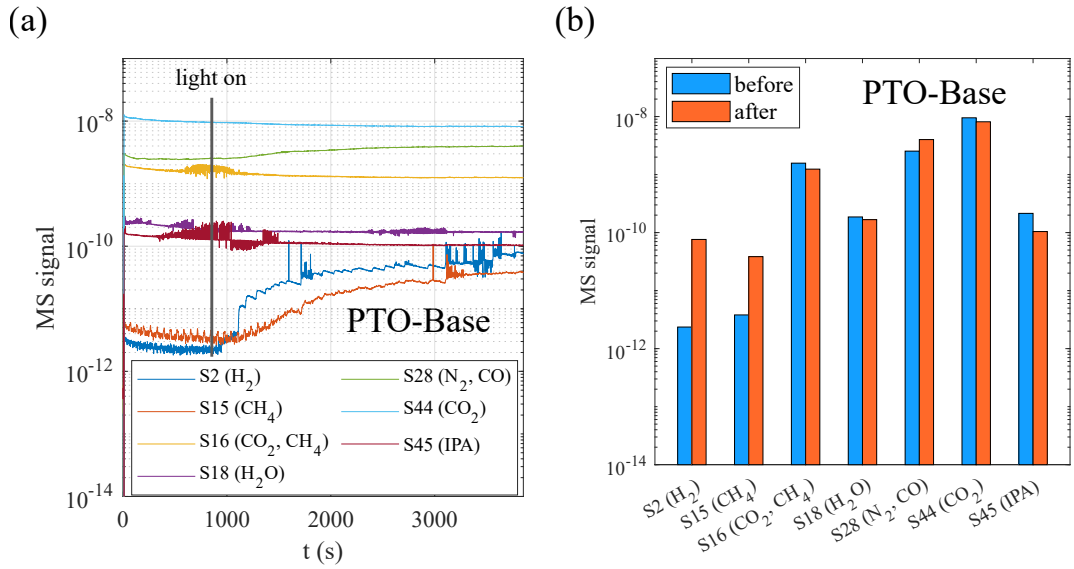


FIGURE B.11: (a) Real-time mass spectrometer signal raw data and (b) bar plot for the PTO-Base.

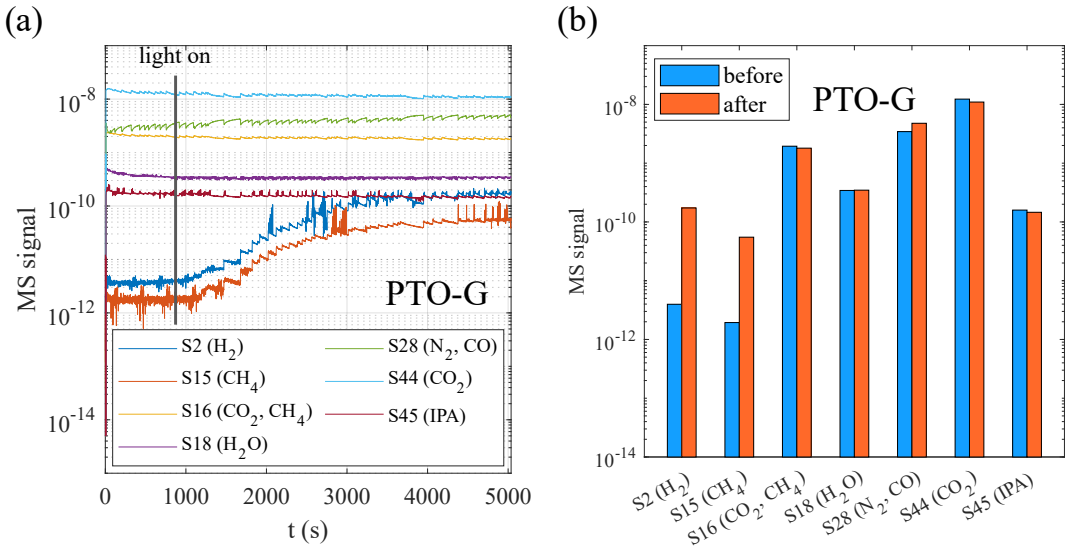


FIGURE B.12: (a) Real-time mass spectrometer signal raw data and (b) bar plot for the PTO-GrTransfer.

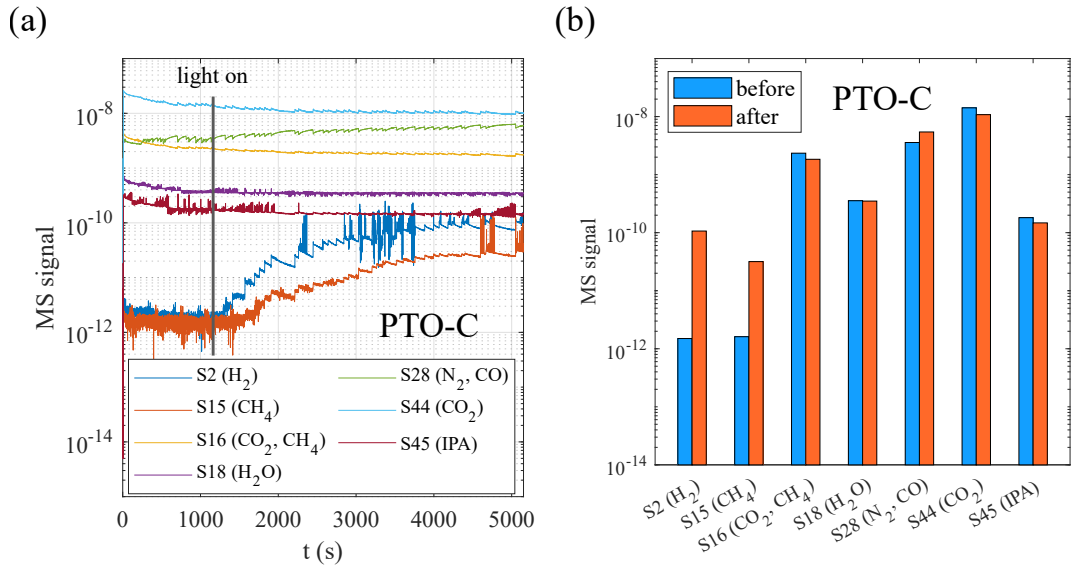


FIGURE B.13: (a) Real-time mass spectrometer signal raw data and (b) bar plot for the PTO-GrPECVD.

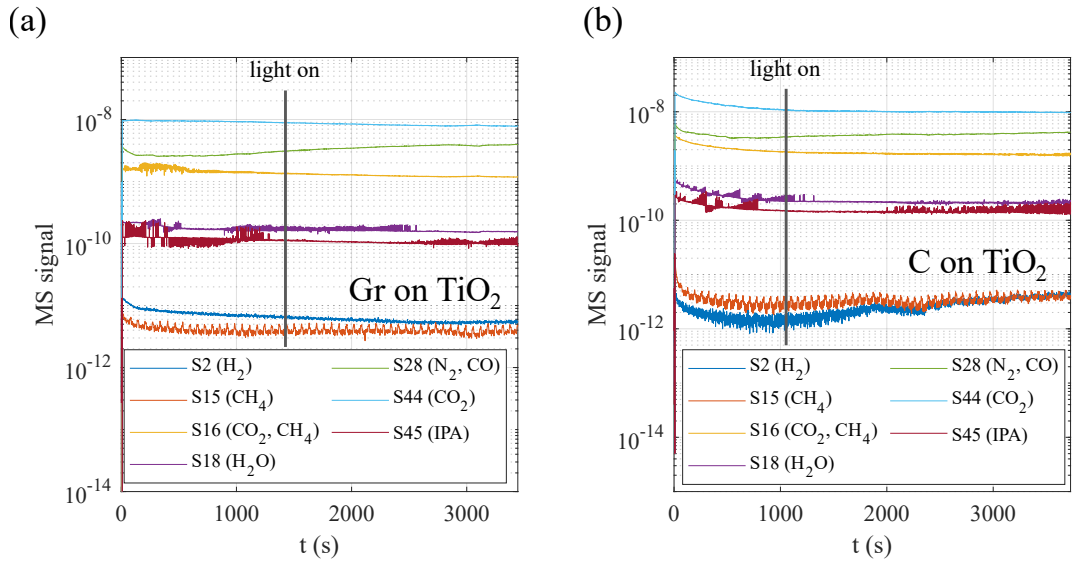


FIGURE B.14: Real-time mass spectrometer signal raw data of (a) a Gr layer and (b) carbon black layer on TiO_2 thin film showing no photocatalytic reaction.

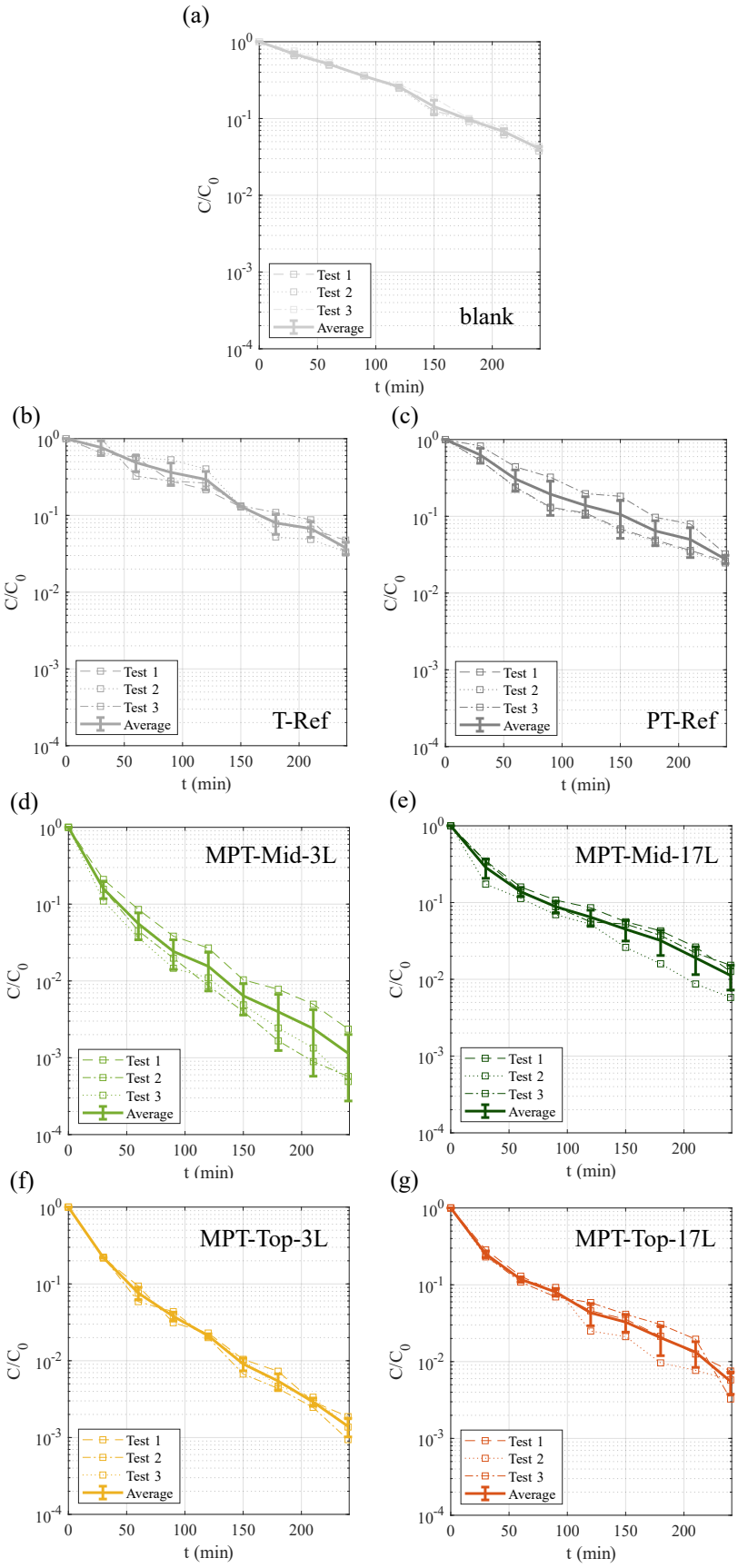


FIGURE B.15: Multiple measurement runs and average curve for the photocatalytic E. Coli bacteria degradation measurement for (a) blank, (b) T-Ref, (c) PT-Ref, (d) MPT-Mid-3L, (e) MPT-Mid-16L, (f) MPT-Top-3L, and (g) MPT-Top-16L.

Bibliography

[1] X. Meng, L. Liu, S. Ouyang, H. Xu, D. Wang, N. Zhao, and J. Ye, "Nanometals for Solar-to-Chemical Energy Conversion: From Semiconductor-Based Photocatalysis to Plasmon-Mediated Photocatalysis and Photo-Thermocatalysis," *Advanced Materials*, vol. 28, pp. 6781–6803, Aug. 2016.

[2] R. Kumar, M. Chaudhary, A. Al-Ahmed, S. Bhattacharyya, S. Von Gratowski, J. Iqbal, and Inamuddin, "Photo-to-chemical energy transformation: Pioneering photocatalysts, surface and interface engineering," *Materials Research Bulletin*, vol. 180, p. 113046, Dec. 2024.

[3] D. Gunawan, J. Zhang, Q. Li, C. Y. Toe, J. Scott, M. Antonietti, J. Guo, and R. Amal, "Materials Advances in Photocatalytic Solar Hydrogen Production: Integrating Systems and Economics for a Sustainable Future," *Advanced Materials*, p. 2404618, June 2024.

[4] P. Mani, S. Shenoy, P. J. J. Sagayaraj, N. Agamendran, S. Son, N. Bernaurdshaw, H.-i. Kim, and K. Sekar, "Scaling up of photocatalytic systems for large-scale hydrogen generation," *Applied Physics Reviews*, vol. 12, p. 011303, Mar. 2025.

[5] A. Fujishima and K. Honda, "Electrochemical Photolysis of Water at a Semiconductor Electrode," *Nature*, vol. 238, pp. 37–38, July 1972.

[6] S. Nishioka, F. E. Osterloh, X. Wang, T. E. Mallouk, and K. Maeda, "Photocatalytic water splitting," *Nature Reviews Methods Primers*, vol. 3, p. 42, June 2023.

[7] M. A. Al-Nuaim, A. A. Alwasiti, and Z. Y. Shnain, "The photocatalytic process in the treatment of polluted water," *Chemical Papers*, vol. 77, pp. 677–701, Feb. 2023.

[8] L. Wang, W. Wu, K. Liang, and X. Yu, "Advanced Strategies for Improving the Photocatalytic Nitrogen Fixation Performance: A Short Review," *Energy & Fuels*, vol. 36, pp. 11278–11291, Oct. 2022.

[9] S. Zhang, Z. He, X. Li, J. Zhang, Q. Zang, and S. Wang, "Building heterogeneous nanostructures for photocatalytic ammonia decomposition," *Nanoscale Advances*, vol. 2, no. 9, pp. 3610–3623, 2020.

[10] G. Segev, J. Kibsgaard, C. Hahn, Z. J. Xu, W.-H. S. Cheng, T. G. Deutsch, C. Xiang, J. Z. Zhang, L. Hammarström, D. G. Nocera, A. Z. Weber, P. Agbo, T. Hisatomi, F. E. Osterloh, K. Domen, F. F. Abdi, S. Haussener, D. J. Miller, S. Ardo, P. C. McIntyre, T. Hannappel, S. Hu, H. Atwater, J. M. Gregoire, M. Z. Ertem, I. D. Sharp, K.-S. Choi, J. S. Lee, O. Ishitani, J. W. Ager, R. R. Prabhakar, A. T. Bell, S. W. Boettcher, K. Vincent, K. Takanabe, V. Artero, R. Napier, B. R. Cuenya, M. T. M. Koper, R. Van De Krol, and F. Houle, "The 2022 solar fuels roadmap," *Journal of Physics D: Applied Physics*, vol. 55, p. 323003, Aug. 2022.

[11] G. Centi and S. Perathoner, "Towards Solar Fuels from Water and CO_2," *ChemSusChem*, vol. 3, pp. 195–208, Feb. 2010.

[12] S. Styring, "Artificial photosynthesis for solar fuels," *Faraday Discuss.*, vol. 155, pp. 357–376, 2012.

[13] F. Cao, Q. Wei, H. Liu, N. Lu, L. Zhao, and L. Guo, "Development of the direct solar photocatalytic water splitting system for hydrogen production in Northwest China: Design and evaluation of photoreactor," *Renewable Energy*, vol. 121, pp. 153–163, June 2018.

[14] H. Nishiyama, T. Yamada, M. Nakabayashi, Y. Maehara, M. Yamaguchi, Y. Kuromiya, Y. Nagatsuma, H. Tokudome, S. Akiyama, T. Watanabe, R. Narushima, S. Okunaka, N. Shibata, T. Takata, T. Hisatomi, and K. Domen, "Photocatalytic solar hydrogen production from water on a 100-m2 scale," *Nature*, vol. 598, pp. 304–307, Oct. 2021.

[15] T. Yamada, H. Nishiyama, H. Akatsuka, S. Nishimae, Y. Ishii, T. Hisatomi, and K. Domen, "Production of Methane by Sunlight-Driven Photocatalytic Water Splitting and Carbon Dioxide Methanation as a Means of Artificial Photosynthesis," *ACS Engineering Au*, vol. 3, pp. 352–363, Oct. 2023.

[16] B. Samanta, Á. Morales-García, F. Illas, N. Goga, J. A. Anta, S. Calero, A. Bieberle-Hütter, F. Libisch, A. B. Muñoz-García, M. Pavone, and M. Caspary Toroker, "Challenges of modeling nanostructured materials for photocatalytic water splitting," *Chemical Society Reviews*, vol. 51, no. 9, pp. 3794–3818, 2022.

[17] J. Wu, W. Zheng, and Y. Chen, "Definition of photocatalysis: Current understanding and perspectives," *Current Opinion in Green and Sustainable Chemistry*, vol. 33, p. 100580, Feb. 2022.

[18] M. A. Nazir, T. Najam, M. Altaf, K. Ahmad, I. Hossain, M. A. Assiri, M. S. Javed, A. U. Rehman, and S. S. A. Shah, "Tuning the photocatalytic hydrogen production via co-catalyst engineering," *Journal of Alloys and Compounds*, vol. 990, p. 174378, June 2024.

[19] S. Ezendam, M. Herran, L. Nan, C. Gruber, Y. Kang, F. Gröbmeyer, R. Lin, J. Gargiulo, A. Sousa-Castillo, and E. Cortés, "Hybrid Plasmonic Nanomaterials for Hydrogen Generation and Carbon Dioxide Reduction," *ACS Energy Letters*, vol. 7, pp. 778–815, Feb. 2022.

[20] C.-Y. Wang, H.-E. Chang, C.-Y. Wang, T. Kurioka, C.-Y. Chen, T.-F. Mark Chang, M. Sone, and Y.-J. Hsu, "Manipulation of interfacial charge dynamics for metal–organic frameworks toward advanced photocatalytic applications," *Nanoscale Advances*, vol. 6, no. 4, pp. 1039–1058, 2024.

[21] H. Huang, B. Pradhan, J. Hofkens, M. B. J. Roeffaers, and J. A. Steele, "Solar-Driven Metal Halide Perovskite Photocatalysis: Design, Stability, and Performance," *ACS Energy Letters*, vol. 5, pp. 1107–1123, Apr. 2020.

[22] Y. Wang, Z. Ding, N. Arif, W.-C. Jiang, and Y.-J. Zeng, "2D material based heterostructures for solar light driven photocatalytic H_2 production," *Materials Advances*, vol. 3, no. 8, pp. 3389–3417, 2022.

[23] R. Verma, R. Belgamwar, and V. Polshettiwar, "Plasmonic Photocatalysis for CO_2 Conversion to Chemicals and Fuels," *ACS Materials Letters*, vol. 3, pp. 574–598, May 2021.

[24] G. V. Belessiotis and A. G. Kontos, "Plasmonic silver (Ag)-based photocatalysts for H_2 production and CO_2 conversion: Review, analysis and perspectives," *Renewable Energy*, vol. 195, pp. 497–515, Aug. 2022.

[25] J. Low, J. Yu, and W. Ho, "Graphene-Based Photocatalysts for CO_2 Reduction to Solar Fuel," *The Journal of Physical Chemistry Letters*, vol. 6, pp. 4244–4251, Nov. 2015.

[26] X. Li, J. Yu, S. Wageh, A. A. Al-Ghamdi, and J. Xie, "Graphene in Photocatalysis: A Review," *Small*, vol. 12, pp. 6640–6696, Dec. 2016.

[27] Z. Li, X. Meng, and Z. Zhang, "Recent development on MoS_2-based photocatalysis: A review," *Journal of Photochemistry and Photobiology C: Photochemistry Reviews*, vol. 35, pp. 39–55, June 2018.

[28] N. Thomas, S. Mathew, K. Nair, K. O'Dowd, P. Forouzandeh, A. Goswami, G. McGranaghan, and S. Pillai, "2D MoS_2: structure, mechanisms, and photocatalytic applications," *Materials Today Sustainability*, vol. 13, p. 100073, Sept. 2021.

[29] E. Parzinger, B. Miller, B. Blaschke, J. A. Garrido, J. W. Ager, A. Holleitner, and U. Wurstbauer, "Photocatalytic Stability of Single- and Few-Layer MoS_2," *ACS Nano*, vol. 9, pp. 11302–11309, Nov. 2015.

[30] Y. Liang, B.-H. Li, Z. Li, G. Zhang, J. Sun, C. Zhou, Y. Tao, Y. Ye, Z. Ren, and X. Yang, "Spatially heterogeneous ultrafast interfacial carrier dynamics of 2D-MoS_2 flakes," *Materials Today Physics*, vol. 21, p. 100506, Nov. 2021.

[31] S. Zhang, Y. Si, B. Li, L. Yang, W. Dai, and S. Luo, "Atomic-Level and Modulated Interfaces of Photocatalyst Heterostructure Constructed by External Defect-Induced Strategy: A Critical Review," *Small*, vol. 17, p. 2004980, Jan. 2021.

[32] J. Liu, N. Ma, W. Wu, and Q. He, "Recent progress on photocatalytic heterostructures with full solar spectral responses," *Chemical Engineering Journal*, vol. 393, p. 124719, Aug. 2020.

[33] A. Shafiee, N. Rabiee, S. Ahmadi, M. Baneshi, M. Khatami, S. Iravani, and R. S. Varma, "Core–Shell Nanophotocatalysts: Review of Materials and Applications," *ACS Applied Nano Materials*, vol. 5, pp. 55–86, Jan. 2022.

[34] R. Guo, J. Wang, Z. Bi, X. Chen, X. Hu, and W. Pan, "Recent Advances and Perspectives of Core-Shell Nanostructured Materials for Photocatalytic CO_2 Reduction," *Small*, vol. 19, p. 2206314, Mar. 2023.

[35] Y.-H. Chiu, S. B. Naghadeh, S. A. Lindley, T.-H. Lai, M.-Y. Kuo, K.-D. Chang, J. Z. Zhang, and Y.-J. Hsu, "Yolk-shell nanostructures as an emerging photocatalyst paradigm for solar hydrogen generation," *Nano Energy*, vol. 62, pp. 289–298, Aug. 2019.

[36] Y.-A. Chen, Y.-T. Wang, H. S. Moon, K. Yong, and Y.-J. Hsu, "Yolk–shell nanostructures: synthesis, photocatalysis and interfacial charge dynamics," *RSC Advances*, vol. 11, no. 20, pp. 12288–12305, 2021.

[37] K. P. Sundar and S. Kanmani, "Progression of Photocatalytic reactors and it's comparison: A Review," *Chemical Engineering Research and Design*, vol. 154, pp. 135–150, Feb. 2020.

[38] Y. Wei, Z. Zhang, W. Wang, Z. Song, M. Cai, and S. Sun, "Photocatalytic Z-scheme Overall Water Splitting: Insight into Different Optimization Strategies for Powder Suspension and Particulate Sheet Systems," *ChemPhysChem*, vol. 24, p. e202300216, Aug. 2023.

[39] B. A. Pinaud, J. D. Benck, L. C. Seitz, A. J. Forman, Z. Chen, T. G. Deutsch, B. D. James, K. N. Baum, G. N. Baum, S. Ardo, H. Wang, E. Miller, and T. F. Jaramillo, "Technical and economic feasibility of centralized facilities for solar hydrogen production via photocatalysis and photoelectrochemistry," *Energy & Environmental Science*, vol. 6, no. 7, p. 1983, 2013.

[40] S. Nandy, T. Hisatomi, T. Takata, T. Setoyama, and K. Domen, "Recent advances in photocatalyst sheet development and challenges for cost-effective solar hydrogen production," *Journal of Materials Chemistry A*, vol. 11, no. 38, pp. 20470–20479, 2023.

[41] Y. Goto, T. Hisatomi, Q. Wang, T. Higashi, K. Ishikiriyama, T. Maeda, Y. Sakata, S. Okunaka, H. Tokudome, M. Katayama, S. Akiyama, H. Nishiyama, Y. Inoue, T. Takewaki, T. Setoyama, T. Minegishi, T. Takata, T. Yamada, and K. Domen, "A Particulate Photocatalyst Water-Splitting Panel for Large-Scale Solar Hydrogen Generation," *Joule*, vol. 2, pp. 509–520, Mar. 2018.

[42] Q. Wang, T. Hisatomi, Q. Jia, H. Tokudome, M. Zhong, C. Wang, Z. Pan, T. Takata, M. Nakabayashi, N. Shibata, Y. Li, I. D. Sharp, A. Kudo, T. Yamada, and K. Domen, "Scalable water splitting on particulate photocatalyst sheets with a solar-to-hydrogen energy conversion efficiency exceeding 1%," *Nature Materials*, vol. 15, pp. 611–615, June 2016.

[43] M. Pérez-González, S. Tomás, J. Santoyo-Salazar, and M. Morales-Luna, "Enhanced photocatalytic activity of TiO_2-ZnO thin films deposited by dc reactive magnetron sputtering," *Ceramics International*, vol. 43, pp. 8831–8838, Aug. 2017.

[44] P. C. Sherrell, P. Palczynski, M. S. Sokolikova, F. Reale, F. M. Pesci, M. Och, and C. Mattevi, "Large-Area CVD MoS_2 /WS_2 Heterojunctions as a Photoelectrocatalyst for Salt-Water Oxidation," *ACS Applied Energy Materials*, vol. 2, pp. 5877–5882, Aug. 2019.

[45] V. Gupta, S. Sarkar, O. Aftenieva, T. Tsuda, L. Kumar, D. Schletz, J. Schultz, A. Kiriy, A. Fery, N. Vogel, and T. A. F. König, "Nanoimprint Lithography Facilitated Plasmonic-Photonic Coupling for Enhanced Photoconductivity and Photocatalysis," *Advanced Functional Materials*, vol. 31, p. 2105054, Sept. 2021.

[46] D. K. Oh, T. Lee, B. Ko, T. Badloe, J. G. Ok, and J. Rho, "Nanoimprint lithography for high-throughput fabrication of metasurfaces," *Frontiers of Optoelectronics*, vol. 14, pp. 229–251, June 2021.

[47] X. Zhang, Y. L. Chen, R.-S. Liu, and D. P. Tsai, "Plasmonic photocatalysis," *Reports on Progress in Physics*, vol. 76, p. 046401, Apr. 2013.

[48] S. Hamdad, A. T. Diallo, M. Chakaroun, and A. Boudrioua, "The role of Rayleigh anomalies in the coupling process of plasmonic gratings and the control of the emission properties of organic molecules," *Scientific Reports*, vol. 12, p. 3218, Feb. 2022.

[49] C. Fei Guo, T. Sun, F. Cao, Q. Liu, and Z. Ren, "Metallic nanostructures for light trapping in energy-harvesting devices," *Light: Science & Applications*, vol. 3, pp. e161–e161, Apr. 2014.

[50] A. Sihvola, "Metamaterials in electromagnetics," *Metamaterials*, vol. 1, pp. 2–11, Mar. 2007.

[51] J. Schneidewind, "How Much Technological Progress is Needed to Make Solar Hydrogen Cost-Competitive?," *Advanced Energy Materials*, vol. 12, p. 2200342, May 2022.

[52] S. Fang, M. Rahaman, J. Bharti, E. Reisner, M. Robert, G. A. Ozin, and Y. H. Hu, "Photocatalytic CO_2 reduction," *Nature Reviews Methods Primers*, vol. 3, p. 61, Aug. 2023.

[53] M. Z. Rahman, F. Raziq, H. Zhang, and J. Gascon, "Key Strategies for Enhancing H_2 Production in Transition Metal Oxide Based Photocatalysts," *Angewandte Chemie*, vol. 135, p. e202305385, Nov. 2023.

[54] P. Zhou, I. A. Navid, Y. Ma, Y. Xiao, P. Wang, Z. Ye, B. Zhou, K. Sun, and Z. Mi, "Solar-to-hydrogen efficiency of more than 9% in photocatalytic water splitting," *Nature*, vol. 613, pp. 66–70, Jan. 2023.

[55] S. Ali, M. C. Flores, A. Razzaq, S. Sorcar, C. B. Hiragond, H. R. Kim, Y. H. Park, Y. Hwang, H. S. Kim, H. Kim, E. H. Gong, J. Lee, D. Kim, and S.-I. In,

"Gas Phase Photocatalytic CO_2 Reduction, "A Brief Overview for Benchmarking"," *Catalysts*, vol. 9, p. 727, Aug. 2019.

[56] E. Mikyskova, I. Martiniakova, R. Zouzelka, and J. Rathousky, "Photocatalytic NO_x abatement: The effect of high air flow velocity," *Environmental Technology & Innovation*, vol. 28, p. 102820, Nov. 2022.

[57] M. Tahir and N. S. Amin, "Photocatalytic reduction of carbon dioxide with water vapors over montmorillonite modified TiO_2 nanocomposites," *Applied Catalysis B: Environmental*, vol. 142-143, pp. 512–522, Oct. 2013.

[58] A. A. Khan and M. Tahir, "Recent advancements in engineering approach towards design of photo-reactors for selective photocatalytic CO_2 reduction to renewable fuels," *Journal of CO2 Utilization*, vol. 29, pp. 205–239, Jan. 2019.

[59] Q. Wang, C. Pornrungroj, S. Linley, and E. Reisner, "Strategies to improve light utilization in solar fuel synthesis," *Nature Energy*, vol. 7, pp. 13–24, Nov. 2021.

[60] M. T. H. Van Vliet, E. R. Jones, M. Flörke, W. H. P. Franssen, N. Hanasaki, Y. Wada, and J. R. Yearsley, "Global water scarcity including surface water quality and expansions of clean water technologies," *Environmental Research Letters*, vol. 16, p. 024020, Feb. 2021.

[61] Y. Nosaka and A. Y. Nosaka, "Generation and Detection of Reactive Oxygen Species in Photocatalysis," *Chemical Reviews*, vol. 117, pp. 11302–11336, Sept. 2017.

[62] S. Murgolo, C. De Ceglie, C. Di Iaconi, and G. Mascolo, "Novel TiO_2-based catalysts employed in photocatalysis and photoelectrocatalysis for effective degradation of pharmaceuticals (PhACs) in water: A short review," *Current Opinion in Green and Sustainable Chemistry*, vol. 30, p. 100473, Aug. 2021.

[63] A. Kumar, V. Hasija, A. Sudhaik, P. Raizada, V.-H. Nguyen, Q. V. Le, P. Singh, D. Nguyen, S. Thakur, and C. M. Hussain, "The practicality and prospects for disinfection control by photocatalysis during and post-pandemic: A critical review," *Environmental Research*, vol. 209, p. 112814, June 2022.

[64] P. Van De Vuurst and L. E. Escobar, "Climate change and infectious disease: a review of evidence and research trends," *Infectious Diseases of Poverty*, vol. 12, p. 51, May 2023.

[65] Y. Ding, G. Yang, S. Zheng, X. Gao, Z. Xiang, M. Gao, C. Wang, M. Liu, and J. Zhong, "Advanced photocatalytic disinfection mechanisms and their challenges," *Journal of Environmental Management*, vol. 366, p. 121875, Aug. 2024.

[66] Y. Lu, S. Guan, L. Hao, H. Yoshida, S. Nakada, T. Takisawa, and T. Itoi, "Inactivation of SARS-CoV-2 and photocatalytic degradation by TiO_2 photocatalyst coatings," *Scientific Reports*, vol. 12, p. 16038, Sept. 2022.

[67] J.-Y. Wu, Y.-A. Chen, Y.-A. Chien, T. Kurioka, M. Sone, C.-Y. Chen, T.-F. M. Chang, and Y.-J. Hsu, "Photocatalytic Fibers for Environmental Purification: Challenges and Opportunities in the Post-Pandemic Era," *Advanced Energy and Sustainability Research*, vol. 5, p. 2300212, Feb. 2024.

[68] C. F. Liriano-Jorge, U. Sohmen, A. Özkan, H. Gulyas, and R. Otterpohl, "TiO_2 Photocatalyst Nanoparticle Separation: Flocculation in Different Matrices and Use of Powdered Activated Carbon as a Precoat in Low-Cost Fabric Filtration," *Advances in Materials Science and Engineering*, vol. 2014, pp. 1–12, 2014.

[69] M. Muscetta, P. Ganguly, and L. Clarizia, "Solar-powered photocatalysis in water purification: applications and commercialization challenges," *Journal of Environmental Chemical Engineering*, vol. 12, p. 113073, June 2024.

[70] C. Kittel, *Introduction to solid state physics*. Hoboken, NJ: Wiley, global edition, [9th edition] ed., 2018.

[71] G. Liu, L. Wang, H. G. Yang, H.-M. Cheng, and G. Q. (Max) Lu, "Titania-based photocatalysts—crystal growth, doping and heterostructuring," *J. Mater. Chem.*, vol. 20, no. 5, pp. 831–843, 2010.

[72] S. Bai, N. Zhang, C. Gao, and Y. Xiong, "Defect engineering in photocatalytic materials," *Nano Energy*, vol. 53, pp. 296–336, Nov. 2018.

[73] D. K. Schroder, *Semiconductor material and device characterization*. [Piscataway, NJ] : Hoboken, N.J: IEEE Press ; Wiley, 3rd ed ed., 2006. OCLC: ocm59360243.

[74] T. Deka and R. G Nair, "Recent advancements in surface plasmon resonance and Schottky junction assisted photocatalytic water splitting of noble metal decorated Titania: A review," *International Journal of Hydrogen Energy*, vol. 59, pp. 322–342, Mar. 2024.

[75] D. V. Morgan and R. H. Williams, eds., *Physics and Technology of Heterojunction Devices*. Institution of Engineering and Technology, Jan. 1991.

[76] J. Low, J. Yu, M. Jaroniec, S. Wageh, and A. A. Al-Ghamdi, "Heterojunction Photocatalysts," *Advanced Materials*, vol. 29, p. 1601694, May 2017.

[77] R. L. Anderson, "Germanium-Gallium Arsenide Heterojunctions [Letter to the Editor]," *IBM Journal of Research and Development*, vol. 4, pp. 283–287, July 1960.

[78] X. He, T. Kai, and P. Ding, "Heterojunction photocatalysts for degradation of the tetracycline antibiotic: a review," *Environmental Chemistry Letters*, vol. 19, pp. 4563–4601, Dec. 2021.

[79] Z. Wang, Z. Lin, S. Shen, W. Zhong, and S. Cao, "Advances in designing heterojunction photocatalytic materials," *Chinese Journal of Catalysis*, vol. 42, pp. 710–730, May 2021.

[80] H. Yang, "A short review on heterojunction photocatalysts: Carrier transfer behavior and photocatalytic mechanisms," *Materials Research Bulletin*, vol. 142, p. 111406, Oct. 2021.

[81] B. Luo, G. Liu, and L. Wang, "Recent advances in 2D materials for photocatalysis," *Nanoscale*, vol. 8, no. 13, pp. 6904–6920, 2016.

[82] A. K. Geim, "Graphene: Status and Prospects," *Science*, vol. 324, pp. 1530–1534, June 2009.

[83] M. A. Ahmed and A. A. Mohamed, "Recent progress in semiconductor/graphene photocatalysts: synthesis, photocatalytic applications, and challenges," *RSC Advances*, vol. 13, no. 1, pp. 421–439, 2023.

[84] R. Nandee, M. A. Chowdhury, A. Shahid, N. Hossain, and M. Rana, "Band gap formation of 2D materialin graphene: Future prospect and challenges," *Results in Engineering*, vol. 15, p. 100474, Sept. 2022.

[85] H. J. Conley, B. Wang, J. I. Ziegler, R. F. Haglund, S. T. Pantelides, and K. I. Bolotin, "Bandgap Engineering of Strained Monolayer and Bilayer MoS_2," *Nano Letters*, vol. 13, pp. 3626–3630, Aug. 2013.

[86] K. G. Mondal, P. C. Jana, and S. Saha, "Optical and structural properties of 2D transition metal dichalcogenides semiconductor MoS_2," *Bulletin of Materials Science*, vol. 46, p. 15, Jan. 2023.

[87] C. Zhang, K. Ren, S. Wang, Y. Luo, W. Tang, and M. Sun, "Recent progress on two-dimensional van der Waals heterostructures for photocatalytic water splitting: a selective review," *Journal of Physics D: Applied Physics*, vol. 56, p. 483001, Nov. 2023.

[88] S. A. Maier, *Plasmonics: Fundamentals and Applications*. New York, NY: Springer US, 2007.

[89] V. Amendola, R. Pilot, M. Frasconi, O. M. Maragò, and M. A. Iatì, "Surface plasmon resonance in gold nanoparticles: a review," *Journal of Physics: Condensed Matter*, vol. 29, p. 203002, May 2017.

[90] P. Spinelli and A. Polman, "Prospects of near-field plasmonic absorption enhancement in semiconductor materials using embedded Ag nanoparticles," *Optics Express*, vol. 20, p. A641, Sept. 2012.

[91] L. Mascaretti and A. Naldoni, "Hot electron and thermal effects in plasmonic photocatalysis," *Journal of Applied Physics*, vol. 128, p. 041101, July 2020.

[92] I. Zorić, M. Zäch, B. Kasemo, and C. Langhammer, "Gold, Platinum, and Aluminum Nanodisk Plasmons: Material Independence, Subradiance, and Damping Mechanisms," *ACS Nano*, vol. 5, pp. 2535–2546, Apr. 2011.

[93] J. Y. Y. Loh, M. Safari, C. Mao, C. J. Viasus, G. V. Eleftheriades, G. A. Ozin, and N. P. Kherani, "Near-Perfect Absorbing Copper Metamaterial for Solar Fuel Generation," *Nano Letters*, vol. 21, pp. 9124–9130, Nov. 2021.

[94] T. Wang, H.-J. Wang, J.-S. Lin, J.-L. Yang, F.-L. Zhang, X.-M. Lin, Y.-J. Zhang, S. Jin, and J.-F. Li, "Plasmonic photocatalysis: Mechanism, applications and perspectives," *Chinese Journal of Structural Chemistry*, vol. 42, p. 100066, Sept. 2023.

[95] D. Liu and C. Xue, "Plasmonic Coupling Architectures for Enhanced Photocatalysis," *Advanced Materials*, vol. 33, p. 2005738, Nov. 2021.

[96] J. Zhang, L. Zhang, and W. Xu, "Surface plasmon polaritons: physics and applications," *Journal of Physics D: Applied Physics*, vol. 45, p. 113001, Mar. 2012.

[97] J. J. Mock, M. Barbic, D. R. Smith, D. A. Schultz, and S. Schultz, "Shape effects in plasmon resonance of individual colloidal silver nanoparticles," *The Journal of Chemical Physics*, vol. 116, pp. 6755–6759, Apr. 2002.

[98] B. J. Wiley, S. H. Im, Z.-Y. Li, J. McLellan, A. Siekkinen, and Y. Xia, "Maneuvering the Surface Plasmon Resonance of Silver Nanostructures through Shape-Controlled Synthesis," *The Journal of Physical Chemistry B*, vol. 110, pp. 15666–15675, Aug. 2006.

[99] K.-i. Murata and H. Tanaka, "Surface-wetting effects on the liquid–liquid transition of a single-component molecular liquid," *Nature Communications*, vol. 1, p. 16, May 2010.

[100] V. M. Silkin, R. Díez Muiño, I. P. Chernov, E. V. Chulkov, and P. M. Echenique, "Tuning the plasmon energy of palladium–hydrogen systems by varying the hydrogen concentration," *Journal of Physics: Condensed Matter*, vol. 24, p. 104021, Mar. 2012.

[101] V. Palenskis, "Free Electron Characteristic Peculiarities Caused by Lattice Vibrations in Metals," *World Journal of Condensed Matter Physics*, vol. 12, no. 02, pp. 9–17, 2022.

[102] C. Clavero, "Plasmon-induced hot-electron generation at nanoparticle/metal-oxide interfaces for photovoltaic and photocatalytic devices," *Nature Photonics*, vol. 8, pp. 95–103, Feb. 2014.

[103] M. Ahlawat, D. Mittal, and V. Govind Rao, "Plasmon-induced hot-hole generation and extraction at nano-heterointerfaces for photocatalysis," *Communications Materials*, vol. 2, p. 114, Nov. 2021.

[104] A. Furube and S. Hashimoto, "Insight into plasmonic hot-electron transfer and plasmon molecular drive: new dimensions in energy conversion and nanofabrication," *NPG Asia Materials*, vol. 9, pp. e454–e454, Dec. 2017.

[105] O. Neumann, A. S. Urban, J. Day, S. Lal, P. Nordlander, and N. J. Halas, "Solar Vapor Generation Enabled by Nanoparticles," *ACS Nano*, vol. 7, pp. 42–49, Jan. 2013.

[106] Y. Gu, L. Zhang, J. K. W. Yang, S. P. Yeo, and C.-W. Qiu, "Color generation *via* subwavelength plasmonic nanostructures," *Nanoscale*, vol. 7, no. 15, pp. 6409–6419, 2015.

[107] I. L. Rasskazov, N. Sonwalkar, and P. Scott Carney, "Light scattering by plasmonic disks and holes arrays: different or the same?," *Journal of Physics D: Applied Physics*, vol. 55, p. 455104, Nov. 2022.

[108] L. Wen, R. Xu, C. Cui, W. Tang, Y. Mi, X. Lu, Z. Zeng, S. L. Suib, P.-X. Gao, and Y. Lei, "Template-Guided Programmable Janus Heteronanostructure Arrays for Efficient Plasmonic Photocatalysis," *Nano Letters*, vol. 18, pp. 4914–4921, Aug. 2018.

[109] D. Daskalova, G. Aguila Flores, U. Plachetka, M. Möller, J. Wolters, T. Wintgens, and M. C. Lemme, "Combined Structural and Plasmonic Enhancement of Nanometer-Thin Film Photocatalysis for Solar-Driven Wastewater Treatment," *ACS Applied Nano Materials*, vol. 6, pp. 15204–15212, Aug. 2023.

[110] J. Barnett, U. Plachetka, C. Nowak, and H. Wackerbarth, "Highly periodic Au nano-disc arrays for plasmon-resonant SERS structures on fused silica using UV-NIL based double-layer lift-off process," *Microelectronic Engineering*, vol. 172, pp. 45–48, Mar. 2017.

[111] S. N. Habisreutinger, L. Schmidt-Mende, and J. K. Stolarczyk, "Photocatalytic Reduction of CO_2 on TiO_2 and Other Semiconductors," *Angewandte Chemie International Edition*, vol. 52, pp. 7372–7408, July 2013.

[112] S. Peiris, H. B. De Silva, K. N. Ranasinghe, S. V. Bandara, and I. R. Perera, "Recent development and future prospects of TiO_2 photocatalysis," *Journal of the Chinese Chemical Society*, vol. 68, pp. 738–769, May 2021.

[113] F. Bhom and Y. M. Isa, "Photocatalytic Hydrogen Production Using TiO_2 - based Catalysts: A Review," *Global Challenges*, vol. 8, p. 2400134, Nov. 2024.

[114] S. Kahng, H. Yoo, and J. H. Kim, "Recent advances in earth-abundant photocatalyst materials for solar H_2 production," *Advanced Powder Technology*, vol. 31, pp. 11–28, Jan. 2020.

[115] S. Nakabayashi, R. Shinozaki, Y. Senda, and H. Y. Yoshikawa, "Hydrogen nanobubble at normal hydrogen electrode," *Journal of Physics: Condensed Matter*, vol. 25, p. 184008, May 2013.

[116] H. Li, H. Hu, C. Bai, C. Bao, C. Liu, Q. Wang, F. Guo, Z. Feng, H. Yu, M. Chen, and K. Qu, "Prediction of a Stable Organic Metal-Free Porous Material as a Catalyst for Water-Splitting," *Catalysts*, vol. 10, p. 836, July 2020.

[117] J. H. Kim, D. Hansora, P. Sharma, J.-W. Jang, and J. S. Lee, "Toward practical solar hydrogen production – an artificial photosynthetic leaf-to-farm challenge," *Chemical Society Reviews*, vol. 48, no. 7, pp. 1908–1971, 2019.

[118] M. M. Walczak, D. A. Dryer, D. D. Jacobson, M. G. Foss, and N. T. Flynn, "pH Dependent Redox Couple: An Illustration of the Nernst Equation," *Journal of Chemical Education*, vol. 74, p. 1195, Oct. 1997.

[119] M. Edelmannová, M. De Los Milagros Ballari, M. Přibyl, and K. Kočí, "Experimental and modelling studies on the photocatalytic generation of hydrogen during water-splitting over a commercial TiO_2 photocatalyst P25," *Energy Conversion and Management*, vol. 245, p. 114582, Oct. 2021.

[120] T. Baran, A. Visibile, M. Busch, X. He, S. Wojtyla, S. Rondinini, A. Minguzzi, and A. Vertova, "Copper Oxide-Based Photocatalysts and Photocathodes: Fundamentals and Recent Advances," *Molecules*, vol. 26, p. 7271, Nov. 2021.

[121] C. Cao, B. Zhang, and S. Lin, "p-type ZnO for photocatalytic water splitting," *APL Materials*, vol. 10, p. 030901, Mar. 2022.

[122] K. A. Gomari, H. Y. Hafeez, J. Mohammed, U. Dankawu, C. E. Ndikilar, and A. B. Suleiman, "A recent development and future prospect of g–C_3N_4–based photocatalyst for stable hydrogen (H_2) generation via photocatalytic water-splitting," *International Journal of Hydrogen Energy*, vol. 85, pp. 598–624, Oct. 2024.

[123] C. Avcıoğlu, S. Avcıoğlu, M. F. Bekheet, and A. Gurlo, "Photocatalytic Overall Water Splitting by $SrTiO_3$: Progress Report and Design Strategies," *ACS Applied Energy Materials*, vol. 6, pp. 1134–1154, Feb. 2023.

[124] J. Ran, M. Jaroniec, and S. Qiao, "Cocatalysts in Semiconductor-based Photocatalytic CO_2 Reduction: Achievements, Challenges, and Opportunities," *Advanced Materials*, vol. 30, p. 1704649, Feb. 2018.

[125] P. Millet, "Fundamentals of Water Electrolysis," in *Hydrogen Production* (A. Godula-Jopek, ed.), pp. 33–62, Wiley, 1 ed., Apr. 2015.

[126] M. Arumugam and H.-H. Yang, "A review of the application of wide-bandgap semiconductor photocatalysts for CO_2 reduction," *Journal of CO2 Utilization*, vol. 83, p. 102808, May 2024.

[127] M. Zhang, Y. Yang, X. An, and L.-a. Hou, "A critical review of g-C_3N_4-based photocatalytic membrane for water purification," *Chemical Engineering Journal*, vol. 412, p. 128663, May 2021.

[128] Y. He, L. Yin, N. Yuan, and G. Zhang, "Adsorption and activation, active site and reaction pathway of photocatalytic CO_2 reduction: A review," *Chemical Engineering Journal*, vol. 481, p. 148754, Feb. 2024.

[129] F. Ding and B. I. Yakobson, "Challenges in hydrogen adsorptions: from physisorption to chemisorption," *Frontiers of Physics*, vol. 6, pp. 142–150, June 2011.

[130] S. Hosseinpour, F. Tang, F. Wang, R. A. Livingstone, S. J. Schlegel, T. Ohto, M. Bonn, Y. Nagata, and E. H. G. Backus, "Chemisorbed and Physisorbed Water at the TiO_2 /Water Interface," *The Journal of Physical Chemistry Letters*, vol. 8, pp. 2195–2199, May 2017.

[131] A. J. Medford, A. Vojvodic, J. S. Hummelshøj, J. Voss, F. Abild-Pedersen, F. Studt, T. Bligaard, A. Nilsson, and J. K. Nørskov, "From the Sabatier principle to a predictive theory of transition-metal heterogeneous catalysis," *Journal of Catalysis*, vol. 328, pp. 36–42, Aug. 2015.

[132] E. Pomerantseva, C. Resini, K. Kovnir, and Y. V. Kolen'ko, "Emerging nanostructured electrode materials for water electrolysis and rechargeable beyond Li-ion batteries," *Advances in Physics: X*, vol. 2, pp. 211–253, Mar. 2017.

[133] J. K. Nørskov, F. Abild-Pedersen, F. Studt, and T. Bligaard, "Density functional theory in surface chemistry and catalysis," *Proceedings of the National Academy of Sciences*, vol. 108, pp. 937–943, Jan. 2011.

[134] Ž. Kovačič, B. Likozar, and M. Huš, "Photocatalytic CO_2 Reduction: A Review of Ab Initio Mechanism, Kinetics, and Multiscale Modeling Simulations," *ACS Catalysis*, vol. 10, pp. 14984–15007, Dec. 2020.

[135] A. Serov, K. Kovnir, M. Shatruk, and Y. V. Kolen'ko, "Critical Review of Platinum Group Metal-Free Materials for Water Electrolysis: Transition from the Laboratory to the Market: Earth-abundant borides and phosphides as catalysts for sustainable hydrogen production," *Johnson Matthey Technology Review*, vol. 65, pp. 207–226, Apr. 2021.

[136] Y. Wy, H. Jung, J. W. Hong, and S. W. Han, "Exploiting Plasmonic Hot Spots in Au-Based Nanostructures for Sensing and Photocatalysis," *Accounts of Chemical Research*, vol. 55, pp. 831–843, Mar. 2022.

[137] J. Liu, Y.-Z. Fan, X. Li, Z. Wei, Y.-W. Xu, L. Zhang, and C.-Y. Su, "A porous rhodium(III)-porphyrin metal-organic framework as an efficient and selective photocatalyst for CO_2 reduction," *Applied Catalysis B: Environmental*, vol. 231, pp. 173–181, Sept. 2018.

[138] X. Huang and E. Meggers, "Asymmetric Photocatalysis with Bis-cyclometalated Rhodium Complexes," *Accounts of Chemical Research*, vol. 52, pp. 833–847, Mar. 2019.

[139] R. Kuriki, K. Sekizawa, O. Ishitani, and K. Maeda, "Visible-Light-Driven CO_2 Reduction with Carbon Nitride: Enhancing the Activity of Ruthenium Catalysts," *Angewandte Chemie International Edition*, vol. 54, pp. 2406–2409, Feb. 2015.

[140] R. Kuriki, H. Matsunaga, T. Nakashima, K. Wada, A. Yamakata, O. Ishitani, and K. Maeda, "Nature-Inspired, Highly Durable CO_2 Reduction System Consisting of a Binuclear Ruthenium(II) Complex and an Organic Semiconductor Using Visible Light," *Journal of the American Chemical Society*, vol. 138, pp. 5159–5170, Apr. 2016.

[141] W. K. Fan and M. Tahir, "Recent advances on cobalt metal organic frameworks (MOFs) for photocatalytic CO_2 reduction to renewable energy and fuels: A review on current progress and future directions," *Energy Conversion and Management*, vol. 253, p. 115180, Feb. 2022.

[142] Z. Wang, J. Fan, B. Cheng, J. Yu, and J. Xu, "Nickel-based cocatalysts for photocatalysis: Hydrogen evolution, overall water splitting and CO_2 reduction," *Materials Today Physics*, vol. 15, p. 100279, Dec. 2020.

[143] T. Takata, L. Lin, T. Hisatomi, and K. Domen, "Best Practices for Assessing Performance of Photocatalytic Water Splitting Systems," *Advanced Materials*, vol. 36, p. 2406848, Nov. 2024.

[144] S. Sorcar, Y. Hwang, C. A. Grimes, and S.-I. In, "Highly enhanced and stable activity of defect-induced titania nanoparticles for solar light-driven CO 2 reduction into CH 4," *Materials Today*, vol. 20, pp. 507–515, Nov. 2017.

[145] S. Cao and L. Piao, "Considerations for a More Accurate Evaluation Method for Photocatalytic Water Splitting," *Angewandte Chemie International Edition*, vol. 59, pp. 18312–18320, Oct. 2020.

[146] M. Dilla, N. G. Moustakas, A. E. Becerikli, T. Peppel, A. Springer, R. Schlögl, J. Strunk, and S. Ristig, "Judging the feasibility of TiO_2 as photocatalyst for chemical energy conversion by quantitative reactivity determinants," *Physical Chemistry Chemical Physics*, vol. 21, no. 24, pp. 13144–13150, 2019.

[147] M. R. Singh, E. L. Clark, and A. T. Bell, "Thermodynamic and achievable efficiencies for solar-driven electrochemical reduction of carbon dioxide to transportation fuels," *Proceedings of the National Academy of Sciences*, vol. 112, Nov. 2015.

[148] T. A. Kandiel, L. Robben, A. Alkaima, and D. Bahnemann, "Brookite versus anatase TiO_2 photocatalysts: phase transformations and photocatalytic activities," *Photochemical & Photobiological Sciences*, vol. 12, pp. 602–609, Apr. 2013.

[149] T. Luttrell, S. Halpegamage, J. Tao, A. Kramer, E. Sutter, and M. Batzill, "Why is anatase a better photocatalyst than rutile? - Model studies on epitaxial TiO_2 films," *Scientific Reports*, vol. 4, p. 4043, Feb. 2014.

[150] N. S. Allen, N. Mahdjoub, V. Vishnyakov, P. J. Kelly, and R. J. Kriek, "The effect of crystalline phase (anatase, brookite and rutile) and size on the photocatalytic activity of calcined polymorphic titanium dioxide (TiO 2)," *Polymer Degradation and Stability*, vol. 150, pp. 31–36, Apr. 2018.

[151] C. Lu and R. Lipson, "Interference lithography: a powerful tool for fabricating periodic structures," *Laser & Photonics Reviews*, vol. 4, pp. 568–580, June 2010.

[152] R. Liu, L. Cao, D. Liu, L. Wang, S. Saeed, and Z. Wang, "Laser Interference Lithography—A Method for the Fabrication of Controlled Periodic Structures," *Nanomaterials*, vol. 13, p. 1818, June 2023.

[153] A. Raza, Z. Saeed, A. Aslam, S. M. Nizami, K. Habib, and A. N. Malik, "Advances, Application and Challenges of Lithography Techniques," in *2024 5th International Conference on Advancements in Computational Sciences (ICACS)*, (Lahore, Pakistan), pp. 1–6, IEEE, Feb. 2024.

[154] P. Makuła, M. Pacia, and W. Macyk, "How To Correctly Determine the Band Gap Energy of Modified Semiconductor Photocatalysts Based on UV–Vis Spectra," *The Journal of Physical Chemistry Letters*, vol. 9, pp. 6814–6817, Dec. 2018.

[155] J. Tauc, R. Grigorovici, and A. Vancu, "Optical Properties and Electronic Structure of Amorphous Germanium," *physica status solidi (b)*, vol. 15, pp. 627–637, Jan. 1966.

[156] G.-Y. Yao, Q.-L. Liu, and Z.-Y. Zhao, "Studied Localized Surface Plasmon Resonance Effects of Au Nanoparticles on TiO_2 by FDTD Simulations," *Catalysts*, vol. 8, p. 236, June 2018.

[157] H. Ren, J.-L. Yang, W.-M. Yang, H.-L. Zhong, J.-S. Lin, P. M. Radjenovic, L. Sun, H. Zhang, J. Xu, Z.-Q. Tian, and J.-F. Li, "Core–Shell–Satellite Plasmonic Photocatalyst for Broad-Spectrum Photocatalytic Water Splitting," *ACS Materials Letters*, vol. 3, pp. 69–76, Jan. 2021.

[158] M. Y. H. Widianto, C. Imron, and B. Widodo, "A Short Review of Numerical Modelling for Photocatalytic Degradation in Dye Systems," in *Applied and Computational Mathematics* (D. Adzkiya and K. Fahim, eds.), vol. 455, pp. 77–86, Singapore: Springer Nature Singapore, 2024. Series Title: Springer Proceedings in Mathematics & Statistics.

[159] N. I. Landy, S. Sajuyigbe, J. J. Mock, D. R. Smith, and W. J. Padilla, "Perfect Metamaterial Absorber," *Physical Review Letters*, vol. 100, p. 207402, May 2008.

[160] T. J. Cui, D. Smith, and R. Liu, eds., *Metamaterials: Theory, Design, and Applications*. Boston, MA: Springer US, 2010.

[161] N. I. Zheludev and Y. S. Kivshar, "From metamaterials to metadevices," *Nature Materials*, vol. 11, pp. 917–924, Nov. 2012.

[162] R. Kumar, M. Kumar, J. S. Chohan, and S. Kumar, "Overview on metamaterial: History, types and applications," *Materials Today: Proceedings*, vol. 56, pp. 3016–3024, 2022.

[163] R. Qian, H. Zong, J. Schneider, G. Zhou, T. Zhao, Y. Li, J. Yang, D. W. Bahnemann, and J. H. Pan, "Charge carrier trapping, recombination and transfer during TiO_2 photocatalysis: An overview," *Catalysis Today*, vol. 335, pp. 78–90, Sept. 2019.

[164] J. Langer, D. Jimenez De Aberasturi, J. Aizpurua, R. A. Alvarez-Puebla, B. Auguié, J. J. Baumberg, G. C. Bazan, S. E. J. Bell, A. Boisen, A. G. Brolo, J. Choo, D. Cialla-May, V. Deckert, L. Fabris, K. Faulds, F. J. García De Abajo, R. Goodacre, D. Graham, A. J. Haes, C. L. Haynes, C. Huck, T. Itoh, M. Käll,

J. Kneipp, N. A. Kotov, H. Kuang, E. C. Le Ru, H. K. Lee, J.-F. Li, X. Y. Ling, S. A. Maier, T. Mayerhöfer, M. Moskovits, K. Murakoshi, J.-M. Nam, S. Nie, Y. Ozaki, I. Pastoriza-Santos, J. Perez-Juste, J. Popp, A. Pucci, S. Reich, B. Ren, G. C. Schatz, T. Shegai, S. Schlücker, L.-L. Tay, K. G. Thomas, Z.-Q. Tian, R. P. Van Duyne, T. Vo-Dinh, Y. Wang, K. A. Willets, C. Xu, H. Xu, Y. Xu, Y. S. Yamamoto, B. Zhao, and L. M. Liz-Marzán, "Present and Future of Surface-Enhanced Raman Scattering," *ACS Nano*, vol. 14, pp. 28–117, Jan. 2020.

[165] G. Barbillon, "Latest Advances in Metasurfaces for SERS and SEIRA Sensors as Well as Photocatalysis," *International Journal of Molecular Sciences*, vol. 23, p. 10592, Sept. 2022.

[166] S. Jung, K. L. Shuford, and S. Park, "Optical Property of a Colloidal Solution of Platinum and Palladium Nanorods: Localized Surface Plasmon Resonance," *The Journal of Physical Chemistry C*, vol. 115, pp. 19049–19053, Oct. 2011.

[167] M. Hassani-Gangaraj, D. Veysset, K. A. Nelson, and C. A. Schuh, "Impact-bonding with aluminum, silver, and gold microparticles: Toward understanding the role of native oxide layer," *Applied Surface Science*, vol. 476, pp. 528–532, May 2019.

[168] W. Jiang, X. Wang, Z. Wu, X. Yue, S. Yuan, H. Lu, and B. Liang, "Silver Oxide as Superb and Stable Photocatalyst under Visible and Near-Infrared Light Irradiation and Its Photocatalytic Mechanism," *Industrial & Engineering Chemistry Research*, vol. 54, pp. 832–841, Jan. 2015.

[169] A. Augustin, P. Ganguly, S. Shenoy, C. Chuaicham, S. C. Pillai, K. Sasaki, A. F. Lee, and K. Sekar, "Impact of Hole Scavengers on Efficient Photocatalytic Hydrogen Production," *Advanced Sustainable Systems*, vol. 8, p. 2400321, Dec. 2024.

[170] X. Pang, C. Chen, H. Ji, Y. Che, W. Ma, and J. Zhao, "Unraveling the Photocatalytic Mechanisms on TiO_2 Surfaces Using the Oxygen-18 Isotopic Label Technique," *Molecules*, vol. 19, pp. 16291–16311, Oct. 2014.

[171] H. Park, H.-H. Ou, U. Kang, J. Choi, and M. R. Hoffmann, "Photocatalytic conversion of carbon dioxide to methane on TiO_2/CdS in aqueous isopropanol solution," *Catalysis Today*, vol. 266, pp. 153–159, May 2016.

[172] A. H. Assi, ed., *Engineering Education and Research Using MATLAB*. Erscheinungsort nicht ermittelbar: IntechOpen, 2011.

[173] S. Yu and P. K. Jain, "Selective Branching of Plasmonic Photosynthesis into Hydrocarbon Production and Hydrogen Generation," *ACS Energy Letters*, vol. 4, pp. 2295–2300, Sept. 2019.

[174] H. Huang, R. Shi, Z. Li, J. Zhao, C. Su, and T. Zhang, "Triphase Photocatalytic CO_2 Reduction over Silver-Decorated Titanium Oxide at a Gas–Water Boundary," *Angewandte Chemie International Edition*, vol. 61, p. e202200802, Apr. 2022.

[175] D. Hong, L.-M. Lyu, K. Koga, Y. Shimoyama, and Y. Kon, "Plasmonic Ag@TiO_2 Core–Shell Nanoparticles for Enhanced CO_2 Photoconversion to CH_4," *ACS Sustainable Chemistry & Engineering*, vol. 7, pp. 18955–18964, Dec. 2019.

[176] S. Feng, M. Wang, Y. Zhou, P. Li, W. Tu, and Z. Zou, "Double-shelled plasmonic Ag-TiO_2 hollow spheres toward visible light-active photocatalytic conversion of CO_2 into solar fuel," *APL Materials*, vol. 3, p. 104416, Oct. 2015.

[177] R. Wang, J. Shen, K. Sun, H. Tang, and Q. Liu, "Enhancement in photocatalytic activity of CO_2 reduction to CH_4 by 0D/2D Au/TiO_2 plasmon heterojunction," *Applied Surface Science*, vol. 493, pp. 1142–1149, Nov. 2019.

[178] M. Tahir, B. Tahir, and N. A. S. Amin, "Gold-nanoparticle-modified TiO_2 nanowires for plasmon-enhanced photocatalytic CO_2 reduction with H_2 under visible light irradiation," *Applied Surface Science*, vol. 356, pp. 1289–1299, Nov. 2015.

[179] W. Hou, W. H. Hung, P. Pavaskar, A. Goeppert, M. Aykol, and S. B. Cronin, "Photocatalytic Conversion of CO_2 to Hydrocarbon Fuels via Plasmon-Enhanced Absorption and Metallic Interband Transitions," *ACS Catalysis*, vol. 1, pp. 929–936, Aug. 2011.

[180] A. Pougin, G. Dodekatos, M. Dilla, H. Tüysüz, and J. Strunk, "Au@TiO_2 Core–Shell Composites for the Photocatalytic Reduction of CO_2," *Chemistry – A European Journal*, vol. 24, pp. 12416–12425, Aug. 2018.

[181] A. Durga Devi, S. Pushpavanam, N. Singh, J. Verma, M. P. Kaur, and S. C. Roy, "Enhanced methane yield by photoreduction of CO_2 at moderate temperature and pressure using Pt coated, graphene oxide wrapped TiO_2 nanotubes," *Results in Engineering*, vol. 14, p. 100441, June 2022.

[182] W.-N. Wang, W.-J. An, B. Ramalingam, S. Mukherjee, D. M. Niedzwiedzki, S. Gangopadhyay, and P. Biswas, "Size and Structure Matter: Enhanced CO_2 Photoreduction Efficiency by Size-Resolved Ultrafine Pt Nanoparticles on TiO_2 Single Crystals," *Journal of the American Chemical Society*, vol. 134, pp. 11276–11281, July 2012.

[183] M. Moradi, F. Khorasheh, and A. Larimi, "Pt nanoparticles decorated Bi-doped TiO_2 as an efficient photocatalyst for CO_2 photo-reduction into CH_4," *Solar Energy*, vol. 211, pp. 100–110, Nov. 2020.

[184] S. Xie, Y. Wang, Q. Zhang, W. Deng, and Y. Wang, "MgO- and Pt-Promoted TiO_2 as an Efficient Photocatalyst for the Preferential Reduction of Carbon Dioxide in the Presence of Water," *ACS Catalysis*, vol. 4, pp. 3644–3653, Oct. 2014.

[185] Y. Ma, X. Yi, S. Wang, T. Li, B. Tan, C. Chen, T. Majima, E. R. Waclawik, H. Zhu, and J. Wang, "Selective photocatalytic CO_2 reduction in aerobic environment by microporous Pd-porphyrin-based polymers coated hollow TiO_2," *Nature Communications*, vol. 13, p. 1400, Mar. 2022.

[186] T. Yui, A. Kan, C. Saitoh, K. Koike, T. Ibusuki, and O. Ishitani, "Photochemical Reduction of CO_2 Using TiO_2 : Effects of Organic Adsorbates on TiO_2 and Deposition of Pd onto TiO_2," *ACS Applied Materials & Interfaces*, vol. 3, pp. 2594–2600, July 2011.

[187] K.-Y. Su, C.-Y. Chen, and R.-J. Wu, "Preparation of Pd/TiO_2 nanowires for the photoreduction of CO_2 into renewable hydrocarbon fuels," *Journal of the Taiwan Institute of Chemical Engineers*, vol. 96, pp. 409–418, Mar. 2019.

[188] Y. Jiang, H. Chen, J. Li, J. Liao, H. Zhang, X. Wang, and D. Kuang, "Z-Scheme 2D/2D Heterojunction of $CsPbBr_3$ /Bi_2 WO_6 for Improved Photocatalytic CO_2 Reduction," *Advanced Functional Materials*, vol. 30, p. 2004293, Dec. 2020.

[189] S. M. Kim, C. Lee, K. C. Goddeti, and J. Y. Park, "Hot plasmonic electron-driven catalytic reactions on patterned metal–insulator–metal nanostructures," *Nanoscale*, vol. 9, no. 32, pp. 11667–11677, 2017.

[190] J. W. Sadowski, J. Lekkala, and I. Vikholm, "Biosensors based on surface plasmons excited in non-noble metals," *Biosensors and Bioelectronics*, vol. 6, pp. 439–444, Jan. 1991.

[191] F. Yan, Y. Wang, J. Zhang, Z. Lin, J. Zheng, and F. Huang, "Schottky or Ohmic Metal–Semiconductor Contact: Influence on Photocatalytic Efficiency of Ag/ZnO and Pt/ZnO Model Systems," *ChemSusChem*, vol. 7, pp. 101–104, Jan. 2014.

[192] A. Ziashahabi, M. Prato, Z. Dang, R. Poursalehi, and N. Naseri, "The effect of silver oxidation on the photocatalytic activity of Ag/ZnO hybrid plasmonic/metal-oxide nanostructures under visible light and in the dark," *Scientific Reports*, vol. 9, p. 11839, Aug. 2019.

[193] C. Casado, J. Marugán, R. Timmers, M. Muñoz, and R. Van Grieken, "Comprehensive multiphysics modeling of photocatalytic processes by computational fluid dynamics based on intrinsic kinetic parameters determined in a differential photoreactor," *Chemical Engineering Journal*, vol. 310, pp. 368–380, Feb. 2017.

[194] R. Li, J. Luan, Y. Zhang, L. Jiang, H. Yan, Q. Chi, and Z. Yan, "A review of efficient photocatalytic water splitting for hydrogen production," *Renewable and Sustainable Energy Reviews*, vol. 206, p. 114863, Dec. 2024.

[195] K. S. Novoselov, A. K. Geim, S. V. Morozov, D. Jiang, Y. Zhang, S. V. Dubonos, I. V. Grigorieva, and A. A. Firsov, "Electric Field Effect in Atomically Thin Carbon Films," *Science*, vol. 306, pp. 666–669, Oct. 2004.

[196] R. Mas-Ballesté, C. Gómez-Navarro, J. Gómez-Herrero, and F. Zamora, "2D materials: to graphene and beyond," *Nanoscale*, vol. 3, no. 1, pp. 20–30, 2011.

[197] Y. Xu, S. Li, M. Chen, J. Zhang, and F. Rosei, "Carbon-based nanostructures for emerging photocatalysis: CO_2 reduction, N_2 fixation, and organic conversion," *Trends in Chemistry*, vol. 4, pp. 984–1004, Nov. 2022.

[198] X. Liang, B. A. Sperling, I. Calizo, G. Cheng, C. A. Hacker, Q. Zhang, Y. Obeng, K. Yan, H. Peng, Q. Li, X. Zhu, H. Yuan, A. R. Hight Walker, Z. Liu, L.-m. Peng, and C. A. Richter, "Toward Clean and Crackless Transfer of Graphene," *ACS Nano*, vol. 5, pp. 9144–9153, Nov. 2011.

[199] N. T. Padmanabhan, N. Thomas, J. Louis, D. T. Mathew, P. Ganguly, H. John, and S. C. Pillai, "Graphene coupled TiO_2 photocatalysts for environmental applications: A review," *Chemosphere*, vol. 271, p. 129506, May 2021.

[200] Y. Zhang, L. Zhang, and C. Zhou, "Review of Chemical Vapor Deposition of Graphene and Related Applications," *Accounts of Chemical Research*, vol. 46, pp. 2329–2339, Oct. 2013.

[201] L. Guo, Z. Zhang, H. Sun, D. Dai, J. Cui, M. Li, Y. Xu, M. Xu, Y. Du, N. Jiang, F. Huang, and C.-T. Lin, "Direct formation of wafer-scale single-layer graphene films on the rough surface substrate by PECVD," *Carbon*, vol. 129, pp. 456–461, Apr. 2018.

[202] G. Giovannetti, P. A. Khomyakov, G. Brocks, V. M. Karpan, J. Van Den Brink, and P. J. Kelly, "Doping Graphene with Metal Contacts," *Physical Review Letters*, vol. 101, p. 026803, July 2008.

[203] P. A. Khomyakov, G. Giovannetti, P. C. Rusu, G. Brocks, J. Van Den Brink, and P. J. Kelly, "First-principles study of the interaction and charge transfer between graphene and metals," *Physical Review B*, vol. 79, p. 195425, May 2009.

[204] D. O. Scanlon, C. W. Dunnill, J. Buckeridge, S. A. Shevlin, A. J. Logsdail, S. M. Woodley, C. R. A. Catlow, M. J. Powell, R. G. Palgrave, I. P. Parkin, G. W. Watson, T. W. Keal, P. Sherwood, A. Walsh, and A. A. Sokol, "Band alignment of rutile and anatase TiO_2," *Nature Materials*, vol. 12, pp. 798–801, Sept. 2013.

[205] A. C. Ferrari, J. C. Meyer, V. Scardaci, C. Casiraghi, M. Lazzeri, F. Mauri, S. Piscanec, D. Jiang, K. S. Novoselov, S. Roth, and A. K. Geim, "Raman Spectrum of Graphene and Graphene Layers," *Physical Review Letters*, vol. 97, p. 187401, Oct. 2006.

[206] V. Kumar, A. Kumar, D.-J. Lee, and S.-S. Park, "Estimation of Number of Graphene Layers Using Different Methods: A Focused Review," *Materials*, vol. 14, p. 4590, Aug. 2021.

[207] A. J. Pollard, B. Brennan, H. Stec, B. J. Tyler, M. P. Seah, I. S. Gilmore, and D. Roy, "Quantitative characterization of defect size in graphene using Raman spectroscopy," *Applied Physics Letters*, vol. 105, p. 253107, Dec. 2014.

[208] L. Bokobza, J.-L. Bruneel, and M. Couzi, "Raman Spectra of Carbon-Based Materials (from Graphite to Carbon Black) and of Some Silicone Composites," *C*, vol. 1, pp. 77–94, Dec. 2015.

[209] M. Pawlyta, J.-N. Rouzaud, and S. Duber, "Raman microspectroscopy characterization of carbon blacks: Spectral analysis and structural information," *Carbon*, vol. 84, pp. 479–490, Apr. 2015.

[210] S. Wang, M. Xu, T. Peng, C. Zhang, T. Li, I. Hussain, J. Wang, and B. Tan, "Porous hypercrosslinked polymer-TiO_2-graphene composite photocatalysts for visible-light-driven CO_2 conversion," *Nature Communications*, vol. 10, p. 676, Feb. 2019.

[211] W. Tu, Y. Zhou, Q. Liu, S. Yan, S. Bao, X. Wang, M. Xiao, and Z. Zou, "An In Situ Simultaneous Reduction-Hydrolysis Technique for Fabrication of TiO_2 -Graphene 2D Sandwich-Like Hybrid Nanosheets: Graphene-Promoted Selectivity of Photocatalytic-Driven Hydrogenation and Coupling of CO_2 into Methane and Ethane," *Advanced Functional Materials*, vol. 23, pp. 1743–1749, Apr. 2013.

[212] L. Wang, B. Zhu, B. Cheng, J. Zhang, L. Zhang, and J. Yu, "In-situ preparation of TiO_2/N-doped graphene hollow sphere photocatalyst with enhanced photocatalytic CO_2 reduction performance," *Chinese Journal of Catalysis*, vol. 42, pp. 1648–1658, Oct. 2021.

[213] Y. Xia, Z. Tian, T. Heil, A. Meng, B. Cheng, S. Cao, J. Yu, and M. Antonietti, "Highly Selective CO_2 Capture and Its Direct Photochemical Conversion on Ordered 2D/1D Heterojunctions," *Joule*, vol. 3, pp. 2792–2805, Nov. 2019.

[214] C. Bie, B. Zhu, F. Xu, L. Zhang, and J. Yu, "In Situ Grown Monolayer N-Doped Graphene on CdS Hollow Spheres with Seamless Contact for Photocatalytic CO_2 Reduction," *Advanced Materials*, vol. 31, p. 1902868, Oct. 2019.

[215] C. J. Shearer, A. D. Slattery, A. J. Stapleton, J. G. Shapter, and C. T. Gibson, "Accurate thickness measurement of graphene," *Nanotechnology*, vol. 27, p. 125704, Mar. 2016.

[216] S. Huang, C. Song, G. Zhang, and H. Yan, "Graphene plasmonics: physics and potential applications," *Nanophotonics*, vol. 6, pp. 1191–1204, Oct. 2016.

[217] F. J. García De Abajo, "Graphene Plasmonics: Challenges and Opportunities," *ACS Photonics*, vol. 1, pp. 135–152, Mar. 2014.

[218] R. Liu, T. Gong, K. Zhang, and C. Lee, "Graphene oxide papers with high water adsorption capacity for air dehumidification," *Scientific Reports*, vol. 7, p. 9761, Aug. 2017.

[219] M. Isah, R. Lawal, and S. A. Onaizi, "CO_2 capture and conversion using graphene-based materials: A review on recent progresses and future outlooks," *Green Chemical Engineering*, p. S2666952824000827, Sept. 2024.

[220] N. Takeda, N. Iwata, T. Torimoto, and H. Yoneyama, "Influence of carbon black as an adsorbent used in TiO_2 photocatalyst films on photodegradation behaviors of propyzamide," *Journal of Catalysis*, vol. 177, pp. 240–246, July 1998.

[221] S. Varnagiris, A. Medvids, M. Lelis, D. Milcius, and A. Antuzevics, "Black carbon-doped TiO_2 films: Synthesis, characterization and photocatalysis," *Journal of Photochemistry and Photobiology A: Chemistry*, vol. 382, p. 111941, Sept. 2019.

[222] B. Tang, H. Chen, Y. He, Z. Wang, J. Zhang, and J. Wang, "Influence from defects of three-dimensional graphene network on photocatalytic performance of composite photocatalyst," *Composites Science and Technology*, vol. 150, pp. 54–64, Sept. 2017.

[223] J. Zeng, Z. Li, H. Jiang, and X. Wang, "Progress on photocatalytic semiconductor hybrids for bacterial inactivation," *Materials Horizons*, vol. 8, no. 11, pp. 2964–3008, 2021.

[224] C. Liu, D. Kong, P.-C. Hsu, H. Yuan, H.-W. Lee, Y. Liu, H. Wang, S. Wang, K. Yan, D. Lin, P. A. Maraccini, K. M. Parker, A. B. Boehm, and Y. Cui, "Rapid water disinfection using vertically aligned MoS_2 nanofilms and visible light," *Nature Nanotechnology*, vol. 11, pp. 1098–1104, Dec. 2016.

[225] A. Sethulekshmi, A. Saritha, K. Joseph, A. S. Aprem, and S. B. Sisupal, "MoS_2 based nanomaterials: Advanced antibacterial agents for future," *Journal of Controlled Release*, vol. 348, pp. 158–185, Aug. 2022.

[226] J. Shen, J. Liu, X. Fan, H. Liu, Y. Bao, A. Hui, and H. A. Munir, "Unveiling the antibacterial strategies and mechanisms of MoS_2 : a comprehensive analysis and future directions," *Biomaterials Science*, vol. 12, no. 3, pp. 596–620, 2024.

[227] M. Belete, S. Kataria, U. Koch, M. Kruth, C. Engelhard, J. Mayer, O. Engström, and M. C. Lemme, "Dielectric Properties and Ion Transport in Layered MoS_2 Grown by Vapor-Phase Sulfurization for Potential Applications in Nanoelectronics," *ACS Applied Nano Materials*, vol. 1, pp. 6197–6204, Nov. 2018.

[228] R. Bhatt, S. Bhattacharya, R. Basu, A. Singh, U. Deshpande, C. Surger, S. Basu, D. Aswal, and S. Gupta, "Growth of Pd_4S, PdS and PdS_2 films by controlled sulfurization of sputtered Pd on native oxide of Si," *Thin Solid Films*, vol. 539, pp. 41–46, July 2013.

[229] R. G. Dickinson and L. Pauling, "THE CRYSTAL STRUCTURE OF MOLYBDENITE," *Journal of the American Chemical Society*, vol. 45, pp. 1466–1471, June 1923.

[230] R. F. Frindt, "Single Crystals of MoS_2 Several Molecular Layers Thick," *Journal of Applied Physics*, vol. 37, pp. 1928–1929, Mar. 1966.

[231] Y. Zou, C. Cheng, Y. Guo, A. J. Ong, R. Goei, S. Li, and A. I. Yoong Tok, "Atomic layer deposition of rhodium and palladium thin film using low-concentration ozone," *RSC Advances*, vol. 11, no. 37, pp. 22773–22779, 2021.

[232] L.-C. Chen, Q. Peng, H. Yu, H.-J. Pang, B.-B. Jiang, L. Su, X. Shi, L.-D. Chen, and X.-J. Chen, "Lattice dynamics of thermoelectric palladium sulfide," *Journal of Alloys and Compounds*, vol. 798, pp. 484–492, Aug. 2019.

[233] H. Li, Q. Zhang, C. C. R. Yap, B. K. Tay, T. H. T. Edwin, A. Olivier, and D. Baillargeat, "From Bulk to Monolayer MoS_2 : Evolution of Raman Scattering," *Advanced Functional Materials*, vol. 22, pp. 1385–1390, Apr. 2012.

[234] L. Yang, X. Cui, J. Zhang, K. Wang, M. Shen, S. Zeng, S. A. Dayeh, L. Feng, and B. Xiang, "Lattice strain effects on the optical properties of MoS_2 nanosheets," *Scientific Reports*, vol. 4, p. 5649, July 2014.

[235] N. Wu, Y. Yu, T. Li, X. Ji, L. Jiang, J. Zong, and H. Huang, "Investigating the Influence of MoS_2 Nanosheets on E. coli from Metabolomics Level," *PLOS ONE*, vol. 11, p. e0167245, Dec. 2016.

[236] C. Zhang, Y. Li, C. Wang, and X. Zheng, "Different inactivation behaviors and mechanisms of representative pathogens (Escherichia coli bacteria, human adenoviruses and Bacillus subtilis spores) in g-C_3N_4-based metal-free visible-light-enabled photocatalytic disinfection," *Science of The Total Environment*, vol. 755, p. 142588, Feb. 2021.

[237] M. Wang, B. L. Bodirsky, R. Rijneveld, F. Beier, M. P. Bak, M. Batool, B. Droppers, A. Popp, M. T. H. Van Vliet, and M. Strokal, "A triple increase in global river basins with water scarcity due to future pollution," *Nature Communications*, vol. 15, p. 880, Feb. 2024.

[238] A. Panhwar, A. Sattar Jatoi, S. Ali Mazari, A. Kandhro, U. Rashid, and S. Qaisar, "Water resources contamination and health hazards by textile industry effluent and glance at treatment techniques: A review," *Waste Management Bulletin*, vol. 1, pp. 158–163, Mar. 2024.

[239] E. Serra-Pérez, G. Dražić, M. Takashima, B. Ohtani, S. Kovačič, G. Žerjav, and N. N. Tušar, "Influence of the surface structure of the TiO_2 support on the properties of the Au/TiO_2 photocatalyst for water treatment under visible light," *Catalysis Today*, vol. 437, p. 114764, July 2024.

[240] Z. Peng, Y. Zhang, C. L. R. Choi, P. Zhang, T. Wu, and Y. K. Chan, "Continuous roller nanoimprinting: next generation lithography," *Nanoscale*, vol. 15, no. 27, pp. 11403–11421, 2023.

[241] R. Binjhade, R. Mondal, and S. Mondal, "Continuous photocatalytic reactor: Critical review on the design and performance," *Journal of Environmental Chemical Engineering*, vol. 10, p. 107746, June 2022.

[242] M. M. Kandy and V. G. Gaikar, "Enhanced photocatalytic reduction of CO_2 using CdS/Mn_2O_3 nanocomposite photocatalysts on porous anodic alumina support with solar concentrators," *Renewable Energy*, vol. 139, pp. 915–923, Aug. 2019.

[243] S. Fang and Y. H. Hu, "Thermo-photo catalysis: a whole greater than the sum of its parts," *Chemical Society Reviews*, vol. 51, no. 9, pp. 3609–3647, 2022.

[244] Z. Chai, "Light-Driven Alcohol Splitting by Heterogeneous Photocatalysis: Recent Advances, Mechanism and Prospects," *Chemistry – An Asian Journal*, vol. 16, pp. 460–473, Mar. 2021.

[245] M. Lou, J. L. Bao, L. Zhou, G. N. Naidu, H. Robatjazi, A. I. Bayles, H. O. Everitt, P. Nordlander, E. A. Carter, and N. J. Halas, "Direct H_2S Decomposition by Plasmonic Photocatalysis: Efficient Remediation plus Sustainable Hydrogen Production," *ACS Energy Letters*, vol. 7, pp. 3666–3674, Oct. 2022.

[246] L. S. Frowijn and W. G. Van Sark, "Analysis of photon-driven solar-to-hydrogen production methods in the Netherlands," *Sustainable Energy Technologies and Assessments*, vol. 48, p. 101631, Dec. 2021.

[247] P. Nikolaidis and A. Poullikkas, "A comparative overview of hydrogen production processes," *Renewable and Sustainable Energy Reviews*, vol. 67, pp. 597–611, Jan. 2017.

[248] J.-i. Fujisawa, T. Eda, and M. Hanaya, "Comparative study of conduction-band and valence-band edges of TiO_2, $SrTiO_3$, and $BaTiO_3$ by ionization potential measurements," *Chemical Physics Letters*, vol. 685, pp. 23–26, Oct. 2017.

[249] V. Mansfeldova, M. Zlamalova, H. Tarabkova, P. Janda, M. Vorokhta, L. Piliai, and L. Kavan, "Work Function of TiO_2 (Anatase, Rutile, and Brookite) Single Crystals: Effects of the Environment," *The Journal of Physical Chemistry C*, vol. 125, pp. 1902–1912, Jan. 2021.

[250] F. A. Rasmussen and K. S. Thygesen, "Computational 2D Materials Database: Electronic Structure of Transition-Metal Dichalcogenides and Oxides," *The Journal of Physical Chemistry C*, vol. 119, pp. 13169–13183, June 2015.

[251] L. A. H. Jones, Z. Xing, J. E. N. Swallow, H. Shiel, T. J. Featherstone, M. J. Smiles, N. Fleck, P. K. Thakur, T.-L. Lee, L. J. Hardwick, D. O. Scanlon, A. Regoutz, T. D. Veal, and V. R. Dhanak, "Band Alignments, Electronic Structure, and Core-Level Spectra of Bulk Molybdenum Dichalcogenides (MoS_2 , $MoSe_2$, and $MoTe_2$)," *The Journal of Physical Chemistry C*, vol. 126, pp. 21022–21033, Dec. 2022.

[252] M. Barawi, I. J. Ferrer, J. R. Ares, and C. Sánchez, "Hydrogen Evolution Using Palladium Sulfide (PdS) Nanocorals as Photoanodes in Aqueous Solution," *ACS Applied Materials & Interfaces*, vol. 6, pp. 20544–20549, Nov. 2014.

[253] P. T. Moseley, "Progress in the development of semiconducting metal oxide gas sensors: a review," *Measurement Science and Technology*, vol. 28, p. 082001, Aug. 2017.